Advances in Materials Science and Engineering

Materials for Electrical Insulation and Dielectrics Technologies

Lead Guest Editor: Ravi Samikannu
Guest Editors: Albert Alexander Stonier and Kumarasamy Sathiyasekar

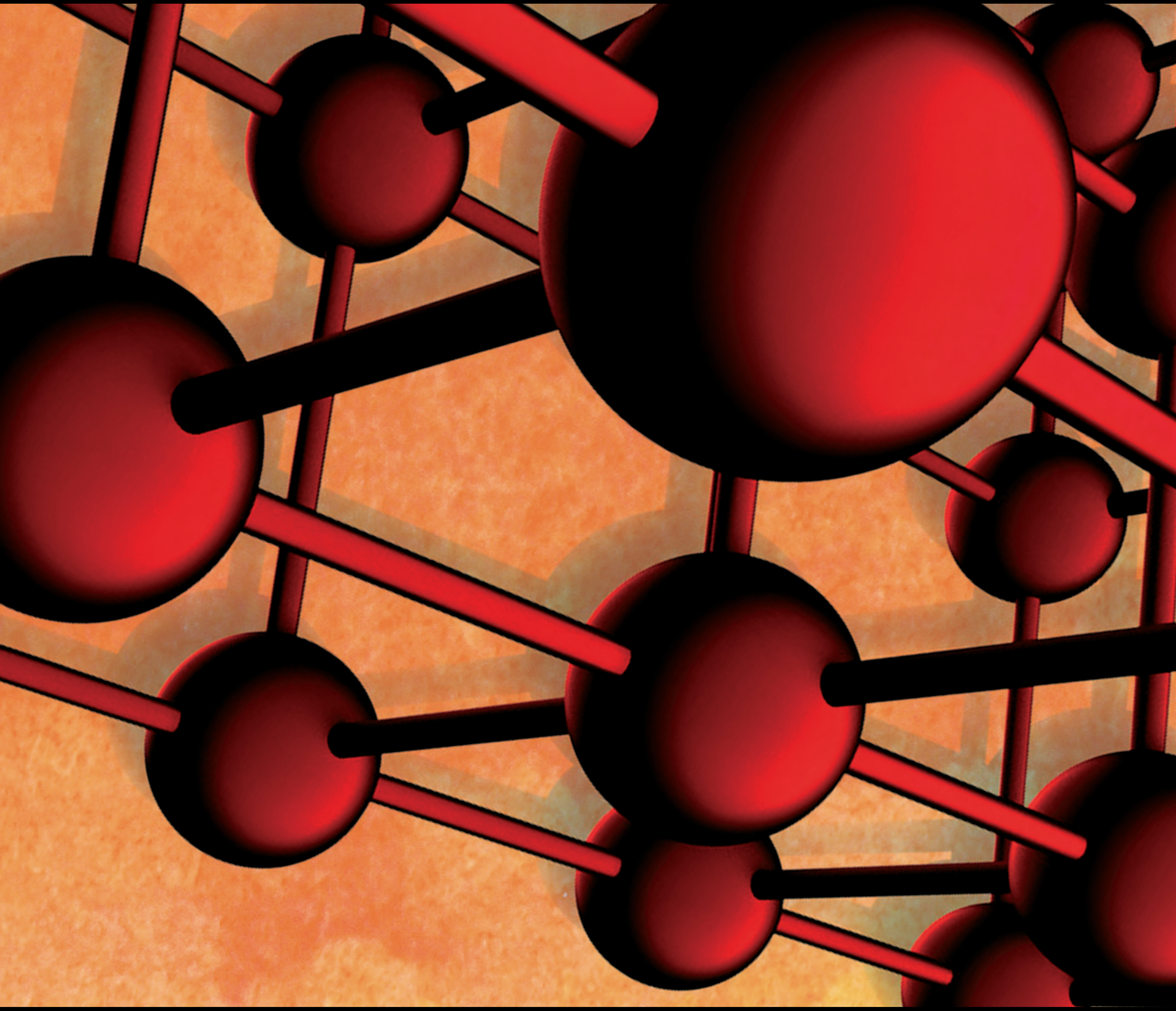

Materials for Electrical Insulation and Dielectrics Technologies

Materials for Electrical Insulation and Dielectrics Technologies

Lead Guest Editor: Ravi Samikannu
Guest Editors: Albert Alexander Stonier and Kumarasamy Sathiyasekar

Claudio Pettinari, Italy
Giorgio Pia, Italy
Candido Fabrizio Pirri, Italy
Marinos Pitsikalis, Greece
Alain Portavoce, France
Simon C. Potter, Canada
Ulrich Prahl, Germany
Veena Ragupathi, India
Kawaljit singh Randhawa, India
Baskaran Rangasamy, Zambia
Paulo Reis, Portugal
Hilda E. Reynel-Avila, Mexico
Yuri Ribakov, Israel
Aniello Riccio, Italy
Anna Richelli, Italy
Antonio Riveiro, Spain
Marco Rossi, Italy
Fernando Rubio-Marcos, Spain
Francesco Ruffino, Italy
Giuseppe Ruta, Italy
Sachin Salunkhe, India
P Sangeetha, India
Carlo Santulli, Italy
Fabrizio Sarasini, Italy
Senthil Kumaran Selvaraj, India
Raffaele Sepe, Italy
Aabid H Shalla, India
Poorva Sharma, China
Mercedes Solla, Spain
Tushar Sonar, Russia
Donato Sorgente, Italy
Charles C. Sorrell, Australia
Damien Soulat, France
Adolfo Speghini, Italy
Antonino Squillace, Italy
Koichi Sugimoto, Japan
Jirapornchai Suksaeree, Thailand
Baozhong Sun, China
Sam-Shajing Sun, USA
Xiaolong Sun, China
Yongding Tian, China
Hao Tong, China
Achim Trampert, Germany
Tomasz Trzepieciński, Poland
Kavimani V, India
Matjaz Valant, Slovenia
Mostafa Vamegh, Iran
Lijing Wang, Australia
Jörg M. K. Wiezorek, USA
Guosong Wu, China
Junhui Xiao, China
Guoqiang Xie, China
YASHPAL YASHPAL, India
Anil Singh Yadav, India
Yee-wen Yen, Taiwan
Hao Yi, China
Wenbin Yi, China
Tetsu Yonezawa, Japan
Hiroshi Yoshihara, Japan
Bin Yu, China
Rahadian Zainul, Indonesia
Lenka Zaji#c#kova#, Czech Republic
Zhigang Zang, China
Michele Zappalorto, Italy
Gang Zhang, Singapore
Jinghuai Zhang, China
Zengping Zhang, China
You Zhou, Japan
Robert Černý, Czech Republic

Contents

Hindawi
Advances in Materials Science and Engineering
Volume 2024, Article ID 9840238, 1 page
https://doi.org/10.1155/2024/9840238

Retraction

Retracted: Genetic Algorithm Integrated Fuzzy AHP-VIKOR Approach for the Investigation of W-Cut Insert Heat Exchanger for Cooling of Dielectric Fluid Used in Ultra-High Voltage Transformer

Advances in Materials Science and Engineering

Received 8 January 2024; Accepted 8 January 2024; Published 9 January 2024

This article has been retracted by Hindawi following an investigation undertaken by the publisher [1]. This investigation has uncovered evidence of one or more of the following indicators of systematic manipulation of the publication process:

(1) Discrepancies in scope
(2) Discrepancies in the description of the research reported
(3) Discrepancies between the availability of data and the research described
(4) Inappropriate citations
(5) Incoherent, meaningless and/or irrelevant content included in the article
(6) Manipulated or compromised peer review

The presence of these indicators undermines our confidence in the integrity of the article's content and we cannot, therefore, vouch for its reliability. Please note that this notice is intended solely to alert readers that the content of this article is unreliable. We have not investigated whether authors were aware of or involved in the systematic manipulation of the publication process.

Wiley and Hindawi regrets that the usual quality checks did not identify these issues before publication and have since put additional measures in place to safeguard research integrity.

We wish to credit our own Research Integrity and Research Publishing teams and anonymous and named external researchers and research integrity experts for contributing to this investigation.

The corresponding author, as the representative of all authors, has been given the opportunity to register their agreement or disagreement to this retraction. We have kept a record of any response received.

References

[1] N. V. Gowri, J. S. Isaac, T. Muralikrishna et al., "Genetic Algorithm Integrated Fuzzy AHP-VIKOR Approach for the Investigation of W-Cut Insert Heat Exchanger for Cooling of Dielectric Fluid Used in Ultra-High Voltage Transformer," *Advances in Materials Science and Engineering*, vol. 2022, Article ID 2819688, 24 pages, 2022.

Hindawi
Advances in Materials Science and Engineering
Volume 2024, Article ID 9810320, 1 page
https://doi.org/10.1155/2024/9810320

Retraction

Retracted: Improvement of Microstructure and Properties of Q235 Steel by Iron-Based Laser Cladding Coating

Advances in Materials Science and Engineering

Received 8 January 2024; Accepted 8 January 2024; Published 9 January 2024

This article has been retracted by Hindawi following an investigation undertaken by the publisher [1]. This investigation has uncovered evidence of one or more of the following indicators of systematic manipulation of the publication process:

(1) Discrepancies in scope
(2) Discrepancies in the description of the research reported
(3) Discrepancies between the availability of data and the research described
(4) Inappropriate citations
(5) Incoherent, meaningless and/or irrelevant content included in the article
(6) Manipulated or compromised peer review

The presence of these indicators undermines our confidence in the integrity of the article's content and we cannot, therefore, vouch for its reliability. Please note that this notice is intended solely to alert readers that the content of this article is unreliable. We have not investigated whether authors were aware of or involved in the systematic manipulation of the publication process.

Wiley and Hindawi regrets that the usual quality checks did not identify these issues before publication and have since put additional measures in place to safeguard research integrity.

We wish to credit our own Research Integrity and Research Publishing teams and anonymous and named external researchers and research integrity experts for contributing to this investigation.

The corresponding author, as the representative of all authors, has been given the opportunity to register their agreement or disagreement to this retraction. We have kept a record of any response received.

References

[1] Y. He, Y. Gu, L. Tang, and H. Wang, "Improvement of Microstructure and Properties of Q235 Steel by Iron-Based Laser Cladding Coating," *Advances in Materials Science and Engineering*, vol. 2022, Article ID 2790770, 9 pages, 2022.

Hindawi
Advances in Materials Science and Engineering
Volume 2023, Article ID 9847204, 1 page
https://doi.org/10.1155/2023/9847204

Retraction

Retracted: Interfacial Transport Study of Ultra-Thin InN-Enhanced Quantum Dot Solar Cells

Advances in Materials Science and Engineering

Received 26 September 2023; Accepted 26 September 2023; Published 27 September 2023

This article has been retracted by Hindawi following an investigation undertaken by the publisher [1]. This investigation has uncovered evidence of one or more of the following indicators of systematic manipulation of the publication process:

(1) Discrepancies in scope
(2) Discrepancies in the description of the research reported
(3) Discrepancies between the availability of data and the research described
(4) Inappropriate citations
(5) Incoherent, meaningless and/or irrelevant content included in the article
(6) Peer-review manipulation

The presence of these indicators undermines our confidence in the integrity of the article's content and we cannot, therefore, vouch for its reliability. Please note that this notice is intended solely to alert readers that the content of this article is unreliable. We have not investigated whether authors were aware of or involved in the systematic manipulation of the publication process.

Wiley and Hindawi regrets that the usual quality checks did not identify these issues before publication and have since put additional measures in place to safeguard research integrity.

We wish to credit our own Research Integrity and Research Publishing teams and anonymous and named external researchers and research integrity experts for contributing to this investigation.

The corresponding author, as the representative of all authors, has been given the opportunity to register their agreement or disagreement to this retraction. We have kept a record of any response received.

References

[1] S. Wang, D. Zhang, and Z. Ju, "Interfacial Transport Study of Ultra-Thin InN-Enhanced Quantum Dot Solar Cells," *Advances in Materials Science and Engineering*, vol. 2022, Article ID 5862204, 10 pages, 2022.

Hindawi
Advances in Materials Science and Engineering
Volume 2023, Article ID 1346872, 8 pages
https://doi.org/10.1155/2023/1346872

Research Article

Reaction Gas Pressure, Temperature, and Membrane Water Content Modulate Electrochemical Process of a PEMFC: A Simulation Study

Bin Xia,[1] Pengyan Guo,[2] Xinjing Wei,[2] and Hehui Zong[2]

[1]*Henan Agricultural University, College of Information and Management Science, Zhengzhou 450002, Henan, China*
[2]*North China University of Water Resources and Electric Power, School of Mechanical Engineering, Zhengzhou 450002, Henan, China*

Correspondence should be addressed to Pengyan Guo; tr@bbc.edu.cn

Received 1 July 2022; Revised 3 August 2022; Accepted 5 August 2022; Published 20 May 2023

Academic Editor: Ravi Samikannu

Proton exchange membrane fuel cells (PEMFC) are widely used in transportation systems owing to their desirable characteristics such as high efficacy and low operating temperature. However, the fuel cell systems exhibit load changes as well as voltage and power losses so as to reduce dependence on the battery. The aim of the present study was to explore the composition and basic working principle of PEMFC. A PEMFC electrochemical reaction model was then established according to the electrochemical reaction principle of fuel cell to evaluate the effects of Nernst electromotive force, activation overvoltage, Ohmic overvoltage, concentration overvoltage, and electric double layer. The effects of activation loss, concentration loss, and Ohmic loss on the fuel cell were evaluated through simulation analysis. The effect of various factors on the dynamic output of a 60 kW PEMFC was explored through dynamic simulations. The findings showed that a change in current modulated a change in voltage through the Ohmic loss equivalent resistance. The activation loss equivalent resistance and the concentration loss equivalent resistance decreased the voltage loss owing to the presence of the capacitor. The output voltage of the fuel cell decreased with an increase in load current, whereas the output power increased with an increase in load current. Increase in partial pressure of oxygen caused an increase in output power and output voltage of the cell. The internal chemical reaction rate and the voltage output of the fuel cell increases with an increase in the working temperature. The findings of this study provide a basis for conducting further studies to produce efficient fuel cells for application in various systems.

1. Introduction

A fuel cell is an electrochemical reactor that directly converts chemical energy into electrical energy without burning it [1–3]. Fuel cells exist in different types, and each type has distinct temperature requirements. Low-temperature fuel cells typically work at temperatures below 200°C, and excessive temperatures damage the electrolyte in these types of fuel cells. Low-temperature fuel cells include alkaline fuel cell (AFC), phosphoric acid fuel cell (PAFC), and proton exchange membrane fuel cell (PEMFC). Low-temperature fuel cells use platinum (Pt) as catalyst. Platinum is very sensitive to carbon monoxide; therefore, this type of fuel cell uses pure hydrogen as fuel. High temperature fuel cells can directly oxidize other hydrocarbon fuels (such as methane). Fuel cells that directly oxidize hydrocarbon fuels include molten carbonate fuel cells (MCFC) and solid oxide fuel cells (600–1000°C). The operation temperature range of these fuel cells is 600–700°C.

The PEM fuel cell is a fuel cell type that works under a temperature range of 50–80°C. This fuel cell consists a polymer electrolyte membrane placed between two gas diffusion layers and two electrodes. The layers facilitate hydrogen and oxygen reactions at the anode and cathode, respectively. The PEM fuel cell type is characterized by high working efficiency (40%–50%), fast startup, relatively good power density, and high reliability. PEM fuel cell is widely used in various fields. Therefore, the current study sought to

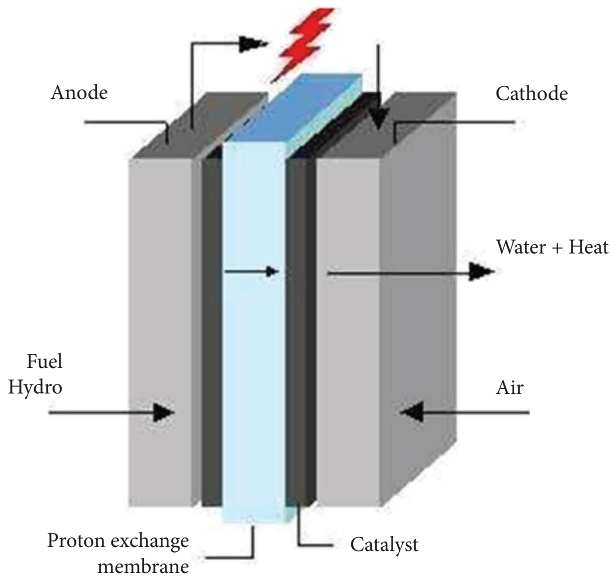

Figure 1: A representation of the working principle of PEMFC.

explore the potential application of PEMFC as a vehicle energy source.

The working principle of the hydrogen-oxygen fuel cell is the reverse process of electrolysis of water. The electrochemical reaction between hydrogen at the anode and air at the cathode leads to conversion of chemical energy into electrical energy that can be used in various equipment. A continuous supply of hydrogen and air must be supplied to the anode and cathode of the proton exchange membrane fuel cell, respectively, for generation of electricity. Hydrogen and air penetrate the flow field structure of the bipolar plate and diffuse to the anode and cathode, respectively, through the diffusion layer (Figure 1). Hydrogen at the anode releases an electron to become a proton under the action of the catalyst. An electric current is generated through flow of electrons along the external circuit, which drives the load and is transferred to the cathode. The electron combines with oxygen to become oxygen ions in the presence of a catalyst. The protons are transferred to the cathode through the selective passage across the proton exchange membrane. The protons combine with cations at the cathode to generate water molecules [4, 5]. The water generated at the cathode is released through the flow channel under the purging action of the cathode air. The electrochemical reaction in the fuel cell is characterized by generation of heat. Therefore, it is imperative to include cooling channels on the bipolar plate to regulate the temperature of the fuel cell.

2. PEMFC Electrochemical Model

The aim of this study was to explore the overall output performance and factors that affect operation of PEMFC. In the current study, the effect of the spatial location difference of variables in the internal structure of PEMFC was not evaluated. The lumped parameter modeling method was adopted in this study to study performance of the PEMFC system. The fuel cell stack is referred as a DC power supply if the fuel cell air, hydrogen, and cooling water output are stable. The fuel cell stack voltage is an essential performance indicator of the fuel cell. Each single cell is assumed to be consistent when establishing the lumped parameter PEMFC model. In addition, the external output voltage of the fuel cell is defined as the sum of the levels of voltage generated by all the cells.

Therefore, the fuel cell voltage V_{st} is expressed as shown in the following formula:

$$V_{\mathrm{st}} = n_{\mathrm{cell}} V_{fc}, \tag{1}$$

where n_{cell} represents the number of single cells and V_{fc} represents the voltage of single cells.

The current generated by the fuel cell is directly proportional to the level of fuel consumed. This implies that n moles of electrons are provided for each mole of fuel. As a result, a decrease in the fuel cell voltage is associated with a decrease in the electrical power produced per unit of fuel. The fuel cell output voltage can thus be used to determine the efficiency of the fuel cell. Notably, maintaining a high voltage under current load is challenging, and the output voltage of actual fuel cells is lower than the voltage output predicted under thermodynamic theory. Previous studies report three primary types of loss of output voltage of fuel cells, namely activation loss, Ohmic loss, and concentration loss. The definite output voltage of the fuel cell is obtained by the difference between the thermodynamically predicted voltage output and the voltage drop due to the three types losses, as shown below.

$$V_{\mathrm{fc}} = E - v_{\mathrm{act}} - v_{\mathrm{ohm}} - v_{\mathrm{conc}}, \tag{2}$$

where E denotes the thermodynamically predicted open circuit voltage, also referred as the Nernst voltage; v_{act} represents the activation overvoltage; v_{ohm} indicates the Ohmic overvoltage; v_{conc} represents the concentration overvoltage.

The reversible voltage E^0 of the hydrogen-oxygen fuel cell under the standard state and the Gibbs free energy ΔG^0 released by the chemical reaction of hydrogen oxidation are governed by the following relationship:

$$\Delta G^0 = -nFE^0, \tag{3}$$

where the number of electrons transferred by the hydrogen reaction is 2 mol, thus n is 2. ΔG^0 is −273.2 kJ in thermodynamics. Gibbs free energy represents the maximum amount of work performed by a thermodynamic system at a constant pressure and temperature.

The reversible voltage is affected by temperature changes, and the effect by the change in temperature is expressed as shown in the following formula:

$$E^T = E^0 + \frac{\Delta S}{nF}\left(T_{st} - 298.15\right), \tag{4}$$

where ΔS represents the thermodynamic entropy change of the chemical reaction of hydrogen oxidation, which is equal to 164.025 J/mol•K, and T_{st} indicates the operating temperature (K) of the fuel cell stack.

Change in reversible voltage with the concentration of reactants is expressed as shown in the following formula:

$$E^C = E^0 - \frac{RT_{st}}{2F} \ln \frac{1}{\left. p_{an}^{H_2} p_{ca}^{O_2} 1/2 \right)}, \quad (5)$$

where $p_{an}^{H_2}$ represents the partial pressure of hydrogen and $p_{ca}^{O_2}$ represents the partial pressure of oxygen.

The reversible voltage at different temperatures and reactant concentrations can be determined by combining formulas (3)–(5) to obtain the Nernst voltage of the electrochemical reaction of hydrogen and oxygen, as presented in the following formula:

$$E = -\frac{\Delta G^0}{2F} + \frac{\Delta S}{2F}(T_{st} - 298.15) + \frac{RT_{st}}{2F}\left[\ln\left(p_{an}^{H_2}\right) + \frac{1}{2}\ln\left(p_{ca}^{O_2}\right)\right]. \quad (6)$$

Activation polarization is irreversible and is the main cause of decrease in voltage. Electrons should break and form covalent bonds during transfer from the anode to the cathode. Therefore, the hydrogen oxidation reaction at the anode occurs very fast, whereas the oxygen reduction reaction at the cathode is relatively slow, implying that the cathode plays a significant role in the activation overvoltage. Some energy is lost during transfer of electrons from or to the electrode, thus the activation overvoltage is represented as the potential deviation from the original equilibrium position when the electrode surface is about to initiate the electrochemical reaction. The Tafel equation was used to establish an empirical model for the activation overvoltage as shown in the following formula:

$$v_{act} = v_0 + v_a\left(1 - e^{-\xi_1 i}\right), \quad (7)$$

where i represents the current density, which is the current generated per unit of the effective active area of the proton exchange membrane and was obtained using formula (8) below; the voltage drop at zero current density of v_0 was determined using formula (9),ξ_1 represent the empirical parameter, and v_a was determined using equation (10).

$$i = \frac{I_{st}}{A}, \quad (8)$$

$$v_0 = 0.279 - \frac{\Delta S}{2F}(T_{st} - 298.15) + \frac{RT_{st}}{2F}\left[\ln\left(\frac{P_{ca} - P_{sat}}{P_{atm}}\right) + \frac{1}{2}\ln\left(\frac{0.1173(P_{ca} - P_{sat})}{p_{atm}}\right)\right], \quad (9)$$

$$v_a = \left(-1.618\times10^{-5}T_{st} + 1.618\times10^{-2}\right)\left(\frac{P_{O_2}}{0.1173} + P_{sat}\right)^2 + \left(1.8\times10^{-4}T_{st} - 0.166\right)\left(\frac{P_{O_2}}{0.1173} + P_{sat}\right) + \left(\frac{\Delta S}{2F}T_{st} + 0.5736\right), \quad (10)$$

P_{sat} represents the saturated vapor pressure of water, which is a function of temperature, and can be obtained as shown in the following equation:

$$\lg(P_{sat}) = 0.0295\times(T - 273.15) - 9.18\times10^{-5}(T - 273.15)^3 + 1.44\times10^{-7}(T - 273.15)^3 - 2.18. \quad (11)$$

Ohmic overvoltage is the voltage drop caused by the ionic resistance and electronic resistance inside the fuel cell. It comprises two parts: the voltage loss caused by resistance of the proton exchange membrane to hinder passage of protons and resistance of the electrode or collector plate to electron transfer. Ohm's Law is used to express Ohmic overvoltage as shown below:

$$v_{ohm} = R_{ohm} I_{st} = \left(R_e + R_p\right) I_{st}, \quad (12)$$

where R_{ohm} represents the fuel cell impedance (Ω), R_e denotes the electron flow impedance (Ω), and R_p represents the membrane impedance, which can be determined using formula (13).

$$R_p = \frac{\rho_M * t_m}{A}, \quad (13)$$

where ρ_M denotes the membrane resistivity, which is correlated with the temperature and humidity of the proton exchange membrane and is determined using formula (14) and t_m represents the thickness of the electrolyte membrane (cm).

$$\rho_M = \frac{181.6\left[1 + 0.03 * (I_{st}/A) + 0.062 * (T_{st}/303)^2 * (I_{st}/A)^{2.5}\right]}{\left[\lambda_m - 0.634 - 3 * (I_{st}/A)\right] * \exp\left[4.18 * (T_{st} - 303/T_{st})\right]}, \quad (14)$$

where λ_m denotes the water content of the membrane.

Concentration overvoltage is associated with changes in the concentration of the reactants consumed during the reaction. The rapid consumption rate of reactants causes a decrease in the partial pressure of reactants and decrease in the reaction rate at high current density, which results in voltage loss in the fuel cell. The concentration overvoltage is expressed as shown in the following equation:

$$v_{conc} = i\left(\xi_3 \frac{i}{i_{max}}\right)^{\xi_2}, \quad (15)$$

where ξ_2 denotes the equation coefficient, which is correlated with the properties of the fuel cell and its working environment, i_{max} represents the maximum current density that the fuel cell can achieve under the working state, usually 2.2, ξ_3 denotes the operating temperature of the fuel cell stack. Coefficients related to the partial pressure of oxygen are expressed as shown below:

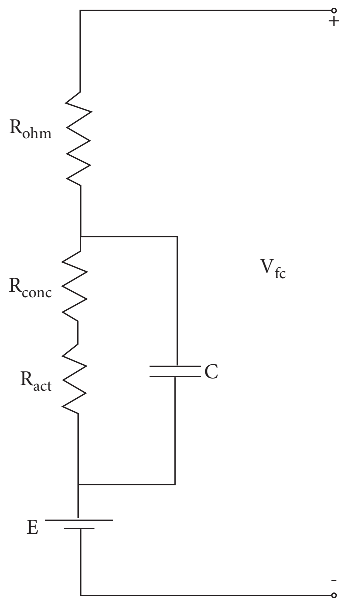

Figure 2: A PEMFC equivalent circuit.

$$\xi_3 = \begin{cases} \left(7.16\times10^{-4}T_{st}-0.622\right)\left(\dfrac{P_{ca}^{O_2}}{0.1173\times10^5}+\dfrac{P_{sat}}{10^5}\right) \\ +\left(-1.45\times10^{-3}T_{st}+1.68\right)\dfrac{P_{ca}^{O_2}}{0.1173}+P_{sat}<2P_{atm} \\ \left(8.66\times10^{-5}T_{st}-0.068\right)\left(\dfrac{P_{ca}^{O_2}}{0.1173\times10^5}+\dfrac{P_{sat}}{10^5}\right) \\ +\left(-1.63\times10^{-3}T_{st}+0.54\right)\dfrac{P_{ca}^{O_2}}{0.1173}+P_{sat}\geq 2P_{atm} \end{cases}. \quad (16)$$

3. PEMFC Dynamic Characteristics

The fuel cell exhibits dynamic behavior when it releases power to the outside [6–9]. Contact between two dissimilar materials at the electrode and electrolyte interface in a fuel cell produces a charge layer that resembles a capacitor. This charge layer is referred as a "charge double layer" and can be used to store charge and energy [10]. Abrupt change in the current caused by the presence of the electric double-layer structure results in the activation overvoltage by the blocking effect of the capacitor. Subsequently, change in the concentration overvoltage is gradual and exhibits a hysteresis effect.

The activation overvoltage and concentration overvoltage in the equivalent circuit of the fuel cell are markedly affected by the electric double layer. An equivalent circuit diagram of the fuel cell is presented in Figure 2. The Ohmic loss equivalent resistance R_{ohm} rapidly causes a change in the voltage when the current changes. The activation loss equivalent resistance (R_{act}) and the concentration loss equivalent resistance (R_{conc}) reduced the voltage drop of the resistance due to the presence of a capacitor. The charge double-layer effect can be expressed as shown below:

$$\begin{aligned} R_a i &= R_{act} i + R_{conc} i = v_{act} + v_{conc}, \\ C\frac{dV_c}{dt} &= i - \frac{v_c}{v_{act}+v_{conc}}, \end{aligned} \quad (17)$$

where R_a represents the equivalent resistance, C represents the equivalent capacitance, which is a constant, and v_c denotes the dynamic overvoltage under the action of the electric double layer. The single cell output voltage of the fuel cell can be expressed as presented below:

$$v_{fc} = E - v_{ohm} - v_c. \quad (18)$$

4. Establishment and Simulation of PEMFC Model

MATLAB is a software widely used in the engineering field and is effective for application in nonlinear and linear dynamic simulations. Simulink is a toolbox in MATLAB software. System models built using the Simulink toolbox is characterized by simplicity, strong operability, and convenient maintenance. Simulink has been widely used in academic and industrial fields for simulation studies. In the present study, the PEMFC model was established using Simulink in MATLAB software as shown in Figure 3. The model parameters are presented in Table 1.

The input section of the model comprises fuel cell load current, anode hydrogen partial pressure, cathode oxygen partial pressure, cathode pressure, PEMFC stack temperature, and water content of the proton exchange membrane. The system output constitutes the output voltage and power of the fuel cell. The steady-state conditions used for the simulation are shown in Table 2.

5. Results and Discussion

The fuel cell polarization curve obtained after simulation is shown in Figure 4. The polarization curve exhibited typical characteristics of the fuel cell performance. The simulation results indicated that the polarization curve of the fuel cell can be divided into three regions, namely activation overvoltage region, Ohmic overvoltage region, and concentration overvoltage region. The three regions result from the different effects exerted by the three losses on the output voltage of the fuel cell under increase in the current density. The effects of the three losses on the Nernst electromotive force when the three losses act together and individually are presented in Figure 5. The activation overvoltage represents the region of low current density and indicates the energy limit that the chemical reaction should overcome. The results indicate that when the current density is very small, the activation overvoltage is the main source of voltage loss when the energy from the fuel cell is released to the outside (Figure 6). The fuel cell efficiency in this region is not high due to the lower current density. The

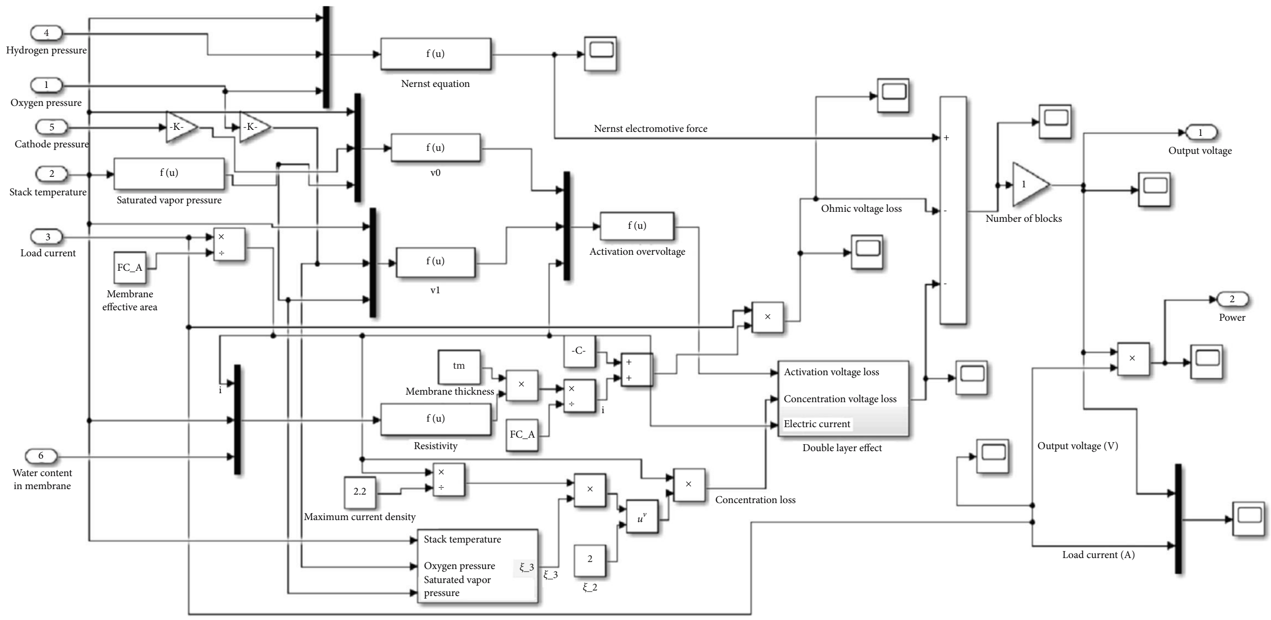

Figure 3: PEMFC electrochemical model simulated using Simulink toolbox.

Table 1: PEMFC system model simulation parameters.

Parameter	Description	Numerical value	Unit
T_{st}	Stack temperature	348.15	K
A	Single-cell activation area	220	cm^2
F	Faraday constant	96485	C/mol
P_{atm}	Standard atmospheric pressure	101325	Pa
T_{atm}	Atmospheric temperature	298.15	K
t_m	Proton exchange membrane thickness	125	μm
ξ_1	Empirical parameters	10	
ξ_2	Empirical parameters	2	
C	Double-layer charge equivalent capacitance	2.5	F
R	Universal gas constant	8.314472	
$\rho_{m,dry}$	Dry film density	0.002	kg/cm^3
$M_{m,dry}$	Dry film molar mass	1.1	kg/mol
A_{fc}	Effective area of proton exchange membrane	220	cm^2

Table 2: Steady state simulation conditions.

Parameter	Numerical value	Description
T_{st} (K)	348.15	Stack temperature
$P_{ca}^{O_2}$ (Pa)	3×10^4	Cathode oxygen partial pressure
P_{ca} (Pa)	3×10^5	Cathode pressure
$p_{an}^{H_2}$ (Pa)	2.6×10^5	Anode hydrogen partial pressure
λ_m	14	Proton exchange membrane water content

Ohmic overvoltage is the main voltage loss when the current density increases, which is attributed to the resistance loss of the electrolyte and electrodes (Figure 5(b)). The change in current density in this exhibits a linear trend according to the Ohm's law. The

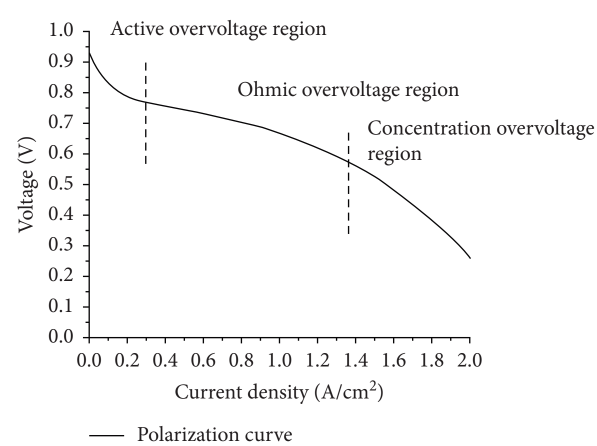

Figure 4: Fuel cell polarization curve.

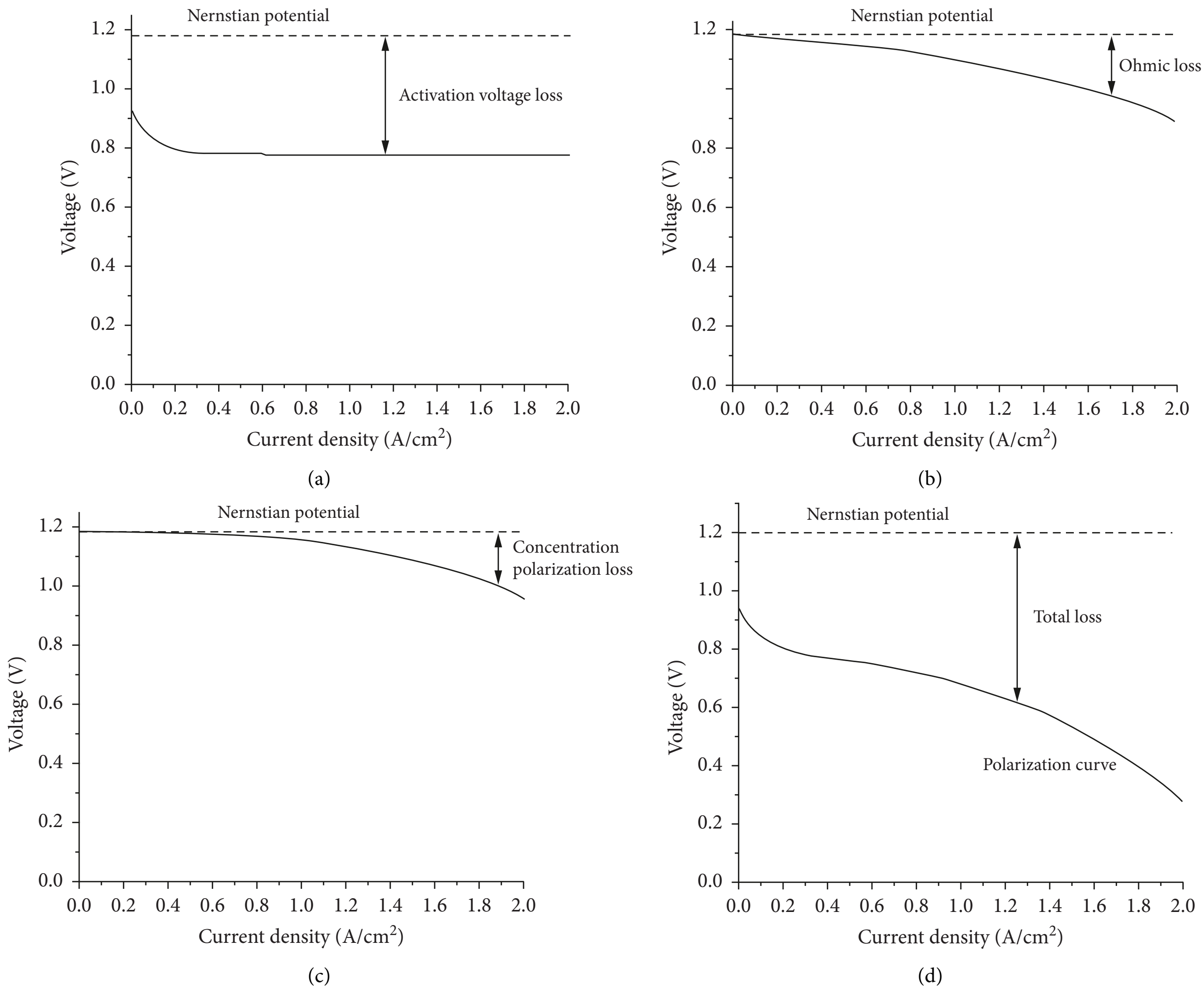

Figure 5: effect of the three voltage losses on output voltage.

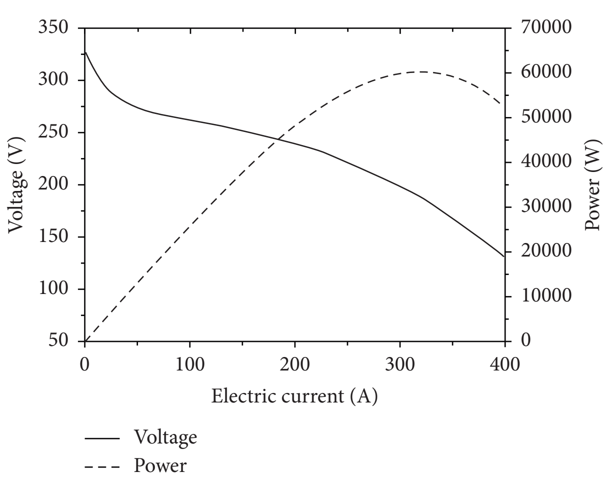

Figure 6: Current-voltage-power curve of a 60 kW PEMFC.

reactants on the catalyst surface rapidly decrease when the current density increases, and the replenishment speed of the reactants reduces the output voltage of the fuel cell. The concentration overvoltage is the main voltage loss in this region (Figure 5(c)). The overall loss of the output voltage of the fuel cell is presented in Figure 5(d). The polarization curve of the fuel cell was obtained under the combined action of the three losses.

The effective activation area of the PEMFC electrochemical model determined in this study was 220 cm^2, and the number of PEMFC cells was set to 350. Changes in the output voltage and output power with the load current were obtained after simulation. The findings showed that the maximum output power of the fuel cell was 60.42 kW when the load current was 317.19 A.

The dynamic performance of the 60 kW fuel cell was simulated, and the dynamic changes of the load current, oxygen partial pressure, hydrogen partial pressure, operating temperature, and membrane water content are presented in Table 3. The simulation results are presented in Figures 7 and 8.

The initial load current was 80 A, and the output voltage significantly decreased from the initial 322.2 V to a steady state of 269.8 V, under the action of activation polarization. Notably, the load current first jumped increased to 180 A between 5 s and 10 s, then decreased to 150 A. The output voltage changes were −20.39 V and 7.02 V. The output power

Table 3: Dynamic simulation conditions.

Simulation time (s)	0–5	5–10	10–15	15–20	20–25	25–30	30–35
Load current (A)	80	180	150	150	150	150	150
Partial pressure of oxygen (kPa)	30	30	30	40	40	40	40
Hydrogen partial pressure (kPa)	260	260	260	260	300	300	300
Operating temperature (°C)	75	75	75	75	75	80	80
Membrane water content	14	14	14	14	14	14	12

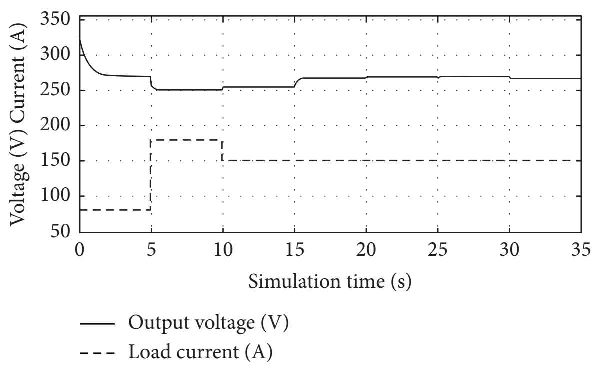

Figure 7: Dynamic response characteristics of PEMFC output voltage.

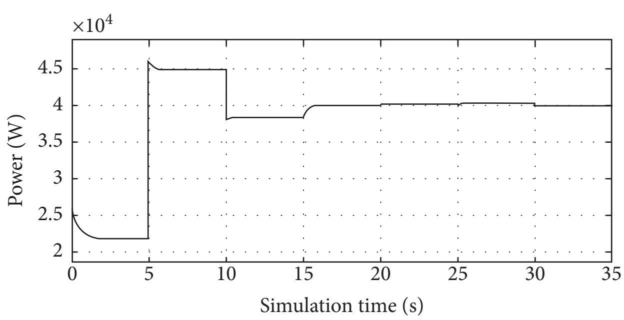

Figure 8: Dynamic response characteristics of PEMFC output power.

change values were 23.30 kW and −6.425 kW. The results show that the output voltage of the fuel cell decreases with an increase in the load current, and the output power increased with an increase in the load current under these working conditions. The findings indicate transitional changes in output voltage and output power.

The oxygen partial pressure and hydrogen partial pressure changed between 15 s and 20 s, whereas other conditions did not change. The output voltage increased by 10.95 V and the output power increased by 1.642 kW when the partial pressure of oxygen increases by 10 kPa. Moreover, the output voltage increased by 0.751 V whereas the output power increased by 0.113 kW when the partial pressure of hydrogen increases by 40 kPa. The simulation results indicate that the oxygen partial pressure had a greater impact on the fuel cell output compared with the effect by the change in hydrogen partial pressure. This is because activation overvoltage is the main factor that affects the output voltage, and oxygen reduction, which is the main factor that modulates the activation overvoltage was relatively low on the cathode side. Therefore, the partial pressure of oxygen had a significant effect on the voltage drop of the fuel cell compared with the effect of the partial pressure of hydrogen. Hydrogen is typically in excess in the fuel cell anode. Nitrogen from air is the main gas on the cathode side, thus the partial pressure of oxygen in the cathode is relatively low. Therefore, it is necessary to compress the air using an air compressor to improve the output performance of the fuel cell. However, excessive gas partial pressure adversely affects the airtightness of the stack, and increases the energy consumption of the air compressor, so the oxygen partial pressure should be maintained in an appropriate range.

The operating temperature of the fuel cell increased by 5°C at 25 s, the output voltage increased by 2.07 V, and the output power increased by 0.3109 kW whereas other conditions did not change. The internal chemical reaction rate of the fuel cell increased with an increase in the working temperature. In addition, the output voltage and the output power increases with an increase in the working temperature. Notably, a large amount of liquid water in the proton exchange membrane will be vaporized under too high temperature, thus reducing the performance of the fuel cell, and even, in serious cases, eventually damaging the fuel cell. The water content of the proton exchange membrane decreased from 14 to 12 at 30 s, the output voltage decreased by 3.528 V, and the output power decreased by 0.52 kW whereas other parameters did not change. The water content of the proton exchange membrane serves as a medium for protons to pass through the exchange membrane and take part in the reaction. A lower water content is associated with a greater effect on the reaction rate and a significant polarization effect. However, too high water content, above 14, causes "flooding" of the proton exchange membrane ultimately blocking the channel and stopping the reaction.

6. Conclusion

The simulation results in the present study show that the electrochemical reaction process of the fuel cell is modulated by various factors such as reaction gas pressure, temperature, and membrane water content. Therefore, the working parameters of the fuel cell should be relatively stable and within an appropriate range to ensure efficient and reliable functioning of the fuel cell.

Data Availability

The datasets used and analyzed during the current study are available from the corresponding author upon reasonable request.

Conflicts of Interest

The authors declare that they have no conflicts of interest.

Acknowledgments

Henan Province Science and Technology Research Project 202102310591, 212102210061, 212102310992 for their contribution.

References

[1] Z. Li and H. Yun, "Research on design and control of protonex change membrane fuel cell system," *Chinese Journal of Power Sources*, vol. 44, no. 04, pp. 574–639, 2020.
[2] B. Zhang, Z. H. U. A. N. G. Cai-ao, and Yu Zheng, "Simulation technical route of proton exchange membrane fuel cells for vehicles," *Chinese Internal Combustion Engine & Parts*, vol. 06, pp. 210–212, 2021.
[3] X. Luo, "PEMFC performance research of different flow field," *Chinese Battery Bimonthly*, vol. 47, no. 04, pp. 208–211, 2017.
[4] Su Zhou, K. Gao, and Z. Xuelei, "An improved dynamic model for proton exchange membrane fuel cell systems," *Chinese Journal of Tongji University (Natural Science)*, vol. 34, no. 6, pp. 882–887, 2015.
[5] W. Ze-jun, M. Ling-yun, X. Yi, and X. Ling-chao, "Review on modeling and control of proton exchange membrane fuel cells," *Chinese Journal of Power Sources*, vol. 42, no. 11, pp. 1757–1760, 2018.
[6] S. Sun, J. Yang, H. Tang, A. Ge, T. Xing, and M. A. Chao, "PEMFC output characteristics modeling and multi-factor simulation analysis," *Chinese Journal of Harbin Institute of Technology*, vol. 51, no. 10, pp. 144–151, 2019.
[7] D. Li, "Self-growing hybrid neural network and its application for fuel cell modelling," *CIE Journal*, vol. 66, no. 01, pp. 333–337, 2015.
[8] Z. Yang, L. Fan, and Z. X. Decheng, "Study on the neural network control for proton exchange membrane fuel cell," *Chinese Process Automation Instrumentation*, vol. 35, no. 05, pp. 63–68, 2014.
[9] Z. Jian and H. Chen, "A Humidity Identification Method for proton exchange membrane fuel cell based on cuckoo algorithm," *Chinese Journal of Electron Devices*, vol. 41, no. 03, pp. 679–683, 2018.
[10] R. T. Meyer and B. Yao, "Modeling and simulation of a modern PEM fuel cell system," in *Proceedings of the 4th InternationalConferenceon Fuel Cell Science, Engineering and Technology*, Sanya, China, April 2006.

Hindawi
Advances in Materials Science and Engineering
Volume 2023, Article ID 5657609, 10 pages
https://doi.org/10.1155/2023/5657609

Research Article

Experimental Investigation on Incorporation of Zinc-Ferrite Nanocoated Baffles for Improving the Performance of Field Power Electrical Transformer Integrated with a Solar Air Heater

Nithiyananthan Kannan,[1] N. Vasantha Gowri,[2] T. Muralikrishna,[2] Avinash Kumar,[3] F. Mary Anjalin,[4] M. Ramesh,[5] B. Muthuraj,[6] and Habtewolde Ababu Birhanu[7]

[1]*Department of Electrical Engineering, Faculty of Engineering, Rabigh King Abdulaziz University, Jeddah, Saudi Arabia*
[2]*Department of Electrical and Electronics Engineering, Chaitanya Bharathi Institute of Technology (A), Hyderabad 500075, Telangana, India*
[3]*Department of Electrical and Electronics Engineering, Guru Gobind Singh Educational Society's Technical Campus, Bokaro University-Jharkhand University of Technology, Ranchi 827013, Jharkhand, India*
[4]*Department of Physics, Saveetha School of Engineering, Saveetha Institute of Medical and Technical Sciences, Chennai 602105, Tamil Nadu, India*
[5]*Department of Electrical and Electronic Engineering, Vaageswari College of Engineering, Karimnagar 505527, Telangana, India*
[6]*Department of Electrical and Electronics Engineering, Panimalar Engineering College, Chennai 600123, Tamil Nadu, India*
[7]*Faculty of Mechanical Engineering, Arba Minch Institute of Technology, Arba Minch University, P.O. Box 21, Arba Minch, Ethiopia*

Correspondence should be addressed to Habtewolde Ababu Birhanu; habtewold.ababu@amu.edu.et

Received 16 May 2022; Revised 27 July 2022; Accepted 2 August 2022; Published 17 April 2023

Academic Editor: Ravi Samikannu

Solar energy is the most accessible, eco-friendly, and renewable energy source available to meet the world's expanding energy needs. Solar collectors are commonly utilized to convert solar energy directly into heat for purposes ranging from house heating to timber seasoning and crop drying. The purpose of this research is to design a modified solar air heater (SAH) with a baffle plate and to examine the performance due to the provision of zinc-ferrite nanocoated baffles. The entire system is mounted over a transformer for effective cooling and also produces hot air for industrial requirements. A flat plate collector and a centrifugal blower were used in the experiment. Maximum output air temperatures of 55°C, 62°C, and 72°C were measured for collectors without baffles, baffled collectors, and inverted baffled collectors, respectively. It was also found that the thermal efficiency of flat plate collectors without baffles was 36%, with baffles, it was 44%, and with inverted baffles it was 54%. This study shows that inverted SAH with zinc-ferrite nanocoated baffle plates works better than SAH without baffle plates or with baffle plates in the normal position.

1. Introduction

Solar radiation contains a significant amount of thermal energy in both direct and indirect forms, making it one of the most abundant renewable sources of energy available on the planet. The sun releases approximately 3.8×10^{23} kW of energy; but due to the 150 million kilometers between the sun and the Earth, 1.8×10^{23} kW of energy is lost [1]. The Earth's surface receives around 3.4×10^{6}exa Joules of solar energy per year. This thermal energy is not equivalent to the thermal energy generated by nontraditional energy sources such as fossil fuels or nuclear energy [2]. Currently, fossil fuels account for 80% of global energy consumption. Global demand for fossil fuels will almost certainly exceed annual output within the next two decades. Oil or gas shortages have the potential to spark global financial and political crises and confrontations [3].

In his research study, Karsli [4] compared four distinct types of solar flat plate air heaters. These included a collector with a finned collector at 75 degrees, a collector with a finned collector at 70 degrees, a collector with tubes, and a base-collector. The determination of the efficiency of the air heater is dependent on solar radiation and the surface shape of the solar collectors, as well as the fact that the overall loss is lower at a greater decreased temperature parameter. Otham et al. [5] came up with and tried out four new solar-aided forced convection air heaters: the V-groove air heater, the multipass collector with an energy storage arrangement, the dehumidifier for herbs, and a photovoltaic collector system. It was suggested that the likelihood of the construction of a self-sufficient solar flat plate collector, which will not require any external electrical energy to operate, would be high. The solar air heaters operated at single pass and counterflow operating conditions, Nowzari–Aldabbagh [6] and found that a solar collector with a quarter ($1/4^{th}$)-perforated sheet did better than one with a half (1/2th) -perforated sheet. The average efficiency of the multipass solar energy extractors with 10D and 20D quarter-perforated glass sheets was 51.23% and 54.61%, respectively, while the average efficiency of the collector with half-perforated covers was 48.21% and 51.17%, respectively. It was 50.92% efficient at the same mass flow rate when the double-pass air heater with a regular cover had the same amount of air coming through it. Abuskha–Şevik [7] investigated thermal efficiency values that ranged from 44.8% to 66%, depending on the rate at which the water was being circulated. The mean performance of SAH in terms of thermal efficiency of a v-groove SAC is about 6% higher than the average thermal efficiency of a flat plate SAC. According to the results of the 0.1 kg/s test, a 13–15% gain in thermal efficiency over the 0.04 kg/s test may be attained using this strategy when compared to the previous test. The practicality of placing an aluminum can formulated absorbing plate into the multipass channel of conventional solar energy extractors in order for it to absorb the sun's heat is being investigated by Esen [8]. In order to carry out the experiment, three distinct absorber plates were produced and put through their paces under a variety of circumstances. Because Type I users put the cans on the absorber plate in the wrong place at the wrong time, the order of the cans on the plate became a jumbled mess. These objects were placed in an orderly fashion by people who employed Type II technology. It is a form of a plate that appears to be flat on the surface (without cans). It was determined that the investigations were carried out for working fluid flow rates ranging from 0.03 kg/s to 0.05 kg/s, respectively, and that the results were in favor of the hypothesis is supported. Type I was the most efficient of the three when moving at a rate of 0.05 kg per second.

According to Yeh and Lin [9], a flat plate solar air heater's double-pass channel might use an aluminum absorption plate to absorb the sun's heat (SAH). For the purpose of research, three alternative absorber plates were created and tested. Type I users messed up the order of the cans on the absorber plate by putting them out of order. They were placed in a straight line by those who utilized Type II. It is a type of plate that is flat in appearance (without cans). The studies showed that the air induction capacity of SAH ranges between 0.03 kg/s and 0.05 kg/s, and that the results were positive. Type I was most efficient while moving at a rate of 0.05 kg/s. Bansal et al. [10] conducted an experiment to compare SAHs with and without longitudinal fins in order to better understand SAHs. They discovered that SAHs with fins have greater performance at lower mass flow rates. Omojaro–Aldabbagh [11] conducted a test using a single and double-finned plate SAH with a steel wire mesh to determine their effectiveness. They demonstrated that the energy efficiency of the collector with many passes is superior to that of the collector with a single pass. During the course of their investigation, Alta et al. [12] constructed three distinct variants of the SAH: one without expanded surfaces, one with larger surfaces, and one that combined enlarged surfaces with a double-glass cover. According to the results of this investigation, the dual glass finned plate SAH is the most efficient of the three designs tested. According to the study, it was also discovered that the length of time that air circulates in the SAH has an impact on the temperature of the air that comes out of the SAH, according to the study. Lin et al. [13] investigated the thermal efficiency of two distinct types of SAH integrated with corrugated designed absorber plates and identified that they were both effective and efficient. The researchers noticed that when they used a cross-corrugated surface instead of a flat plate, the thermal efficiency of the heater increased dramatically when compared to the former. Karim–Hawlader [14] analysed the energy conversion characteristics of a SAH integrated with conventional, v-corrugated, and finned absorber plates. One of the investigations conducted by the researchers was the fact that an air heater with V corrugation profiles can be converted into a flat plate air heater. Furthermore, it was discovered that second-pass air flow improves heater efficiency [15]. Furthermore, the flat plate was heated with respect to roughness profiles, geometrical aspects of which were defined in previous research [16].

Roughness geometry and performance factors were studied in an experiment done by Saini–Verma [17] on experimental mixed convection roughened duct. A variety of factors, including Reynolds number, roughness pitch, and height, were found to have an impact, as well as the effects of nuzzling number and friction factor, among others [18]. They were able to demonstrate that when the absorption plate's roughness geometry was in the shape of a dimple, the Nusselt number and friction factor were both increased as a result. The roughness parameter, they said, should be set in accordance with the intended energy gain for fan operations, in more detail [19]. In order to evaluate the thermohydraulic performance of a SAH with a 60-degree v-shaped rib roughness on the absorption plate on the absorption plate [20]. Mahmood et al. [21] carried out an experiment on the absorption plate. After doing their research, they came to the conclusion that increasing the roughness of the absorption plate boosted heat efficiency while decreasing heat loss. Additionally, they discovered that when the mass flow rate was low, the thermal and effective thermal efficiency of the heater were typically similar. However, as the mass flow rate increased, the effective thermal efficiency decreased as a result of the friction factor and the additional pump effort that was required to operate the heater. El-Sebaii et al. [19] conducted an experiment on the absorption plate of a SAH using ribs of various roughness's, including continuous ribs, transverse continuous, an *d* cracked continuous rib v-shaped ribs and determined that all ribs should be used [22]. Luan–Phu [23] attained the maximum effective efficiency of 63% at an optimum baffle angle position of 60° with a flow Reynolds number of 24000. Khanlari et al. [24] and Venkateshwar et al. [25] used Cuo nanocoated baffles for solar air heaters and obtained a maximum efficiency of 76.22% [24, 25]. Venkateshwar et al. [26] integrate the SAH with a thermoelectric generator and improve its performance by a reduction in process heat generation of 1 to 6.25%. Sivakumar et al. [27] coated a solar absorber sheet with CuO nanoparticles and black paint to increase heat transmission. The nanoembedded modification reduced the drying time by 6%. Abd-Elhady et al. [28] examined solar cookers utilizing metallic wires and nanographene. According to their findings, nanoadditives raised the oil temperature by 8%. Shanmugan et al. [29] evaluated the influence of SiO_2/TiO_2 nano-coating on a stepped solar box cooker's thermal performance. Nanocoating enhanced thermal performance by 31%. This study's objectives are to build a modified SAH with a baffle plate and investigate the performance of the SAH as a result of providing zinc-ferrite nanocoated baffles. The complete system is built on top of a transformer for efficient cooling, and it also generates hot air to fulfill the requirements of various industries. After reviewing the available research in the published works, it was determined that improving the overall performance of SAHs might be accomplished by employing strategies that are both straightforward and efficient. Within the scope of the current investigation, a baffled SAH has been conceived, and its functionality has been enhanced by making use of baffles and an absorber with zinc nanocoating. In this regard, experimental analysis has been applied to the task of specifying a suitable baffle design for SAH. After that, SAHs with and without nanocoating have been produced, and the experimental investigation of their performance has been carried out. The primary objectives of this research are to (1) develop solar air heating systems for industrial applications that are both environmentally friendly and highly effective, and (2) to investigate the effect that integrating nanoembedded absorber coating has on the efficiency of solar air heaters. Figure 1 depicts the primary design configurations that were taken into consideration for this work.

2. Methodology

2.1. Experimental Setup. The experimental setup was planned and constructed in the Coimbatore climatic conditions of Tamil Nadu, India. The schematic layout in Figure 1 depicts the experimental setup for the SAH with zinc -ferrite nanocoated baffle plate. This analysis considers a standard flat plate collector with a surface area of 0.5 m^2. As zinc-ferrite nanocoated baffle type absorber panel, an aluminum sheet (1.4 mm thickness) is employed that has been black coated to absorb more solar radiation [30]. The spacing between baffles is maintained at 100 mm to make the flow more turbulent. A glass frame serves as a clear cover for the SAH. The glass wool insulation insulates the system from the sides and bottom, minimizing heat loss. The entire apparatus is mounted on a 10° inclined stand that corresponds to the test location's latitude. A blower with a capacity of 1.0 hp is used to supply the solar collector with the necessary air. While the zinc-ferrite nanocoated baffle type absorber plate arrangement is similar to that of a typical SAH, the airflow inside the SAH is zigzagged, as illustrated in Figure 2, which is connected to the blower. Without a baffle plate, with a baffle plate, and with an inverted baffle plate, the system is investigated in a SAH with a mass flow rate range of 0.01 kg/s. The SAH is put through its paces and graphs are created.

2.2. Instrumentation. SMIS Instruments, Bangalore, supplies a top-of-the-line pyranometer (type LP PYRA02, Delta Ohm) that is used to monitor solar radiation during the day. The sensitivity and resolution are, respectively, 12V and 25 W/m2. A pyranometer is additionally equipped with a shadow ring to monitor global radiation [31]. At the beginning of an experiment, the airflow rate is measured. The EQTM-4001 hot wire anemometer has a temperature range of about 0–50°C, an air velocity range of approximately 0–25 m/s, and a relative humidity range of approximately 20–80 percent [32]. It measures the incoming air speed with a precision of up to 2 percent. There is room for up to 99 readings. The K-type thermocouple sensor is used to measure the intake and outlet air temperatures, as well as the temperatures of the glass and absorber plate [33]. With a resolution of 0.1°C, a data logger (type Logger 02 or MEZARIT) shows and retains all temperatures. The precision and kind of the instruments are detailed in Table 1.

2.3. Thermal Performance of the SAH. The following parameters are used to determine the thermal performance of SAH without baffle, with baffle and inverted baffle are analyzed [34, 35].

(i) Mass flow rate

$$(\dot{m}) = \rho AC. \tag{1}$$

(ii) Reynolds number

$$(\mathrm{Re}) = \frac{\rho AV}{\mu}. \tag{2}$$

(iii) Hydraulic diameter

$$(d_e)\frac{4A}{P}. \tag{3}$$

Useful heat gain [32]

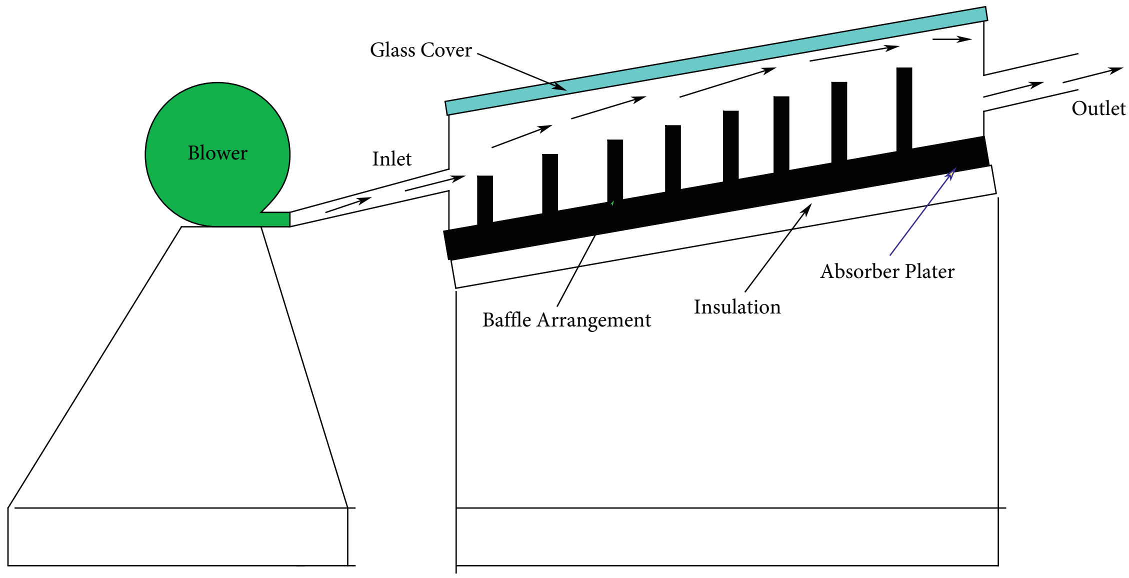

FIGURE 1: Schematic view of the solar air heating system.

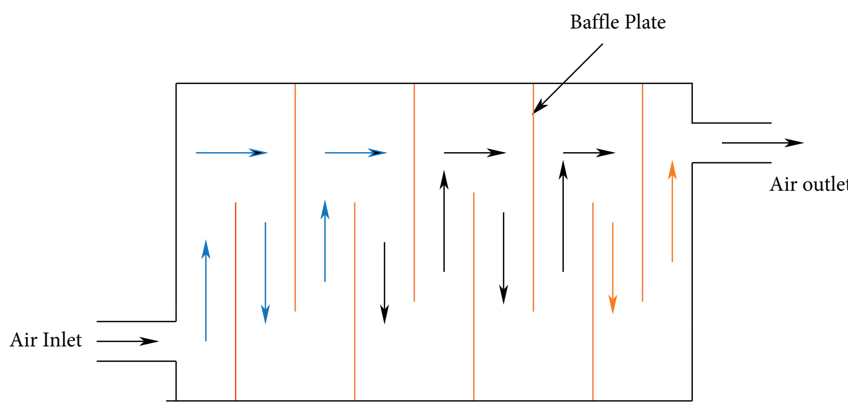

FIGURE 2: Flow of air inside the solar air heater.

TABLE 1: Accuracy and range of measuring instruments.

S.N	Instrument	Accuracy	Range
1	Pyranometer	±1.89%	0 to 1700 W/m^2
2	Thermocouple	1°C	0 to 175°C
2	Anemometer	2%	0 to 25 m/s

$$(Q_u) = \dot{m}\, c_p\, \Delta T. \quad (4)$$

(iv) Energy efficiency

$$\eta = \frac{Q_u}{AI}. \quad (5)$$

(v) Nusselt number =

$$0.023 Re_d^{0.8} \times \mathrm{Pr}^n. \quad (6)$$

3. Results and Discussion

The performance of the flat plate SAH is carried out in three different conditions; they are SAH without a baffle plate, with zinc-ferrite nanocoated baffle plate, and inverted baffle plate. The readings were observed in the climatic conditions of Coimbatore, Tamil Nadu, India.

Figure 3 depicts the outlet temperature of a SAH in relation to solar insolation during the daytime, with and without a baffle, and with and without an inverted baffle. The graph showed that the output temperature of the SAH

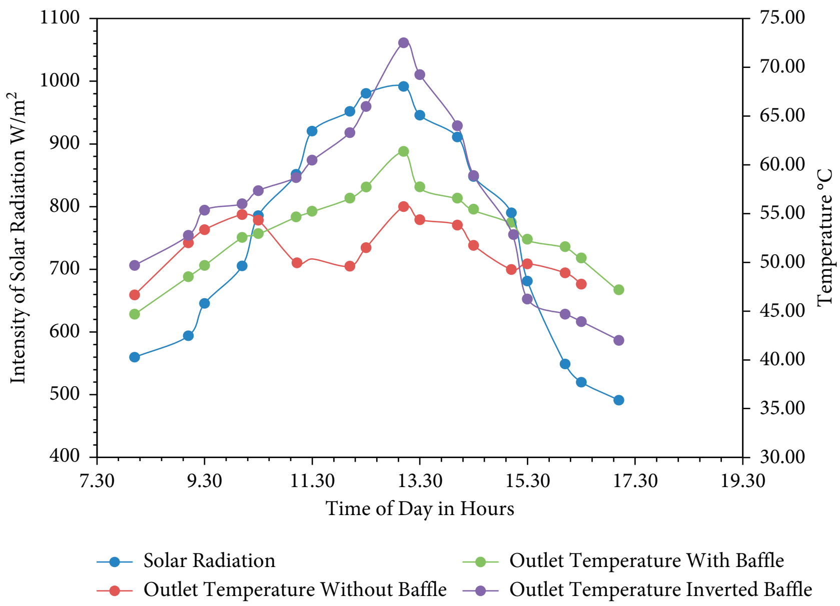

Figure 3: Outlet temperatures with respect to solar radiation of SAH.

gradually increases with solar radiation and that it gradually decreases with solar radiation, as seen in the graph. The highest outlet temperature for all of the above scenarios is 55°C at 980 W/m^2 for SAH without baffle plate, 62°C at 992 W/m^2 for SAH with a baffle plates, and 72°C at 1045 W/m^2 for SAH with inverted baffle plate when exposed to maximum solar radiation.

Figure 4 depicts the beneficial heat gain in W for SAH with, without, and inverted baffle plate in relation to the time of day in hours for SAH with, without, and inverted baffle plate. From 8.00 to 14.00 hours, the useable heat gain increases with the passage of time; after 14.00 hours, the useful heat gain decreases with the passage of time and is also related to the amount of solar insolation received. The highest usable heat gains for SAH without a baffle plate are 178.8 W, for SAH with a zinc-ferrite nanocoated baffle plate is 220 W, and for SAH with an inverted baffle plate is 340 W. The time it takes for air to circulate within the SAH may enhance the useful heat gain.

Experiments were performed both with and without baffle plates, and studies were carried out both with and without an inverted baffle plate. All of these tests were carried out in the SAH with a flow condition of air ranges of approximately 0.01 kg/s and under the climatic conditions of Coimbatore. Among these tests were experiments with and without an inverted baffle plate. As a function of the passage of time during the day, the fluctuations in solar radiation, as well as the temperatures of the air, the glass, and the absorber plate for the SAH with an inverted baffle plate are depicted in Figure 5. When the solar insolation reaches its maximum value of 950 W/m^2, the temperature of the air leaving the building ranges from 60 to 72°C.

The thermal efficiency of the SAH with inverted zinc-ferrite nanocoated baffle plate is depicted in Figure 6 (right). The efficiency of the SAH will rise as the amount of usable heat gain increases. As solar radiation increases, the amount of useful heat gain will increase as well, increasing the efficiency of the SAH. The long air circulation time in the inverted baffle plate results in a large increase in air temperature.

The heat transfer coefficient varies depending on the temperature of the air exiting the system, the Reynolds number, and the Nusslet number. The baffle configurations generate a turbulent flow within the SAH's internal chamber. The heat transmission coefficient is high during the first 12–14 hours of operation because of the increased heat accumulation by the air within the SAH. After that, the amount would gradually decrease. Figure 7 displays the evolution of the SAH's heat transfer coefficient over time.

With respect to the pressure drop, Figure 8 displays the link between the effective thermal efficiency and the effective useful heat gain. When compared to the mass flow rate of 0.010819 kg/s the pressure drop measures around 1.8 bars. The effective thermal efficiency has grown significantly, going from 9 hours to 14 hours when compared to their effective usable heat gain, which is a major increase. When something like this takes place, the value of the effective efficiency drops until it is equal to the value of the effective useful heat gain. Any further increase in the airflow rate will result in a decline in thermal performance as a direct consequence of the increased fan power required to offset the frictional losses brought on by the increased airflow rate.

An energy study was performed on the inverted a baffle plate SAH with a mass flow rate of 0.010819 kg/s, and the results are displayed in Figure 9. The maximum energy gain is about 74.69 W with a solar intensity of 1045 W/m^2 at 1pm; the corresponding energy efficiency is 14%.

3.1. Comparison Analysis. The comparison between the present results with earlier published results is shown in Table 2. The zinc nanocoated solar air heater enhances the thermal efficiency by 21.78%, 59.4%, and 66.23% compared

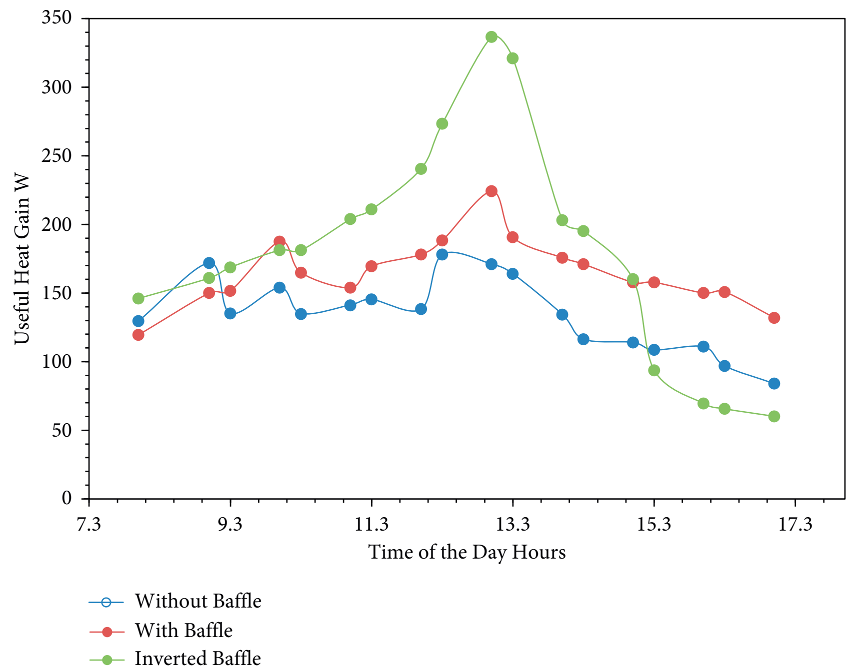

FIGURE 4: Useful heat gain for SAH without, with zinc -ferrite nanocoated baffle, and inverted baffle plate.

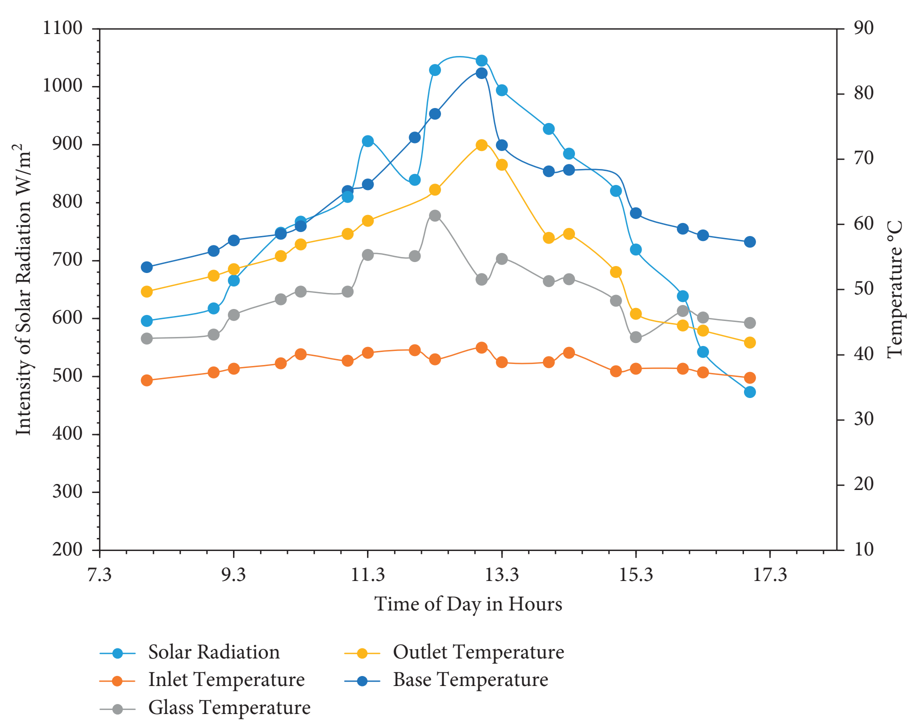

FIGURE 5: Hourly variations of solar radiation and temperature of air, glass, and absorber plate on day time in hours.

with conventional baffle, sequential array, and staggered array baffled SAH. The zinc-ferrite coating improves the absorptivity of the absorber plate and enhances the temperature differences between the baffled absorber and flowing fluid, which improves the energy efficiency by 70.3%, 26.03, and 7.3%, respectively.

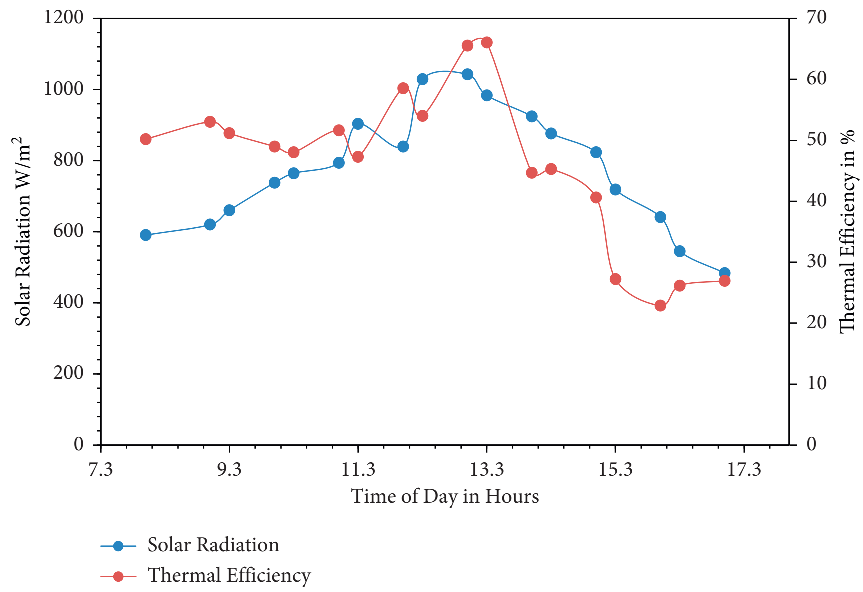

Figure 6: Thermal efficiency of the SAH with inverted baffle plate.

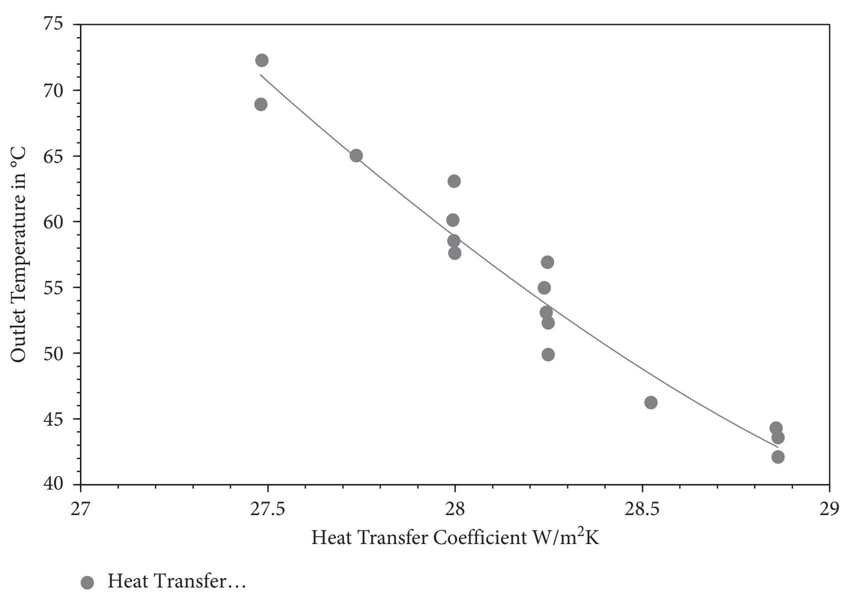

Figure 7: Heat transfer coefficient variation with outlet temperature of air.

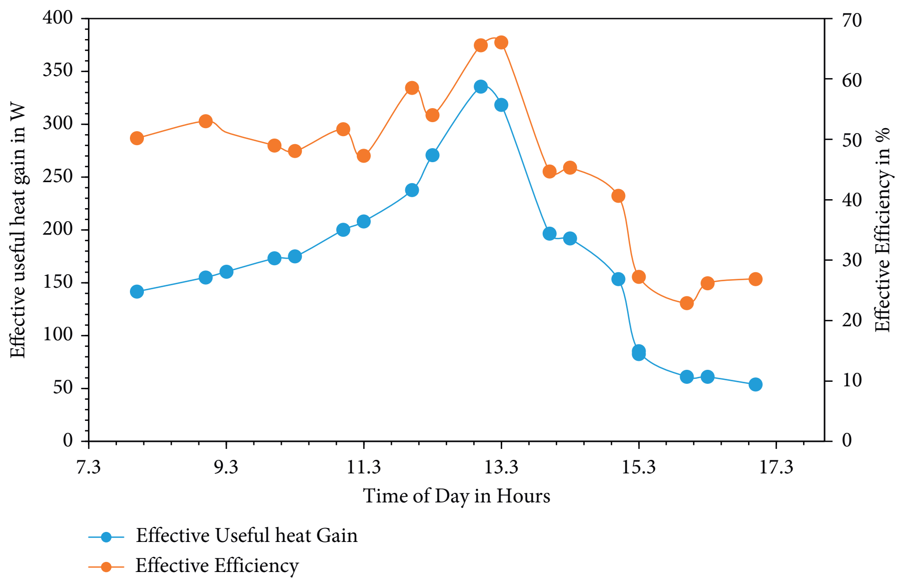

FIGURE 8: Hourly variations of effective useful heat gain and effective efficiency of the SAH with inverted baffle plate.

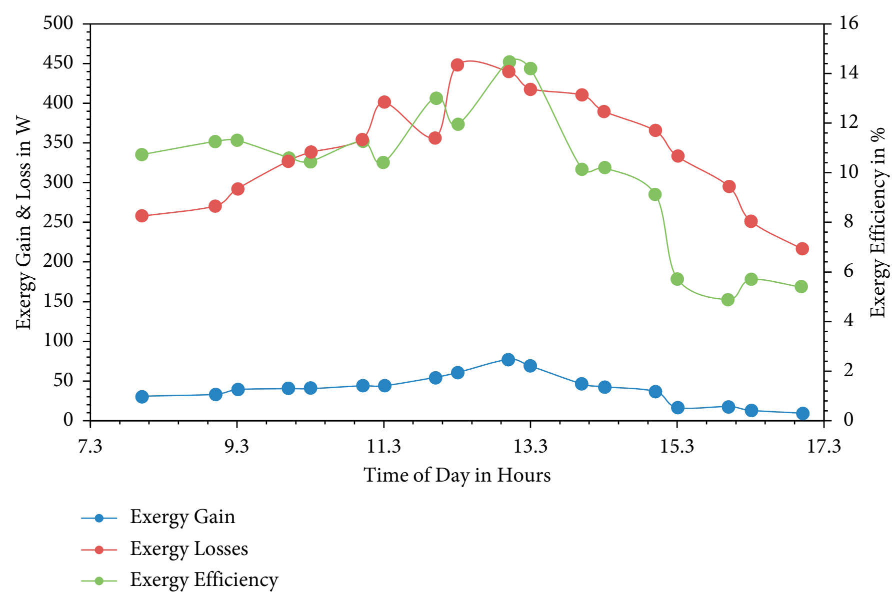

FIGURE 9: Hourly variations of energy gain, energy loss, and energy efficiency of the SAH with inverted baffle plate.

TABLE 2: Performance comparison with other configurations of SAH.

Configuration	Thermal efficiency (%)	Thermo hydraulic efficiency	Exergy efficiency (%)	Author
Finned baffle solar air heater	51.64	50.25%	4.3	Mohammadi and Sabzpooshani [36]
Baffled solar air heater-sequential array	26.78	—	10.71	Ghiami and Ghiami [37]
Baffled solar air heater-staggered array	22.29	—	13.41	Ghiami and Ghiami [37]
Zinc-ferrite nanocoated baffles in SAH	66.02	64.49%	14.48	Present work

4. Conclusion

In an experiment, a flat plate SAH was put through its paces using a baffle plate absorber. After careful thought, it can be said that the performance of the flat plate SAH was good. The highest temperature of the air coming out of the collector without baffles was 55°C, while the highest temperature of the air coming out of the collector with baffles was 62°C and the highest temperature of the air coming out of the collector with inverted baffles was 72°C. In this study, it was also found that the thermal efficiency of flat plate collectors without baffles, with baffles, and with inverted baffles was 36%, 44%, and 54%, respectively. It was found that the output of the traditional SAH with an upside-down baffle plate was better than in the other two cases. It maintains the electric transformer at 50°C, improves its operating performance, and also produces hot air for industrial applications. In subsequent research, a wide variety of nanoparticle kinds and concentrations may be utilized in order to examine the thermal behavior of this change.

Data Availability

The data used to support the findings of this study are included within the article.

Conflicts of Interest

The authors declare that they have no conflicts of interest regarding the publication of this article.

References

[1] A. Saxena, A. A. El-Sebaii, and A. El-Sebaii, "A thermodynamic review of solar air heaters," *Renewable and Sustainable Energy Reviews*, vol. 43, pp. 863–890, 2015.

[2] V. J. Manoj Praveen, R. Vigneshkumar, N. Karthikeyan, A. Gurumoorthi, R. Vijayakumar, and P. Madhu, "Heat transfer enhancement of air-concrete thermal energy storage system–CFD simulation and experimental validation under transient condition," *Proceedings of the Institution of Mechanical Engineers - Part E: Journal of Process Mechanical Engineering*, vol. 235, no. 5, pp. 1304–1314, 2021.

[3] C. Vibhakar, R. S. Sabeenian, S. Kaliappan et al., "Production and optimization of energy rich biofuel through Co-pyrolysis by utilizing mixed agricultural residues and mixed waste plastics," *Advances in Materials Science and Engineering*, vol. 2022, Article ID 8175552, 9 pages, 2022.

[4] S. Karsli, "Performance analysis of new-design solar air collectors for drying applications," *Renewable Energy*, vol. 32, no. 10, pp. 1645–1660, 2007.

[5] M. Y. H. Othman, K. Sopian, B. Yatim, and W. R. W. Daud, "Development of advanced solar assisted drying systems," *Renewable Energy*, vol. 31, no. 5, pp. 703–709, 2006.

[6] R. Nowzari and L. B. Y. Aldabbagh, "Experimental study on a solar air heater with various perforated covers," *Sādhanā*, vol. 42, no. 9, pp. 1585–1593, 2017.

[7] M. Abuşka and S. Şevik, "Energy, exergy, economic and environmental (4E) analyses of flat-plate and V-groove solar air collectors based on aluminium and copper," *Solar Energy*, vol. 158, pp. 259–277, 2017.

[8] H. Esen, "Experimental energy and exergy analysis of a double-flow solar air heater having different obstacles on absorber plates," *Building and Environment*, vol. 43, no. 6, pp. 1046–1054, 2008.

[9] H. M. Yeh and T. T. Lin, "Efficiency improvement of flat-plate solar air heaters," *Energy*, vol. 21, no. 6, pp. 435–443, 1996.

[10] N. K. Bansal, N. Bansal, and H. Garg, "An experimental study on a finned type and non-porous type solar air heater with a solar simulator," *Energy Conversion and Management*, vol. 25, no. 2, pp. 135–138, 1985.

[11] A. P. Omojaro and L. B. Y. Aldabbagh, "Experimental performance of single and double pass solar air heater with fins and steel wire mesh as absorber," *Applied Energy*, vol. 87, no. 12, pp. 3759–3765, 2010.

[12] D. Alta, E. Bilgili, C. Ertekin, and O. Yaldiz, "Experimental investigation of three different solar air heaters: energy and exergy analyses," *Applied Energy*, vol. 87, no. 10, pp. 2953–2973, 2010.

[13] W. Lin, W. Gao, and T. Liu, "A parametric study on the thermal performance of cross-corrugated solar air collectors," *Applied Thermal Engineering*, vol. 26, no. 10, pp. 1043–1053, 2006.

[14] M. A. Karim and M. N. A. Hawlader, "Performance investigation of flat plate, v-corrugated and finned air collectors," *Energy*, vol. 31, no. 4, pp. 452–470, 2006.

[15] R. P. Saini and J. Verma, "Heat transfer and friction factor correlations for a duct having dimple-shape artificial roughness for solar air heaters," *Energy*, vol. 33, no. 8, pp. 1277–1287, 2008.

[16] R. Karwa and G. Chitoshiya, "Performance study of solar air heater having v-down discrete ribs on absorber plate," *Energy*, vol. 55, pp. 939–955, 2013.

[17] G. Tanda, "Performance of solar air heater ducts with different types of ribs on the absorber plate," *Energy*, vol. 36, no. 11, pp. 6651–6660, 2011.

[18] H. M. Yeh, C. D. Ho, and J. Z. Hou, "Collector efficiency of double-flow solar air heaters with fins attached," *Energy*, vol. 27, no. 8, pp. 715–727, 2002.

[19] A. A. El-Sebaii, S. Aboul-Enein, M. R. I. Ramadan, S. M. Shalaby, and B. M. Moharram, "Thermal performance investigation of double pass-finned plate solar air heater," *Applied Energy*, vol. 88, no. 5, pp. 1727–1739, 2011.

[20] P. Naphon, "On the performance and entropy generation of the double-pass solar air heater with longitudinal fins," *Renewable Energy*, vol. 30, no. 9, pp. 1345–1357, 2005.

[21] A. J. Mahmood, L. B. Y. Aldabbagh, and F. Egelioglu, "Investigation of single and double pass solar air heater with transverse fins and a package wire mesh layer," *Energy Conversion and Management*, vol. 89, pp. 599–607, 2015.

[22] A. E. Kabeel, A. Khalil, S. M. Shalaby, and M. E. Zayed, "Investigation of the thermal performances of flat, finned, and v-corrugated plate solar air heaters," *Journal of Solar Energy Engineering*, vol. 138, no. 5, Article ID 051004, 2016.

[23] N. T. Luan and N. M. Phu, "Thermohydraulic correlations and exergy analysis of a solar air heater duct with inclined baffles," *Case Studies in Thermal Engineering*, vol. 21, Article ID 100672, 2020.

[24] A. Khanlari, A. D. Tuncer, A. Sözen, İ. Aytaç, E. Çiftçi, and H. İ. Variyenli, "Energy and exergy analysis of a vertical solar air heater with nano-enhanced absorber coating and perforated baffles," *Renewable Energy*, vol. 187, pp. 586–602, 2022.

[25] F. Selimefendigil, C. Şirin, K. Ghachem, L. Kolsi, T. Alqahtani, and S. Algarni, "Enhancing the performance of a greenhouse drying system by using triple-flow solar air collector with

nano-enhanced absorber coating," *Case Studies in Thermal Engineering*, vol. 34, Article ID 102011, 2022.

[26] K. Venkateshwar, A. Raihan Mohammad Siddique, S. Tasnim, H. Simha, and S. Mahmud, "Thermoelectric generator–integrated solar air heater: a compact passive system," *Journal of Energy Resources Technology*, vol. 143, no. 4, 2021.

[27] S. Sivakumar, C. Velmurugan, D. E. J. Dhas, A. B. Solomon, and K. L. Dev Wins, "Effect of nano cupric oxide coating on the forced convection performance of a mixed-mode flat plate solar dryer," *Renewable Energy*, vol. 155, pp. 1165–1172, 2020.

[28] M. S. Abd-Elhady, A. N. A. Abd-Elkerim, S. A. Ahmed, M. A. Halim, and A. Abu-Oqual, "Study the thermal performance of solar cookers by using metallic wires and nanographene," *Renewable Energy*, vol. 153, pp. 108–116, 2020.

[29] S. Shanmugan, S. Gorjian, A. H. Elsheikh, F. A. Essa, Z. M. Omara, and A. V. Raghu, "Investigation into the effects of SiO2/TiO2 nanolayer on the thermal performance of solar box type cooker," *Energy Sources, Part A: Recovery, Utilization, and Environmental Effects*, vol. 43, no. 21, pp. 2724–2737, 2021.

[30] A. Fudholi, K. Sopian, M. Y. Othman, M. H. Ruslan, and B. Bakhtyar, "Energy analysis and improvement potential of finned double-pass solar collector," *Energy Conversion and Management*, vol. 75, pp. 234–240, 2013.

[31] A. Fudholi, K. Sopian, M. H. Ruslan, and M. Y. Othman, "Performance and cost benefits analysis of double-pass solar collector with and without fins," *Energy Conversion and Management*, vol. 76, pp. 8–19, 2013.

[32] A. E. Kabeel and K. Mečárik, "Shape optimization for absorber plates of solar air collectors," *Renewable Energy*, vol. 13, no. 1, pp. 121–131, 1998.

[33] F. K. Forson, M. A. Nazha, and H. Rajakaruna, "Experimental and simulation studies on a single pass, double duct solar air heater," *Energy Conversion and Management*, vol. 44, no. 8, pp. 1209–1227, 2003.

[34] C. D. Ho, C. W. Yeh, and S. M. Hsieh, "Improvement in device performance of multi-pass flat-plate solar air heaters with external recycle," *Renewable Energy*, vol. 30, no. 10, pp. 1601–1621, 2005.

[35] A. A. El-Sebaii, S. Aboul-Enein, M. R. I. Ramadan, S. M. Shalaby, and B. M. Moharram, "Investigation of thermal performance of-double pass-flat and v-corrugated plate solar air heaters," *Energy*, vol. 36, no. 2, pp. 1076–1086, 2011.

[36] K. Mohammadi and M. Sabzpooshani, "Appraising the performance of a baffled solar air heater with external recycle," *Energy Conversion and Management*, vol. 88, pp. 239–250, 2014.

[37] A. Ghiami and S. Ghiami, "Comparative study based on energy and exergy analyses of a baffled solar air heater with latent storage collector," *Applied Thermal Engineering*, vol. 133, pp. 797–808, 2018.

Hindawi
Advances in Materials Science and Engineering
Volume 2023, Article ID 9096874, 9 pages
https://doi.org/10.1155/2023/9096874

Research Article

Bioinspired Sandwich Structure in Composite Panels

Deepak Sampathkumar,[1] **Ashokkumar Mohankumar**,[2] **Yuvaraja Teekaraman**,[3] **Ramya Kuppusamy**,[4] **and Arun Radhakrishnan**[5]

[1]*Department of Mechanical and Automation Engineering, Agni College of Technology, Talambur, Chennai 600130, Tamil Nadu, India*
[2]*Department of Mechanical Engineering, Government College of Engineering, Bargur 635104, Tamil Nadu, India*
[3]*School of Engineering & Computing, American International University (AIU), Jahra, Kuwait*
[4]*Department of Electrical and Electronics Engineering, Sri Sairam College of Engineering, Bangalore 562106, India*
[5]*Faculty of Electrical & Computer Engineering, Jimma Institute of Technology, Jimma University, Jimma, Ethiopia*

Correspondence should be addressed to Arun Radhakrishnan; arun.radhakriahnan@ju.edu.et

Received 1 June 2022; Revised 15 October 2022; Accepted 25 November 2022; Published 22 February 2023

Academic Editor: Achraf Ghorbal

The phenomenon of separation into constituent layers connecting the core and laminate of a composite sandwich complex is a vital complication that leads to early failure of such material. The direction of the sandwich construction's exfoliation rigidity is increased between interlaminar low fiber augmentation. The bioinspired technique of hybrid material layers was used on an aluminium face sheet with an interlayer composition of PET foam core and glass fabric of a material that appears to have greater potential as a flimsy substitute for materials currently used in automotive, aeronautical, and marine applications. This examination seeks to develop the making of such material along the retardation in fibre supplements. Fibre bridging has been recognized as an important appliance in the progress of this operating procedure. Consequently, this method points to promoting the event of fibre bridging by differing aggregates, including the mass and extent of augmented fibres and the quantity of epoxy resin applied. A few advancements were made to the production methods, and though the outcomes for the resisting ability of specimens were found to be indecisive, it was found that the layer separation hardness had even improved. This was confirmed through the operation of scanning electron microscopy and also predicted the mechanically peeled material surfaces which identified the adhesive strength variations with respect to the face sheet surface modified with the sand blasting process. The analysis also revealed the need for further research into optimizing the attachment between aluminium sheet and pet foam and glass fabric based hybrid sandwich panels.

1. Introduction

Composites, the meander materials with elevated strength-to-weight proportion, feathery in nature, and firmness, have induced a long path of substituting traditional materials that include metals and wood. To fully comprehend the role and involvement of composite materials in construction [1], a thorough understanding of the component materials themselves, as well as the numerous ways in which they can be analysed, is required. In most of its common form, a composite indicator [2] is made up of at least two elements that interact together to provide material qualities that are distinct from those of the individual constituents. In applications, many of the composites are made up of a huge amount of stuff (the "matrix") and some form of supplements, which are added to boost the matrix's firmness and rigidity. Typically, this augmentation is performed in the form of fibres. Polymer matrix composites (PMCs) are a type of polymer matrix composite. These are the most prevalent, and they will be the focus of this article. Fibre-reinforced polymers (or plastics) are materials that use a polymer-deployed resin as a matrix and various types of fibres as reinforcement, such as glass, carbon, and aramid [3].

Creation has supplied us with incredible wealth that addresses the outlines of the issues that today's society faces. Multistate architectures motivated by soft-shell turtles are shown to develop composite laminate collision resistance [4]. The goal of this research is to determine the crash reactions and crashworthiness of bioinspired interlaying constructions made of glass fibre augmented plastic (GFRP) panels and aluminium sheets. The impacts of core side dimensions and the influence of velocity on peak load and energy absorption, as well as the crash responses, failure mechanisms, and influence of core side dimensions and collision velocity on peak load and energy absorption, were examined in this paper. The crashworthiness variations in the middle of the GFRP aluminium and the bare GFRP panel were obtained and noted [5–8]. The testing revealed two archetypal load-displacement relationships: single-peak and double-hump bends. The slopes representing nonsuccess models of higher and lower face sheets are more than the failure stage in the energy-displacement curve [9–13], showing that the bare aluminium sheet had poorer energy attainment levels than the GFRP face sheet. In turn, honeycomb infill, on the other hand, was a successful technique to develop the collision resistance of GFRP structures, resulting in a gradual increase in energy absorption and reduced peak load during the influence [14]. The crashworthiness features were likewise shown to be more sensitive to core length compared to core height, with specific energy absorption (SEA) change being minimal as the core height increased. Under high impact velocity, peak load, absorbed energy, and SEA rose notably [15, 16].

The bioinspired sandwich construction on an aluminium face sheet with glass fibre reinforcement, epoxy resin matrix, and pet foam core material is the focus of this research [17–30]. The materials' characteristics were determined experimentally in accordance with ASTM standards [31–40].

The present experimental work on the aluminium face sheet with glass fibre reinforcement, epoxy resin matrix, and pet foam core material-based sandwich composite panels is available for limited studies in the literature. It has many advantages: lightweight, high mechanical strength, chemical, and heat resistance. Limited disadvantages are at the end of their life, and recycling and material separations are difficult.

Furthermore, the experimental results were compared to both the composites and the values used to determine the application.

2. Experimental Study

2.1. Materials. "Skin" is the outer side of the hybrid structure. Aluminium (1100) sheets are employed as the skin material for the improved sandwich composition. The thickness of the sheet is 0.3 mm. By using snipping, the sheet is cut into the required dimension of the skin. Two skins are required to develop one hybrid structure. The matrix material is used to create a bond between the polyethylene terephthalate (PET) foam and the skin materials. As the sandwich matrix material, bisphenol-A (Araldite LY556 resin & Aradur HY951hardnear) epoxy resin is used as the base. It is a very light material, so it is used to reduce the weight of the composite. Abrasive material is used for glass beads and SS beads to improve the surface roughness of the skin material and for uniform binding with the core. Woven glass fibres are employed as a reinforcement material. It is placed in between the PET foam and the face sheets. Table 1 shows the materials required for the fabrication of sandwich panels.

The aluminium1100 grade face sheet property has more correction, heat, and chemical resistance. It helps uniform load transfer to the core material. Energy dissipation in the face sheet for various energies transmitted in the form of quasistatic, tensile, compressive, impact, and dynamic loading has been experimented with by many researchers. The bisphenol-A (Araldite LY556 & Aradur HY951) epoxy resin has low viscosity, long shelf life, good fibre impregnation, and better mechanical, thermal, and chemical properties. The core structural thermoplastic PET foam (thermo-formable closed cell structure) core material is ideal for a variety of sandwich applications that require increased performance while reducing weight. Its properties are better chemical resistance, thermal resistance, sound insulator, very low water absorption, better resin bonding, and screw retention capability. The material has a density range (ISO 845) of 75–85 kg/m^3, a thermal conductivity of 0.033 W/(m-K), a compressive strength (ASTM D 1621) of 0.8–1 MPa, and a compressive modulus (ASTM D 1621 B-73) of 65–80 MPa. There are various grades of glass fibres available. The E-glass fabric is the general purpose low-cost material and also has ASTM standard specifications for characteristics such as high mechanical strength, heat resistance, good water resistance, heat insulation, and better process ability.

2.2. Methods. The main objective of our project is to manufacture a composite material using an aluminium face sheet of 0.3 mm thickness, epoxy resin, glass fibre, and PET foam.

To get a good result, primary work has to be carried out on aluminium sheets. It contains oily layers. An acetone solution is used to remove the oily surface of the sheet completely. Preparing the aluminium face sheet is carried out before going into the process.

2.2.1. Preparation Steps for Sandwich Composite Panels. The following steps are for preprocessing work. Step 1: cut the aluminium sheet to dimensions of $20 * 30$ cm; Step 2: remove any moisture and rust from the aluminium sheet; Step 3: blast the aluminium sheet at the appropriate pressure (3, 5, 7 bar); Step 4: combine the epoxy resin and hardener in a 10 : 2 ratio; Step 5: cut the glass fibre into 25×35 cm pieces. Step 6: the glass fibre with PET foam must be free of moisture and air. This is the preprocessing work that has to be performed to avoid failures that have happened in the final product.

2.2.2. Fabrication Process. After performing the preprocessing (cleaning the face sheet) work, the material is put into the fabrication process. Before moving to the process,

Table 1: Materials required for the fabrication of sandwich panels.

Material	Description	Dimension/grade
Face sheet	Aluminium sheet	0.3 mm thickness & 20×30 cm
Matrix (resin)	Epoxy + hardener	10 : 2 ratio
Core material	PET foam	25×35 cm
Reinforcing material	Glass fabric	E-glass

we ensure the material is free from dust and moisture, and also ensure the quality of the material. To get a better result, we maintain the room temperature at around 30°C. Hand gloves and a face mask are worn during the process for safety.

The schematic representation of the hybrid sandwich panel preparation process is shown in Figure 1, and its process steps are as follows: Step 1: the aluminium sheet (0.3 mm thick) is blasted using various methods (sand blast and glass blast) at various pressures, such as 3 bar, 5 bar, and 7 bar, and a mixed (10 : 2) ratio of epoxy resin with hardener. Step 2: glass fibre is cut into the required dimensions and placed on the aluminium sheet. Spread the epoxy resin evenly over the glass fabric. Now, we take the pet foam (core material) and cut it into dimensions of 25×35 cm that should be placed on the glass fibre. Step 4: the process is repeated until the sandwich structure of two required composite materials is obtained. Step 5: the compression moulding process is used to fabricate the hybrid sandwich panel. The fabrication of control samples is the same as the above procedure, except for aluminium face sheet surface blasting (step 1).

The Araldite LY556 resin is preheated at 30 to 50°C before adding the Aradur HY951 hardener to improve the performance of the matrix preparation process. There are many accelerators available to improve the performance of matrices. The premixing of the hardener and accelerator can allow the use of two-component mixing; it has a longer self-life for several days of usage. The processing of the total matrix mixing system shows the best results at 30 to 40°C.

2.2.3. Design Considerations. It is confirmed that a prepared sandwich panel construction has the ability to accept the structural loads along with design life. It maintains its systemic probity in service conditions in favour of experimental calculation.

The face sheets are provided with essential rigidity so as to withstand the tensile, compaction, and shear strains for applied loads. The core is present to provide the necessary firmness to withstand the shear strains caused by the application of loads. The core has the eligible shear modulus to resist complete buckling of the interlaying composition under loads. The firmness of the core and the compliant solidity of the face sheets should be sufficient to resist the crinkling of the face sheets under applied loads. The core cells are precise enough to avert intercell buckling of the face sheets under modelling loads. More compressive solidity is required in the core to prevent suppression caused by applied loads reacting normally to the face sheets or by suppressing pressure generated by flexure. The sandwich

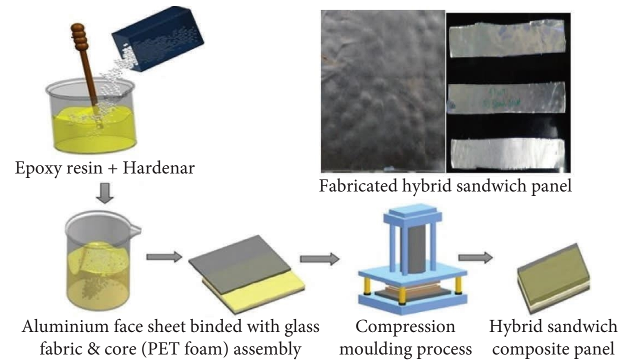

Figure 1: Preparation process for the hybrid sandwich panel.

construction has essential flexural and shear firmness to resist additional deviations under given loads. Sandwich stuff (face sheet, core, and adhesive) must support constructional coherence during in-service conditions. Based on this design consideration, the sandwich panel is fabricated as shown in Figure 1.

2.3. Characterization Techniques Used. The fabricated panels are characterised using an artificial environmental weathering test, which is conducted with accelerated weathering equipment. It has a programmable low-temperature humidity control range of −20°C to 50°C as well as a programmable high-temperature humidity control range of −70°C to 150°C. The peeled sandwich composite surfaces were analysed using a Hitachi S-4700 scanning electron microscope (SEM) operated at an accelerating voltage of 10 kV. The optimization of blast pressure using a sand/glass blasting machine, abrasive Eco blast, make: sandstorm, model: SEC-SB-12090, up to 10 bar pressure. The blast surface damage is analysed using vision measurement equipment, make: OPUS, lens magnification: 0.75–4.5 X, high-resolution multicolor CCD camera inbuilt. The peel testing is carried out using a universal testing machine (UTM), make: Instron, model: 3328, up to a 100 kN capacity.

3. Results and Discussion

3.1. A Weathering Trail Is Conducted for Prepared Samples. The completely cured sandwich composite materials are placed in the weathering chamber under the following conditions shown in Table 2 and Figure 2.

Table 2 shows the test conditions programmed in the weathering chamber. Three standard test conditions are selected to evaluate hybrid sandwich panels. For all the conditions, the temperature and test timing are constant, while the humidity value is varied with respect to predicting the sandwich panel face sheet and core bonding damage with respect to time and temperature. UV radiation is present in the outdoor environment. It contains temperature and humidity differences with time and temperature. So, it is the most important damaging component; it changes the chemical structures of the materials. The weathering test is the very important parameter to determine the prepared composite sandwich panel's bonding performance.

Table 2: Weathering test conditions for sandwich panels.

Target samples	Temperature (°C)	Humidity (%)	Time (hrs)
Control sample	60	100, 95 & 85	72
Hybrid sandwich panel 1	60	100	72
Hybrid sandwich panel 2	60	95	72
Hybrid sandwich panel 3	60	85	72

Figure 2: Prepared sandwich composite panels in artificial weathering chamber.

The standard test parameters are set in the weathering chamber. The obtained test results recommend the prepared hybrid sandwich panels 1, 2, and 3 where there is not much material or chemical damage predicted on visual inspection. But the control samples are all three conditions. Natural peel occurred at the end corners of the panels due to the lack of surface roughness. The material bonding strength was affected. These weathered samples are further tested for various characterizations and a mechanical peel test.

3.2. Scanning Electron Microscopy. Weathering samples, peeled sandwich composite surfaces with sand blast and without sand blast specimens, are shown in Figure 3(a). The PET foam is bonded with epoxy resin and compressed with blasted aluminium sheet at an optimised pressure of 5 bar. The surfaces are distinctly transparent. The depth of this surface damage, however, appears to vary with an aluminium exterior. The film is thick and essential to some extent so that it completely wraps around the resin on the surface, and the nonhomogeneous powder mixture is visible, as shown in Figure 3(c). The fully compressed PET foam surface morphology is clearly visible in Figure 3(d). In additional areas, the peeled PET foam surface is much thinner, and the cured adhesive bonding is still distinctly visible, see Figure 3(b).

3.3. Optimization of Blast Pressure. The blasted exterior was pacified for surface rigidity computation and vision quantification analysis so as to examine the effects of blasting on external rigidity and surface patterning. During blasting, due to molecular interactions, the exterior layer is subordinated to abrasiveness and generates crudeness. However, blasting compression plays a key role in creating the desired firmness. Figure 4 illustrates the difference in surface firmness for numerous blasting influences. It is apparent from the figure that mean surface roughness (Ra) increases with an increase in blast pressure. The surface indentation observed was to be increased up to 5 bar of blasting pressure using both glass and SS sand, as well as increasing the pressure that showed a decrease in exterior roughness. The measured surface roughness values are shown in Table 3. And it was measured using a surface roughness tester, Mitutoyo, SJ210 model, Tokyo, Japan.

3.4. Blast Surface Damage Analysis. Surface blasting was done through a blasting machine setup, make: OPUS, vision measuring instrument, CIPET, Chennai, India. The failure modes of the blasted aluminium surface vary with pressure difference, blasting specimen handling, or holding position in the blasting machine, and material damage also occurs due to abrasive material selection. Proper rectifying of the FML materials via fabrication was required to achieve fine structural equities [15]. Figure 5 depicts the failure of the sandwich composite skin structure's aluminium sheet sandblasted face sheets.

3.5. Peel Test Results. The peel strength increased from the original value due to the various surface roughness. Due to abrasive molecular collusion in the blasting nozzle, the peel strength will drop after a certain pressure limit, the surface roughness value will decrease, and the adhesive strength will also decrease. For the 5 bar glass blast and SS sand blasting, the optimal value was recorded. In both glass and SS sand abrasives, inadequate adhesion strength suggests pressures of 6 bar and 7 bar. However, as the alumina/PET foam adhesion was enhanced, there was a greater potential for unstable crack propagation.

Figure 6(a) shows the force-displacement curve of peel resistance of an artificial weathered sample. Peel resistances are measured between the aluminium face sheet reinforced with glass fabric and the PET foam core. This complex binding cross section (aluminium sheet/glass fabric/PET foam) may fail at any time with respect to critical atmospheric weathering conditions. So, the peel resistance test is the most suitable test method to identify the target samples' peak force, crack point, crack path, and fracture energy. The peel resistance test is conducted with the universal testing machine (UTM) as shown in Figure 6(b), and sample dimensions are shown in Figure 6(c). The samples are fixed in T-shape. 180° peel-off was carried out in tensile mode with a cross-head speed of 2 mm/min. The peel test load vs. displacement graph is plotted with the average of five sample values. The obtained graph shows that there are not many variations in the hybrid sandwich panels 1, 2, and 3 weathered samples fracture energy. But the control sample performance is poor in fracture energy, as shown in Table 4.

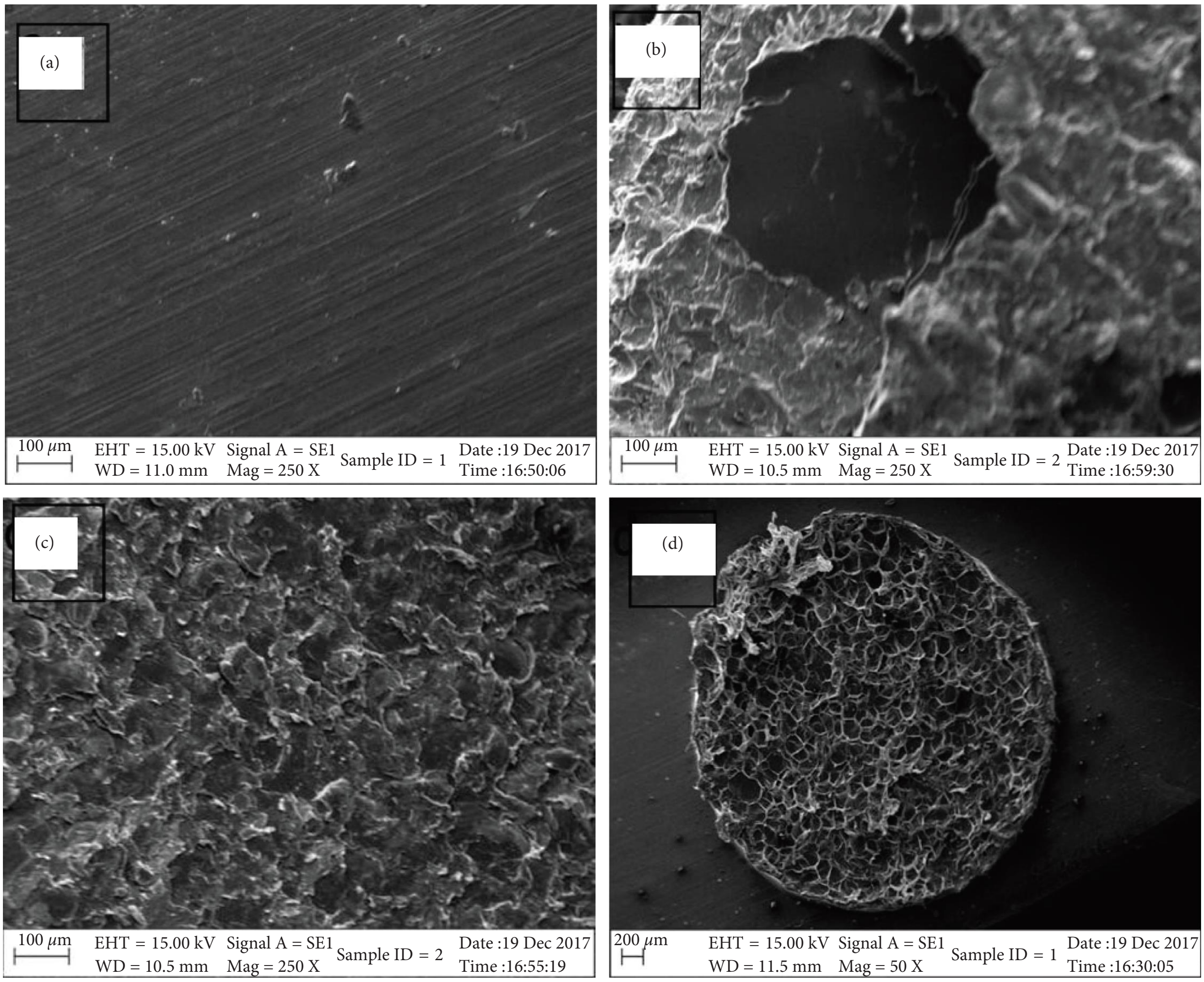

Figure 3: (a) Aluminium sheet with e-glass epoxy coated surface; (b) aluminium sheet with 5 bar SS sandblasted and resin coated peeled surface; (c) peel surface with cured resin and coating; and (d) PET form compressed with a fully peeled surface.

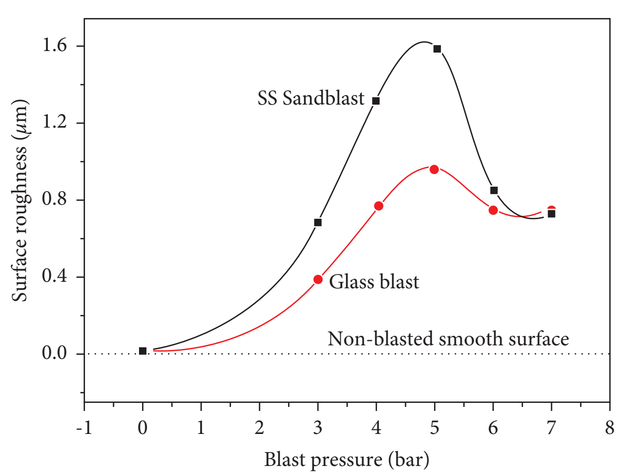

Figure 4: Surface roughness for different blasting pressures.

Table 3: Surface roughness for blasted aluminium skin.

Pressure	Glass blast	SS sandblast
Plain sheet roughness (μm) control sample	0.0169	0.0175
3 Bar (μm)	0.39	0.6865
5 Bar (μm)	0.9627	1.319
6 Bar (μm)	0.7519	0.8560

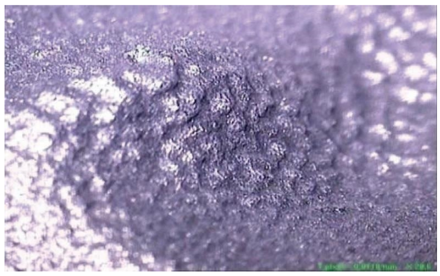

(a)

(b)

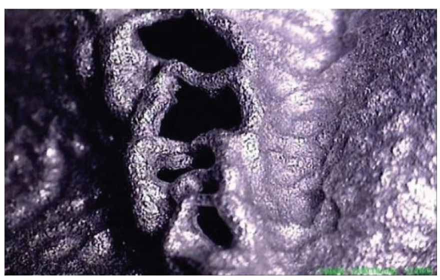

(c)

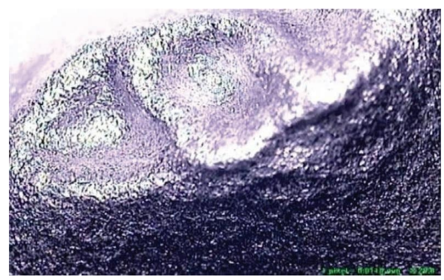

(d)

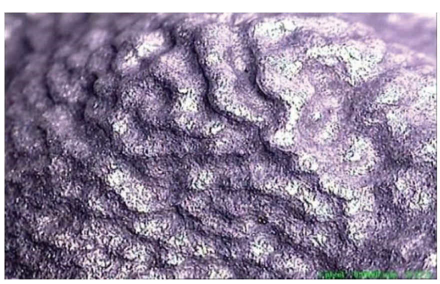

(e)

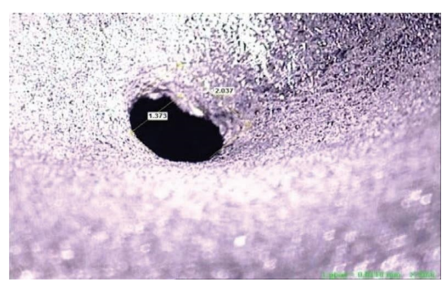

(f)

Figure 5: Maximum blast damage predicted for glass and SS sand blasting on aluminium surface. (a) Glass blast 5 bar pressure, (b) SS sand blast 5 bar pressure, (c) glass blast 6 bar pressure, (d) SS sand blast 6 bar pressure, (e) glass blast 7 bar pressure, and (f) SS sand blast 7 bar pressure.

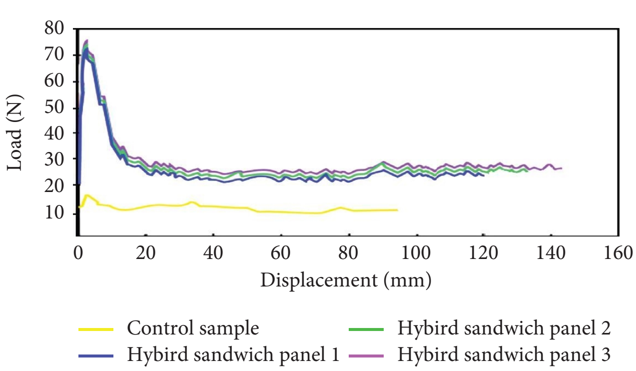

(a)

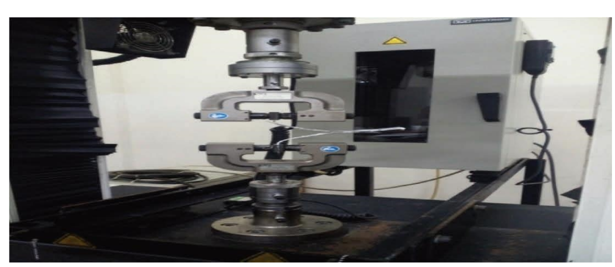

(b)

Figure 6: Continued.

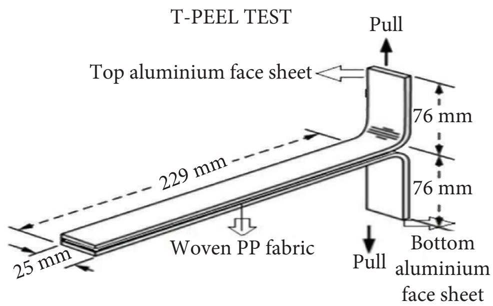

(c)

Figure 6: (a) Load vs. displacement curve for hybrid sandwich panels, (b) peel test setup in universal testing machine, and (c) schematic representation of peel test sample.

Table 4: T-peel experimental test results.

Target samples	Peak load (N)	Displacement (mm)	Crack formation before complete delamination (mm)	Fracture energy (J/m^2)
Control sample	18	94	6	211
Hybrid sandwich panel 1	75	120	6.5	535
Hybrid sandwich panel 2	76	136	6.9	537
Hybrid sandwich panel 3	78	142	7	540

4. Conclusions

The glass and stainless-steel sandblasted performance of the sandwiched hybrid laminate was expanded using aluminium as the skin and an epoxy/glass fabric/PET foam composite as the core. It could be investigated at various surface roughness, peel strength, and surface damage levels, as well as tested in real-time artificial weather conditions in a test chamber. The aluminium skin surface was modified by blasting (glass and SS sand) at various blast pressures. The peel strength of the tested laminate could be optimised as a result of the surface roughness. The adhesive strength of the laminate was estimated. The surface roughness is high at 5 bar of blasting without any defects. The adhesion strength is also observed to be high at 5 bar pressure blasted laminates. The various blasting defects are described in detail; the proper optimization of blast pressure will reduce the surface damage in aluminium skin material. In future work, the corona treatment increases the surface energy of aluminium skin and the adhesion of core materials. The fabricated target samples are best suitable for humid atmospheres.

Data Availability

The data used to support the findings of this study are available from the corresponding author upon request.

Conflicts of Interest

The authors declare that there are no conflicts of interest.

Acknowledgments

This work was supported by Jimma University, Ethiopia, for writing and editing the manuscript.

References

[1] S. Deepak, K. P. Bhuvana, R. J. Bensingh, K. Prakalathan, and S. K. Nayak, "Development of hybrid composites and joining technology for lightweight structures," *Advances in Polymer Sciences and Technology*, pp. 123–131, 2018.

[2] L. Yang, Z. Chen, Y. Dong, F. Zi, J. Yang, and L. Wu, "Ballistic performance of composite armor with dual layer piecewise ceramic tiles under sequential impact of two projectiles," *Mechanics of Advanced Materials and Structures*, vol. 29, pp. 1–14, 2020.

[3] S. Mathiazhagan and S. Anup, "Mechanical behaviour of bio-inspired brittle-matrix nanocomposites under different strain rates using molecular dynamics," *Molecular Simulation*, vol. 42, no. 18, pp. 1490–1501, 2016.

[4] M. Agarwal and A. K. N. Shukla, "Synthesis of novel bio-composite by powder processing: an assessment," *Materials and Manufacturing Processes*, vol. 36, no. 2, pp. 178–187, 2021.

[5] R. Mwesigwa and J. I. Mwasiagi, "Use of regression models to study the factors affecting the tensile and compressive properties of banana bio-composites," *Journal of Natural Fibers*, vol. 16, no. 7, pp. 1055–1063, 2019.

[6] T. Akagi, H. Cabral, and P. Mi, "Bio-inspired nanomaterials for biomedical innovation," *Science and Technology of Advanced Materials*, vol. 19, pp. 420-421, 2020.

[7] K. K. Sadasivuni, J. J. Cabibihan, K. Deshmukh et al., "A review on porous polymer composite materials for multi-functional electronic applications," *Polymer-Plastics Technology and Materials*, vol. 58, no. 12, pp. 1253–1294, 2019.

[8] T. V. Aradhyula, D. Bian, A. B. Reddy et al., "Compounding and the mechanical properties of catla fish scales reinforced-polypropylene composite–from biowaste to biomaterial," *Advanced Composite Materials*, vol. 29, no. 2, pp. 115–128, 2020.

[9] F. Wang, H. Yuan, and J. Huang, "A bio-inspired nanofibrous Co3O4/TiO2/carbon composite as high-performance anodic material for lithium-ion batteries," *Journal of Alloys and Compounds*, vol. 819, Article ID 153375, 2020.

[10] D. Jia, X. Li, and J. Huang, "Bio-inspired sandwich-structured carbon/silicon/titanium-oxide nanofibers composite as an anode material for lithium-ion batteries," *Composites Part A: Applied Science and Manufacturing*, vol. 101, pp. 273–282, 2017.

[11] V. Rodríguez-García and R. G. de Villoria, "Automated manufacturing of bio-inspired carbon-fibre reinforced polymers," *Composites Part B: Engineering*, vol. 215, Article ID 108795, 2021.

[12] A. Melaibari, A. Wagih, M. Basha, A. M. Kabeel, G. Lubineau, and M. A. Eltaher, "Bio- inspired composite laminate design with improved out-of-plane strength and ductility," *Composites Part A: Applied Science and Manufacturing*, vol. 144, Article ID 106362, 2021.

[13] B. Gyarmati and B. Pukánszky, "Natural polymers and bio-inspired macromolecular materials," *European Polymer Journal*, vol. 93, pp. 612–617, 2017.

[14] R. Shu, X. Jiang, H. Sun, Z. Shao, T. Song, and Z. Luo, "Recent researches of the bio- inspired nano-carbon reinforced metal matrix composites," *Composites Part A: Applied Science and Manufacturing*, vol. 131, Article ID 105816, 2020.

[15] J. Li, M. Wang, and Huang, "J. Bio-inspired hierarchical nanofibrous SnS/C composite with enhanced anodic performances in lithium-ion batteries," *Journal of Alloys and Compounds*, vol. 860, Article ID 157897, 2021.

[16] S. Mathiazhagan and S. Anup, "Effect of interface strength on the mechanical behaviour of bio-inspired composites: a molecular dynamics study," *Mechanics of Materials*, vol. 132, pp. 93–100, 2019.

[17] X. Hu, Z. Sun, C. Zhang, X. Wang, and K. Wu, "Microstructure and mechanical properties of bio-inspired Cf/Ti/Mg laminated composites," *Journal of magnesium and alloys*, vol. 6, no. 2, pp. 164–170, 2018.

[18] R. Häsä and S. T. Pinho, "A novel aluminium/CFRP hybrid composite with a bio-inspired crossed-lamellar microstructure for preservation of structural integrity," *Composites Science and Technology*, vol. 182, Article ID 107760, 2019.

[19] X. Cui, K. Yan, and J. Guo, "Bio-inspired fabrication, mechanical characterization and cutting performance evaluation of Al2O3/TiC micro-nano-composite ceramic with varying microscopic surfaces," *Ceramics International*, vol. 45, no. 7, pp. 8286–8299, 2019.

[20] M. Sharabi, D. Varssano, R. Eliasy, Y. Benayahu, D. Benayahu, and R. Haj-Ali, "Mechanical flexure behavior of bio-inspired collagen-reinforced thin composites," *Composite Structures*, vol. 153, pp. 392–400, 2016.

[21] M. Ashokkumar and S. Rajesh, "Experimental investigation of carbon/glass/epoxy hybrid composites," *International Journal of Renewable Energy Technology*, vol. 1, no. 4, pp. 56–59, 2016.

[22] S. Deepak, D. Thirumalaikumarasamy, M. Ashokkumar, and S. K. Nayak, "Experimental analyzing the static puncture resistance performance of shear thickening fluid impregnated polypropylene hybrid composite target structures for armour application," *Journal of the Textile Institute*, pp. 1–13, 2022.

[23] D. SampathKumar, T. Duraisamy, T. Pattabi, and A. Mohankumar, "Static puncture resistance characteristics with various indenter nose shape geometry perforation of shear thickening fluid impregnated polypropylene fabric for soft armour application," *Polymers and Polymer Composites*, vol. 30, Article ID 09673911211063303, 2022.

[24] S. Deepak, D. Thirumalaikumarasamy, P. Thirumal et al., "Preparation and characterization of shear thickening fluid coated polypropylene fabric for soft armour application," *Journal of the Textile Institute*, vol. 112, no. 10, pp. 1555–1567, 2021.

[25] A. Mohankumar, T. Duraisamy, R. Chidambaramseshadri et al., "Enhancing the corrosion resistance of low pressure cold sprayed metal matrix composite coatings on AZ31B Mg alloy through friction stir processing," *Coatings*, vol. 12, no. 2, p. 135, 2022.

[26] A. Mohankumar, T. Duraisamy, D. Sampathkumar, and S. Ranganathan, "Optimization of cold spray process inputs to minimize porosity and maximize hardness of metal matrix composite coatings on AZ31B magnesium alloy," *Journal of Nanomaterials*, vol. 2022, Article ID 7900150, 17 pages, 2022.

[27] P. R. Rajendran, T. Duraisamy, R. Chidambaram Seshadri et al., "Optimisation of HVOF spray process parameters to achieve minimum porosity and maximum hardness in WC-10Ni-5Cr coatings," *Coatings*, vol. 12, no. 3, p. 339, 2022.

[28] M. Ashokkumar, D. Thirumalaikumarasamy, P. Thirumal, and R. Barathiraja, "Influences of Mechanical, Corrosion, erosion and tribological performance of cold sprayed Coatings A review," *Materials Today Proceedings*, vol. 46, pp. 7581–7587, 2021.

[29] M. Kannan, T. Duraisamy, T. Pattabi, and A. Mohankumar, "Investigate the corrosion properties of stellite coated on AZ91D alloy by plasma spray technique," *Thermal Science*, vol. 26, no. 2, pp. 911–920, 2022.

[30] K. Mathivanan, D. Thirumalaikumarasamy, M. Ashokkumar, S. Deepak, and M. Mathanbabu, "Optimization and prediction of AZ91D stellite-6 coated magnesium alloy using Box Behnken design and hybrid deep belief network," *Journal of Materials Research and Technology*, vol. 15, pp. 2953–2969, 2021.

[31] A. B. H. Kueh, M. Yazid Yahya, and M. Uzir Wahit, "Impact resistance efficiency of bio-inspired sandwich beam with different arched core materials," *Steel and Composite Structures*, vol. 44, no. 1, pp. 105–117, 2022.

[32] M. Hanifehzadeh and M. M. R. Mousavi, "Predicting the structural performance of sandwich concrete panels subjected to blast load considering dynamic increase factor," *Journal of Civil Engineering, Science and Technology*, vol. 10, no. 1, pp. 45–58, 2019.

[33] A. B. H. Kueh and Y. Y. Siaw, "Impact resistance of bio-inspired sandwich beam with side-arched and honeycomb dual-core," *Composite Structures*, vol. 275, Article ID 114439, 2021.

[34] S. H. Drahman, A. Beng Hong Kueh, and A. Razin Zainal Abidin, "Low-velocity impact of composite sandwich plate with facesheet indentation description," *Jurnal Teknologi*, vol. 77, p. 16, 2015.

[35] N. San Ha, T. M. Pham, T. T. Tran, H. Hong, and G. Lu, "Mechanical properties and energy absorption of bio-inspired hierarchical circular honeycomb," *Composites Part B: Engineering*, vol. 236, Article ID 109818, 2022.

[36] L. Lam, W. Chen, H. Hong, Z. Li, N. San Ha, and T. M. Pham, "Numerical study of bio-inspired energy-absorbing device using shear thickening fluid (STF)," *International Journal of Impact Engineering*, vol. 162, Article ID 104158, 2022.

[37] M. Ashokkumar, D. Thirumalaikumarasamy, S. Deepak, and T. Sonar, "Electrochemical corrosion performance of friction stir processed cold spray metal matrix composite coatings on AZ31B magnesium alloy under sodium chloride environment" surface topography," *Metrology and Properties*, vol. 10, no. 3, Article ID 035010, 2022.

[38] M. Ashokkumar, D. Thirumalaikumarasamy, T. Sonar, S. Deepak, P. Vignesh, and M. Anbarasu, "An overview of cold

spray coating in additive manufacturing, component repairing and other engineering applications," *Journal of the Mechanical Behavior of Materials*, vol. 31, no. 1, pp. 514–534, 2022.

[39] S. Seshaiah, D. Sampathkumar, M. Mariappan et al., "Optimization on material removal rate and surface roughness of stainless steel 304 wire cut EDM by response surface methodology," *Advances in Materials Science and Engineering*, vol. 2022, Article ID 6022550, 10 pages, 2022.

[40] M. Mathanbabu, D. Thirumalaikumarasamy, P. Thirumal, and M. Ashokkumar, "Study on thermal, mechanical, microstructural properties and failure analyses of lanthanum zirconate based thermal barrier coatings: a review," *Materials Today Proceedings*, vol. 46, pp. 7948–7954, 2021.

Hindawi
Advances in Materials Science and Engineering
Volume 2024, Article ID 9810320, 1 page
https://doi.org/10.1155/2024/9810320

Retraction

Retracted: Improvement of Microstructure and Properties of Q235 Steel by Iron-Based Laser Cladding Coating

Advances in Materials Science and Engineering

Received 8 January 2024; Accepted 8 January 2024; Published 9 January 2024

This article has been retracted by Hindawi following an investigation undertaken by the publisher [1]. This investigation has uncovered evidence of one or more of the following indicators of systematic manipulation of the publication process:

(1) Discrepancies in scope
(2) Discrepancies in the description of the research reported
(3) Discrepancies between the availability of data and the research described
(4) Inappropriate citations
(5) Incoherent, meaningless and/or irrelevant content included in the article
(6) Manipulated or compromised peer review

The presence of these indicators undermines our confidence in the integrity of the article's content and we cannot, therefore, vouch for its reliability. Please note that this notice is intended solely to alert readers that the content of this article is unreliable. We have not investigated whether authors were aware of or involved in the systematic manipulation of the publication process.

Wiley and Hindawi regrets that the usual quality checks did not identify these issues before publication and have since put additional measures in place to safeguard research integrity.

We wish to credit our own Research Integrity and Research Publishing teams and anonymous and named external researchers and research integrity experts for contributing to this investigation.

The corresponding author, as the representative of all authors, has been given the opportunity to register their agreement or disagreement to this retraction. We have kept a record of any response received.

References

[1] Y. He, Y. Gu, L. Tang, and H. Wang, "Improvement of Microstructure and Properties of Q235 Steel by Iron-Based Laser Cladding Coating," *Advances in Materials Science and Engineering*, vol. 2022, Article ID 2790770, 9 pages, 2022.

Hindawi
Advances in Materials Science and Engineering
Volume 2022, Article ID 2790770, 9 pages
https://doi.org/10.1155/2022/2790770

Research Article

Improvement of Microstructure and Properties of Q235 Steel by Iron-Based Laser Cladding Coating

Yuanwei He,[1] Yu Gu,[1] Li Tang,[2] and Hu Wang[1]

[1]*Mechanical-Electrical Engineering Faculty, Hunan Institute of Traffic Engineering, Hengyang 421001, China*
[2]*National University of Defense Technology, Changsha 410000, China*

Correspondence should be addressed to Hu Wang; 161849039@masu.edu.cn

Received 18 April 2022; Accepted 13 July 2022; Published 13 August 2022

Academic Editor: Ravi Samikannu

Laser cladding is a repair and surface-strengthening technology for the protection of metal parts. It is an effective method for improving the properties of various metal substrates. The process involves melting and solidifying alloy powder on the surface of the substrate. The aim of the present study was to explore the effect of iron-based alloy laser cladding coating on Q235 substrate. Three types of specimens were obtained from Q235 base material using a 5 kW cross-flow CO_2 laser beam. Sample 1 and sample 2 were obtained by the addition of rosin to the iron-based alloy powder. Sample 3 was obtained through the addition of rosin and vanadium to the iron-based alloy powder. A gas curtain was used to wrap the molten pool of samples 2 and 3. The surface hardness of the specimens was determined using a Rockwell hardness tester, and the tensile strength was evaluated using the universal mechanical testing machine. The microstructure of the cladding coating was explored using an Olympus optical microscope and SEM. The results showed that the average hardness of sample 2 and sample 3 was 6.42% and 19.84% higher than that of sample 1. The average tensile strength of samples 2 and 3 was 7.42% and 10.37% higher than that of sample 1. The grain of sample 3 was finer than that of sample 2, and that of sample 2 was finer than that of sample 1 under the same magnification. Rosin minimized oxidation of the substrate, whereas the gas curtain prevented the entry of air into the molten pool, hence the improved properties of samples 2 and 3 compared with that of sample 1. Rosin and the gas curtain protected the powder from oxidation loss and improved the quality of the cladding coating. The results of the present study show that rosin reduced the oxidation of iron-based powder, whereas vanadium improved the hardness and strength of the substrate as well as refined the grain size.

1. Introduction

Laser forming technology can significantly improve the surface physical, chemical, and mechanical properties of steel parts. This technique is widely used in aviation, automobile, shipbuilding, biomedicine, and other fields. It is a green manufacturing technology extensively used globally [1]. Several factors affect the quality and properties of laser-formed samples. The material used to form the laser layer is the main factor that affects the quality and property of samples. Several studies have been conducted on laser-modified samples using iron-based, nickel-based, and cobalt-based alloy powder materials. Iron-based alloy powder is widely used in the laser forming process owing to its low price and ease of manipulation. However, iron-based alloy powder can be easily oxidized and burned during the laser forming process, resulting in defects such as pores and slag inclusion, which affects the mechanical properties of the final samples [2]. Currently, scholars use protective gas under an atmospheric environment to minimize oxidation of the sample. Air is drawn into the protective gas due to the jet entrainment effect, therefore, oxidation and burning loss occur when using this approach. The use of powder with antioxidation burning loss ability on the laser melting pool significantly improves the properties of the laser-formed sample. In the present study, the transient reducing protective atmosphere formed by gasification and combustion of rosin in the laser molten pool was used to reduce the oxidation and burning loss of alloy powder by oxygen in the atmosphere. In addition, it minimizes defects such as pores and slag inclusion on the sample so as to improve the quality of the final samples [3].

The materials used for the laser cladding process include alloy powder, wire, paste, and rod. Most commonly used materials include iron-based, nickel-based, cobalt-based, ceramic powder, composite powder, and amorphous alloy powder with different particle sizes. Self-fusible alloy powder is an alloy powder with various alloying elements (such as Si and B.) added to Ni, Fe, CO, and other matrix alloys [4–8]. This type of powder has a low melting point and is effective for the cladding process. The ceramic powder has a high melting point and hardness and can be classified as carbide ceramic powder, oxide ceramic powder, and silicide ceramic powder. Composite powder mainly refers to alloy powder formed by combining carbide, oxide, boride, silicide, and other high melting points hard ceramic materials with metal materials. The amorphous shape and low interface energy of amorphous alloy powder provide good wettability properties to the matrix material. Moreover, it melts uniformly during cladding [9–13]. The cladding product has higher yield strength, large elastic strain limit, high wear resistance, and excellent corrosion resistance. The most widely used material during laser cladding remanufacturing is iron-based alloy powder. Iron-based alloy powder has low cost, reliable performance, and wear and corrosion resistance, and meets the needs of laser cladding remanufacturing of key metal parts in mining machinery, engineering machinery, steel, and other industries [14–18].

Laser cladding is an effective method for preparing large-area coatings. It is widely used in improving the surface properties of metal parts and repairing surface damage of mechanical products [19–21]. Laser cladding is a new surface modification and damage repair technology widely used in the fields of coating, repair, and prototype manufacturing. Farahmand and Kovacevic used induction heating composite laser cladding technology to reduce the sensitivity of laser cladding to cracks and pores. The findings showed that the use of induction heating significantly improved the transfer efficiency of tungsten carbide (TC). Bidron et al. conducted a study to eliminate thermal cracks in laser cladding through induction preheating. Preheating by induction heating effectively prevents thermal cracks during laser cladding when the preheating temperature range is 800~1100°C [22–24].

Laser cladding technology is used for the formation of cladding coating with excellent properties such as corrosion resistance, high temperature resistance, wear resistance as well as fatigue resistance on low-performance and low-cost steel to meet various harsh requirements [21, 25–29]. Moreover, it reduces cost, minimizes overuse of scarce and precious materials, reduces energy consumption, reduces pollution, and improves the service life of metal parts. Nickel-based powders are currently the most widely used type, but the cost of these powders is about three times higher than that of iron-based powders [30]. However, the iron-based powder is easily oxidized and burnt during the cladding process. In addition, the prepared cladding coating exhibits several defects such as slag inclusion, pores, and cracks [31]. This limitation can be circumvented by using rosin to coat the surface of the iron alloy powder particles, under the action of the laser beam. Rosin forms a reducing protective atmosphere to protect the molten pool from oxidation. Furthermore, it reduces or even eliminates various defects on the cladding coating, thereby markedly improving the mechanical properties of the cladding coating [32]. Vanadium is used to refine steel structures and grains. Therefore, vanadium is added to the alloy powder, forming stable compounds with carbon and oxygen under the action of high-temperature laser. It is mainly dispersed in the cladding coating in the form of vanadium-carbon (VC) which further improves the mechanical properties of the metal part [33].

2. Experimental Materials and Procedures

2.1. Preparation of the Material and Morphological Analysis. The Q235 steel plate has low cost as well as high compatibility with the wire cutting treatment subjected to the substrate and laser clad coating after the test. Therefore, a Q235 steel plate was selected as the substrate in the present study. A high temperature is used in the process of laser rapid prototyping, leading to bending deformation of the substrate, which affects the formation of the sample. The substrate should be appropriately thick to circumvent the effect of high temperatures. A steel plate with more than 15 mm thickness is suitable for experimental requirements. The bending degree of the whole substrate is not significantly different after the laser experiment when using an appropriate thickness; thus, it has little effect on the experimental results. Both sides of the substrate are crushed with a grinder before the experiment. The substrate is first washed with water and detergent to remove oil and impurities. Subsequently, it is cleaned with clean water, then with ethanol to further remove impurities. The substrate is wiped with acetone after cleaning and then dried with a blower. Furthermore, the substrate is dried in a drying oven. The surface of the steel plate is then sandblasted using a sand blasting machine. Sandblasting removes the remaining oil stains and rust, as well as makes the surface of the substrate rough and reduces reflection of the substrate to the laser, for use in the subsequent experiment.

Rosin was added in excess to the iron-based powder and remained in excess after several experiments and attempts. Slag inclusion occurs when the combustion is not complete, and the hydrogen element in the rosin dissolves the metal, resulting in deterioration of the substrate properties. Formation of the gas is ineffective if an insufficient amount of rosin is used; therefore, it does not play the role of protection from reduction. Several experiments and findings from previous studies indicate that the rosin film coating on the surface of iron-based powder particles exhibited a good effect at the micron level. The iron-based powder particles combined with rosin were observed under a scanning electron microscope, and the findings indicated that rosin uniformly covered the powder particles (Figure 1).

Furthermore, a 5 kW cross-flow CO_2 laser was used for the laser rapid prototyping test. The dried powder was placed on the powder feeding device. The 15 mm Q235 steel plate was placed on the experimental workbench, and the distance between the laser nozzle and the substrate was adjusted. The lateral synchronous powder feeding method was used to scan the substrate along the X direction, with the substrate driven by the NC workbench. The laser parameters obtained

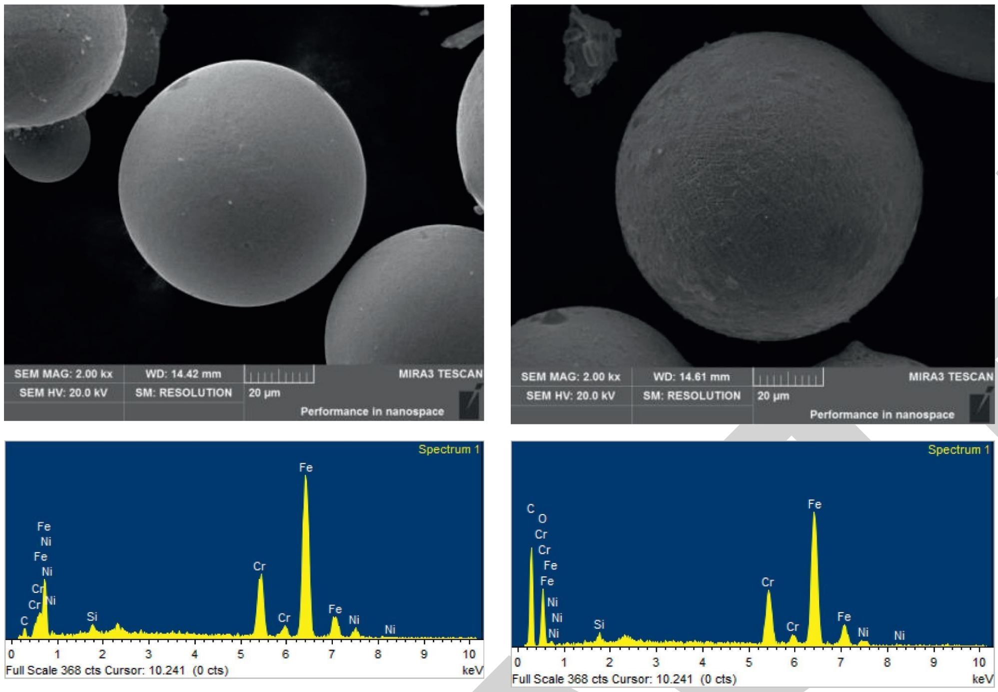

(a) (b)

FIGURE 1: SEM image of iron-based alloy powder particles: (a) no rosin added and (b) rosin added.

after several experiments are presented in Table 1. The number of scanning layers was 6. The final forming size was approximately 90 mm × 30 mm × 3 mm. The surface of the formed sample did not exhibit any cracks or defects.

The mass percentage of chemical composition of the iron-based alloy powder was C ≦ 0.2%; B ≦ 1.5%; Si ≦ 1.5% Cr = (18~20)%; Ni = (8.0~11)%; and Fe formed the remaining component (Table 1).

The particle size was −150~325 mesh. The mass percentages of chemical compositions of the three powders are shown in Table 2.

Rosin was dissolved in alcohol, and then powders no. 2 and no. 3 were poured into the solvent. The mixture was stirred evenly, dried, crushed, and passed through an 80-mesh sieve. FeCNiBSi was added to the powder to form rosin-coated iron-based alloy powders (FeCNiBSi and FeCNiBSiV). Rosin-coated FeCNiBSi and FeCNiBSiV powders were placed in a drying oven and dried at 45–60°C for more than 8 hours to remove the water in the powder before conducting the experiment. The synchronous powder feeding method was used for drying the powders. The process parameters are presented in Table 3. Model TJ-5050H laser (Wuhan Unity) with 6 scanning layers was used for the experiment. The forming test specimens corresponding to FeCNiBSi powder, rosin-coated FeCNiBSi powder, and rosin-coated FeCNiBSiV powder were labeled as test specimen 1, test specimen 2, and test specimen 3, respectively. The cladding coating was cut through electrode-wire cutting to obtain the nonstandard tensile test specimen as shown in Figure 2.

The iron-based alloy powder without rosin reacts violently with oxygen in the air due to the high temperature of

TABLE 1: Levels of different elements in the ion-based alloy powder particles (a) before and (b) after addition of rosin.

Element	Weight%	Atomic%
A		
C	10.53	34.87
Si	1.16	1.65
Cr	17.48	13.37
Fe	62.05	44.18
Ni	8.77	5.94
Total	100.00	
B		
C	36.63	63.71
O	13.10	17.11
Si	0.42	0.31
Cr	9.51	3.82
Fe	38.37	14.35
Ni	1.97	0.70
Totals	100.00	

TABLE 2: Composition of the three types of powders.

No.	Composition		
	Iron-based alloy powder (%)	Rosins (rosin)	*V*
1	100	—	—
2	99.4	0.6%	—
3	99.2	0.6%	0.2%

the laser, and the combustion phenomenon was observed (Figure 3). However, the combustion phenomenon was significantly weakened after the addition of rosin. A synchronous powder feeding nozzle device with an outer ring

Table 3: Laser process parameters.

Power	Scanning speed	Spot size	Synchronous powder feeding speed	Protective gas	Overlap rate (%)
2.2kw	6 mm/min	3 ∗ 5 mm	6 g/min	Argon	50

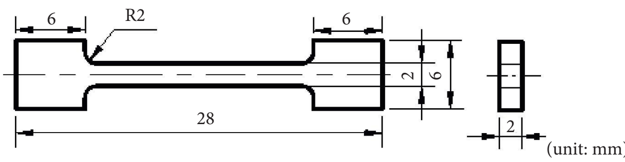

Figure 2: Schematic diagram of tensile test specimen.

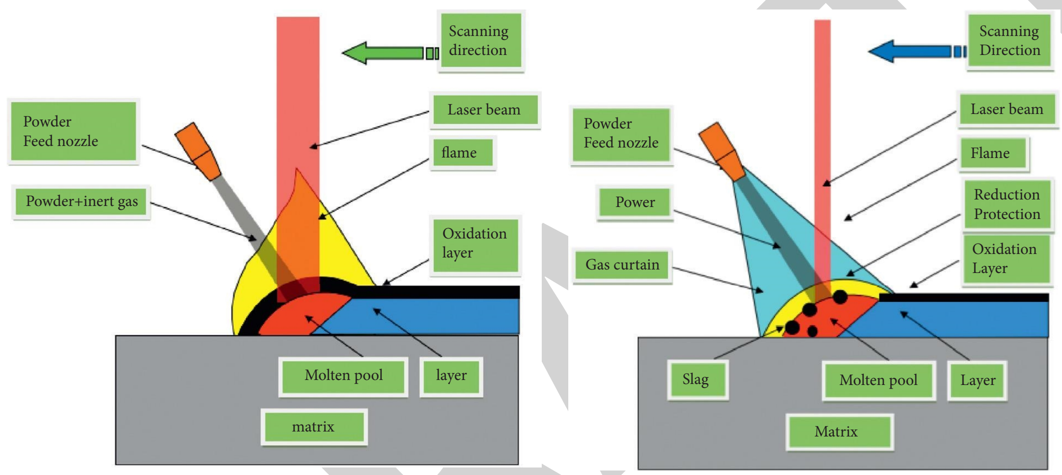

Figure 3: Schematic diagram showing the laser cladding process. (a) Formation of the laser cladding coating without the addition of rosin. (b) Formation of the laser cladding coating after addition of rosin under outer ring protective gas curtain.

protective gas curtain was used to further reduce the oxidation and burning loss of iron-based alloy powder during the cladding process. Argon gas was used in the cladding process. The reduction protection zone formed by rosin firstly reacted with oxygen to protect the molten pool, and the nozzle released the outer ring protective gas curtain to cover the reduction protection zone formed by rosin to further prevent reaction with oxygen and strengthen the protection of the molten pool.

The formation of the laser layer cladding without the gas curtain and after the application of a gas curtain is presented in Figure 4. The results showed that the oxidation phenomenon was more evident without the gas curtain (Figure 4(a)) than with the presence of the gas curtain (Figure 4(b)).

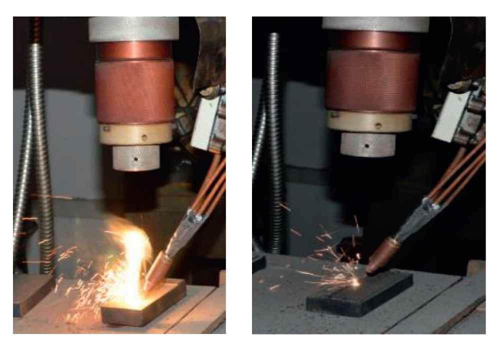

(a) (b)

Figure 4: Oxidation of the sample during the cladding process (a) without a gas curtain and (b) with a gas curtain.

2.1.1. Hardness Test. The sample surface was cleaned with acetone to remove foreign matters introduced after grinding the surface of the cladding coating. The TH320 Rockwell hardness tester was then used to determine the hardness of 10 randomly selected points on the surface of the sample. The average value of microhardness was determined after eliminating minimum and maximum values. The microhardness of the three samples was determined every 0.2 mm along the depth direction from the coating to the substrate. A 6 s holding time was used with a test load of 150 kg (1471 N) to determine the sample hardness.

2.1.2. Microstructure Analysis. A small part (10 mm × 10 mm × 15 mm) of each of the three test specimens was obtained by wire-electrode cutting. The test specimens were polished using coarse- to fine-grade sandpaper to obtain metallographic specimens. Subsequently, the specimens were treated with aqua regia, and then observed under an OLYMPUS GX51F optical microscope. Furthermore, the microstructures of the test samples were observed using a TESCAN MIRA3 LMU JSM-6701F scanning electron microscope. The phase components of the samples were determined by X-ray diffraction (XRD-7000 S Shimadzu, Japan). The X-ray source for the process was Cu-Kα radiation at 40 kV and 200 mA. The samples were scanned at an angular 2 θ angle between 20° and 80° with a step size of 0.2° and a collection time of 10 s.

2.1.3. Tensile Property Test. An electrohydraulic servo dynamic and static universal testing machine PWS-E100 (Jinan) was used to test the tensile properties of the specimen. The specimens were polished using sandpaper to remove the wire-cut marks on the surface before conducting the tensile test. Subsequently, the samples were then mounted on the self-made fixture. Experiments were carried out at room temperature with a tensile rate of 0.2 mm/min.

3. Analysis of the Experimental Results

3.1. Appearance and Morphology of the Specimen. The morphology of the cladding coating was observed after the cladding coating was formed. The findings showed that the laser cladding coating without rosin was covered with an oxide film and had no metallic luster, whereas the laser cladding coating with rosin had evident metallic luster (Figure 5). The experimental results showed that the addition of rosin effectively reduced the oxidation and burning loss of iron-based alloy powder. Notably, oxidation was further reduced under the protection of a gas curtain.

Morphology analysis of the laser-forming sample showed the highest level of oxidation for the sample without rosin and gas curtain, moderate level of oxidation for the sample with rosin but without the gas curtain, and the least oxidation for the sample with rosin and the gas curtain (Figure 5).

3.2. Hardness Analysis. The values of the hardness of each specimen are shown in Figure 6. The average Rockwell hardness values of test specimen 1, test specimen 2, and test specimen 3 were 26.96 HRC, 28.69 HRC, and 32.31 HRC, respectively (Figure 6). The results showed that the hardness level of test specimen 2 was 6.41% higher compared than that of test specimen 1. The hardness level of test specimen 3 was 12.62% higher than that of test specimen 2. The findings indicated that the hardness of the cladding coating was improved by adding rosin and vanadium. The hardness of vanadium-carbon produced by combining vanadium and carbon at high temperature was high because it was dispersed in the cladding coating, hence increasing the hardness of the sample.

3.3. Tensile Property Analysis. Furthermore, the tensile strength of the three specimens was determined (Table 4). The findings showed that the average tensile strength of test specimen 3 was 2.7% higher than that of test specimen 2, and 10.37% higher than that of test specimen 1. The average tensile strength of test specimen 2 was 7.4% higher than that of test specimen 1. The findings indicate that the addition of rosin and V to the powder improved the average tensile strength of the test specimen, with a more significant effect observed after the addition of rosin. Oxidation and burning loss of the iron-based powder were markedly reduced after the addition of rosin, thereby significantly reducing the defects in the cladding coating. This explains the significant effect on improving the tensile strength of the specimen (see Figure 7).

3.4. Microstructure Analysis. The laser rapid prototyping process comprises sudden heating and rapid cooling. The grains in the formed sample were small and dense because the crystal nucleus had no time to grow during the forming process. The structure showed a growth trend with an increase in temperature. Therefore, the hardness, tensile strength, and fatigue properties of the sample were significantly higher than the properties of the casting. The findings showed that the structure of each sample had a specific characteristic (Figure 8). The specimens presented a dendritic structure. The microstructure of sample 2 after the addition of rosin was finer compared with that of sample 1. Notably, sample 3 showed the finest microstructure. The oxidation and burning loss of various alloy elements in sample 2 and sample 3 were markedly reduced; hence, the effect of alloy grain refinement was significant. Vanadium was added to sample 3 to improve the nucleation rate, and the microstructure was finer. The dispersion strengthening effect of sample 2 and sample 3 alloy elements was higher than that of sample 1. The findings indicate that the addition of rosin to the sample reduced the burning loss of alloy elements and enhanced the grain refining effect of alloy elements. This explains the effect of dispersion strengthening and the effect of solid solution strengthening in sample 2 and sample 3. In addition, the microhardness and increase in tensile strength, and improvement of fatigue properties are attributed to the ability of rosin to reduce the burning loss.

Further microstructure analysis of the test samples was conducted by observing the samples under the TESCAN MIRA3 LMU JSM-6701F scanning electron microscope. The microstructure of test specimen 1 was coarser, the microstructure of test specimen 2 exhibited a fine-grained structure, and the microstructure of test specimen 3 exhibited a high nucleation rate and more evident refinement (Figure 9). This finding indicates that the tensile property of test specimen 3 was better than that of test specimen 2 and test specimen 1. The experimental results showed that the addition of rosin and vanadium refined microstructure grains and optimized the mechanical properties of the cladding coating.

Figure 5: Macromorphology variation of the laser forming samples. (a) Sample without rosin and a gas curtain. (b) Sample with rosin but without a gas curtain. (c) Sample with rosin and a gas curtain.

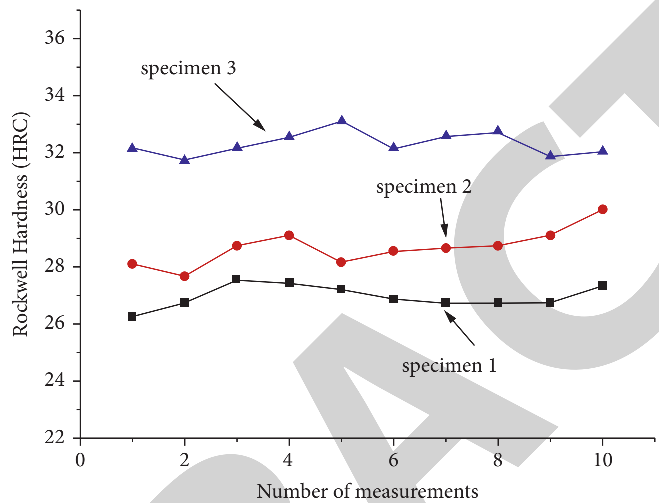

Figure 6: Rockwell hardness of the three test specimens.

Table 4: Tensile strength of the three test specimens.

Test specimen no.	Tensile strength (MPa)			Average (MPa)
Test specimen 1	922	917	909	916
Test specimen 2	998	971	983	984
Test specimen 3	1003	1009	1021	1011

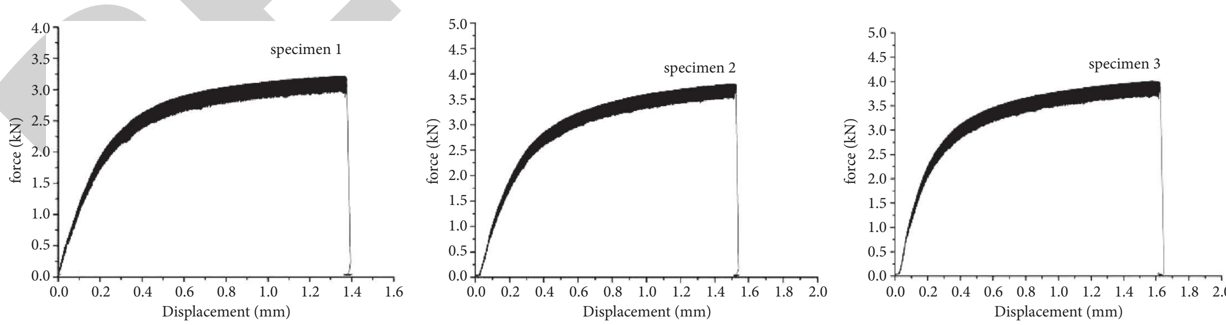

Figure 7: Stress-strain curves of the three specimens: specimen 1 (cross-sectional area: 3.50 mm^2); specimen 2 (cross-sectional area: 3.82 mm^2); specimen 3 (cross-sectional area: 4.00 mm^2).

3.5. XRD Analysis. XRD analysis showed that the cladding coating mainly comprised the α-Fe phase and γ-Fe phase. The spectra of the three samples and the position of the diffraction peak were compared. The findings showed that the intensity of the austenite diffraction peak generated by sample 3 was stronger than that of sample 2, and the intensity of the diffraction peak for sample 2 was stronger than that of sample 1 (Figure 10). This further verifies that the rosin coating on the surface of the alloy powder played a chemical protection role during laser cladding. Rosin

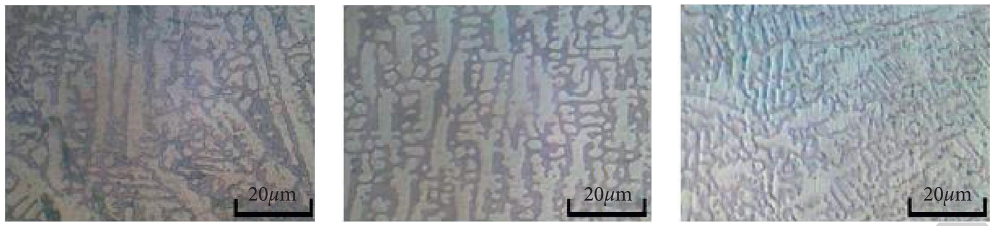

(a) (b) (c)

Figure 8: Morphology of the three specimens: (a) microstructure diagram of test specimen 1; (b) microstructure diagram of test specimen 2; (c) microstructure diagram of test specimen 3.

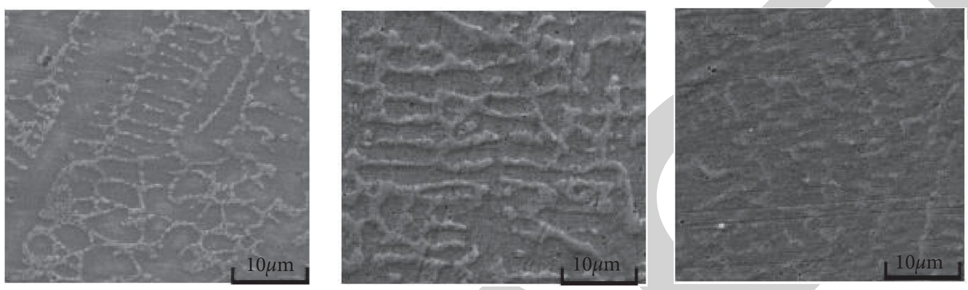

(a) (b) (c)

Figure 9: SEM images showing microstructure of the three samples: (a) SEM image of test specimen 1; (b) SEM image of test specimen 2; (c) SEM image of test specimen 3.

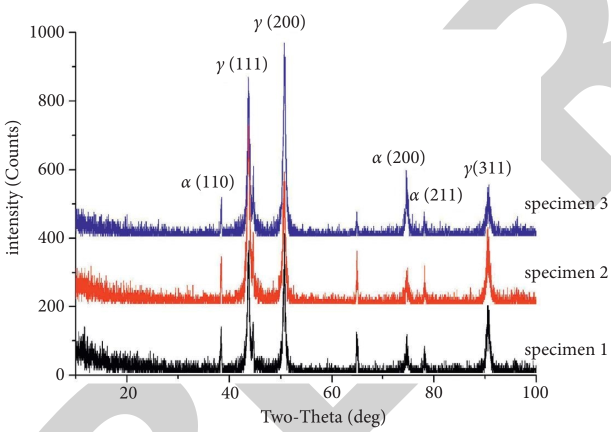

Figure 10: XRD patterns of the three specimens.

weakened the oxidative burning loss of iron-based alloy powder as well as reduced the burning loss of medium elements resulting in a high-intensity peak value.

4. Conclusion

The findings of the present study show that the rosin film coated on the surface of powder particles protects the molten pool during laser cladding. In addition, it prevents oxidation of liquid metal and minimizes oxidation and burning loss of the iron-based alloy powder during cladding. Moreover, rosin coating minimizes defects such as slag inclusion. Furthermore, the rosin refines the microstructure grains, and improves the mechanical properties of the cladding coating. Furthermore, a combination of rosin and gas curtain minimizes the entry of air into the molten powder, which further reduces oxidation.

The addition of rosin to iron-based alloy powder minimizes the loss of alloying elements and increases the effect of alloying elements. This increases the dispersion strengthening phase as well as causes segregation of the alloy element, resulting in increase in the value of Rockwell hardness and tensile strength.

Vanadium and carbon combine to form vanadium-carbon, which has a high level of hardness. This property causes dispersion of the cladding coating and significantly increases the hardness of the sample. Moreover, vanadium increases the nucleation rate and plays a significant role in grain refinement.

Data Availability

The datasets used and analysed during the current study are available from the corresponding author upon reasonable request.

Conflicts of Interest

The authors declare that they have no conflicts of interest.

Acknowledgments

This work was supported by the Natural Science Foundation of Hunan Province (2020JJ6091).

References

[1] J. Li and S. Pogodin, ""Made in China 2025": China experience in industry 4.0," *IOP Conference Series: Materials Science and Engineering*, vol. 497, no. 1, Article ID 012079, 2019.

[2] J. Laeng, J. G. Stewart, and F. W. Liou, "Laser metal forming processes for rapid prototyping -a review," *International Journal of Production Research*, vol. 38, no. 16, 2000.

[3] D. W. Deng, J. H. Sun, and X. L. Wang, "Effect of laser power on the structure and properties of laser cladding nickel-based alloy coating," *Chinese Journal of rare Metals*, vol. 40, no. 1, p. 20, 2016, in Chinese.

[4] A. Gopalakrishnan, M. Rajkumar, J. Sun, and J. P. Trilles, "Occurrence of double parasitism on black-barred halfbeak fish from the southeast coast of India," *Chinese Journal of Oceanology and Limnology*, vol. 28, no. 4, pp. 832–835, 2010.

[5] S. Singh, P. Kumar, D. K. Goyal, and A. Bansal, "Erosion behavior of laser cladded Colmonoy-6 + 50%WC on SS410 steel under accelerated slurry erosion testing," *International Journal of Refractory Metals and Hard Materials*, vol. 98, Article ID 105573, 2021.

[6] S. Roy, N. Sridharan, E. Cakmak, H. Ghaednia, A. Gangopadhyay, and J. Qu, "Post weld heat treatment and operating temperature effect on tribological behavior of laser cladded stellite 21 coating," *Wear*, vol. 482–483, Article ID 203990, 2021.

[7] F. A. d. Lucena, G. Y. Koga, R. Riva, and C. R. M. Afonso, "Production and characterization of laser cladding coating of Fe66Co7Nb4B23 (at.%) gas-atomized and ball-milled powders," *Journal of Materials Research and Technology*, vol. 14, pp. 2267–2280, 2021.

[8] S. T. Nyadongo, E. O. Olakanmi, and S. L. Pityana, "Experimental and numerical analyses of geometrical and microstructural features of Tribaloy T-800 composite coating deposited via laser cladding-assisted with pre-heat (LCAP) process," *Journal of Manufacturing Processes*, vol. 69, pp. 84–111, 2021.

[9] S. Bajda, Y. Liu, R. Tosi et al., "Laser cladding of bioactive glass coating on pure titanium substrate with highly refined grain structure," *Journal of the Mechanical Behavior of Biomedical Materials*, vol. 119, Article ID 104519, 2021.

[10] A. Malachowska, G. Paczkowski, T. Lampke, and A. Ambroziak, "Characterization of FeP-based metallic glass coatings prepared with laser cladding," *Surface and Coatings Technology*, vol. 405, Article ID 126733, 2021.

[11] N. N. Soboleva and A. V. Makarov, "Effect of conditions of high-temperature treatment on the structure and tribological properties of nickel-based laser-clad coating," *Russian Journal of Non-ferrous Metals*, vol. 62, no. 6, pp. 682–691, 2022.

[12] L. Shen and T. Yamaguchi, "High-temperature oxidation behavior of laser-cladded refractory NiSi0.5CrCoMoNb0.75 high-entropy coating," *Journal of Materials Research and Technology*, vol. 17, 2022.

[13] Q. Wang, R. Qian, J. Yang et al., "Effect of high-speed powder feeding on microstructure and tribological properties of Fe-based coatings by laser cladding," *Coatings*, vol. 11, no. 12, 2021.

[14] H. Ge, H. Fang, C. Zhang, L. Wang, Q. Zhang, and J. Yao, "The evolution of element distribution during laser cladding under static magnetic field," *Metallurgical and Materials Transactions A*, prepublish, 2021.

[15] T. Perrin, A. Sofiane, M. Pierre-Jean, and S. Frederic, "Characterization of WC-doped NiCrBSi coatings deposited by Laser Cladding; effects of particle size and content of WC powder," *Surface and Coatings Technology*, vol. 425, 2021.

[16] Y. Zhao, Y. Chen, T. Zhang, and T. Yu, "Laser fabricated nickel-based coating with different overlap modes," *Materials and Manufacturing Processes*, vol. 36, no. 14, pp. 1618–1630, 2021.

[17] M. Zeng, H. Yan, B. Yu, and Z. Hu, "Microstructure, microhardness and corrosion resistance of laser cladding Ni–WC coating on AlSi5Cu1Mg alloy," *Transactions of Nonferrous Metals Society of China*, vol. 31, no. 9, pp. 2716–2728, 2021.

[18] D. Zhang, Z. Li, H. Fan, H. Rui, and F. Gao, "Microstructure and tribological properties of Fe-based laser cladding layer on nodular cast iron for surface remanufacturing," *Coatings*, vol. 11, no. 8, 2021.

[19] S. Nam, H. W. Lee, I. Jung, and Y. M. Kim, "Microstructural characterization of TiC-reinforced metal matrix composites fabricated by laser cladding using FeCrCoNiAlTiC high entropy alloy powder," *Applied Sciences*, vol. 11, no. 14, 2021.

[20] J. Dong, H. Gao, and J. Shen, "Development and application of laser remanufacturing technology," *Mining Machinery*, vol. 47, no. 1, pp. 1–6, 2019.

[21] J. Liu, M. Song, C. Chen, and H. Yu, "Research progress of laser cladding technology on titanium alloy surface," *Metal Heat Treatment*, vol. 44, no. 5, pp. 87–96, 2019.

[22] Q. Ai, X. Feng, J. Cao, and Z. Su, "Research progress of laser cladding technologyly," *Materials Review: Review*, pp. 24–32, 2010.

[23] T. Yu, B. Song, W. Xi, and Y. Zhao, "Analysis on effect of process parameters on laser cladding of iron-based alloy powder," *Hot Working Technology*, vol. 1-5, 2021.

[24] S. Zhao, Y. Guo, R. Chai, and M. Yao, "Effect of scanning speed on the microstructure and properties of laser-clad iron-based alloys," *Applied Laser*, vol. 40, no. 5, pp. 811–820, 2020.

[25] B. Yang, Z. Wang, J. Zuo, X. Jiang, and X. Zhang, "Iron-based composite coating prepared by laser cladding and its heat and corrosion resistance," *Chinese Journal of Lasers*, vol. 47, no. 10, pp. 38–44, 2020.

[26] G. Wei, Z. Liping, X. Chao, and C. Rongxia, "Findings from xi'an university of science and technology in the area of materials research described (study on the wear resistance of laser cladding iron-base alloy by heat treatment)," *Journal of Technology*, vol. 6, 2019.

[27] P. Farahmand and R. Kovacevic, "Laser cladding assisted with an induction heater (LCAIH) of Ni – 60% WC coating," *Journal of Materials Processing Technology*, vol. 222, pp. 244–258, 2015.

[28] G. Bidron, A. Doghri, T. Malot, M. Thomas, and P. Peyre, "Reduction of the hot cracking sensitivity of CM - 247LC superalloy processed by laser cladding using induction preheating," *Journal of Materials Processing Technology*, vol. 277, Article ID 116461, 2019.

Hindawi
Advances in Materials Science and Engineering
Volume 2024, Article ID 9840238, 1 page
https://doi.org/10.1155/2024/9840238

Retraction

Retracted: Genetic Algorithm Integrated Fuzzy AHP-VIKOR Approach for the Investigation of W-Cut Insert Heat Exchanger for Cooling of Dielectric Fluid Used in Ultra-High Voltage Transformer

Advances in Materials Science and Engineering

Received 8 January 2024; Accepted 8 January 2024; Published 9 January 2024

This article has been retracted by Hindawi following an investigation undertaken by the publisher [1]. This investigation has uncovered evidence of one or more of the following indicators of systematic manipulation of the publication process:

(1) Discrepancies in scope
(2) Discrepancies in the description of the research reported
(3) Discrepancies between the availability of data and the research described
(4) Inappropriate citations
(5) Incoherent, meaningless and/or irrelevant content included in the article
(6) Manipulated or compromised peer review

The presence of these indicators undermines our confidence in the integrity of the article's content and we cannot, therefore, vouch for its reliability. Please note that this notice is intended solely to alert readers that the content of this article is unreliable. We have not investigated whether authors were aware of or involved in the systematic manipulation of the publication process.

Wiley and Hindawi regrets that the usual quality checks did not identify these issues before publication and have since put additional measures in place to safeguard research integrity.

We wish to credit our own Research Integrity and Research Publishing teams and anonymous and named external researchers and research integrity experts for contributing to this investigation.

The corresponding author, as the representative of all authors, has been given the opportunity to register their agreement or disagreement to this retraction. We have kept a record of any response received.

References

[1] N. V. Gowri, J. S. Isaac, T. Muralikrishna et al., "Genetic Algorithm Integrated Fuzzy AHP-VIKOR Approach for the Investigation of W-Cut Insert Heat Exchanger for Cooling of Dielectric Fluid Used in Ultra-High Voltage Transformer," *Advances in Materials Science and Engineering*, vol. 2022, Article ID 2819688, 24 pages, 2022.

Hindawi
Advances in Materials Science and Engineering
Volume 2022, Article ID 2819688, 24 pages
https://doi.org/10.1155/2022/2819688

Research Article

Genetic Algorithm Integrated Fuzzy AHP-VIKOR Approach for the Investigation of W-Cut Insert Heat Exchanger for Cooling of Dielectric Fluid Used in Ultra-High Voltage Transformer

N. Vasantha Gowri,[1] J. Samson Isaac,[2] T. Muralikrishna,[1] G. Suresh Babu,[1] Melvin Victor Depoures,[3] S. Sekar,[4] P. Sasirekha,[5] M. Ramesh,[6] and S. Prabhakar[7]

[1]*Department of Electrical and Electronics Engineering, Chaitanya Bharathi Institute of Technology (A), Gandipet 500075, Telangana, India*
[2]*Department of Biomedical Engineering, Surgical and Critical Care Equipments Laboratory, Karunya Institute of Technology and Sciences, Coimbatore 641114, Tamil Nadu, India*
[3]*Department of Thermal Engineering, Saveetha School of Engineering, Saveetha Institute of Medical and Technical Sciences, Chennai 602105, Tamil Nadu, India*
[4]*Department of Mechanical Engineering, Rajalakshmi Engineering College, Thandalam, Chennai 602105, Tamil Nadu, India*
[5]*Department of Electrical and Electronics Engineering, M.Kumarasamy College of Engineering, Karur 639113, Tamil Nadu, India*
[6]*Department of Electrical and Electronic Engineering, Vaageswari College of Engineering, Karimnagar 505527, Telangana, India*
[7]*Department of Mechanical Engineering, Automotive Engineering Stream, Wollo University-KIOT, 208, Kombolcha, Ethiopia*

Correspondence should be addressed to S. Prabhakar; prabhakar@kiot.edu.et

Received 9 May 2022; Revised 27 June 2022; Accepted 4 July 2022; Published 31 July 2022

Academic Editor: Kumarasamy Sathiyasekar

This study proposes a novel W-cut twisted tape to evaluate and enhance the effectiveness of novel grooved tube heat exchanger. The experimental investigations are carried out with W-cut inserts, which possess two main control factors, namely, twist tape ratio ($y = 3.5$ to 6.5) and width tape ratio ($\mathrm{WR} = 0.43$ to 0.6). The investigation results prove that in all cases the energy transmission and friction factor of W-cut insert along with the first law and second law efficiency are considerably higher than the conventional tube arrangement. The empirical model equations for friction factor, performance enhancement ratio, Nusselt number, and rational efficiency are developed, and they show good affinity with experimental data. Since the abovementioned factors have conflicting terms, it is essential to select the proper operating configuration of the heat exchanger in order to increase the thermal energy transfer rate with reduced consumption of pumping energy. The multi-objective genetic algorithm (GA) tool is used to identify the optimum operating conditions. Further, the hybrid multi-criteria decision-making model, FAHP-VIKOR, is applied to select the perfect model from the set of non-dominated solution. The ranking of alternatives is as follows: A4 > A11 > A2 > A9 > A21 > A17 > A1 > A24 > A11 > A23 > A7 > A18 > A13 > A10 > A20 > A5 > A19 > A14 > A16 > A22 > A25 > A6 > A15 > A3 > A8. The optimized configuration of W-cut insert is compared with the former inserts, and the optimal configuration exhibits supreme performance than other inserts.

1. Introduction

The global thirst for energy is constantly increasing. The increased demand for the cost of energy and materials has led to the production of high-performance compact heat exchanger systems. Heat transfer augmentation techniques are often used in several thermal system applications such as air conditioning and refrigeration systems, heat recovery process, and chemical reactors to increase the overall performance. Augmentation methods such as eddy flow devices (especially twisted tapes) are extensively used in industrial heat exchangers for enhancing convective heat transfer. The presence of typical twisted tape in the tube leads to increased pumping power, which results in thermal performance below unity, so that proper design of twisted tape is required to increase the heat transfer of the equipment with reduced pressure drop [1]. Many research studies have been carried out in past decades to bring down the friction loss by modifying peripheral of twisted tape with different geometry, which includes double V-ribbed twisted tapes [2], horizontal wing-cut TT [3], perforated V-cut and U-cut TT [4], tapered twisted tape [5], TT consisting of wire nails [6], loose-fit perforated twisted tapes [7], twisted tape with alternate axis [8], ribbed twisted tape inserts [9], finned twisted tape [10], cross hollow TT [11], peripherally cut dual TT [12], helix TT with V-cut [13], square and V-cut twisted tape [14], centre-cleared twisted tape [15], dual TT [16], rectangular-cut TT [17], circular tube with lanced ring insert [18], and perforated helical TT [19]. The double V-cut perforated TT with width ratio and twist ratio of 0.27 and 2 enhances the heat transfer by 3.5 times while operating at the flow Reynolds number ranging from 2000 to 25000 [20]. These modified geometry twisted tapes are generally designed to induce enhanced swirl flow near the wall region, which affects the increase in fluid velocity and reduction in boundary layer thickness. This results in augmented heat transfer when compared to typical twisted tape [21]. In general, the performance enhancement ratios of these tapes are higher than the former typical twisted tapes. For instance, the mean performance ratio of the abovementioned tapes is about 2–4 times higher than the typical one. All these aforementioned researches were carried out in plain tube. Wijayanta et al. [22] utilized short-length twisted tape in concentrated tube heat exchangers that improve heater transfer and friction factor by 0.51 and 2.84 times as compared with the conventional heat exchangers for the Reynolds number ranging from 4500 to 18500. Wijayanta et al. [23] compared the thermo-hydraulic performance of classical and square-cut twisted tapes and resulted that the maximum performance of the heat exchangers is ranging from 74.7 to 80.7%. Then, the researchers modified the tabulators into V shapes and enhanced the performance by 97% [24]. Further modifications are carried out in the turbulators by attaching trapezoidal tape winglet that improves the heat transfer and friction factor by 1.91 and 5.2 times, respectively [25]. Yaningsih et al. incorporated perforated holes in the twisted tapes and improved the heater transfer and friction factor performance in the concentric tube heat exchanger by 32% and 47%, respectively [26].

In the recent past, the combined passive method has been extensively used to increase the heat transfer rate. The investigations are carried out with geometrically modified twisted tapes, which are fitted in altered test sections. Most of the researchers revealed that the overall performance of the combined insert performs best compared with the individual ones. Bharadwaj et al. [27] initiated the study on thermal and flow characteristics of the grooved tube fitted with twisted tapes. The grooved tube with twisted tape showed better performance than the simple grooved tube. Kumbhar and Sane [28] made an investigation on heat transfer and pressure drop of the dimpled tube with regularly spaced twisted tape insert. The result showed that full-length twisted tape gave a better performance with dimpled tube. Hong et al. [29] made an experimental study on thermal and friction characteristics of spirally grooved tube fitted with twin overlapped twisted tapes. The function of overlapped tapes in spiral grooved tube was not effective when compared to the simple grooved tube. Verma et al. [30] utilized modified helical coil twisted tapes and improved the heat transfer and friction factor by 3.14 times and 19.9 times as compared with the conventional system. Promvonge et al. [31] studied the effect of twisted ratio on performance characteristics in a helical-ribbed tube with twin TTs. Hong et al. [32] numerically examined the effect of thermal and flow performance of the geometrically modified twin TT's built-in converging-diverging tube. As mentioned above, the combined twisted tape and grooved tube lead to higher heat transfer rate and friction factor than plain tube. Increased Nusselt number results in energy saving, whereas a rise in friction factor upsurges the pumping cost. Hence, the optimization of grooved tube heat exchanger is essential for obtaining high performance with energy saving and pumping cost reduction [33, 34]. Blade vortex generator inserts, multiple helical tape inserts, and diverging perforated cones are special types of inserts that are used as turbulators to reduce the flow blockage in downstream conditions and improve the Reynolds number [35]. Wijayanta et al. [36] proposed that delta wing tape turbulators raise the heat transfer performance by 177% and their design configurations are optimized using the ANN method [37]. The maximum enhancement using T-wing tape tabulator is 1.15 [38]. The double-side winglet integrated twisted tapes raise the Nusselt number by 269% and improve the performance by 10.1 times as compared with plain tube [39, 40]. Veerabhadrappa Bidari et al. [41] modified the turbulators for heat exchangers by punched delta winglet vortex shapes and improved thermo-hydraulic performance by 1.22 times as compared with other systems.

The optimization study to improve the design parameters of concentric heat exchangers has been evoked recently. Han et al. [42] did a multi-objective shape optimization study on corrugated tube double pipe heat exchangers using RSM methods. The maximum performance ratio obtained for the *r* optimum design parameter is 1.12. Swamee et al. [43] analyzed the optimization of heat exchanger with single degree of difficulty. The solution gives an optimal design for the parameters, which include inner diameter and outer diameter of the pipe, and utility flow rate. Iqbal et al. [44] made an optimization study to determine the optimum shape of longitudinal fins on the outer pipe of the heat exchanger for maximizing the Nusselt number. The result showed that the optimum fin profile offers a Nusselt number, which was about 312% higher than the conventional design.

Iqbal et al. [45] designed an optimal configuration of a finned annulus with parabolic fins to enhance the heat transfer. As a result, the optimal configuration of parabolic fins is not compared with triangular and trapezoidal fin in all situations and criteria. Despite various researches being carried out on combined passive techniques, very few researchers focused on the optimization of the insert configurations used in heat exchangers. This shortage creates research gap for upcoming researchers to narrow their investigation. The main objective of this study was to perform optimization on design and operating configurations of WCTT fitted in grooved tube heat exchanger using the genetic algorithm and multi-criteria decision-making model.

The genetic algorithm is the searching tool that is available for solving problems when the functional characters are unknown. Some of the researchers used GA to optimize the objective parameters of heat exchangers in order to attain the overall best performance [46, 47]. After a thorough analysis on the performance of the heat exchanger with the effect of WCTT geometrical parameters, the new experimental correlations were developed to predict the Nusselt number and friction factor of the tube under the defined range. These correlations were used as the objective function to find the optimal Pareto front solutions. As the given objectives are conflicting terms, GA-based multi-objective optimization is used to attain optimal configurations. Yet, it was difficult to find the best configuration with MOGA, as all the solutions obtained were optimal. Therefore, this study focuses on achieving the best one using a hybrid MCDM model with four performance criteria. The novel FAHP-VIKOR model is used to evaluate alternative configurations and select the best one with conflicting criteria. The application of MCDM in heat transfer area is very meagre [48, 49]. According to the findings, there is research being done on the selection of twisted tape configurations based on thermal and exergy performance using MCDM models. In this work, the FAHP-VIKOR model is used to select the best from the optimum Pareto front solutions of GA. The structure of the present work is given in Figure 1, and their stages are as follows: (i) initially the experimentation is done and the empirical correlations were developed; (ii) followed by multi-objective GA optimization tool to get set of optimum Pareto solution; (iii) finally, assessment method, which includes FAHP-VIKOR model to rank the optimum Pareto front of GA.

2. Experimental Work

2.1. Twisted Tapes and Grooved Tube. The WCTT is made of aluminium sheets with a width of 0.0235 m, a thickness of 0.003 m, and a length of tape of 1500 mm. Initially, plain twisted tapes are made by twisting one end of the tape at the desired twist tape ratio ($y = 3.5$ to 6.4), while the other end is clamped. Then, a W-shaped element is removed from the peripheral of the plain tape with a given width ratio ($WR = 0.45$, 0.6). In this work, the width ratio is defined as the ratio of the width of the W-cut to the width of the twisted tape. The test section used in this setup is an internally grooved tube, which is composed of internal grooves in the plain copper tube with a specified pitch. These values are fixed based on the boundary layer thickness formulation while maintaining the flow Reynolds number ranging from 3000 to 15000. The cut section of the grooved tube is shown in Figure 2, and the geometry of WCTT is depicted in Table 1 and Figure 3.

2.2. Experimental Apparatus and Test Procedure. Figure 4 represents the schematic diagram of experimental setup of double pipe heat exchanger. The system comprises of calming section, test section (smooth or grooved tube) for transformer mineral oil flow, and outer tube for cold-water flow. The calming section and test sections are made of copper tubes with diameter, length, and thickness of 25 mm, 1500 mm, and 1.5 mm, respectively. The outer tube is made of steel tubes with diameter of 52 mm, thickness of 4 mm, and length of 1500 mm. The outer tube is covered with insulation materials such as foam, asbestos, and glass wool to avoid heat loss to the environment. Some other components of heat exchanger include pump, rotameter, control valves, hot and cold-water tank, fan, and control switches. Besides, U-tube manometer and K-type thermocouples were positioned at inlet and outlet of the test section and outer tube to measure the pressure drop and bulk temperatures of the flow. The temperature of the transformer mineral oil is maintained constantly at 55°C using a temperature sensor and relay control unit, while the cold water is maintained at room temperature. The test procedure follows two sections, namely, transformer mineral oil loop and cold-water loop. In the transformer mineral oil loop, the electric heater with 4 KW is used to heat the water. After reaching the specified temperature, the transformer mineral oil is allowed to flow through calming section followed by the test section and it returns to transformer mineral oil tank. As the transformer mineral oil dissipates a certain temperature to the cold water, loss of temperature is noted. To maintain the set temperature, sensor with temperature control relay is used to maintain the transformer mineral oil tank with fixed temperature. Similarly, the same procedure is followed in cold-water loop section. In this, the cold water at room temperature is allowed to flow through the outer pipe and it takes some temperature from the transformer mineral oil. To maintain cold-water temperature, a cooling section is made in which the added temperature nullifies and returns to the cold-water tank with set temperature. The K-type thermocouples with 0.1°C accuracy are used to measure the surface temperature of the internal tube. They are set up at equal distances from the inlet. An 8 mm steel tube is used to protect the thermocouple from direct contact with the water in the annulus section. This tube is brazed to both the outside and inside tubes of the test sections. Experimentation is conducted to determine the thermal performance of heat exchanger at flow rates of 2–10 LPM for transformer mineral oil and constant 10 LPM for cold water. The temperature and pressure of the fluid at inlet and outlet and the surface temperature are measured under steady-state conditions. The details of experimentation are specified in Table 1. Each experiment is repeated three times to ensure its accuracy and repeatability.

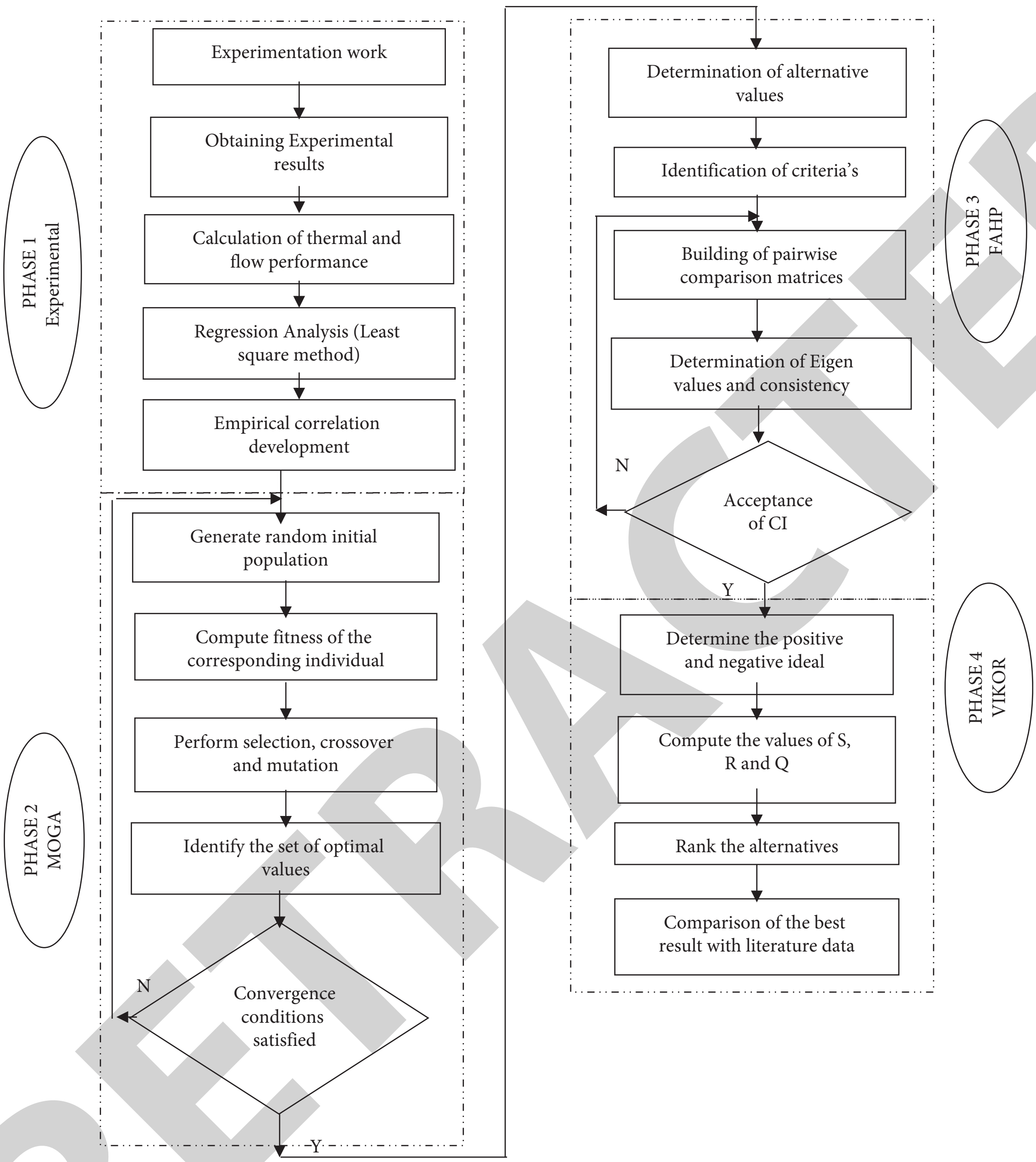

Figure 1: Phases of evaluation procedure.

3. Experimental Calculation

3.1. Data Reduction. The formulas used to obtain the overall performance of the inserts are as follows.

The average of inlet and outlet temperature is taken as bulk temperature, which is expressed as follows:

$$T_C = \frac{T_{ci} + T_{c0}}{2}, \qquad T_h = \frac{T_{hi} + T_{ho}}{2}. \tag{1}$$

The heat transferred to cold water is provided as follows:

$$Q_C = m_c C_p \left(T_{co} - T_{ci}\right). \tag{2}$$

Heat rejected from the transformer mineral oil is given as follows:

$$Q_h = m_h c_p \left(T_{hi} - T_{ho}\right). \tag{3}$$

Assume that the working fluid has a mean temperature of

$$Q_{avg} = \frac{Q_c + Q_h}{2}. \tag{4}$$

The surface temperature of the tube is given as follows:

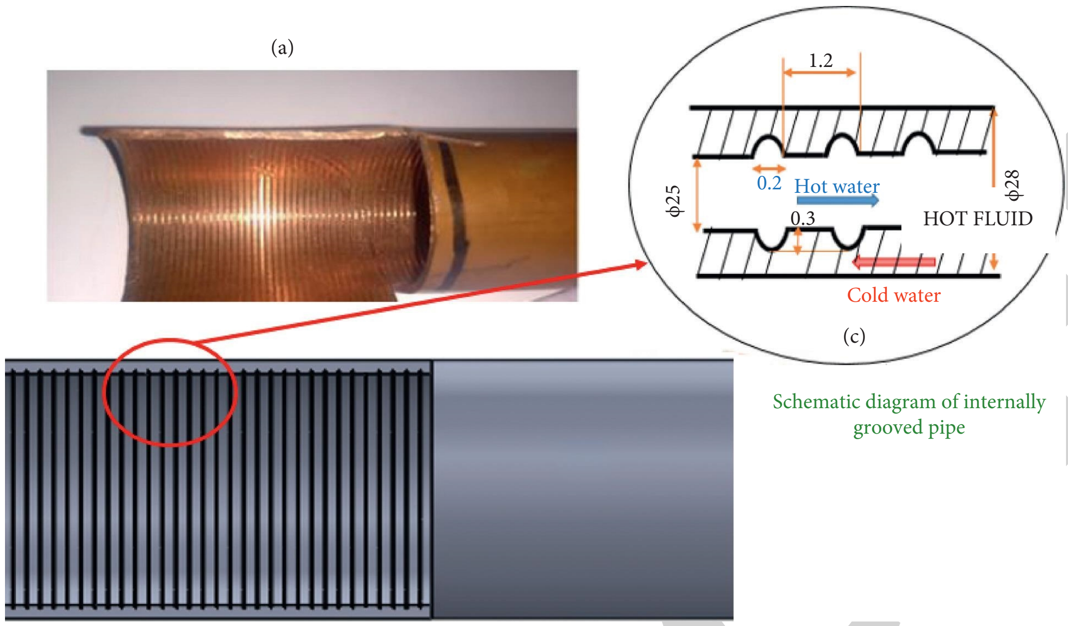

FIGURE 2: Cut section of internally grooved test section: (a) grooved copper pipe, (b) 3D model of grooved pipe, (c) schematic of groove.

TABLE 1: Experimental details.

Test tube condition (A)	
Outer diameter of heat exchanger's inner tube	50.5 mm
Inner diameter of heat exchanger's inner tube	25 mm
Reynolds number	3000–15000
Inlet transformer mineral oil temperature	55°C
Length (*L*)	1500 mm
Groove pitch (*P*)	1.2 mm
Groove thickness (*X*)	0.2 mm
Groove height (*e*)	0.3 mm
Inlet cold-water temperature	31°C
W-cut TT (B)	
Pitch tape length (*H*)	83, 125, and 150 mm
Tape width (*W*)	23.5 mm
Depth of the cut	10 mm
Configuration used	W-cut TT
Twist tape ratio (*y*)	3.5, 5.3 and 6.5
Tape thickness	3 mm
Width ratio (WR)	0.45 and 0.6

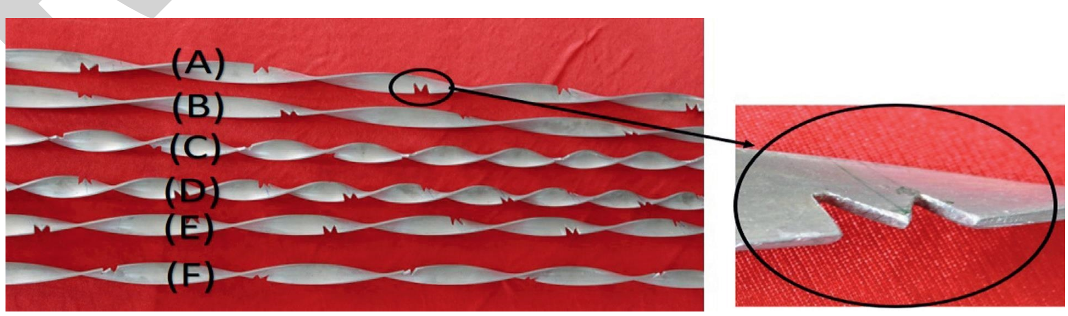

FIGURE 3: Configuration of W-cut TT: (a) $y = 6.4$, WR = 0.6; (b) $y = 6.4$, WR = 0.45; (c) $y = 5.3$, WR = 0.6; (d) $y = 5.3$, WR = 0.45; (e) y of 5.3, WR = 0.6; (f) y of 5.3, WR = 0.45.

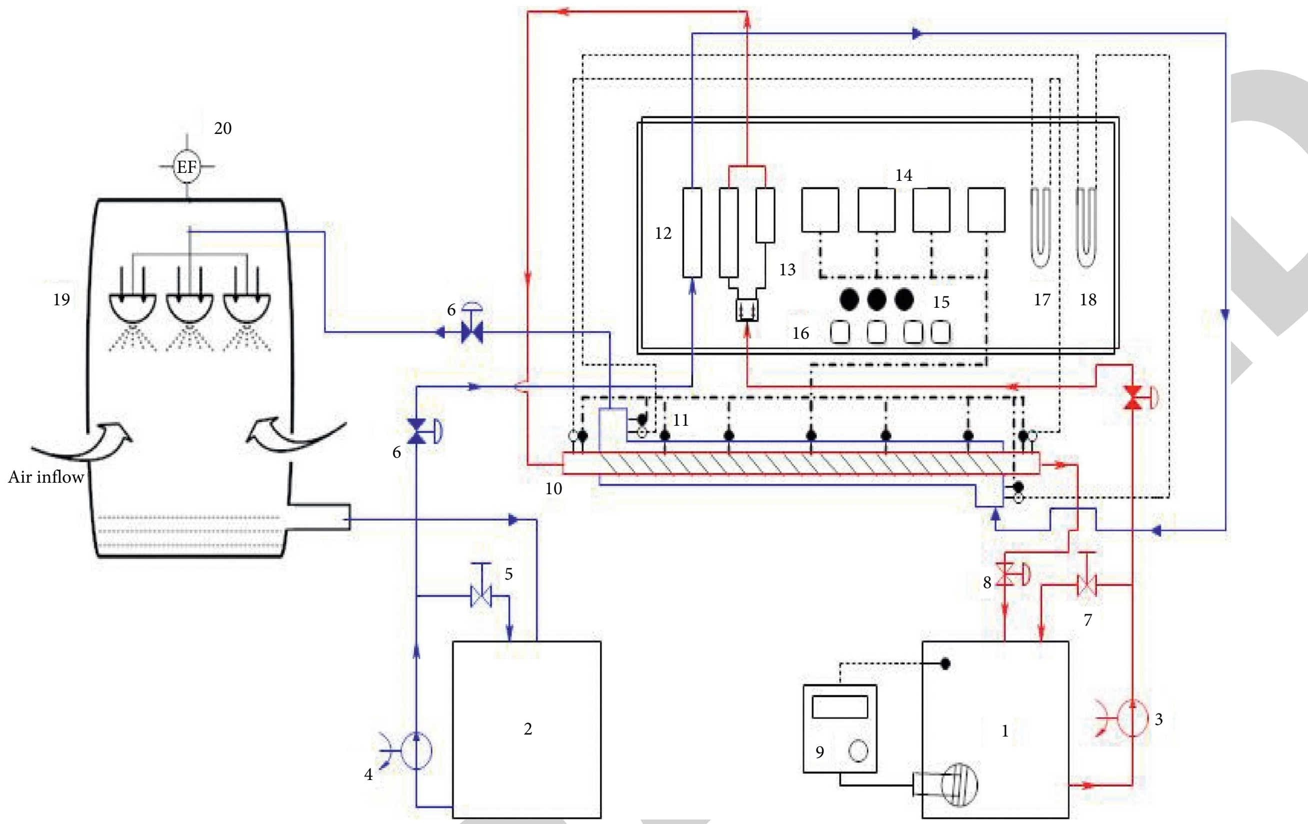

FIGURE 4: Schematic diagram of experimental rig.

$$T_W = \frac{\sum T_{wi}}{5}. \quad (5)$$

The average Nusselt number and average heat transfer coefficient of inner section can be calculated as follows:

$$h_i = \frac{Q_{avg}}{A(T_h - T_W)},$$
$$Nu_i = \frac{h_i d_h}{k}. \quad (6)$$

Equation (7) is used to evaluate the Reynolds number given as follows:

$$\text{Re} = \frac{U_h d_h}{\nu}. \quad (7)$$

The friction factor due to fluid flow is evaluated as a function of pressure drop given as follows:

$$f = \frac{\Delta p}{(L/d_h)(\rho u^2/2)}. \quad (8)$$

The usage of novel W-cut twisted tape and conventional plain tube is compared based on the calculated value of the term performance enhancement factor given as follows:

$$PER = \frac{Nu/Nu_o}{(f/f_o)^{1/3}}. \quad (9)$$

The above equation (9) is used to calculate PER in Section 5.4.

3.2. Exergy Analysis. Rational efficiency also known as exergy efficiency or second law efficiency analyses the efficiency of the system by considering the second law of thermodynamics. The rational efficiency of the heat exchanger is defined as the ratio of net exergy output of the system to net exergy input. In this study, second law efficiency is availed to enhance and select the dimensions for the heat exchanger. In general, the qualitative energy of exergy balance is given as follows [50]:

$$E_{in} - E_{out} = I. \quad (10)$$

From the equation (10), the net rate of exergy of the heat exchanger is given as follows:

$$\begin{aligned} E^{in} &= \sum_{i=1}^{N.stream.In} m_i E^{in}_{stream,i} \\ &\quad + \sum_{i=1}^{N.Q.In} m_i E^{in}_{Q,i} + \sum_{i=1}^{N.W.In} m_i E^{in}_{W,i}, \\ E^{out} &= \sum_{i=1}^{N.stream.Out} m_i E^{out}_{stream,i} \\ &\quad + \sum_{i=1}^{N.Q.out} m_i E^{out}_{Q,i} + \sum_{i=1}^{N.W.Out} m_i E^{out}_{W,i}. \end{aligned} \tag{11}$$

The exergy balance for the fluids in heat exchanger [51] can be stated as follows:

$$E^{in} = E^{out}_{useful} + E^{out}_{waste} + I. \tag{12}$$

The rate of exergy destruction in terms of generation of entropy is given as follows:

$$I = T_o \dot{S}_{gen}. \tag{13}$$

For the concentric heat exchanger, the entropy generation (13) can be written as follows:

$$\begin{aligned} \dot{S}_{gen} &= m_h C_{ph} \ln\left(\frac{T_{h,out}}{T_{h,in}}\right) + m_c C_{pc} \ln\left(\frac{T_{c,out}}{T_{c,in}}\right) \\ &\quad + m_h \frac{\Delta P_h}{\rho_h} \frac{\ln T_{h,out}/T_{h,in}}{T_{h,out} - T_{h,in}} + m_c \frac{\Delta P_c}{\rho_c} \frac{\ln T_{c,out}/T_{c,in}}{T_{c,out} - T_{c,in}}. \end{aligned} \tag{14}$$

The "exergy output attained" divided by "used exergy" gives the value of rational exergy efficiency stated in the following equation [52]:

$$\varepsilon = 1 - \frac{I}{E_{use\,d}}. \tag{15}$$

The overall performance of the system based on the second law is represented by the following equation [53]:

$$E_{use\,d} = E_{obtainedoutput} + I. \tag{16}$$

The aforementioned system's goal to increase the thermal exergy of the hot stream is given as follows:

$$E_{obtainedoutput} = E_h^{\Delta T,out} - E_h^{\Delta T,in}. \tag{17}$$

Then, by combining equations (16) and (17), the useful value of exergy is given as follows:

$$\begin{aligned} E_{use\,d} + I &= E_c^{\Delta p,in} + E_h^{\Delta P,in} + E_c^{\Delta T,in} \\ &\quad - E_c^{\Delta T,out} + E_h^{\Delta P,out} + E_c^{\Delta P,out}. \end{aligned} \tag{18}$$

The system's overall rational exergy efficiency is given as follows:

$$\begin{aligned} \eta_{II} &= \frac{\sum (\dot{E})_{out}}{\sum (\dot{E})_{in}}, \\ \eta_{II} &= \frac{m_h C_{ph} \ln\left(T_{h,out}/T_{h,in}\right)}{m_c C_{pc} \ln\left(T_{c,out}/T_{c,in}\right) + m_h \Delta P_h/\rho_h \ln T_{h,out}/T_{h,in}/T_{h,out} - T_{h,in} + m_c \Delta P_c/\rho_c \ln T_{c,out}/T_{c,in}/T_{c,out} - T_{c,in}}. \end{aligned} \tag{19}$$

The above equation is used to calculate rational exergy efficiency in Section 5.5.

3.3. Uncertainty Analysis. It is possible to calculate the experimental uncertainty of friction factor, Reynolds number, and Nusselt number using the following formulas:

$$\frac{\Delta \mathrm{Re}}{\mathrm{Re}} = \left\{ \left[\frac{\Delta m_h}{m_h}\right]^2 + \left[\frac{\Delta d_i}{d_i}\right]^2 \right\}^{0.5}, \tag{20}$$

$$\frac{\Delta Nu_i}{Nu_i} = \left\{ \left[\frac{\Delta h_i}{h_i}\right]^2 + \left[\frac{\Delta d_i}{d_i}\right]^2 + \left[\frac{\Delta k}{k}\right]^2 \right\}^{0.5}, \tag{21}$$

$$\frac{\Delta f}{f} = \left\{ \left[\frac{\Delta(\Delta P)}{\Delta P}\right]^2 + \left[\frac{\Delta L}{L}\right]^2 + \left[\frac{3\Delta d_i}{d_i}\right]^2 + \left[\frac{2\Delta \mathrm{Re}}{\mathrm{Re}}\right]^2 \right\}^{0.5}. \tag{22}$$

The uncertainties and instrument accuracy of the present work are given in Table 2.

4. Optimization Method

4.1. Multi-Objective Genetic Algorithm (MOGA). Multi-objective optimization (MOO) [54] refers to the solution of problems that deal with more than one objective. In actual engineering problems, most of their objectives are at least in partial conflict with one another. It is difficult to

Table 2: Accuracy of the instruments.

		Accuracy
Instruments	U-tube manometer	±0.0001 m
	Digital thermocouple	±0.1°C
	Rotameter	±0.1 L/min
	Temperature indicators	±0.1%
		Uncertainty (±%)
Simple variable	Pressure head (mm)	2.7
	Temperature (°C)	0.08
		Uncertainty (±%)
Compound variable	Pressure drop (ΔP)	5.55
	Friction factor (f)	4.05
	Nusselt number (Nu)	5.38
	Reynolds number (Re)	2.01
	Heat transfer coefficient (h)	5.38
	Heat transfer (Q)	5.24

detect the maximum or minimum of multi-objectives simultaneously available for single objective optimization. The term MOO generally refers to the set of non-inferior solution points, known as Pareto optimal solutions [38]. The best solution for the multi-objective problem can be selected from the Pareto set rendering to decision-making methods. MOGA is the multi-objective optimization tool for solving problems with more than one design objective, and it has unique supremacy in multi-objective programming. The steps involved in MOGA are as follows:

Step 1: generate random population of chromosomes with a static initial size

Step 2: assess the fitness of the objective function solutions in the population

Step 3: generate new offspring from parent population using selection, crossover, and mutation

Step 4: finally, this process terminates only when the optimal solution is achieved, else it goes to Step 2

Evidently, the offspring population will be comparatively good than the parent population as it undergoes the survival of fittest principle. The solution becomes closer and closer to optimal with gradual evaluation. Finally, when GA is convergent, the set of Pareto front optimized solutions is obtained. In this study, hybrid MCDM (FAHP-VIKOR) is employed to select the finest solution from the set of Pareto front solutions.

4.2. Multi-Criteria Decision-Making (MCDM). Multi-criteria decision-making (MCDM) is a tool, which is used for evaluating the trade-offs between several performance criteria to rank, prioritize, or choose the best from the list of alternatives. The MCDM problem selected in this study is to rank the set of Pareto front solutions (taken as alternatives) obtained from GA. The prioritization of these alternatives is done using the following criteria: thermal enhancement ratio (TER), friction enhancement ratio (FER), performance enhancement ratio (PER), and rational exergetic efficiency (REE). Figure 5 depicts the various criteria used in performance evaluation. In this MCDM model, at the initial stage, the FAHP is used to give weightage for the criteria, followed by the ranking of alternatives with VIKOR.

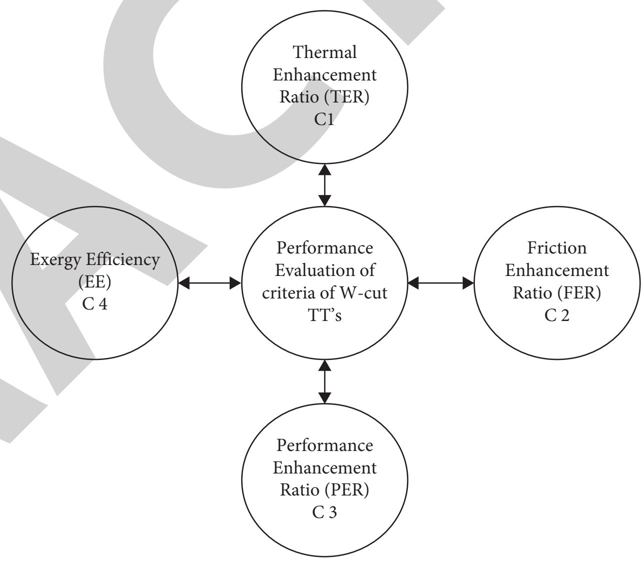

Figure 5: Different criteria for performance evaluation of grooved tube with W-cut twisted insert.

4.2.1. FAHP Method. Satty and decision [55] proposed the AHP method. In AHP, the decision problem is classified into different levels of hierarchy, each level comprising a finite number of elements [56]. A fuzzy set comprises membership function associated in the range of zero and one. Kwong and Bai [46] proposed the concept of fuzzy AHP. FAHP offers triangular and trapezoidal fuzzy number in accordance with the decision-maker need. The authors of past used FAHP tool to assign weightage to their criteria [57, 58]. The hierarchy of decision-making problem is shown in Figure 6. The steps of FAHP method are as follows:

Step 1: complex problem is broken down into simple hierarchy of interconnected criteria.

Step 2: the triangular fuzzy number (TFN) $M = (l, m, u)$ is used to fuzzy the pairwise decision matrix A. The

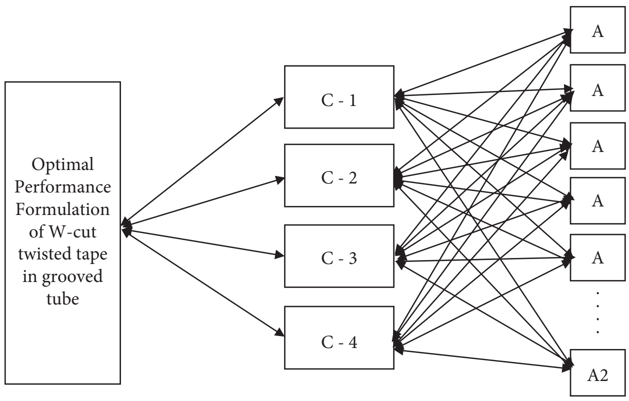

Figure 6: Decision hierarchy for performance prediction of W-cut TT.

membership function of the TFNs used to signify the assessment is M1, M2, M3, M4, M5, M6, M7, M8, and M9 (Table 3). Then, the decision matrix is normalized and the relative weight of each matrix is identified. The expression for eigenvector can be given as follows:

$$A_w = \lambda_{\max} W. \quad (23)$$

Step 3: consistency index (CI) values are identified:

$$CI = \frac{(\lambda_{\max})}{(n-1)}. \quad (24)$$

Step 4:the consistency ratio (CR) is used to define the consistency of the inputs and is given as follows:

$$CR = \frac{(CI)}{(RCI)}. \quad (25)$$

In case the CR value is greater than the acceptable value, inconsistency in judgment occurs and the entire assessment must be reassessed and enhanced. The selection of RCI values based on the number of criteria is given in Table 4.

4.3. VIKOR Method. Opricovic proposed the VIKOR method to solve decision-making problems with conflicting criteria [59]. In this method, the ranking of the alternatives is influenced by the initial weight of the problem and its closeness to the objective. In the study, many researchers used the VIKOR method to solve multi-objective problems due to its aptness and feasibility. Some are as follows: Ilangkumaran et al. [60–62] used VIKOR along with some hybrid MCDM models to prioritize best treatment for wastewater management. The VIKOR approach was used by Yazdani and Payam [63] to prioritize material selection for MEMS applications. From the above facts, it is evident that the VIKOR model can be used as an effective tool for ranking alternatives [64–66].

The VIKOR method is started with the subsequent form Lp metric:

$$L_{Pj} = \left\{ \sum_{i=1}^{n} \left[\frac{w_i\left(f_i^* - f_{ij}\right)}{\left(f_i^* - f_i^-\right)} \right]^p \right\}^{1/P} \quad 1 \le P \le \infty, j = 1, 2, \ldots, J. \quad (26)$$

The compromising ranking method of VIKOR is given as follows:

Step 1. Matrix Normalization: let X_{ij} be the evaluation matrix with values of the jth alternatives and ith criteria, and then, the normalized matrix f_{ij} is calculated using

$$f_{ij} = \frac{x_{ij}}{\sqrt{\sum_{i=1}^{m} x_{ij}^2}}, i = 1, 2m; \; j = 1, 2, n. \quad (27)$$

Step2. *Evaluate the Worst and Best Values* (f^*, f^-): the best and the worst values are given by the following relation:

$$f_i^* = \max_j f_{ij}, f_i^- = \min_j f_{ij.} \quad (28)$$

Step 3. *Calculate the* S_j *and* R_j Values: the utility measure S_j and regret measure R_j are determined using the relation:

$$S_j = \frac{\sum_{i=1}^{n} w_i\left(f_i^* - f_{ij}\right)}{\left(f_i^* - f_i^-\right)}, \quad (29)$$

$$R_j = \max_i \left[\frac{\left(f_i^* - f_{ij}\right)}{\left(f_i^* - f_i^-\right)} \right]. m \quad (30)$$

Step 4. *Compute the VIKOR Index*: the VIKOR index value Q_j is calculated using

$$Q_j = \frac{v\left(S_j - S^*\right)}{\left(S^- - S^*\right)} + \frac{(1-v)\left(R_j - R^*\right)}{\left(R^- - R^*\right)}, \quad (31)$$

where

$$S* = \min_j S_j, S^- = \max_j S_j, R* = \min_j R_j, R^- = \max_j R_j. \quad (32)$$

Here, $v = 0.5$.

Step 5. *Rank the Alternatives*: the option with the lowest VIKOR index is chosen as the best value.

5. Result and Discussion

From the study [49], it is observed that the modification in peripheral geometry of TT in a smooth tube tends to increase the friction factor, but in terms of the Nusselt number, only a minor improvement is found. The current research looks at the effect of WCTT in grooved tubes. From experimental results, it is observed that different geometrical and operating parameters expose their unique influence on heat transfer, pressure drop, performance enhancement ratio, and rational efficiency. The effects of these parameters are conversed as follows.

Table 3: Fuzzy numbers' membership function.

Scale of linguistic importance	Fuzzy number	(L, M, U)-TFN	$(1/U, 1/M, 1/L)$: reciprocal of TFN
Equally: important	M1	(1, 1, 1)	(1, 1, 1)
Equally: moderate important	M2	(1, 2, 3)	(0.33, 0.5, 1)
Weakly: important	M3	(2, 3, 4)	(0.25, 00.33, 0.5)
Moderate: important	M4	(3, 4, 5)	(0.2, 0.25, 0.33)
Moderately: strong important	M5	(4, 5, 6)	(0.16, 0.2, 0.25)
Strongly: important	M6	(5, 6, 7)	(0.14, 0.16, 0.2)
Very strongly: important	M7	(6, 7, 8)	(0.12, 0.14, 0.16)
Very strongly: extreme important	M8	(7, 8, 9)	(0.11, 0.12, 0.14)
Absolutely: important	M9	(8, 9, 10)	(0.10, 0.11, 0.12)

Table 4: Random consistency index.

No.	1	2	3	4	5	6	7	8	9	10
RCI	0	0	0.52	0.89	1.11	1.25	1.35	1.40	1.45	1.49

5.1. Validation Conventional System. To validate the system's reliability, the plain tube result is compared to the result obtained from the standard correlations given in equations (33) to (36). Once the system's consistency is established, the plain tube heat exchanger results are recorded and compared to the standard correlation results (shown in Figure 7). The results showed that the thermal and flow performance of the plain tube agreed well with the standard correlation in the range of 5% to 8%, respectively. As a result, the results show that the experimental facility and measurement techniques are reliable. The plain tube results are used in upcoming calculations.

Convective heat transfer correlations—Dittus–Boelter correlation is as follows:

$$Nu = 0.023\mathrm{Re}^{0.8}\,\mathrm{Pr}^{0.3}\ \ for Re > 10,000. \tag{33}$$

Gnielinski correlation is as follows:

$$Nu = \frac{(f/8)(\mathrm{Re}-1000)\mathrm{Pr}}{1+12.7(f/8)^{0.5}\left(\mathrm{Pr}^{0.33}-1\right)}\ for 3000 < Re < 500,000. \tag{34}$$

Correlations for the friction factor—correlation of Blasius is as follows:

$$f = 0.316\mathrm{Re}^{-.025}\ for Re < 20,000. \tag{35}$$

Petukhov correlation is as follows:

$$f = (0.790\quad \ln \mathrm{Re} - 1.64)^{-2}\ for 3000 < Re < 500,000. \tag{36}$$

5.2. Heat Transfer Investigation of WCTT Insert. The effect of twist ratio (y) on heat transfer features in the grooved tube fitted with WCTT is presented in Figure 8. From Figure 8(a), it is observed that the Nusselt number (Nu) of the tube increases with an increase in Reynolds number and decreases in twist ratio. The WCTT having the value of $y = 3.5$ provides maximum heat transfer compared with the other twist ratios. This eddy flow generated by the TTs provides better flow mixing between core and wall of the tube, (2) strong turbulence and vortices near the W-cut region lead to thermal boundary layer destruction, and (3) in addition, the groove in tube causes flow separation, and reattachment and recirculation of water result in effective fluid mixing. The abovementioned flow phenomenon stimulates an increase in the turbulent intensity and tangential turbulent fluctuation, which affects the hydrodynamic and thermal boundary layer and therefore increases the heat transfer of the tube. Over the range studied, the WCTT in grooved tube with $y = 3.5$ provides the mean Nusselt number of about 12%, 20%, and 48% higher than those in the grooved tube with twist ratio of $y = 5.3$ and $y = 6.5$, and plain tube, respectively.

Similarly, the Nu ratio decreases with increasing Reynolds number in all cases, indicating that at lower Reynolds numbers, the flow cannot generate high turbulence on its own, and thus, introducing TT generates secondary swirl on fluid flow and increases heat transfer. At higher Reynolds numbers, the grooved tube itself creates a massive secondary swirl, and hence, the impact of TT becomes less effective. As expected, the Nu ratio of WCTT in the grooved tube compared with the simple tube is always greater than unity. From Figure 8(b), it is obvious that the Nu ratio of the WCTT in the grooved tube is approximately 2–2.5 times higher than in the simple grooved tube and approximately 3.0–3.4 times higher than in the simple tube.

Further, the heat transfer is also governed by the WR of the tape, as shown in Figure 8(a). It is observed that the effect of WR at a higher range yields a larger value of the Nusselt number compared with the smaller one. This is due to the effect of augmented eddies and vorticities behind the cut, which results in the promotion of turbulent intensity and fluid mixing and additionally increases the heat transfer rate. Figure 8 shows that the mean Nusselt number obtained using a W-cut insert in a grooved tube at $\mathrm{WR} = 0.6$ and $y = 3.5$, 5.3, and 6.4 is 2.08%, 2.13%, and 2.17% greater than the grooved inner tube at the same condition, $\mathrm{WR} = 0.4$.

5.3. Friction Factor Characteristics of W-Cut TT Insert. Figure 9 depicts the magnitude of friction with change in mass flow rate of working fluid passed inside the grooved tube fitted with WCTT and plain tube. It is observed that the friction factor followed the decreasing trend with rise in Reynolds number and showed supremacy at lower twist ratio ($y = 3.5$) compared with that of higher twist ratios

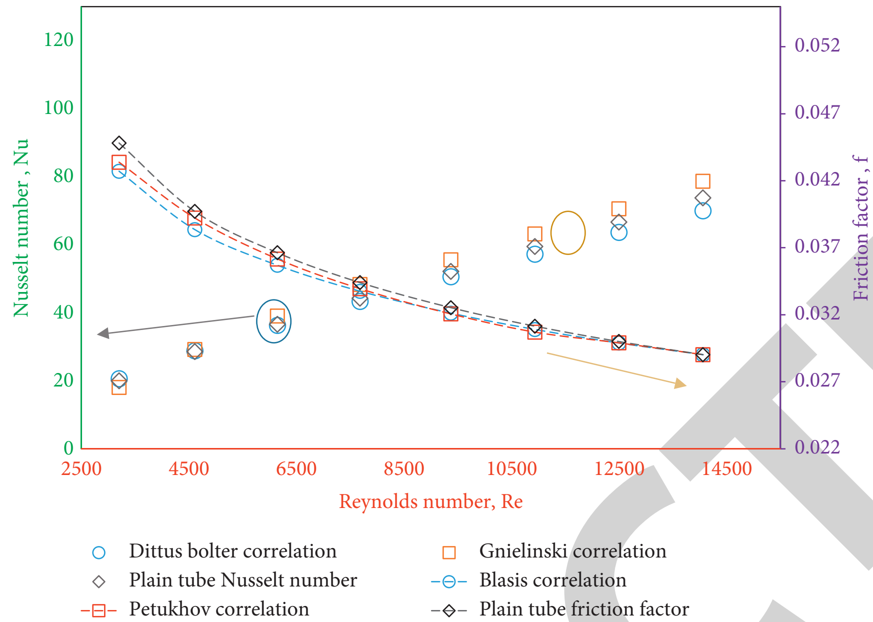

Figure 7: Validation of the plain tube.

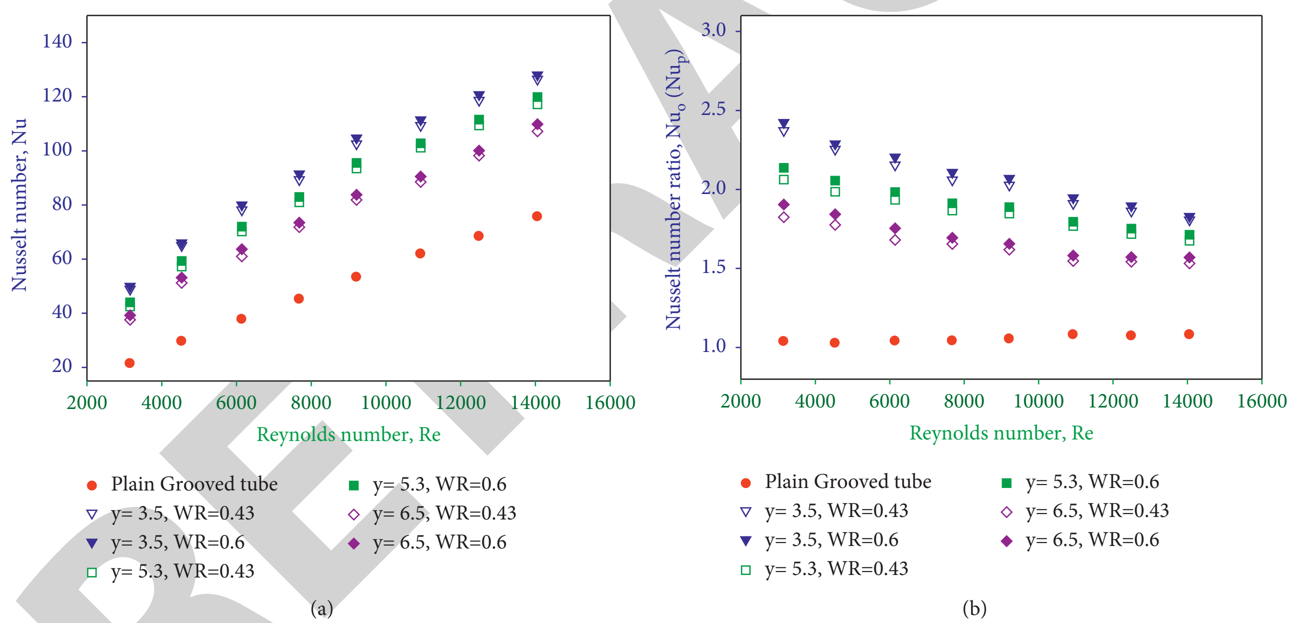

Figure 8: Nusselt number of WCTT: (a) Nu vs. Re. (b) Nu_o/Nu_p vs. Re.

($y = 5.3$ and 6.5). This is due to the effect of secondary flow generated by the WCTTs. At lower twist ratio, the turbulence intensity near the wall increases, which augments the fluid friction. In addition, the lower twist ratio TTs blocks the fluid passage in large volume and increases the surface contact, which results in increased static pressure. Also, the eddies and vortices made by W-cut create extensive friction loss that is normally negligible in case of plain tubes. From the graph, it is clear that the friction factor of the grooved tube with WCTT at $y = 3.5$ is 1.14 and 1.26 times higher than the given tube with $y = 5.3$ and 6.5, consecutively, and 4.5 times greater as compared with plain tube.

Figures 9(a) and 9(b) illustrate the friction factor ratio (f_o/f_P) of WCTT with different twist ratios (y) and width ratios (WRs). The result exposed that the friction factor nature increases with the rise in the Reynolds number. Qualitatively, the pressure loss generated by the WCTT is directly related to the results of the heat transfer discussed in Section 5.2 because an effective heat transfer is caused by the strong turbulence in boundary layer, which concurrently increases the interaction of pressure force with inertia force and thus enhances the dynamic pressure loss. At smaller twist ratio ($y = 3.5$), the friction factor ratio of WCTT is substantially higher than those associated with larger twist

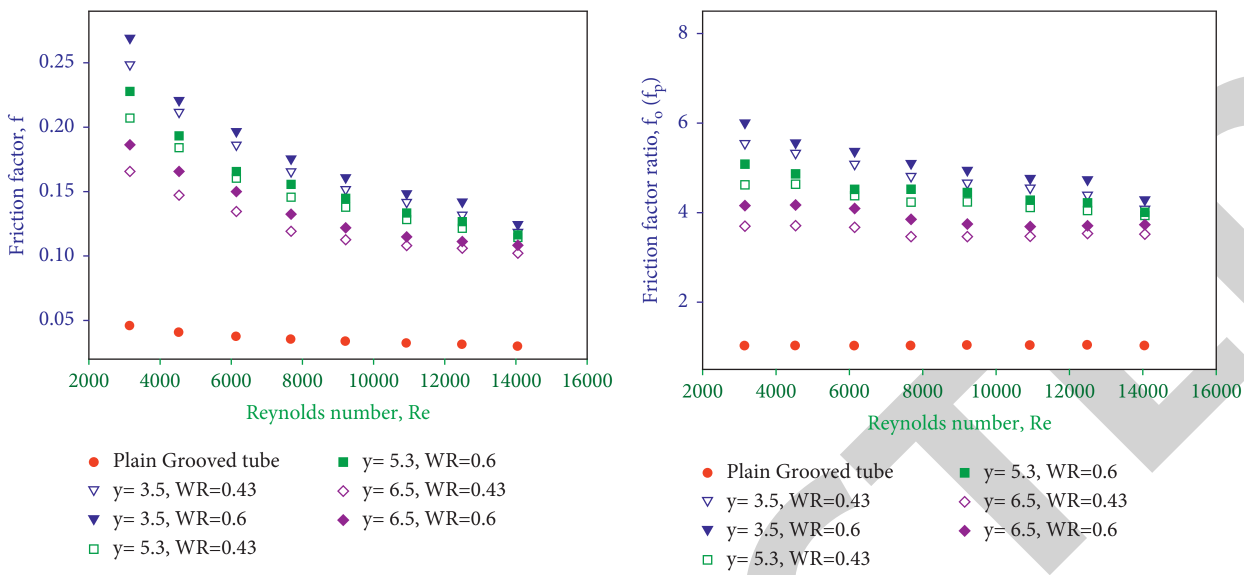

(a) (b)

Figure 9: Friction factor of W-cut insert: (a) f vs. Re. (b) f_o/f_p vs. Re.

ratio ($y = 5.3$ and 6.5), which are, respectively, in range of 1.10–1.45 times and about 4.95 times as improved with the conventional system.

The effect of width ratio (WR) on friction factor follows the same trend as the Nusselt number, whereas the friction factor increases with rise in width ratio. For the present range, the mean friction factor of WCTTs with WR of 0.4 at $y = 3.5$, 5.3, and 6.4 is higher than that caused by the use of W-cut insert at WR of 0.6 for given twist ratio by around 5%, 6%, and 8%, respectively.

5.4. Performance Enhancement Ratio. An equal pumping power comparison is attained to evaluate the heat transfer efficiency in terms of PER of the grooved tube fitted with WCTT. The variation of PER with Reynolds number for WCTT at various twist ratios (y) and width ratios is depicted in Figure 10. In all cases, the value of PER decreases with an increase in the Reynolds number. Also, at a given Reynolds number, the PER of the tube tends to increase with a decrease in y and WR. In all of the above cases, the PER shows how this tape helps save energy, and it also shows how the heat transfer ratio affects the friction penalty.

From the figure, it is observed that the mean enhancement ratio of the grooved tube with WCTT at $y = 3.5$ is 1.05 times, 1.5 times, and 2.08 times higher than the grooved tube with $y = 5.3$ and 6.4 and plain grooved tube, respectively. In addition, the WCTT at WR of 0.45 gives a maximum enhancement ratio and is about 0.9–1.4 times higher than the tape with WR of 0.6. This is due to the effect of added pressure drop at higher WR. Hence, it is concluded that the superior performance can be obtained by lower twist ratio and width ratio. However, the above result cannot be optimum, as the pressure drop reaches extreme at this condition. To overcome this problem, MOO techniques are used in this work, to find the optimum results. The

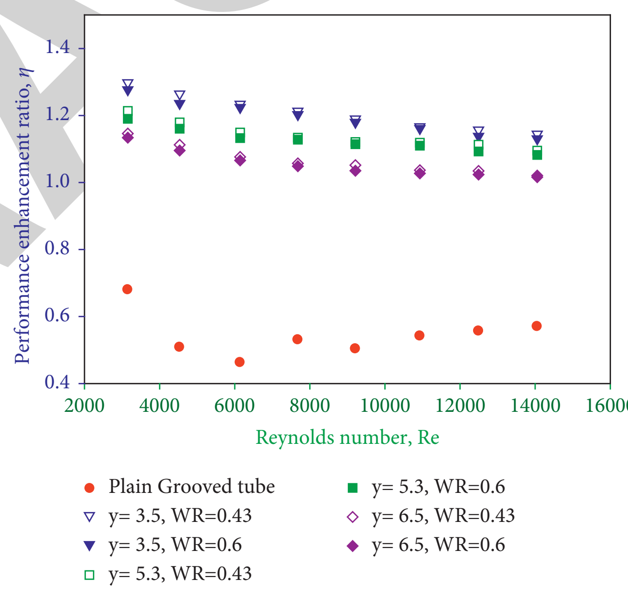

Figure 10: Performance enhancement ratio (η_I) vs. Reynolds number (Re).

parameters such as twist ratio and width ratio of TTs along with the Reynolds number play a major role in selecting optimum thermal performance conditions.

5.5. Rational Analysis of Exergy. The exergetic efficiency of WCTT with various geometries is discussed in this segment. Figure 11 shows the exergy efficiency of the inserts as a function of Reynolds number for various twist ratios and width ratios. When compared to plain grooved tube, the combined effect of WCTTs with grooved tube demonstrated superior rational exergy efficiency. W-cut causes stronger eddies and vortices, which increases decayed boundary layer thickness and turbulent intensity near the walls, increasing exergetic efficiency. The graph clearly shows that the rational exergetic efficiency of the WCTT with lower twist ratio ($y = 3.5$) outperformed the inserts with higher twist ratio ($y = 5.3$ and 6.5), respectively, by 1.04 and 1.10 times. Aside from that, the width ratio, like the PER discussed in Section 5.4, has an effect on rational exergy efficiency. It is difficult to choose the best because its performance in terms of width ratio is contradictory. As a result, the MOO technique is used in this study to achieve the best results.

5.6. Empirical Correlation. The empirical correlation for Nusselt number, friction factor, performance enhancement ratio, and rational efficiency of the grooved tube with WCTT was developed, as a function of tape geometry (y and WR) and Reynolds number using the least-squares regression analysis. The empirical correlations are as follows:

$$Nu = 0.493\mathrm{Re}^{0.635} y^{-0.33} (Wr)^{0.079}, \tag{37}$$

$$f = 12.3\mathrm{Re}^{-0.401} y^{-0.429} (\mathrm{W_r})^{0.21}, \tag{38}$$

$$\eta_I = 2.81\mathrm{Re}^{-0.071} y^{-0.191} (W_r)^{-0.0384}, \tag{39}$$

$$\eta_{II} = 1.69\mathrm{Re}^{-0.095} y^{-0.1041} (W_r)^{0.06}. \tag{40}$$

Figures 12(a) to 12(d) depict the predicted data of Nusselt number, friction factor, performance enhancement ratio, and rational efficiency from the above correlations (equations 37–(40)) in comparison with those obtained from the experimental data. Apparently, the predicted data are in good concordance with the experimental data with the discrepancy of ±4%, ±7%,± 3%, and ±2% for Nu, f, η_I, and η_{II}, respectively.

6. Optimization Results

From the above experimental study, it is clear that the effects of individual geometric variables on thermal and exergetic efficiency are considered one at a time, but the effects of compound variables are not taken into consideration. It is quite difficult to estimate the optimal working parameter of the WCTT using experimental results, and further, this study has two incompatible objectives (Nu and f). Hence, it is proposed to carry out multi-objective optimization (MOO) and multi-criteria decision-making (MCDM) techniques to determine the best possible design configuration for maximum performance in a grooved tube fitted with WCTT.

6.1. Optimization Using Multi-Objective Genetic Algorithm. The main objective of this study is to find the optimum working parameters of the grooved tube with WCTT using GA, which leads to the maximization of the Nusselt number and minimization of pressure drop. Owing to conflicting objectives, the negative Nusselt number (−Nu) is taken as defining parameter, such that lower the value of −Nu gives maximum heat transfer.

The multi-objective problem in the optimization of WCTTs is as follows.

Minimization $f(\mathrm{Re}, y, WR) = [-Nu, f]$.

The abovementioned functions are subjected to the parameters in the range of $2000 \leq \mathrm{Re} \leq 14000$, $3.5 \leq y \leq 6.4$, and $0.45 \leq \mathrm{WR} \leq 0.6$. In the given MOO technique, two geometric variables of WCTTs, namely, twist ratio (y) and width ratio (WR), and Reynolds number (Re) are chosen as the design variables. The maximum and minimum bounds of the design variables are shown in Table 5.

In this study, the GA technique is effectively used to determine the optimal Pareto front for the conflicting objectives. The detailed procedure of GA search method to generate optical Pareto front solutions is provided [50]. The parameter setting of GA is given in Table 6. The optimal Pareto front searched by the GA is shown in Figure 13, and their corresponding values are depicted in Table 7. It is clear that the all points in Pareto front are optimal points and they do not have any supremacy over each other. It is also observed that variation from one optimal point to another leads to the improvement of one objective with inimical change in the other. Thus, in this work, to select the optimal design configuration for heat exchanger with WCTT, the multi-objective genetic algorithm is used, in which the η and η_{II} are used to evaluate the heat transfer against the friction factor. The corresponding values of η and η_{II} compared against the two objective functions in optimal Pareto front are illustrated in Figures 14 and 15, respectively. Evidently, the extreme value of η and η_{II} from the figures gives the optimum geometric parameters for the defined problem.

Though the geometric points obtained using Pareto front of MOGA can be taken as the best, one cannot eliminate the remaining solutions, as all the values specified by Pareto front are optimal. Hence, to identify the best operating configuration from the Pareto front set, this study utilizes FAHP-VIKOR model as decision-making tool.

6.2. Optimization Using MCDM. This study utilizes the hybrid MCDM model to identify the best operating configuration from the set of Pareto values (taken as alternatives). The performance-defining criteria of the given problem are identified and are given in Table 8. In this phase, hybrid MCDM model, FAHP-TOPSIS, is used to rank the alternatives. Here, FAHP is used to assign weightage for the criteria and VIKOR is used to rank the alternatives.

6.2.1. Calculation of Weightage for Criteria. The weightage of criteria used in the study is calculated using the fuzzy analytical hierarchical process (FAHP) method. The nonconformity values of the alternatives associated with predefined criteria are depicted in Figure 16. Once the hierarchy diagram is framed, the FAHP computes the weights of each criterion by making pairwise comparison with Satty's nine-point scale. The fuzzy pairwise comparison results of the criteria are shown in Table 9. The geometric mean values are computed, and the final pairwise comparison matrix is constructed. The weight of each criterion is calculated and tabulated in Table 10 based on the final matrix. Consistency

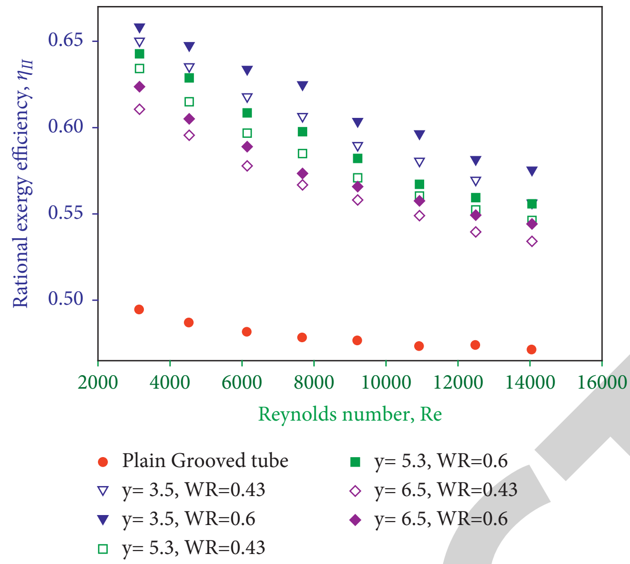

FIGURE 11: Exergy efficiency (η_{II}) vs. Reynolds number (Re).

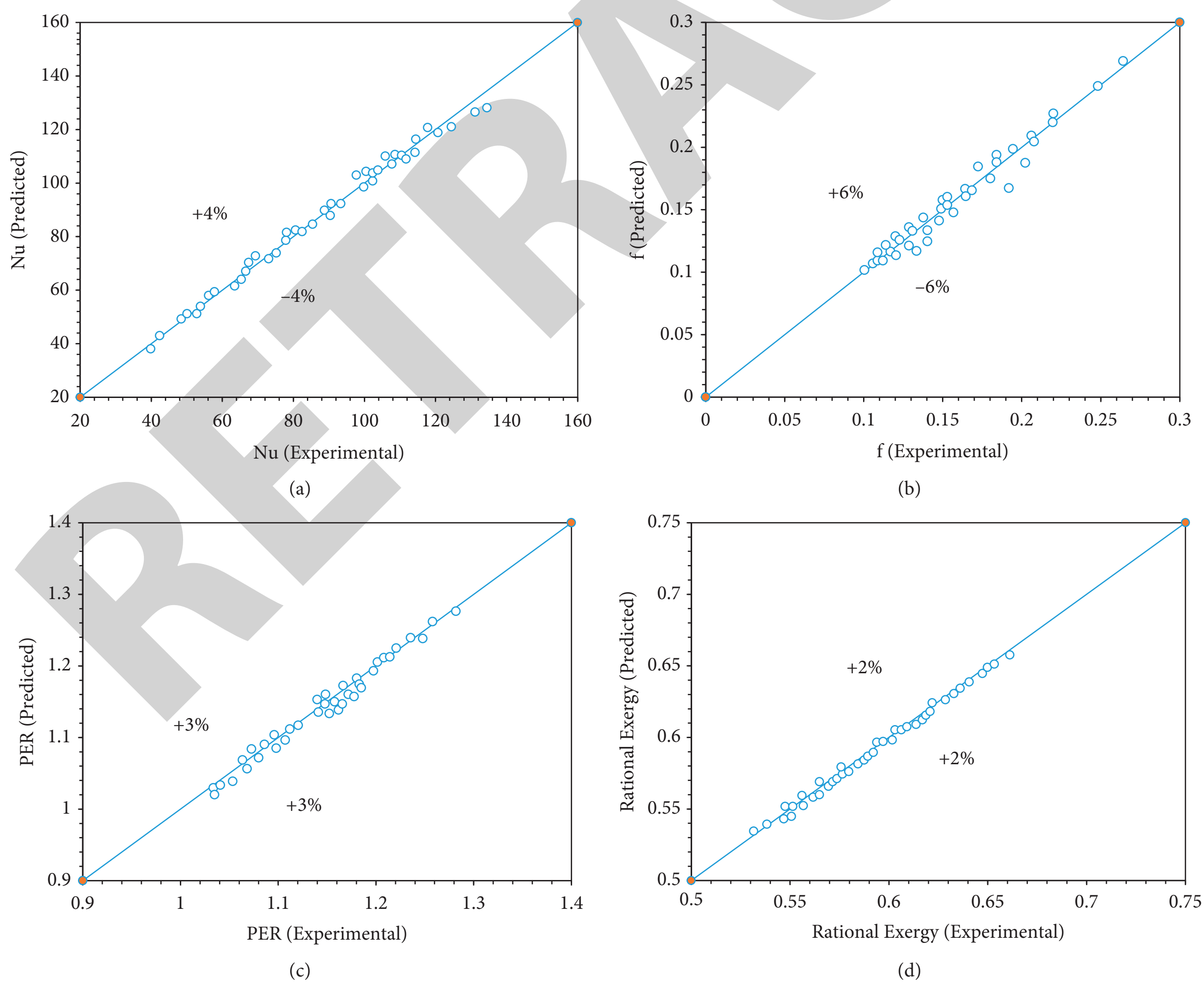

FIGURE 12: Assessment between the experimental and developed correlation results: (a) Nu, (b) fr, (c) η, (d) η_{II}.

Table 5: Range of design variables and the selected values.

Design variables	Lower bound	Higher bound	Selected values
Twist ratio (y)	3.5	6.4	3.5, 5.3, 6.4
Width ratio (WR)	0.45	0.6	0.45, 0.6
Reynolds number	3000	14000	3000, 4500, 6100, 7600, 9200, 10900, 12500, 14000

Table 6: Parameter setting for GA.

Parameter	Value setting
Population size	100
Pareto front population fraction	0.7
Cross fraction	0.8
Generation	500
Fractional tolerance	10^6

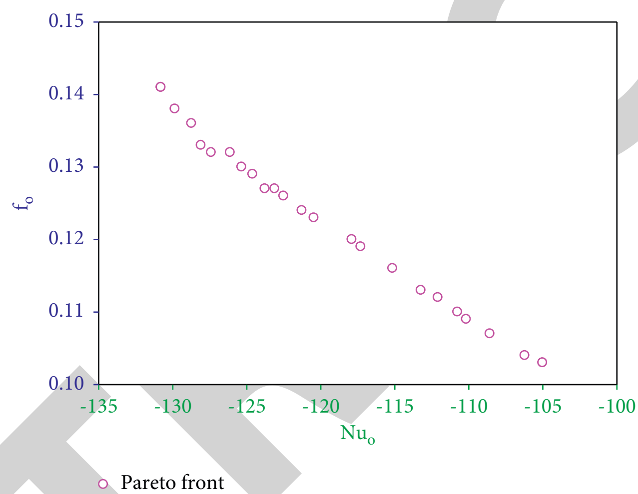

Figure 13: Optimal Pareto front solution.

index (CI) and consistency ratio (CR) values are calculated using equations (28) and (29) to check the consistency of the criteria in the pairwise comparison matrix. The CR value is 0.073, which is less than 0.1, according to the results. As a result, the weights assigned to the criteria are satisfactory and can be used to rank the alternatives.

6.2.2. Ranking the Alternatives. In this section, the VIKOR method is proposed for selecting the optimum design among the list of alternatives. The decision matrix of the stated problem is shown in Table 11, and the values of the decision matrix are normalized using equation (31). The normalized decision matrix values are calculated and tabulated in Table 12. The best and worst values of each criterion are calculated using equation (32) and are depicted in Table 13, followed by the construction of utility measure relation, regret measure relation, and VIKOR index using equations (33)–(35) shown in Table 14. The ranking of the options is prioritized according to the VIKOR index value, as shown in Table 14 and Figure 17. The alternative A4 among the list of 25 alternatives is the most preferred, as it attains the first rank with concern to overall objectives. According to VIKOR index values, the WCTT configuration rankings are as follows: A4 > A11 > A2 > A9 > A21 > A17 > A1 > A24 > A11 > A23 > A7 > A18 > A13 > A10 > A20 > A5 > A19 > A14 > A16 > A22 > A25 > A6 > A15 > A3 > A8. The alternative with twist ratio, $y = 3.55$, width ratio, $WR = 0.489$, and Reynolds number, $Re = 13511$, exhibits the optimal formulation.

To validate the optimum configuration, the obtained result is compared with the other inserts from the past under similar working condition. Figure 18 depicted the comparative result of the optimum configuration of WCTT with other inserts. The result showed that the optimum configuration of WCTT showed supremacy over other inserts in the range of 0.5–31.5%, respectively. The WCTT effectively breaks the viscose and thermal boundary layers formulated inside the tubes at turbulent flow conditions. Further, the W-shaped design offers lower flow resistance. This makes the system higher efficient as compared with other configurations of turbulator designs.

Table 7: Optimal configurations of W-cut twisted tapes (Pareto front solutions from GA).

PDAs	Criteria				
	RE	Y	WR	−Nu	f
A1	13509.24	3.585487	0.447139	−127.404	0.132
A2	13509.22	3.544997	0.594741	−130.796	0.141
A3	13520.53	6.396681	0.431835	−105.015	0.103
A4	13510.76	3.550541	0.488913	−128.730	0.136
A5	13513.59	4.584293	0.43714	−117.294	0.119
A6	13518.59	5.788635	0.434234	−108.572	0.107
A7	13511.20	3.894812	0.437794	−123.776	0.127
A8	13520.53	6.396681	0.431835	−105.015	0.103
A9	13509.22	3.544997	0.594741	−130.796	0.141
A10	1351200	4.218427	0.433286	−120.465	0.123
A11	13510.45	3.507667	0.436446	−128.092	0.133
A12	13509.70	3.530505	0.533291	−129.853	0.138
A13	13511.81	4.137216	0.434913	−121.275	0.124
A14	13515.52	5.104409	0.437658	−113.228	0.113
A15	13518.51	6.192659	0.435724	−106.210	0.104
A16	13518.68	5.480163	0.444343	−110.754	0.110
A17	13510.48	3.781659	0.454154	−125.345	0.130
A18	13511.81	4.012216	0.434913	−122.509	0.126
A19	13514.91	4.846300	0.436005	−115.146	0.116
A20	13512.97	4.524871	0.442025	−117.900	0.120
A21	13510.40	3.761377	0.479983	−126.117	0.132
A22	13516.24	5.263390	0.436984	−112.078	0.112
A23	13510.49	3.972317	0.444530	−123.118	0.127
A24	13509.49	3.835487	0.447139	−124.603	0.129
A25	13518.59	5.538635	0.434234	−110.165	0.109

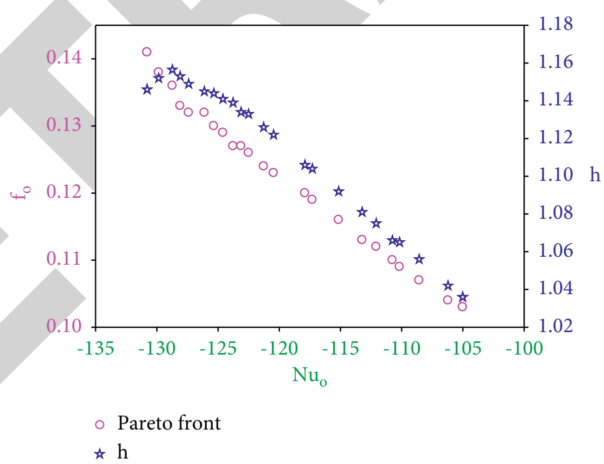

Figure 14: Multi-objective optimization of Pareto front (η).

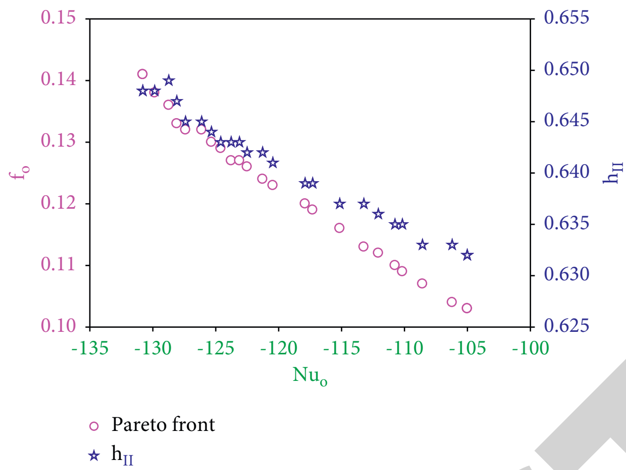

Figure 15: Multi-objective optimization of Pareto front (η_{II}).

Table 8: Details of the different criteria.

Criteria	Notations	Performance implications of different criteria.
Thermal enhancement ratio (TER)	(Nu_o/Nu_p)	C1-higher-the better
Friction enhancement ratio (FER)	(f_o/f_p)	C2-lower-the better
Performance enhancement ratio (PER)	(η_I)	C3-higher-the better
Rational exergy efficiency (REE)	(η_{II})	C4-higher-the better

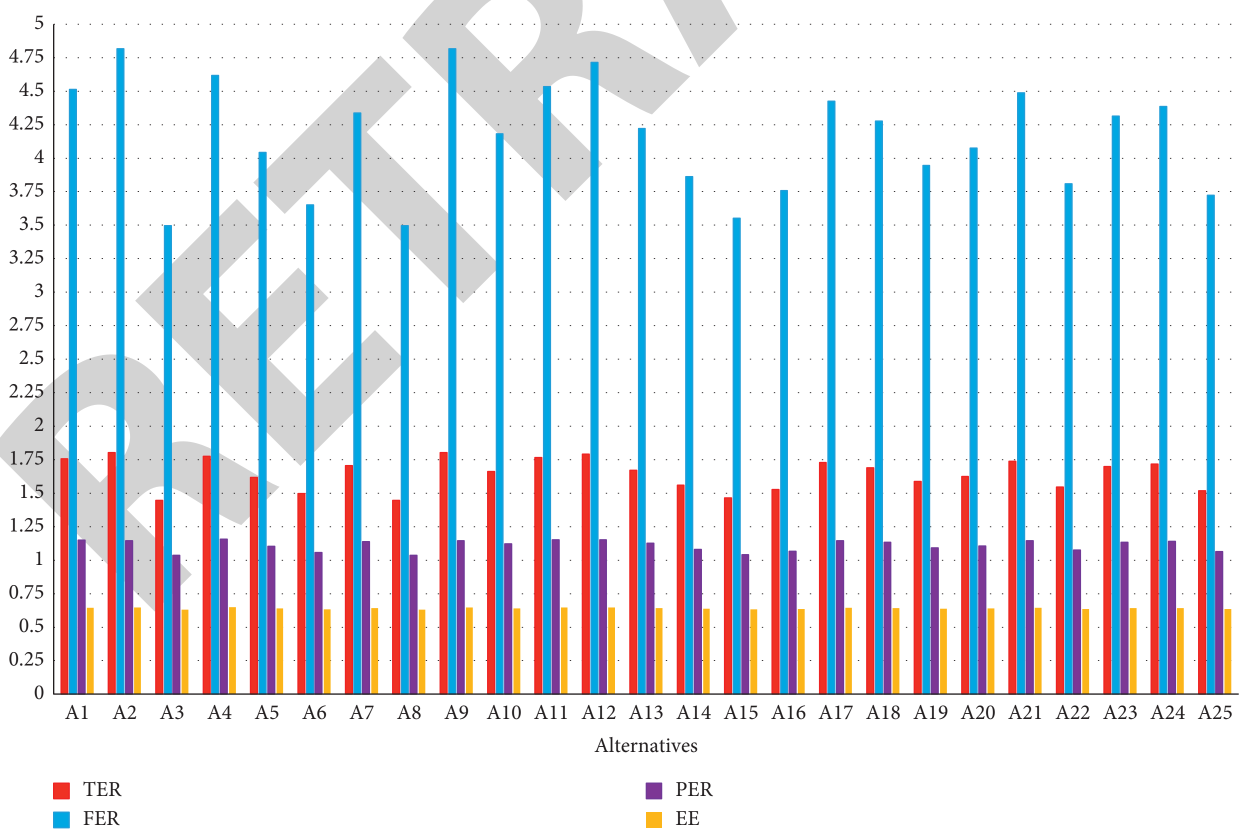

Figure 16: Inconsistency of criteria values with alternatives.

Table 9: Pairwise comparison matrix for criteria.

	TER	FER	PER	REE
TER	(1, 1, 1)	(1, 1, 1)	(0.25, 00.33, 0.5)	(0.25, 00.33, 0.5)
FER	(1, 1, 1)	(1, 1, 1)	(0.25, 00.33, 0.5)	(0.25, 00.33, 0.5)
PER	(2, 3, 4)	(2, 3, 4)	(1, 1, 1)	(00.33, 0.5, 1)
EE	(2, 3, 4)	(2, 3, 4)	(1, 2, 3)	(1, 1, 1)

Table 10: Results obtained with FAHP.

Criteria	Weights	λ_{max}, CI, RCI	CR
TER	0.1198	$\lambda_{max} = 4.201$, CI = 0.0669, RCI = 0.9	0.073
FER	0.1198		
PER	0.3476		
REE	0.4128		

Table 11: Details of alternatives and criteria (decision matrix).

PDAs	Criteria			
	TER	FER	PER	REE
A1	−1.76	4.514	1.149	0.645
A2	−1.8	4.816	1.146	0.648
A3	−1.45	3.495	1.036	0.632
A4	−1.77	4.618	1.157	0.649
A5	−1.62	4.043	1.104	0.639
A6	−1.5	3.652	1.056	0.633
A7	−1.71	4.337	1.139	0.643
A8	−1.45	3.495	1.036	0.632
A9	−1.8	4.816	1.146	0.648
A10	−1.66	4.182	1.122	0.641
A11	−1.77	4.533	1.153	0.647
A12	−1.79	4.715	1.152	0.648
A13	−1.67	4.22	1.126	0.642
A14	−1.56	3.861	1.081	0.637
A15	−1.46	3.551	1.042	0.633
A16	−1.53	3.757	1.066	0.635
A17	−1.73	4.426	1.144	0.644
A18	−1.69	4.276	1.133	0.642
A19	−1.59	3.945	1.092	0.637
A20	−1.63	4.075	1.106	0.639
A21	−1.74	4.488	1.145	0.645
A22	−1.54	3.81	1.075	0.636
A23	−1.7	4.314	1.134	0.643
A24	−1.72	4.385	1.141	0.643
A25	−1.52	3.722	1.065	0.635

Table 12: Weighted normalized decision matrix.

PDAs	Criteria			
	TER	FER	PER	REE
A1	0.1041	0.0924	0.0033	0.2086
A2	0.1198	0.1198	0.0245	0.0442
A3	0.0000	0.0000	0.3476	0.4128
A4	0.1102	0.1019	0.0000	0.0000
A5	0.0571	0.0497	0.1482	0.3071
A6	0.0165	0.0143	0.2894	0.3784
A7	0.0872	0.0764	0.0454	0.2621
A8	0.0000	0.0000	0.3476	0.4128
A9	0.1198	0.1198	0.0245	0.0442

Table 12: Continued.

PDAs	Criteria			
	TER	FER	PER	REE
A10	0.0718	0.0623	0.0949	0.2985
A11	0.1072	0.0942	0.0033	0.2394
A12	0.1154	0.1107	0.0076	0.0108
A13	0.0756	0.0658	0.0831	0.2878
A14	0.0382	0.0332	0.2145	0.3335
A15	0.0056	0.0051	0.3296	0.3907
A16	0.0266	0.0238	0.2594	0.3299
A17	0.0945	0.0845	0.0312	0.1993
A18	0.0813	0.0709	0.0636	0.2798
A19	0.0471	0.0408	0.1823	0.3256
A20	0.0599	0.0526	0.1415	0.2870
A21	0.0981	0.0901	0.0349	0.1147
A22	0.0328	0.0285	0.2330	0.3439
A23	0.0842	0.0743	0.0600	0.2443
A24	0.0911	0.0807	0.0383	0.2262
A25	0.0239	0.0206	0.2630	0.3669

Table 13: Best and worst values of criteria.

	TER	FER	PER	EE
Best value (f_i^*)	1.80	4.82	1.16	0.65
Worst value (f_i^*)	1.45	3.50	1.04	0.63

Table 14: S_i, R_i, and Q_i values and ranking of alternatives using VIKOR.

PDAs	Criteria			
	S_i	R_i	Q_i	Rank
A1	0.41	0.21	0.0750	4
A2	0.31	0.12	0.0768	3
A3	0.76	0.41	1.0000	24
A4	0.21	0.11	0.0076	1
A5	0.56	0.31	0.4878	16
A6	0.70	0.38	0.9067	22
A7	0.47	0.26	0.2029	10
A8	0.76	0.41	1.0000	25
A9	0.31	0.12	0.0768	6
A10	0.53	0.30	0.3441	14
A11	0.44	0.24	0.0304	2
A12	0.24	0.12	0.0480	3
A13	0.51	0.29	0.2822	13
A14	0.62	0.33	0.6411	18
A15	0.73	0.39	0.9341	23
A16	0.64	0.33	0.7791	20
A17	0.41	0.20	0.1397	8
A18	0.50	0.28	0.2686	12
A19	0.60	0.33	0.6196	17
A20	0.54	0.29	0.4841	15
A21	0.34	0.11	0.0849	7
A22	0.64	0.34	0.7070	19
A23	0.46	0.24	0.2129	11
A24	0.44	0.23	0.1994	9
A25	0.67	0.37	0.7807	21

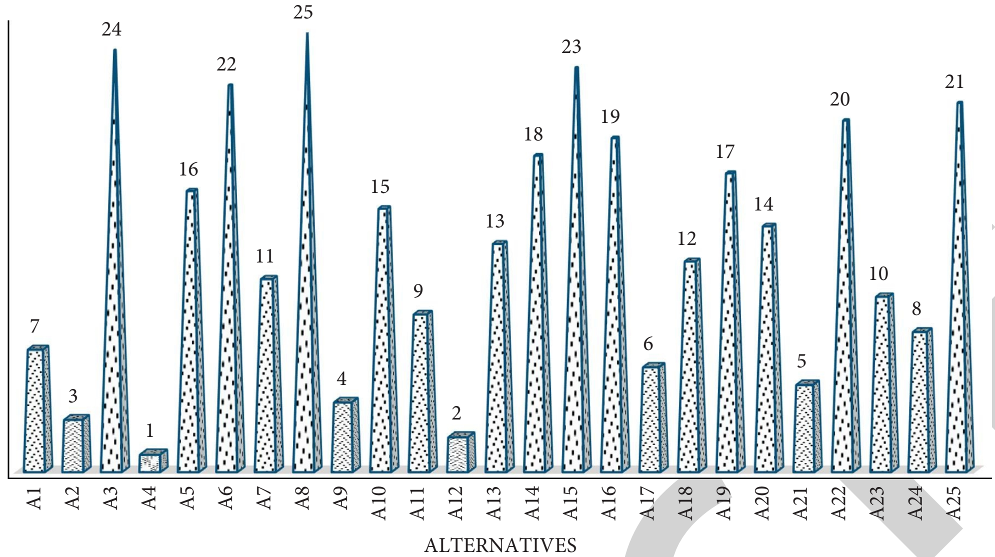

Figure 17: Ranking of alternatives.

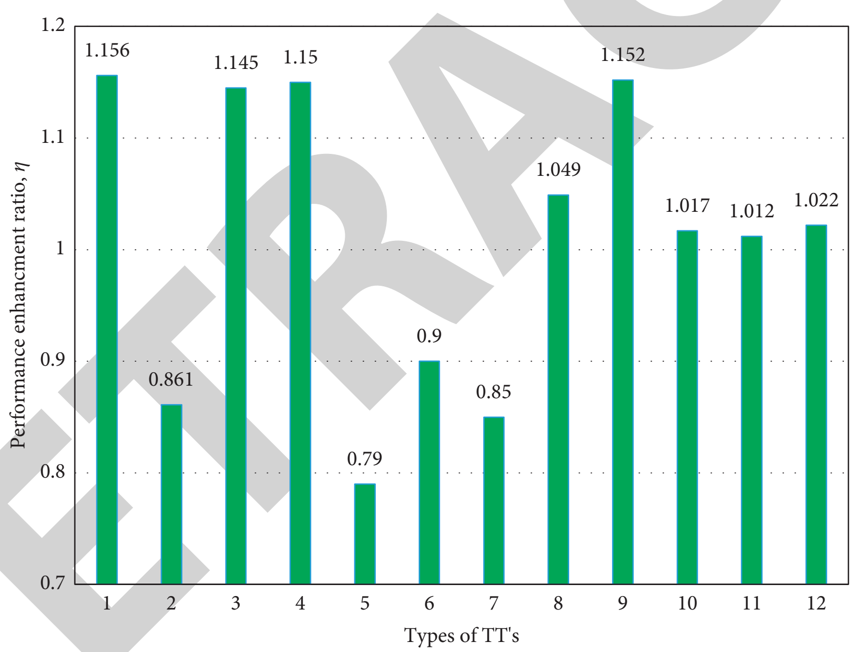

1. Present tape (W-cut TT)
2. Large/small twin TT [26]
3. TT Consisting of Wire-nails [6]
4. Horizontal wing-cut TT [5]
5. Twisted tape inserts [18]
6. Helically TT with alternate axis [23]
7. cross hollow TT [16]
8. Dual TT [16]
9. centre-cleared TT [15]
10. Tapered TT [5]
11. Peripherally cut dual TT [12]
12. perforated helical TT [19]

Figure 18: Performance comparison of optimal configuration WCTT with former tapes.

7. Conclusions

To ascertain the best performance configuration of WCTT, the twist ratio, width ratio, and Reynolds number parameters are to be considered, which consists of conflicting objectives with a major focus on meeting enhanced heat transfer. Therefore, an effective optimization concept is essential to resolve the problem. This work uses optimization tools such as genetic algorithm and FAHP-VIKOR on experimental results with varying parameters to identify the best one. Initially, the effect of grooved tube with WCTT is carried out to show the deviance of objectives with the variation of parameters. Then, the set of optimal solutions for the conflicting objectives is identified using multi-objective GA. Finally, the best optimal solution is obtained using the FAHP-VIKOR model. The results of the current work are as follows.

(i) The Nusselt number increases with rise in Reynolds number and width ratio and with decrease in twist ratio. The Nusselt number of the grooved tube with WCTT showed 44–56% higher heat transfer rate than plain tube.

(ii) The friction factor increases with a decrease in Reynolds number and twist ratio and with the increase in width ratio. The rise in friction factor is noticed for the grooved tube fitted WCTT than the plain tube of about 71–78%.

(iii) The performance enhancement ratio of WCTT is in the range of 1.02–1.30 for the given working conditions, and it raises with the reduction in twist tape ratio, width ratio, and Reynolds number.

(iv) The rational exergy efficiency increases with the increase in width ratio, in addition with the reduction in twist tape ratio and flow rate. The mean exergy efficiency of the grooved tube with WCTT is about 1.17–1.28 times higher than the plain tube.

(v) The empirical correlation for the Nusselt number, friction factor, performance enhancement ratio, and rational efficiency was developed, and they showed the discrepancy of ±3.5%, ±6%, ±2%, and ±1.5%, respectively.

(vi) As the design parameters such as twist ratio, width ratio, and Reynolds number strongly influence the overall system performance and to optimize the best working configuration, the integrated GA and FAHP-VIKOR optimization tools are used.

(vii) The genetic algorithm is used to optimize the given data and provides the set of optimal Pareto front solutions. This optimal design leads to trade-off between Nu and f, which results in the use of multi-objective genetic algorithm.

(viii) As all the given solutions of Pareto front were optimum and in the necessity to prioritize the best, the FAHP-VIKOR model is evaluated.

(ix) The order of criteria that dominate the VIKOR index is REE > PER > FER > TER. These criteria are determined to optimize the overall performance of grooved tube heat exchanger employing WCTTs. These performance criteria weights are calculated using FAHP, and their contribution ratio of order is 41.26%, 34.76%, 11.98%, and 11.98%, respectively.

(x) The optimal formulation is A4 with twist ratio (y): 3.55, width ratio (WR): 0.488, and Reynolds number (Re): 13511, which gives outcomes of thermal enhancement ratio (Nu_o/Nu_p): 1.177; friction enhancement ratio (f_o/f_p): 4.62; performance enhancement ratio: 1.15; and exergy efficiency: 0.649.

Nomenclature

A: Surface area of heat exchanger (m^2)
C_p: Specific heat of hot fluid (J/kg·K)
d_i: Inner diameter of heat exchanger's inner tube (m)
E^{out}: Exergy output (W)
E_{useful}: Useful exergy output (W)
E: Qualitative exergy of HX (W)
f_o/f_p: Ratio of friction factor for HX
I': Exergy lost (W)
L: Heat exchanger tube length (m)
Nu: Nusselt number
ΔP: Drop in pressure due to fluid friction
Q: Energy transfer rate (W)
S: Entropy
WR: Width ratio
d_o: Outer diameter of heat exchanger's inner tube (m)
d_h: Hydraulic diameter (m)
E^{in}: Exergy input (W)
E_{waste}: External exergy loss (W)
f: Fluid friction factor of HX
h: Heat transfer coefficient (W/mK)
H: Tape pitch distance (m)
K: Thermal conductivity (W/mK)
m: Fluid mass flow rate (kg/s)
Nu_o/Nu_p: Nusselt number enhancement ratio
P_r: Prandtl number
Re: Reynolds number
T_o: Ambient temperature (°C)
Y: Twist tape ratio

Greek symbols.

η_{II}: Exergy efficiency
ν: Dynamic viscosity (kg/ms)
ρ: Density (kg/m^3)
μ: Kinematic viscosity (m^2/s)
η: Performance enhancement ratio

Abbreviations

TT: Twisted tape
PER: Performance enhancement ratio
WCTT: W-cut twisted tape

Subscripts

O: Exit or outlet
C: Cold
Stream: Material stream
I: Inlet
H: Hot
Q: Heat stream.

Data Availability

The data used to support the findings of this study are included within the article.

Conflicts of Interest

The authors declare that there are no conflicts of interest regarding the publication of this article.

References

[1] C. N. Kumar and P. Murugesan, "Review on twisted tapes heat transfer enhancement," *International Journal of Scientific Engineering and Research*, vol. 3, no. 4, pp. 726–734, 2012.

[2] S. Tamna, Y. Kaewkohkiat, S. Skullong, and P. Promvonge, "Heat transfer enhancement in tubular heat exchanger with double V-ribbed twisted-tapes," *Case Studies in Thermal Engineering*, vol. 7, pp. 14–24, 2016.

[3] P. Murugesan, K. Mayilsamy, and S. Suresh, "Heat transfer in a tube fitted with vertical and horizontal wing-cut twisted tapes," *Experimental Heat Transfer*, vol. 25, no. 1, pp. 30–47, 2012.

[4] A. Hasanpour, M. Farhadi, and K. Sedighi, "Experimental heat transfer and pressure drop study on typical, perforated, V-cut and U-cut twisted tapes in a helically corrugated heat exchanger," *International Communications in Heat and Mass Transfer*, vol. 71, pp. 126–136, 2016.

[5] N. Piriyarungrod, S. Eiamsa-ard, C. Thianpong, M. Pimsarn, and K. Nanan, "Heat transfer enhancement by tapered twisted tape inserts," *Chemical Engineering and Processing: Process Intensification*, vol. 96, pp. 62–71, 2015.

[6] P. Murugesan, K. Mayilsamy, and S. Suresh, "Heat transfer and friction factor studies in a circular tube fitted with twisted tape consisting of wire-nails," *Chinese Journal of Chemical Engineering*, vol. 18, no. 6, pp. 1038–1042, 2010.

[7] S. Gunes and E. Karakaya, "Thermal characteristics in a tube with loose-fit perforated twisted tapes," *Heat Transfer Engineering*, vol. 36, no. 18, pp. 1504–1517, 2015.

[8] M. Jafaryar, M. Sheikholeslami, Z. Li, and R. Moradi, "Nanofluid turbulent flow in a pipe under the effect of twisted tape with alternate axis," *Journal of Thermal Analysis and Calorimetry*, vol. 135, no. 1, pp. 305–323, 2018.

[9] A. A. Giniyatullin, S. E. Tarasevich, and A. B. YakovlevYakovlev, "Heat transfer in a water flow in tubes with ribbed twisted tape inserts," *High Temperature*, vol. 56, no. 2, pp. 302–305, 2018.

[10] A. V. Shishkin and S. E. Tarasevich, "Heat transfer and structure of flow at boiling of refrigerant R134a in channels with inserts in the form of finned twisted tape," *Journal of Physics: Conference Series*, vol. 980, no. 1, Article ID 012012, 2018, March.

[11] Y. He, L. Liu, P. Li, and L. Ma, "Experimental study on heat transfer enhancement characteristics of tube with cross hollow twisted tape inserts," *Applied Thermal Engineering*, vol. 131, pp. 743–749, 2018.

[12] W. Changcharoen, P. Somravysin, and S. Eiamsa-ard, "Thermal and fluid flow characteristics in a tube equipped with peripherally-cut dual twisted tapes," *Open Engineering*, vol. 5, no. 1, 2014.

[13] A. Saravanan, J. S. Senthilkumaar, and S. Jaisankar, "Performance assessment in V-trough solar water heater fitted with square and V-cut twisted tape inserts," *Applied Thermal Engineering*, vol. 102, pp. 476–486, 2016.

[14] K. Yongsiri, C. Thianpong, K. Nanan, and S. Eiamsa-ard, "Thermal performance enhancement in tubes using helically twisted tape with alternate axis inserts," *Thermophysics and Aeromechanics*, vol. 23, no. 1, pp. 69–81, 2016.

[15] S. Pal and S. K. Saha, "Laminar flow and heat transfer through a circular tube having integral transverse corrugations and fitted with centre-cleared twisted-tape," *Experimental Thermal and Fluid Science*, vol. 57, pp. 388–395, 2014.

[16] W. Changcharoen, P. Samruaisin, P. Eiamsa-ard, and S. Eiamsa-ard, "Heat transfer characteristics of decaying swirl flow through a circular tube with co/counter dual twisted-tape swirl generators," *Thermophysics and Aeromechanics*, vol. 23, no. 4, pp. 523–536, 2016.

[17] B. Salam, S. Biswas, S. Saha, and M. M. K. Bhuiya, "Heat transfer enhancement in a tube using rectangular-cut twisted tape insert," *Procedia Engineering*, vol. 56, pp. 96–103, 2013.

[18] S. Chamoli, R. Lu, and P. Yu, "Thermal characteristic of a turbulent flow through a circular tube fitted with perforated vortex generator inserts," *Applied Thermal Engineering*, vol. 121, pp. 1117–1134, 2017.

[19] K. Nanan, C. Thianpong, P. Promvonge, and S. Eiamsa-ard, "Investigation of heat transfer enhancement by perforated helical twisted-tapes," *International Communications in Heat and Mass Transfer*, vol. 52, pp. 106–112, 2014.

[20] B. Kumar, A. K. Patil, S. Jain, and M. Kumar, "Effects of double V cuts in perforated twisted tape insert: an experimental study," *Heat Transfer Engineering*, vol. 41, no. 17, pp. 1473–1484, 2020.

[21] C. Man, X. Lv, J. Hu, P. Sun, and Y. Tang, "Experimental study on effect of heat transfer enhancement for single-phase forced convective flow with twisted tape inserts," *International Journal of Heat and Mass Transfer*, vol. 106, pp. 877–883, 2017.

[22] A. T. Wijayanta, M. Aziz, and M. Aziz, "Heat transfer augmentation of internal flow using twisted tape insert in turbulent flow," *Heat Transfer Engineering*, vol. 41, no. 14, pp. 1288–1300, 2020.

[23] A. T. Wijayanta, B. Pranowo, M. Mirmanto, B. Kristiawan, and M. Aziz, "Internal flow in an enhanced tube having square-cut twisted tape insert," *Energies*, vol. 12, no. 2, p. 306, 2019.

[24] I. Yaningsih, A. T. Wijayanta, T. Miyazaki, and S. Koyama, "V-cut twisted tape insert effect on heat transfer enhancement of single phase turbulent flow heat exchanger," in *AIP Conference Proceedings*vol. 1931, no. 1, AIP Publishing LLC, Article ID 030038, 2018.

[25] I. Yaningsih and A. T. Wijayanta, "Concentric tube heat exchanger installed by twisted tapes using various wings with

alternate axes," in *AIP Conference Proceedings*vol. 1788, no. 1, AIP Publishing LLC, Article ID 030005, 2017.
[26] I. Yaningsih, T. Istanto, and A. T. Wijayanta, "Experimental study of heat transfer enhancement in a concentric double pipe heat exchanger with different axial pitch ratio of perforated twisted tape inserts," *AIP Conference Proceedings*, AIP Publishing LLC, vol. 1717, no. 1, Article ID 030012, 2016.
[27] P. Bharadwaj, A. D. Khondge, and A. W. Date, "Heat transfer and pressure drop in a spirally grooved tube with twisted tape insert," *International Journal of Heat and Mass Transfer*, vol. 52, no. 7-8, pp. 1938–1944, 2009.
[28] D. G. Kumbhar D.G. and N. K. Sane N.K., "Exploring heat transfer and friction factor performance of a dimpled tube equipped with regularly spaced twisted tape inserts," *Procedia Engineering*, vol. 127, pp. 1142–1149, 2015.
[29] Y. Hong, J. Du, and S. Wang, "Experimental heat transfer and flow characteristics in a spiral grooved tube with overlapped large/small twin twisted tapes," *International Journal of Heat and Mass Transfer*, vol. 106, pp. 1178–1190, 2017.
[30] A. Verma, M. Kumar, and A. K. Patil, "Enhanced heat transfer and frictional losses in heat exchanger tube with modified helical coiled inserts," *Heat and Mass Transfer*, vol. 54, no. 10, pp. 3137–3150, 2018.
[31] P. Promvonge, S. Pethkool, M. Pimsarn, and C. ThianpongThianpong, "Heat transfer augmentation in a helical-ribbed tube with double twisted tape inserts," *International Communications in Heat and Mass Transfer*, vol. 39, no. 7, pp. 953–959, 2012.
[32] Y. Hong, X. Deng, and L. Zhang, "3D numerical study on compound heat transfer enhancement of converging-diverging tubes equipped with twin twisted Tapes," *Chinese Journal of Chemical Engineering*, vol. 20, no. 3, pp. 589–601, 2012.
[33] Y. Zhou, J. Yu, and X. Chen, "Thermodynamic optimization analysis of a tube-in-tube helically coiled heat exchanger for Joule-Thomson refrigerators," *International Journal of Thermal Sciences*, vol. 58, pp. 151–156, 2012.
[34] V. J. Manoj Praveen, R. Vigneshkumar, N. Karthikeyan, A. Gurumoorthi, R. Vijayakumar, and P. Madhu, "Heat transfer enhancement of air-concrete thermal energy storage system - CFD simulation and experimental validation under transient condition," *Proceedings of the Institution of Mechanical Engineers - Part E: Journal of Process Mechanical Engineering*, vol. 235, no. 5, pp. 1304–1314, 2021.
[35] A. T. Wijayanta, I. Yaningsih, W. E. Juwana, M. Aziz, and T. Miyazaki, "Effect of wing-pitch ratio of double-sided delta-wing tape insert on the improvement of convective heat transfer," *International Journal of Thermal Sciences*, vol. 151, Article ID 106261, 2020.
[36] M. Z. A. Khan, M. Aziz, and A. T. Wijayanta, "Prediction of heat transfer enhancement of delta-wing tape inserts using artificial neural network," *Case Studies in Thermal Engineering*, vol. 27, Article ID 101322, 2021.
[37] A. T. Wijayanta, I. Yaningsih, M. Aziz, T. Miyazaki, and S. Koyama, "Double-sided delta-wing tape inserts to enhance convective heat transfer and fluid flow characteristics of a double-pipe heat exchanger," *Applied Thermal Engineering*, vol. 145, pp. 27–37, 2018.
[38] A. T. Wijayanta, M. Aziz, K. Kariya, and A. Miyara, "Numerical study of heat transfer enhancement of internal flow using double-sided delta-winglet tape insert," *Energies*, vol. 11, no. 11, p. 3170, 2018.
[39] I. Yaningsih, A. T. Wijayanta, T. Miyazaki, and S. Koyama, "Impact of blockage ratio on thermal performance of delta-winglet vortex generators," *Applied Sciences*, vol. 8, no. 2, p. 181, 2018.
[40] A. T. Wijayanta, T. Istanto, K. Kariya, and A. Miyara, "Heat transfer enhancement of internal flow by inserting punched delta winglet vortex generators with various attack angles," *Experimental Thermal and Fluid Science*, vol. 87, pp. 141–148, 2017.
[41] M. Veerabhadrappa Bidari, P. B. Nagaraj, and G. Lalagi, "Influence of different types of vortex generators (VGs) to enhance heat transfer performance in heat exchangers: a review," *International Journal of Ambient Energy*, pp. 1–24, 2021.
[42] H. Z. Han, B. X. Li, H. Wu, and W. Shao, "Multi-objective shape optimization of double pipe heat exchanger with inner corrugated tube using RSM method," *International Journal of Thermal Sciences*, vol. 90, pp. 173–186, 2015.
[43] P. K. Swamee, N. Aggarwal, and V. Aggarwal, "Optimum design of double pipe heat exchanger," *International Journal of Heat and Mass Transfer*, vol. 51, no. 9-10, pp. 2260–2266, 2008.
[44] Z. Iqbal, K. S. Syed, and M. Ishaq, "Optimal fin shape in finned double pipe with fully developed laminar flow," *Applied Thermal Engineering*, vol. 51, no. 1-2, pp. 1202–1223, 2013.
[45] Z. Iqbal, K. S. Syed, and M. Ishaq, "Optimal convective heat transfer in double pipe with parabolic fins," *International Journal of Heat and Mass Transfer*, vol. 54, no. 25-26, pp. 5415–5426, 2011.
[46] C. K. Kwong and H. Bai, "A fuzzy AHP approach to the determination of importance weights of customer requirements in quality function deployment," *Journal of intelligent manufacturing*, vol. 13, no. 5, pp. 367–377, 2002.
[47] S. Yijie and S. Gongzhang, "Improved NSGA-II multi-objective genetic algorithm based on hybridization-encouraged mechanism," *Chinese Journal of Aeronautics*, vol. 21, no. 6, pp. 540–549, 2008.
[48] T. A. Khan and W. Li, "Optimal design of plate-fin heat exchanger by combining multi-objective algorithms," *International Journal of Heat and Mass Transfer*, vol. 108, pp. 1560–1572, 2017.
[49] J. Zheng, R. Shen, and J. Zou, "Enhancing diversity for NSGA-II in evolutionary multi-objective optimization," in *Proceedings of the 2012 Eighth International Conference on Natural Computation (ICNC)*, pp. 654–657, IEEE, Sichuan, China, 2012, May.
[50] S. Chamoli, "Preference selection index approach for optimization of V down perforated baffled roughened rectangular channel," *Energy*, vol. 93, pp. 1418–1425, 2015.
[51] C. S. Dhanalakshmi, M. Mathew, and P. Madhu, "Biomass material selection for sustainable environment by the application of multi-objective optimization on the basis of ratio analysis (MOORA)," in *Materials, Design, and Manufacturing for Sustainable Environment*, pp. 345–354, Springer, Singapore, 2021.
[52] M. Mmohammadiun, F. Dashtestani, and M. Alizadeh, "Exergy prediction model of a double pipe heat exchanger using metal oxide nanofluids and twisted tape based on the artificial neural network approach and experimental results," *Journal of Heat Transfer*, vol. 138, no. 1, Article ID 011801, 2016.
[53] W. Liu, P. Liu, J. B. Wang, N. B. Zheng, and Z. C. Liu, "Exergy destruction minimization: a principle to convective heat transfer enhancement," *International Journal of Heat and Mass Transfer*, vol. 122, pp. 11–21, 2018.

Hindawi
Advances in Materials Science and Engineering
Volume 2022, Article ID 3539069, 9 pages
https://doi.org/10.1155/2022/3539069

Research Article

A Novel Approach to the Sintering Schedule of Ba (Co0.7Zn0.3)1/3Nb2/3O3 Dielectric Ceramics for Microwave Applications

Mohamed Mouyane, Brahim Itaalit, Jérôme Bernard, and David Houivet

Laboratoire Universitaire des Sciences Appliquées de Cherbourg (LUSAC), Normandie Univ, UNICAEN, LUSAC, EA 4253, France

Correspondence should be addressed to Mohamed Mouyane; mohamed.mouyane@unicaen.fr

Received 8 March 2022; Revised 9 May 2022; Accepted 24 May 2022; Published 22 July 2022

Academic Editor: Ravi Samikannu

The present research is devoted to the optimization of the sintering schedule of Ba (Co0.7Zn0.3)1/3Nb2/3O3 (BCZN) dielectric ceramics for microwaves applications. A novel approach to the heat treatment of these ceramics based on the rapid-rate sintering (RRS) technique followed by a lower temperature annealing cycle has been developed. The relationships among the heat treatment process optimization, the structural, microstructural characteristics, and the microwave dielectric properties of the BCZN ceramics were investigated using X-ray diffraction, scanning electron microscopy, energy dispersion analysis, and vector network analysis. The RRS-technique shortens substantially the time required for the elaboration of these components in comparison with conventional sintering techniques and prevents simultaneously the formation of secondary phases as Ba5Nb4O15 and Ba8(Co, Zn) 1Nb6O24 on the surface of the ceramics. All of the sintered and annealed ceramics exhibit a high quality factor QF close to 110 000 GHz at 6 GHz. The high dielectric constant εr of ~34.5 and a temperature coefficient of the resonant frequency τf of ~0 ppm.C-1 were obtained in all annealed ceramics.

1. Introduction

In particular, Ba (Co0.7Zn0.3) 1/3Nb2/3O3 (BCZN) is one of the main compounds studied nowadays as a ceramic resonator in microwave applications and as a cheap alternative to Ta-based complex perovskite ceramics such as BaZn1/3Ta2/3O3 (BZT), which have a great commercial success [1]. In Ba (Co0.7Zn0.3)1/3Nb2/3O3, barium as the larger cation occupies the A-sites, while Co, Zn, and Nb are found on B-sites. Ba (Co0.7Zn0.3)1/3Nb2/3O3 shows a typical Ba (B'1/3B''2/3)O3 perovskite structure where B' is a mixture of Co and Zn atoms and B'' is a Nb atom. The structure is characterised by a 1:2 arrangement of Co, Zn (B'), and Nb (B'') atomic columns [2]. This 1: 2 cation ordering, which is obtained only by heat treatments at high temperatures, has been shown to be the essential property responsible for the interesting electric properties of this material [3], such as a high quality factor QF (low dielectric loss), a high dielectric constant εr= 34.5, and a near zero temperature coefficient of the resonant frequency τf [4, 5]. In particular, the QF-factor value is strongly affected by the degree of cation ordering. Recently, it has been reported that the disordered BCZN ceramic has a low value of QF (12 000 to 36 000 GHz at 6 GHz), whereas the ordered BCZN ceramic exhibits a higher QF value up to 123 700 GHz [2, 6]. In dense BCZN ceramic materials, this kind of ordering is difficult to accomplish without the use of additional procedures such as adding impurities [7–9] or the use of a second thermal treatment as an annealing process [2, 3, 6]. In the case of BCZN, an ordered structure was obtained by an annealing process at 1300°C for 12 h [6]. In our previous work [3, 6], we proved that the improvement of the quality factor QF of such ceramic materials is related to the 1:2 cation ordering in the BCZN crystal that occurs during the annealing process. By adding an annealing step as a second thermal treatment following the initial sintering step, we obtained BCZN materials with excellent dielectric properties (εr= 34.5, QF= 123 700 GHz, and τf= 0 ppm/°C). However, the total time required to obtain this result was quite long, 16.25 hours for the sintering step plus 30 hours for the annealing process [6]. As a continuation of our previous work, the present paper describes a novel approach to the sintering of BCZN ceramics by using the rapid-rate sintering (RRS) technique. The comparisons between the present and previous works [3, 6] have been explored to highlight the advantages of the RRS-technique compared to sintering and postsintered annealing of BCZN ceramics. This technique has been largely employed for the synthesis of ceramic materials in order to improve their densification and to avoid undesired grain growth [10–14]. However, the use of the RRS-technique has not yet been reported in the literature for the synthesis of BCZN ceramics. Kim et al. [14] believe that the use of the RRS-technique for sintering indium tin oxide (ITO) could be beneficial to prevent evaporation of ITO material. In the case of BCZN ceramics, it could be expected that the RRS concept allows to obtain dense BCZN materials and to avoid simultaneously the evaporation of cobalt and zinc atoms during the sintering process, preventing in this way the formation of secondary surface phases such as Ba5Nb4O15 and Ba8 (Co, Zn) 1Nb6O24 as they were observed in our previous study [6].

The aim of the present work was thus to produce dense BCZN ceramic materials in a shorter time by simultaneously limiting the formation of undesired surface phases.

2. Experimental Section

The Ba (Co0.7Zn0.3) 1/3Nb2/3O3 (BCZN) ceramics were prepared using the aqueous mixing technique-assisted solid-state method as described previously [3]. Oxides (Co_3O_4, Nb_2O_5, and ZnO) and carbonate precursors (BaCO3) with high purity (≥99%) are used as the raw material. The dried powders were calcined in the air at 1000°C for 2 h in an electric furnace. The BCZN powders were formed into cylindrical pellets of about 10 mm in diameter and 5 mm height by uniaxial pressing with a pressure of 200 MPa. The rapid-rate sintering technique was achieved by placing the pellets in an alumina boat, which was then introduced into a tubular furnace by using a horizontal alumina push rod which moved the sample from the cold to the hot zone of the furnace at a constant speed. An alumina tube with an inside diameter of 6 cm and a length of 150 cm is used. The homogeneous heating zone is 15 cm. The sintering treatment was carried out in an atmosphere of air. The insertion and extraction speed as well as the sintering temperature were controlled by an automated system. The sintering temperature was fixed at 1450°C under air. The insertion/extraction times ranged between 5 and 100 minutes (100 minutes is equivalent to a heating or cooling rate equal to 858°C h^{-1}), and the holding time ranged between 0 and 60 minutes. The illustrative scheme of the RRS equipment is shown in Figure 1. Five samples were sintered under different thermal conditions. These ceramics are called x1s, x2s, x3s, x4s, and x5s. They were then annealed at 1300°C for 30 h in air which gave respectively the so-called samples x1a, x2a, x3a, x4a, and x5a. (The "s" and "a" letters correspond respectively to sintered and annealed samples). The sintering parameters are presented in Table 1. The heating and cooling rates of the annealing process were 200°C h^{-1}. A Siemens D5005 X-ray diffractometer using CuKα radiation (λ = 1.540562 Å) was used to identify surface and bulk crystalline phases in the sintered and annealed ceramics. Diffractograms were recorded in the continuous mode for 2θ angles ranging from 15 to 60°. The X'pert High Score program was used for phase matching. A microstructural observation of the ceramics was performed with a scanning electron microscope (SEM, Hitachi S3400) combined with an energy dispersive spectrometer (EDS, ThermoNoran). The SEM micrographs were collected on the polished and unpolished surfaces. In this context, surfaces of the ceramics were polished successively using various grades of silicon carbide papers, and 1.0 μm diamond paste was used for the final polishing. The polished pellets were treated thermally at 1100°C for 20 minutes to reveal grain boundaries. In addition, the experimental densities of the unpolished sintered pellets were measured with a Micromiritics AccuPyc 1330 helium pycnometer and compared to the geometrical densities of the corresponding samples. The open porosity was derived from the relation between the skeleton and the geometrical densities. The results of BCZN ceramic densities are gathered in Table 2. Finally, the dielectric properties were measured at 6 GHz resonance frequency on the unpolished sintered pellet using an Agilent 8722ES vector network analyzer, and the results are gathered in Table 3.

3. Results and Discussion

3.1. Structural and Microstructural Observations. Figures 2(a) and 2(b) show X-ray diffraction patterns recorded on the surface of the Ba (Co0.7Zn0.3) 1/3Nb2/3O3 (BCZN) ceramics after sintering at 1450°C (samples x1s to x5s) and after annealing at 1300°C for 30 h (samples x1a to x5a). All diffraction peaks of the sintered BCZN ceramics (Figure 2(a)) can be indexed using the structure of BaZn1/3Nb2/3O3 ceramics (JCPDS card No. 39–1474), a cubic perovskite structure with space group Pm3m, indicating that the cosubstitution for Zn atoms does not affect the structure with just a very slight diminution of the cubic cell volume. Only some tiny peaks have not been identified. This result suggests that the as-prepared specimens are not affected by the thermal cycle used for the sintering step (RRS technique). Thus, the rapid-rate sintering technique permits to produce pure BCZN ceramics by avoiding the formation of secondary phases such as Ba5Nb4O15 and Ba8 (Co, Zn) 1Nb6O24 on the surface of the BCZN specimens as they were observed in our previous work [3, 6] after sintering at 1450°C with slower heating/cooling rates (200°C h^{-1}) and a longer dwell time (2 hours). The XRD pattern of the BCZN annealed ceramics at 1300°C for 30 h in air are presented in Figure 2(b). The annealing process leads for all samples (x1a to x5a) to a mixture of three phases Ba (Co0.7Zn0.3)1/3Nb2/3O3 (BaZn1/3Nb1/6O3; JCPDS card No. 39–1474), Ba5Nb4O15 (JCPDS file 14–0028), and Ba8 (Co, Zn) 1Nb6O24 (JCPDS card 89–0693 which is the File N°. Of Ba8Ta6NiO24). The structure of Ba8Ta6NiO24 is used for indexing the Ba8 (Co, Zn) 1Nb6O24 peaks due to

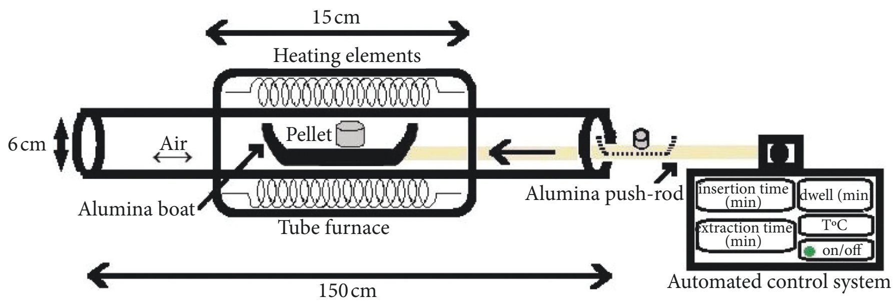

Figure 1: Schematic illustration of the rapid-rate sintering equipment.

Table 1: Sintering and annealing parameters of BCZN ceramics. Larger grain sizes are extracted from bulk samples (Figures 5(a) and 5(b)).

Sample	Sintering parameters at 1450°C					Sample	Heating parameters at 1300°C			
	Insertion time (min)	Dwell time (min)	Extraction time (min)	Sintering process time (min)	Larger grain size (μm)		Heating rate (°C/h)	Dwell time (h)	Cooling rate (°C/h)	Larger grain size (μm)
x1s	5	0	5	10	~2	x1a	200	30	200	~2
x2s	5	10	5	20	~4	x2a				~5
x3s	10	10	10	30	~5	x3a				~6
x4s	100	30	100	230	~7	x4a				~9
x5s	100	60	100	260	~10	x5a				~10

Table 2: Characteristic properties of annealed BCZN ceramics.

Sample	Sintering parameters at 1450°C	Density (g/cm3)		Porosity (%)			Shrinkage Δl/l (%)
	Insertion-dwell-extraction times (min)	Geometrical	Skeleton	Total	Closed	Open	
x1a	5-0-5	6.29	6.37	3.23	2	1.23	15.92
x2a	5-10-5	6.23	6.29	4.15	3.23	0.92	16.41
x3a	10-10-10	6.21	6.3	4.46	3.08	1.38	16.55
x4a	100-30-100	6.22	6.33	4.31	2.62	1.69	16.43
x5a	100-60-100	6.22	6.32	4.31	2.77	1.54	16.62

Table 3: Dielectric properties (measured at 6 GHz) of sintered and annealed BCZN ceramics.

Sintering parameters at 1450°C Insertion-dwell-extraction times (min)	Sintered sample	QF (GHz) After sintering (1450°C)	Annealed sample	QF (GHz) After annealing (1300°C-30 h)
5-0-5	x1s	31 830	x1a	88653
5-10-5	x2s	40 699	x2a	112 598
10-10-10	x3s	40 888	x3a	109 594
100-30-100	x4s	48 003	x4a	107 964
100-60-100	x5s	52 799	x5a	107 491

isostructurality of these two compositions [15]. The intense peak at 2θ= 37.93° shows that the Ba8 (Co, Zn) 1Nb6O24 phase is majority on the BCZN surface ceramics. This result is in accordance with the previous works [7].

Figures 3(a) and 3(b) show X-ray diffraction patterns of the bulk of Ba (Co0.7Zn0.3) 1/3Nb2/3O3 (BCZN) ceramics after rapid-rate sintering at 1450°C with different thermal cycles (samples x1s to x5s) and after annealing at 1300°C for 30 h (samples x1a to x5a). As shown in Figures 3(a) and 3(b), all peaks can be indexed to the cubic structure of Ba(Co0.7Zn0.3)1/3Nb2/3O3 (BaZn1/3Nb1/6O3; JCPDS card No. 39-1474) together with the unidentified peak at 2 = 20° (particularly for x4a sample). Furthermore, for both thermal processes, namely, sintering (RRS technique) or annealing, it was noted that the secondary phases Ba5Nb4O15 and Ba8 (Co, Zn) 1Nb6O24 are not detected in the bulk materials. Ba5Nb4O15 and Ba8 (Co, Zn) 1Nb6O24 secondary phases are thus only present on the surface of the BCZN annealed ceramics. As stated in ref [16], the presence of Ba5Nb4O15 and Ba8 (Co, Zn) 1Nb6O24 phases on the BCZN surface ceramics during the annealing process was mainly due to a deficiency of some zinc and cobalt, which can be attributed to volatilization occurring during the long time the ceramics stayed at high temperature.

Figures 4(a) and 4(b) show the SEM micrographs of the surfaces of the BCZN ceramics after the RRS technique at 1450°C (samples x1s to x5s) and after the annealing process

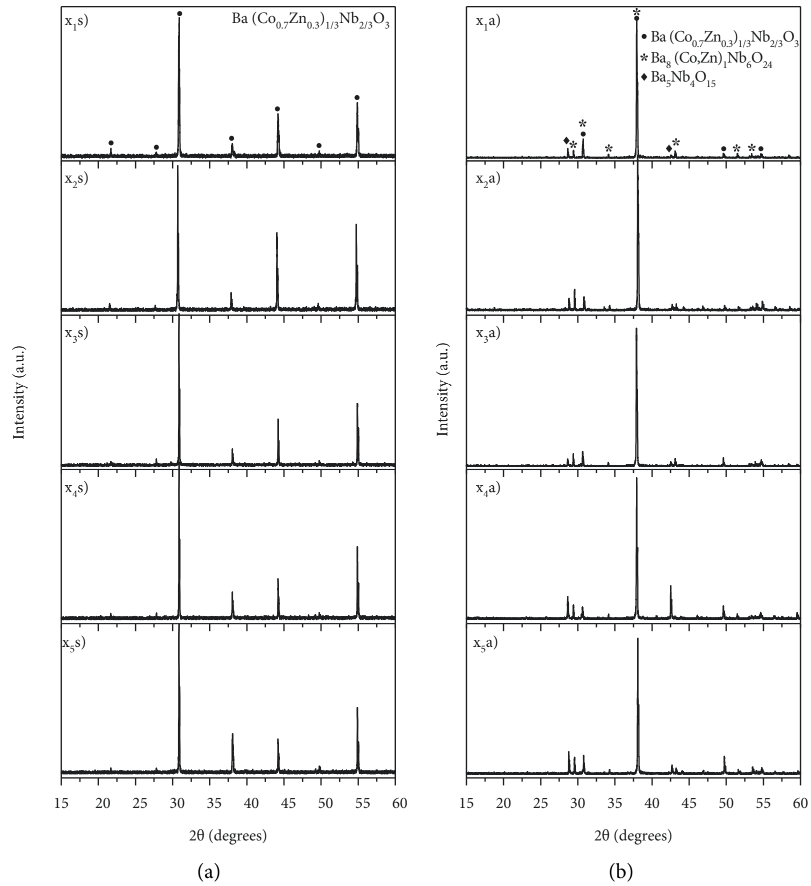

Figure 2: X-ray diffraction pattern taken from the surface of BCZN ceramics: (a) BCZN sintered ceramics recorded for different thermal cycles and (b) BCZN annealed ceramics at 1300°C for 30 (h) •: Ba (Co0.7Zn0.3) 1/3Nb2/3O3, *: Ba8 (Co, Zn) 1Nb6O24, and ◆: Ba5Nb4O15.

at 1300°C (samples x1a to x5a). The RRS-ceramics surfaces are formed of round shaped grains (Figure 4(a)). The grains size increase with the global sintering time (the samples from x1s to x5s are arranged in ascending order of dwell time at 1450°C as is reported in Table 1). On the other hand, we can also note that the larger grains of about 7 μm are observed in x5s-ceramic which corresponds to the insertion/extraction times of 100/100 minutes and a longer holding time of 60 min during the sintering process. Furthermore, the x1s-sample with zero dwell time and insertion/extraction times of 5/5 minutes exhibits the smallest values of the grain size (~1 μm).

The surface microstructures of BCZN ceramics annealed at 1300°C for 30 h are shown in Figure 4(b). The annealing process highlights the development of the secondary phases on the surface of the BCZN specimens with needle-shaped grains. This result is in accordance with that obtained from XRD analysis (see Figure 2(b)). The atomic percentages derived from the EDS spectra (not shown here) clearly revealed that the round particles consist of Ba (Co0.7Zn0.3) 1/3Nb2/3O3 composition, and the needle-shaped grains consist of the Ba8(Co, Zn) 1Nb6O24 phase, in good agreement with the XRD analyses (Figures 2(a) and 2(b)). These results are also in agreement with the literature [3, 7]. Figures 5(a) and 5(b) show the SEM images of the bulk BCZN ceramics after the RRS process at 1450°C (samples x1s to x5s) and after annealing process at 1300°C for 30 h (samples x1a to x5a). The SEM micrographs of BCZN bulk ceramics were taken from a depth of about 120 μm. The microstructure morphology observed for BCZN bulk sintered ceramics (Figure 5(a)) is similar with a round particle morphology observed of BCZN surface sintered ceramics (Figure 4(a)). However, increasing grain sizes were observed with the increasing sintering time process, with a larger typical grain size of 3–10 microns that has been observed in the x5s-sample (Figure 5(a)). This result is in accordance with the SEM analysis obtained on the sintered surface of BCZN specimens (Figure 4(a)). From Figure 5(b), it can be seen that the annealing process leads to similar morphologies as those observed for not annealed ceramics. These results are also in agreement with the XRD analyses (Figure 3(b)). On the basis of these experiments, we conclude that the annealing step at 1300°C for 30 h has a little effect on the grain growth (see Table 1). In contrast, secondary phase formation is developed. Table 2 shows the structural properties of the final annealed BCZN ceramics. The total porosity was calculated by the difference between the geometrical and the theoretical densities of the BCN phase (ρ (BaCo1/3Nb2/3O3)= 6.5 g/cm3, JCPDS card No. 46–0997). The closed porosity was calculated from the

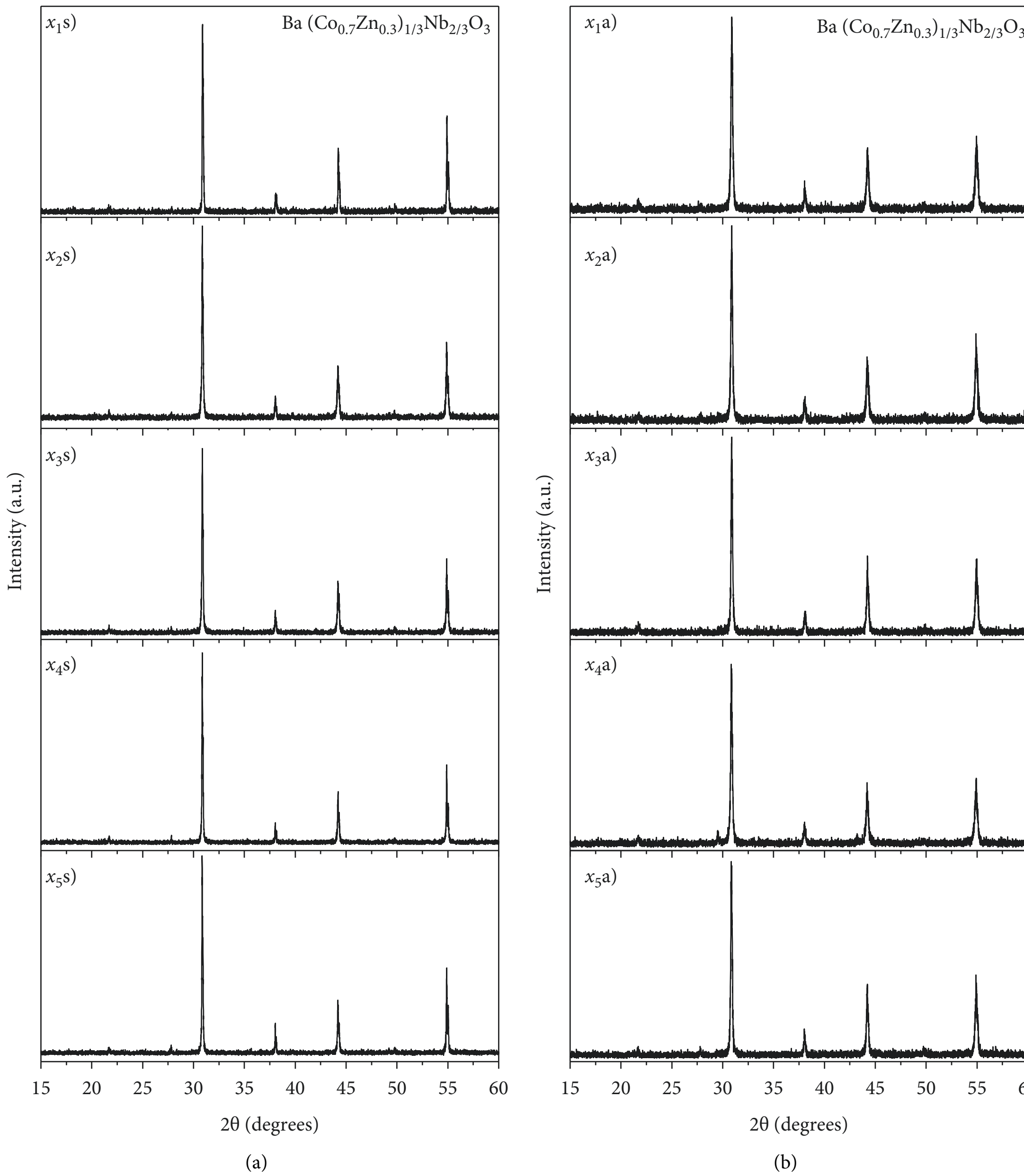

Figure 3: X-ray diffraction pattern for bulk BCZN ceramics: (a) BCZN sintered ceramics recorded for different thermal cycles and (b) BCZN annealed ceramics at 1300°C for 30 h.

skeleton (He pycnometry) and theoretical density, and these latter porosities (total and closed) are used to calculate the open porosity. The linear shrinkage was calculated by using the ΔL/L0 ratio (where ΔL is the change in length of the annealed ceramic, and L0 is the initial length of the specimen). As shown in Table 2, regardless of the heat thermal process, all samples have a large relative density (skeletal) of about 6.3 g/cm3, that is, >96% of the theoretical density (T. D.) (see Figure 6). Therefore, all specimens exhibit low total porosity ranging from 3 to 4.5%. The closed porosity was in the range 2–3%, and the open porosity was about 1%. This lower porosity can be explained by the high density of the BCZN ceramic that is very near to theoretical density. Higher values of shrinkage of about 16% are observed for all the annealed ceramics. This is in good agreement with the skeletal density which is ~6.3 g/cm3.

3.2. Microwave Dielectric Properties. The microwave dielectric properties measured at about 6 GHz of the Ba (Co0.7Zn0.3)1/3Nb2/3O3 (BCZN) ceramics were investigated for all specimens after the RRS technique under air at 1450°C for different thermal cycles and after annealing process at 1300°C for 30 hours in the air. Figure 6 shows the relative density and quality factor (QF) as a function of sintering process time for BCZN ceramics. The results of the dielectric characteristic measurements of the annealed Ba (Co0.7Zn0.3) 1/3Nb2/3O3 specimens are summarized

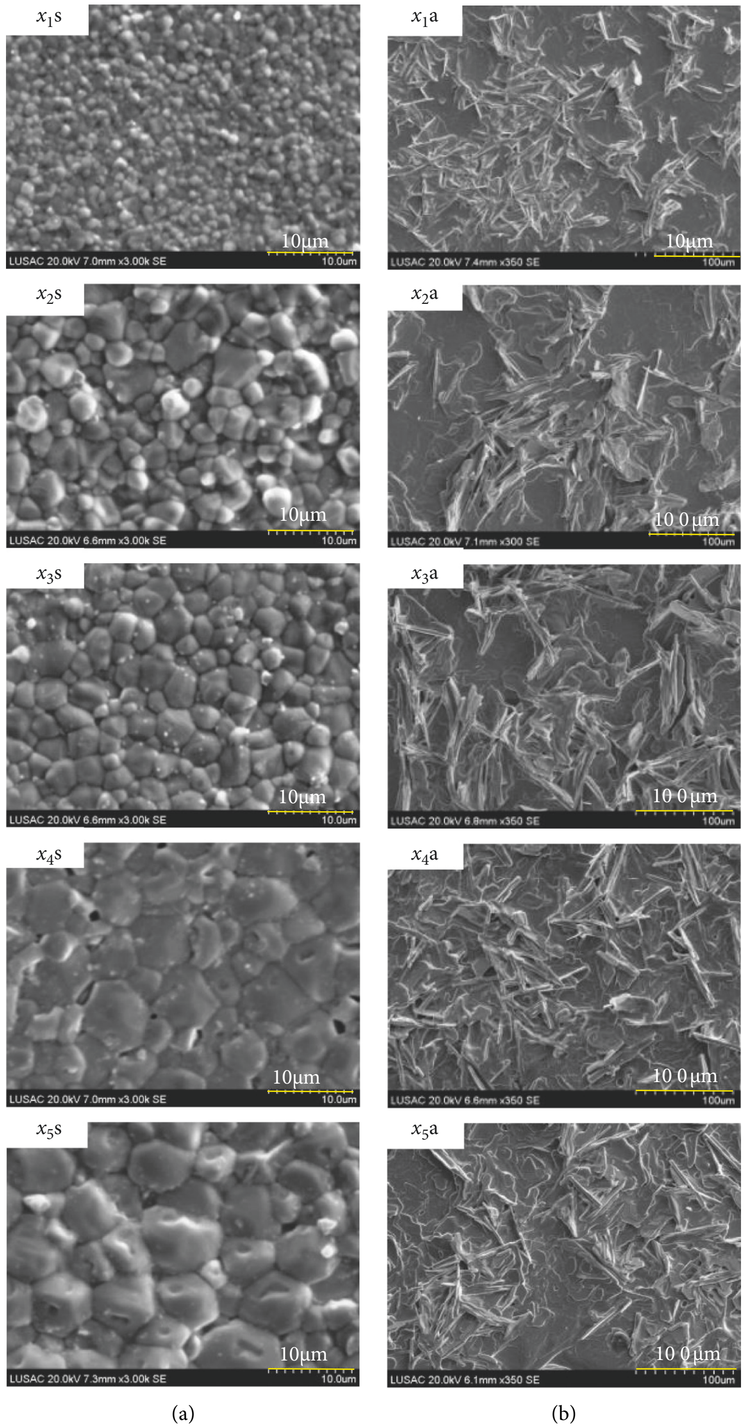

Figure 4: SEM images of the surface of BCZN ceramics. (a) On the surface after sintering. (b) On the surface after annealing.

Table 3. It is interesting to remark on Table 3 that regardless of thermal cycle conditions used of the RRS technique, the sintered BCZN ceramics exhibit low values of QF. The QF values measured in the present work increase with the sintering process time, from 31 830 (x1s-sample) to 52 799 GHz (x5s-sample) together with the increase of the grain size of ceramics (see Figure 4(a)). It should be noted that the presence of these secondary phases on the specimen surface (BCZN) seems to have no effect on the dielectric properties [3]. This is due to good microwave dielectric properties of the Ba5Nb4O15 and Ba8 (Co, Zn) 1Nb6O24 phases [15, 17, 18]. Vanderah et al. reported that the Ba5Nb4O15 is a cation-deficient perovskite and that the general formula can be written as follows: AnBn-1O3n [19]. Densified Ba5Nb4O15 ceramics exhibit the good microwave dielectric properties of εr= 39.2, QF= 27 200 GHz, and τf= 72 ppm C^{-1} [18]. On the other hand, Solomon et al. reported that Ba8ZnNb6O24 has a quality factor (QF) equal to 10 890 GHz

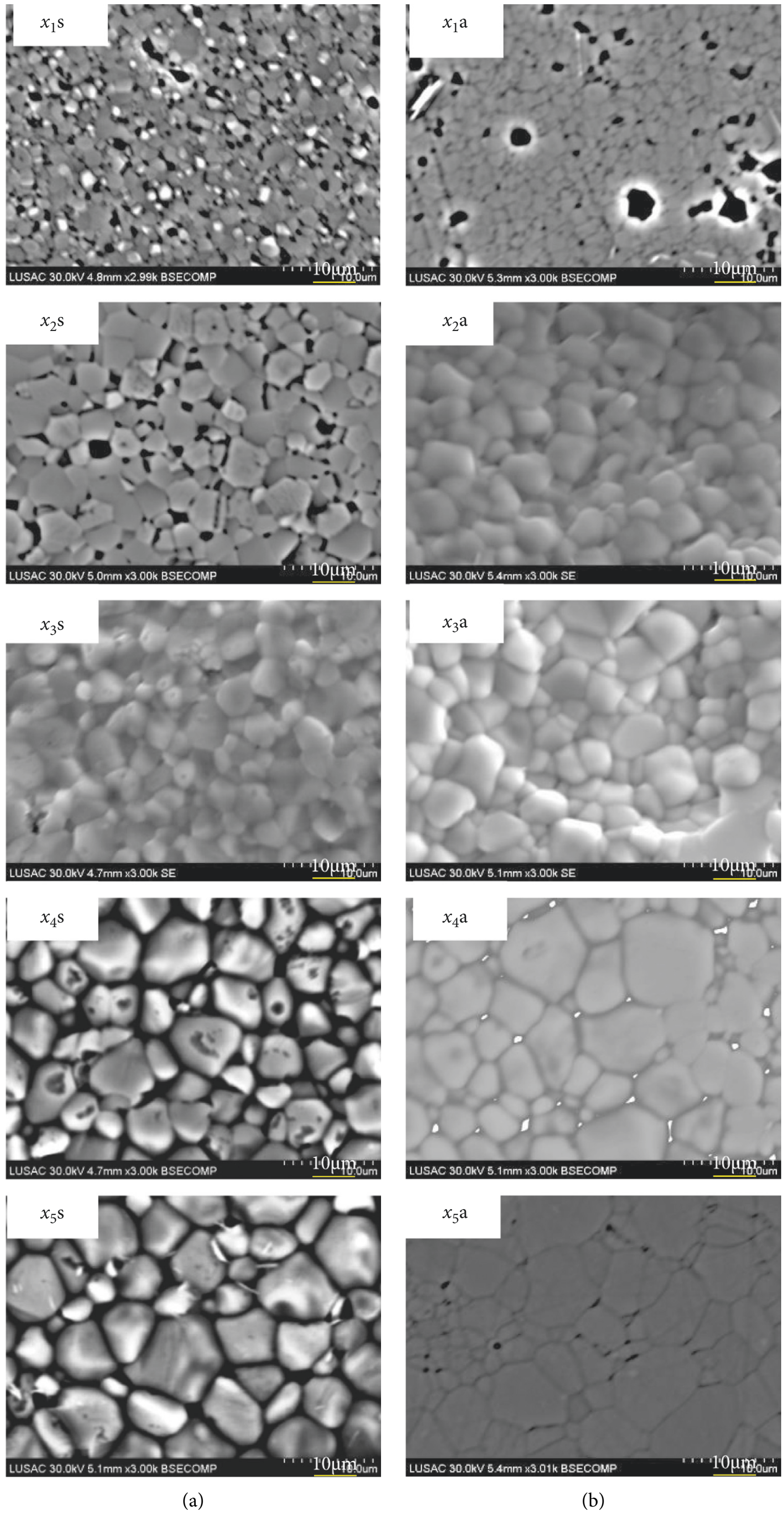

Figure 5: SEM images of BCZN bulk ceramics. (a) BCZN sintered ceramics for different thermal cycles and (b) BCZN annealed ceramics at 1300°C for 30 h.

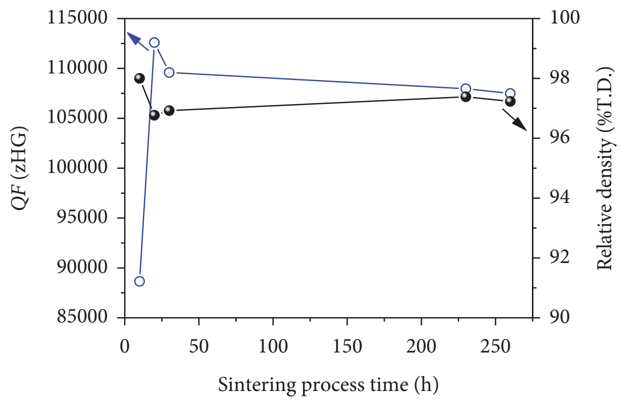

Figure 6: The relative density and QF of BCZN ceramics versus the thermal process time. T.D.: theoretical density.

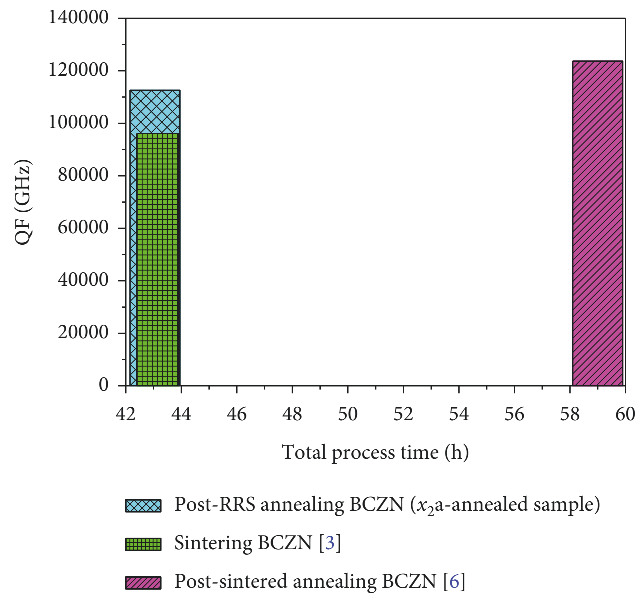

Figure 7: QF values of BCZN ceramics versus the thermal process time for three processes (post-RRS annealing, sintering, and postsintered annealing).

at 3.96 GHz, a relative dielectric constant εr= 36.26, and a temperature coefficient of resonant frequency τf= 49.9 ppm C^{-1} [15]. The thermal annealing process greatly improves the QF values: high QF values close to 110 000 GHz were obtained for all annealed ceramics, except for the x1a-sample which shows a value of 88 653 GHz. On the other hand, if we consider the total treatment time including the RRS technique and annealing process times, the QF values measured in annealed pellets increase significantly with total time to reach a maximum (x2a-sample) followed by stabilization of the QF values (see Figure 6). Furthermore, as shown in Table 3, the maximum QF value of 112 598 GHz is observed of the x2a-annealed sample. As a matter of fact, we have already shown that the improvement of the annealing QFs are due to the degree of 1: 2 cation ordering within the BCZN crystal, which is taking place during the annealing process [6]. The high dielectric constant εr of ~34.5 and a temperature coefficient of the resonant frequency τf of ~0 ppm C^{-1} were obtained in all annealed ceramics. It is important to note that the sintered and annealed pellets exhibit the same values of εr and τf. From these results in this study, it can be concluded that the effect of the grain size and porosity may be small in the improvement of QFs of BCZN ceramics. Moreover, it is noticeable that the 1: 2 cation ordering into the BCZN perovskite structure plays a key role in improving the factor quality.

In order to highlight the advantages of the RRS technique, a comparison between QF values of the RRS sample with those obtained by other processes (given in references [3, 6]) is carried out. The QF values of BCZN ceramics obtained by the RRS technique, sintering, and postsintered annealing are plotted in Figure 7. It is interesting to remark on Figure 7 that the high QF-value of 112 598 GHz is observed of the post-RRS annealed BCZN sample (x2a-annealed sample) corresponding to 43h05 of total process time. Moreover, the postsintered annealing process exhibits the highest QF value (123 700 GHz [6]) for which a longer processing time is required (59h00). The sintering process with a total time of 43h15 permit to have a QF of 96 132. This comparison shows a compromise to be kept between a high QF and a shorter processing time.

4. Conclusion

The influence of the heat treatment by using the RRS technique on the structural and microstructural characteristics of the Ba (Co0.7Zn0.3) 1/3Nb2/3O3 ceramics was investigated by combining XRD and SEM analyses. The relationship between structural/microstructural characteristics and microwave dielectric proprieties of BCZN ceramics was explored. Dense dielectric BCZN ceramic materials can be achieved in a shorter sintering time by using the RRS technique. Thus, the rapid-rate sintering technique permits to produce pure BCZN ceramic materials on both the surface and in bulk by avoiding the secondary phase formation on the BCZN ceramic surface. Ba5Nb4O15 and Ba8 (Co, Zn) 1Nb6O24 are secondary surface phases, and it was detected only when the BCZN sample was annealed at 1300°C for 30 hours, which is different in the case of conventional sintering treatment. The Ba (Co0.7Zn0.3) 1/3Nb2/3O3 ceramics exhibit the morphologies of round shaped grains, and the Ba8 (Co, Zn) 1Nb6O24 phase highlights needle-shaped grains.

The microwave dielectric properties are not affected by the rapid-rate sintering process (RRS); however, they depend sensitively by the second heat treatment (annealing process). The high QF value of 112 101 GHz was observed for the BCZN sample sintered at 1450°C under air with rapid-rate sintering (insertion/extraction times of 5/5 minutes) and with a short holding time of 10 min followed by a longer annealing process time at 1300°C for 30 h in the air.

Finally, and in comparison to the conventional sintering processing, large time savings of 16.25 hours were recorded by using the RRS technique to have cleaner BCZN ceramic materials with the same high microwave dielectric properties (εr= 34.5, QF= 112 598 GHz, and τf= 0 ppm C^{-1}).

Data Availability

The figures, images, tables, and text data used to support the findings of this study are available from the corresponding author upon request.

Conflicts of Interest

The authors declare that they have no conflicts of interest.

Acknowledgments

This work was supported by the French National Research Agency (ANR) [cheap components].

References

[1] R. I. Scott, M. Thomas, and C. Hampson, "Development of low cost, high performance Ba(Zn1/3Nb2/3O3) based materials for microwave resonator applications," *Journal of the European Ceramic Society*, vol. 23, no. 14, pp. 2467–2471, 2003.

[2] F. Azough, R. Freer, D. Iddles, T. Shimada, and B. Schaffer, "The effect of cation ordering and domain boundaries on low loss Ba(BI1/3BII2/3)O3 perovskite dielectrics revealed by high-angle annulardark-field scanning transmission electron microscopy (HAADF STEM)," *Journal of the European Ceramic Society*, vol. 34, no. 10, pp. 2285–2297, 2014.

[3] B. Itaalit, M. Mouyane, J. Bernard, J.-M. Reboul, and D. Houivet, "Improvement of microwave dielectric properties of Ba(Co0.7Zn0.3)1/3Nb2/3O3 ceramics prepared by solid-state reaction," *Ceramics International*, vol. 14, pp. 1937–1942, 2015.

[4] K. Endo, K. Fujimoto, and K. Murakawa, "Dielectric properties of ceramics in Ba (Co1/3 Nb2/3)O3-Ba(Zn1/3Nb2/3)O3 solid solution," *Journal of the American Ceramic Society*, vol. 70, no. 9, pp. C-215–C-218, 1987, C-215-C-218.

[5] C.-W. Ahn, H.-J. Jang, S. Nahm, H.-M. Park, and H.-J. Lee, "Effects of microstructure on the microwave dielectric properties of Ba(Co1/3Nb2/3)O3 and (1−x)Ba(Co1/3Nb2/3)O3−xBa(Zn1/3Nb2/3)O3 ceramics," *Journal of the European Ceramic Society*, vol. 23, no. 14, pp. 2473–2478, 2003.

[6] B. Itaalit, M. Mouyane, J. Bernard, M. Womes, and D. Houivet, "Effect of post-annealing on the microstructure and microwave dielectric properties of Ba(Co0.7Zn0.3)1/3Nb2/3O3 ceramics," *Applied Sciences*, vol. 6, no. 1, p. 2, 2015.

[7] F. Azough, C. Leach, and R. Freer, "Effect of CeO2 on the sintering behaviour, cation order and properties of Ba3Co0.7Zn0.3Nb2O9 ceramics," *Journal of the European Ceramic Society*, vol. 26, no. 10-11, pp. 1883–1887, 2006.

[8] A. Mergen and E. Korkmaz, "Effect of In, Ce and Bi dopings on sintering and dielectric properties of Ba(Zn1/3Nb2/3)O3 ceramics," *Journal of the European Ceramic Society*, vol. 31, no. 14, pp. 2649–2655, 2011.

[9] Y. Zhang, X. Zhou, X. Yang, C. Sun, F. Yang, and H. Chen, "Effects of Y2O3/CeO2 co-doping on microwave dielectric properties of Ba(Co0.6Zn38)1/3Nb2/3O3 ceramics," *Journal of Alloys and Compounds*, vol. 679, pp. 247–253, 2016.

[10] C. Genuist and F. M. Haussonne, "Sintering of BaTiO3: dilatometric analysis of diffusion models and microstructure control," *Ceramics International*, vol. 14, no. 3, pp. 169–179, 1988.

[11] A. Morell and A. Hermosin, "Fast sintering of soft Mn-Zn and Ni-Zn ferrite pot cores," *American Ceramic Society Bulletin*, vol. 59, no. 6, pp. 626–629, 1980.

[12] A. Morell, "Magnetic properties and microstructure of coprecipitated Ni-Zn ferrites sintered by hot-pressing, conventional and fast-firing," *Journal of Magnetism and Magnetic Materials*, vol. 31-34, pp. 997-998, 1983.

[13] J. Wang, K. Ning, J. Zhang et al., "Rapid rate sintering of yttria transparent ceramics," *Journal of the American Ceramic Society*, vol. 99, no. 6, pp. 1935–1942, 2016.

[14] J. H. Lee, B.-C. Kim, J. J. Kim, T. Ikegami, and T. Ikegami, "Rapid rate sintering of nanocrystalline indium tin oxide ceramics: particle size effect," *Materials Letters*, vol. 52, no. 1-2, pp. 114–119, 2002.

[15] S. Solomon, M. K. Suresh, J. K. Thomas, V. S. Prasad, and P. Wariar, "Synthesis, structural analysis and dielectric properties of Ba8(Mg1-xZnx)Nb6O24 hexagonal perovskites," *Ceramics International*, vol. 38, no. 8, pp. 6487–6494, 2012.

[16] F. Azough, C. Leach, and R. Freer, "Effect of nonstoichiometry on the structure and microwave dielectric properties of Ba(Co1/3Nb2/3)O3 ceramics," *Journal of the European Ceramic Society*, vol. 26, no. 14, pp. 2877–2884, 2006.

[17] J. R. Kim, D. W. Kim, H. S. Jung, and K. S. Hong, "Low-temperature sintering and microwave dielectric properties of Ba5Nb4O15 with ZnB2O4 glass," *Journal of the European Ceramic Society*, vol. 26, no. 10-11, pp. 2105–2109, 2006.

[18] H. Zhou, X. Chen, L. Fang, C. Hu, and H. Wang, "Microwave dielectric properties of Ba5Nb4O15 ceramic by molten salt method," *Journal of Materials Science: Materials in Electronics*, vol. 21, no. 9, pp. 939–942, 2010.

[19] T. A. Vanderah, R. S. Roth, T. Siegrist, W. Febo, J. M. Loezos, and W. Wong-Ng, "Subsolidus phase equilibria and crystal chemistry in the system BaO-TiO2-Ta2O5," *Solid State Sciences*, vol. 5, no. 1, pp. 149–164, 2003.

Hindawi
Advances in Materials Science and Engineering
Volume 2023, Article ID 9847204, 1 page
https://doi.org/10.1155/2023/9847204

Retraction

Retracted: Interfacial Transport Study of Ultra-Thin InN-Enhanced Quantum Dot Solar Cells

Advances in Materials Science and Engineering

Received 26 September 2023; Accepted 26 September 2023; Published 27 September 2023

This article has been retracted by Hindawi following an investigation undertaken by the publisher [1]. This investigation has uncovered evidence of one or more of the following indicators of systematic manipulation of the publication process:

(1) Discrepancies in scope
(2) Discrepancies in the description of the research reported
(3) Discrepancies between the availability of data and the research described
(4) Inappropriate citations
(5) Incoherent, meaningless and/or irrelevant content included in the article
(6) Peer-review manipulation

The presence of these indicators undermines our confidence in the integrity of the article's content and we cannot, therefore, vouch for its reliability. Please note that this notice is intended solely to alert readers that the content of this article is unreliable. We have not investigated whether authors were aware of or involved in the systematic manipulation of the publication process.

Wiley and Hindawi regrets that the usual quality checks did not identify these issues before publication and have since put additional measures in place to safeguard research integrity.

We wish to credit our own Research Integrity and Research Publishing teams and anonymous and named external researchers and research integrity experts for contributing to this investigation.

The corresponding author, as the representative of all authors, has been given the opportunity to register their agreement or disagreement to this retraction. We have kept a record of any response received.

References

[1] S. Wang, D. Zhang, and Z. Ju, "Interfacial Transport Study of Ultra-Thin InN-Enhanced Quantum Dot Solar Cells," *Advances in Materials Science and Engineering*, vol. 2022, Article ID 5862204, 10 pages, 2022.

Hindawi
Advances in Materials Science and Engineering
Volume 2022, Article ID 5862204, 10 pages
https://doi.org/10.1155/2022/5862204

Research Article

Interfacial Transport Study of Ultra-Thin InN-Enhanced Quantum Dot Solar Cells

Shuaijie Wang, Dong Zhang, and Zhenhe Ju

School of Renewable Energy, Shenyang Institute of Engineering, Shenyang 110136, China

Correspondence should be addressed to Shuaijie Wang; d11402027@mail.dlut.edu.cn

Received 11 May 2022; Accepted 13 June 2022; Published 7 July 2022

Academic Editor: Ravi Samikannu

For human society, all activities require energy support. Solar cells are a means of converting solar energy into electrical energy using the photovoltaic effect of semiconductor materials. This photoelectric absorber layer has been developed for more than 70 years. Currently, the layered solar panel industry has achieved an energy conversion efficiency of 47%. In addition to efficiency, the cost of solar cells has been optimized, and the cost of commercial silicon solar cells has been greatly reduced. There is an urgent need for energy transfer research through the solar cell interface. Many researchers are studying and discovering new elements in this field. On this basis, the transmission ion interface of ultra-thin in-amplified quantum solar cell panels was studied, and very effective conclusions were drawn on the basis of experimental preparation and analysis.

1. Introduction

Energy is the basis of all activities, the guarantee for the smooth functioning of the physical world, and the backbone force that supports the development of human society. For human society, all activities require the support of energy [1]. In the period of fuel wood energy, people's demand and use of energy were relatively limited, mainly using wood, grass, and other energy sources to boil water and cook [2]. During the fossil energy period, people used coal, oil, natural gas, etc., to power the development of society.

To this day, fossil energy continues to provide us with energy as a major part of the human energy mix. Figure 1 shows the findings on the share of all forms of energy in total energy consumption at the global scale in 2017, which shows that fossil energy accounts for 79.7% of the current global energy supply [3].

Fossil energy has supported the human society through the first and second industrial revolutions and has made an indelible contribution to the development of human society. As society's demand for energy has gradually increased, the use of fossil energy has also increased [4]. However, since the formation of fossil energy requires a long process, the total amount of fossil energy is basically not increasing, which leads to the gradual decrease of fossil energy available to human beings and the imminent crisis of running out of fossil energy. According to the world energy statistical yearbook, even coal, the largest remaining resource, will be depleted in 132 years according to the current usage, while oil and natural gas can only support human use for another 50 years, as shown in Figure 2 [5]. Without energy, the development of human society will come to a halt or even regress back to the slash-and-burn period. Therefore, for the continuity of human development, new energy sources that can replace fossil energy sources need to be developed urgently.

After a long period of unremitting efforts, a series of new energy have been developed and utilized by people. Compared with fossil energy, these new forms of energy have significant advantages in terms of environmental friendliness and sustainable utilization. Solar energy is the energy radiated to the outside world by the sun through thermonuclear fusion, which has the characteristics of large total energy, long availability, uniform distribution, and no pollution, and is an extremely ideal energy source.

But this economy is an economy based on fossil energy sources, and once fossil energy sources face depletion, the

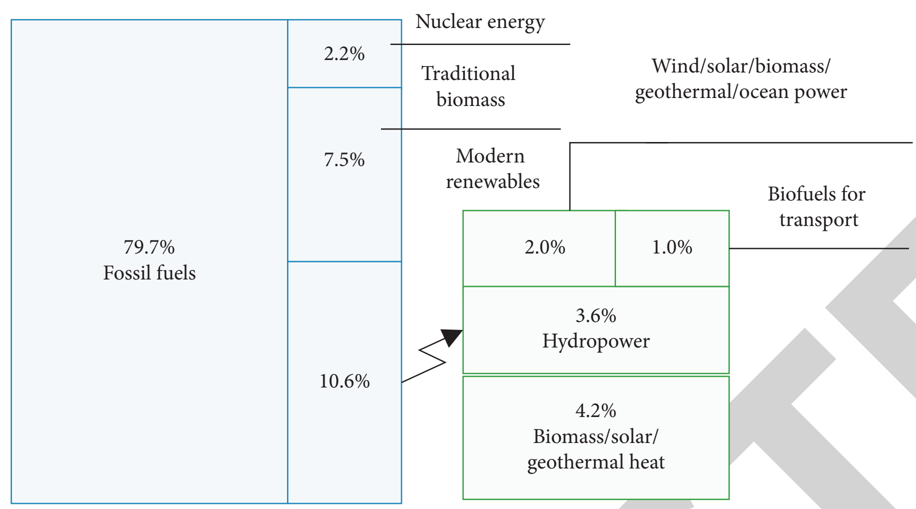

Figure 1: Share of various forms of energy in total energy consumption at the global scale in 2017.

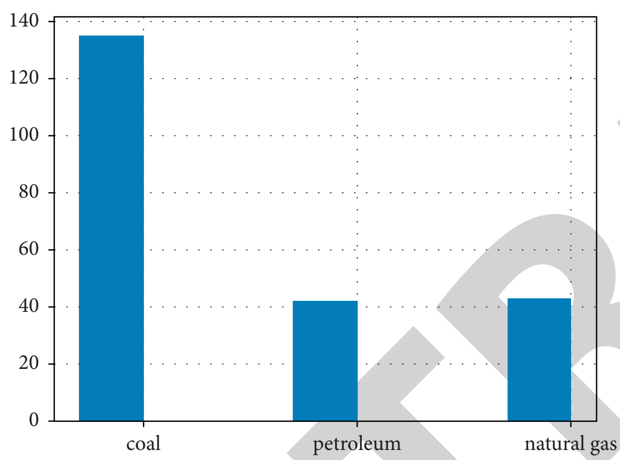

Figure 2: Global fossil fuel storage and production ratio histogram in 2019.

human economy will face heavy damage. The three global oil crises, for example, have had a serious impact on the global economy. According to the rate and trend of global fossil energy consumption, the most optimistic estimate of the American Petroleum Association (APA) is that the fossil energy reserves will only last for more than 100 years [6]. On the other hand, the extraction and use of oil and coal have simultaneously caused irreparable damage to the Earth's environment, most typically in the form of atmospheric pollution and the greenhouse effect. The scientific and orderly exploitation of nuclear energy and natural resources (e.g., wind, solar, hydro, etc.) can effectively improve these problems in light of current human science and technology [7]. At the beginning of 2011, nuclear energy was considered to be at the beginning of a renaissance, but with the Fukushima nuclear accident, the brakes were applied sharply. The development and utilization of solar energy, the most abundant of natural energy sources, has now long been a new field of research worldwide, and initial progress has been made in the collection, storage, and utilization of solar energy.

2. Related Work

Photothermal utilization and photovoltaic utilization are the two main forms of solar energy utilization by humans at present. Photothermal utilization refers to the use of material molecules, converting light energy into heat energy to be utilized. Photovoltaic utilization refers to the use of solar cell devices to convert the energy carried by sun photons into the potential energy of electrons in semiconductor materials and transport it outward. Compared to the photovoltaic utilization of solar energy, photothermal utilization is inefficient because the conversion process requires the participation of a medium [8].

The beginning of solar cells was the discovery of the photovoltaic effect by the French physicist Becquerel in 1839, and the discovery of this effect made the emergence of solar cells possible. In 1905, Albert Einstein proposed the photoelectric effect to explain the phenomenon of electrons emitted by materials exposed to light, and this theory was the basis for the work on solar cells. In the 1950s, PN junctions were prepared by wafers, and a significant photovoltaic effect was found in these PN junctions. With the photovoltaic effect of this PN junction, Bell Laboratories prepared solar cells with 4.5% photovoltaic conversion efficiency, which was later increased to 6% [9]. In the following decades, the performance of solar cells has been continuously improved and the types of solar cells have been enriched [10]. Among them, silicon-based solar cells have the longest history of development and have achieved excellent results both in terms of high-efficiency devices and commercialized modules [11]. Based on the excellent light absorption ability of these new photovoltaic materials, only a few hundred nanometers to a few microns of light absorption layer material are needed to achieve complete absorption of sunlight, which makes the preparation of solar cell devices requires only a very small amount of material, significantly reducing the material cost of device fabrication, thus making this type of solar cell power generation [12]. This reduces the material cost for device fabrication and, thus the cost of power generation for this type of solar cell.

TABLE 1: Classification of solar cells.

Classification	Category	Efficiency (%)	Cost	Advantages and disadvantages
Silicon crystalline solar cells (first generation)	Monocrystalline Silicon	27.5	very high	Complex process, good stability
	Polysilicon	23.3	Higher	Simple process, high development potential
Thin film solar cells (second generation)	Amorphous Silicon	21.5	High	Simple process, poor stability
	Cadmium Telluride (CdTe)	22.3	Lower	Serious environmental pollution
	Gallium Arsenide (GaAs)	27.9	very high	Good stability
	Copper Indium Gallium Selenide (CIGS)	23.3	Higher	Shortage of raw materials for preparation
	Inorganic Cell (CZTSSe)	12.5	Low	Simple process, poor stability
New concept solar cells (third generation)	Dye Sensitization (DSSC)	12.3	Lower	Severe pollution, poor stability
	Quantum dot sensitization (QDSC)	16.7	Low	Low efficiency, good stability
	Calcium Titanite (PSCs)	25.1	Low	Simple process, poor stability

Although the cost of these solar cells has dropped significantly, they are still more expensive than the current thermal power generation and are at a disadvantage in competition with thermal power generation [13]. For example, the maximum capacity of copper indium gallium selenide solar cells is limited by the presence of rare metals indium and gallium in the material, while cadmium telluride solar cells need to consider the possible loss of heavy metal cadmium to the natural environment during the process of use [14]. They mostly use organic materials to construct the devices, and the more representative ones are organic small-molecule solar cells using organic small-molecule materials as the donor and receptor [15]. The new solar cells have the characteristics of little or no pollution to the environment and low material requirement, and also their photoelectric conversion efficiency can be accepted [16–18].

According to the time of its appearance in the market, the development of solar cell technology was divided into three generations by Martin Green, a well-known expert [19]. Table 1 specifies information on the categories, current efficiencies, preparation costs, and advantages and disadvantages of several types of solar cells.

Based on the analysis of the three generations of solar cells, the efficiency of the new chalcogenide solar cells is very close to that of the traditional monocrystalline silicon and gallium arsenide solar cells and has a lower manufacturing cost and process compared to them, thus becoming one of the most popular categories in the solar cell research field in recent years [20].

3. Basic Knowledge

The working principle of solar cell is mainly divided into three processes: light absorption process, electron-hole pair excitation process, and photogenerated carrier separation process. As in Figure 3, firstly, electron-hole pairs are generated when sunlight irradiates on the PN junction sample of the semiconductor, and secondly, the electron-hole pairs generated are transferred.

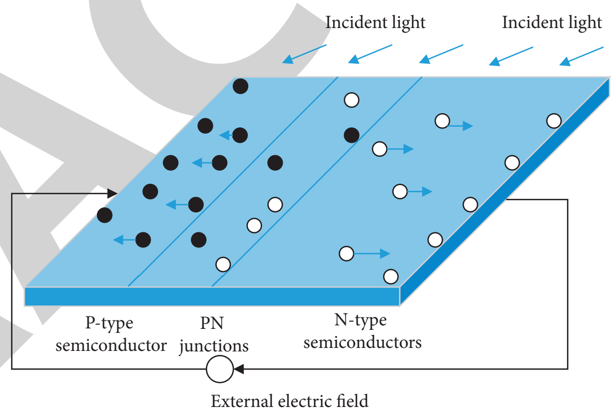

FIGURE 3: Working principle of solar cell.

3.1. Characteristics and Parameters of Solar Cells. The voltammetric characteristic curve is a function of the current I (Current, A) and voltage V (Voltage, V) under certain light intensity and ambient temperature, as shown in Figure 4. Since the magnitude of the current is affected by the solar cell area A (solar cell area, cm^2), the current density J (current density, A/cm^2) is commonly used instead of the current I to describe the voltammetric characteristics. The relationship between the two is $J = I/A$; that is, the size of the current I is proportional to the area of the solar cell.

For the solar cell Ohm's law, if the load resistance R (load resistance, Ω) is added, the formula is $J = V/AR$. Figure 4 shows the correspondence between the size of the load resistance and the operating current and voltage ($R_1 > R_2 > R_3$).

The photovoltaic conversion efficiency (IPCE), energy conversion efficiency (PCE), maximum output power (maximum output power, P_{max}), fill factors (fill factors, FF), energy conversion efficiency (power conversion efficiency, PCE), and other components are the values of these parameters that measure the good and bad of solar cells.

The definition of each parameter and the influencing factors are as follows.

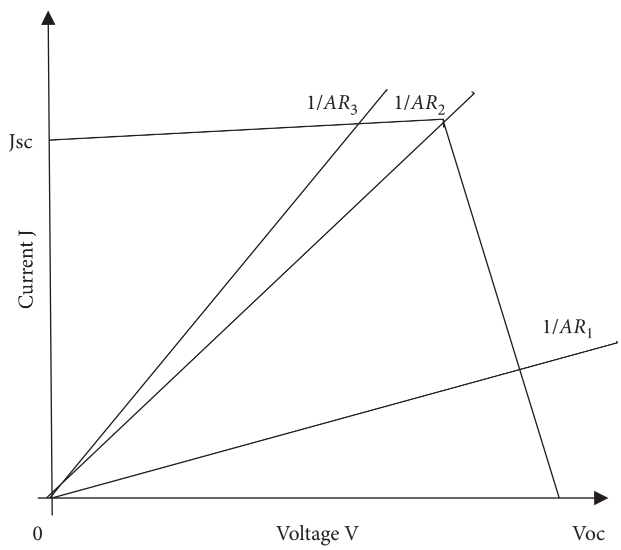

FIGURE 4: Solar cell voltammetric characteristic curve.

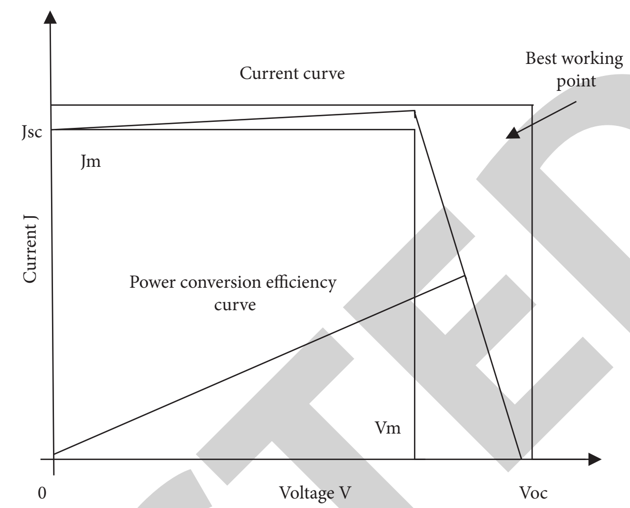

FIGURE 5: Voltammetric characteristic curve of the solar cell.

3.1.1. Open-Circuit Voltage V_{oc}. In the voltammetric characteristic curve is expressed as the intercept of the curve on the voltage axis shown in Figure 4. The V_{oc} size of solar cells is largely determined by the energy. In addition, different cell structures, different absorber layer materials, interface properties, and the degree of charge compounding in the device.

3.1.2. Short-Circuit Current Density J_{sc}. In the voltammetric characteristic curve is expressed as the intercept of the curve on the current density axis shown in Figure 4. There are various factors affecting the short-circuit current, including light intensity, cell structure, thickness of different layer materials, the nature of carrier transport, and the type of absorber layer material. The smaller the band gap of the absorber layer material, the greater the absorption spectrum can match the solar spectrum so that more photons can be converted into electricity.

The short-circuit current J_{sc} with IPCE and the solar photon flux, whose integral equation is shown in the following equation:

$$J_{ph} = J_{sc} = q\int_0^\infty QE(E)b_s(E,T_s)\mathrm{d}E. \quad (1)$$

It indicates the number of solar radiation photons per unit time, area energy in the range of E to $E + dE$, $b_s(E,T_s)$, and the temperature of the sun T_s related.

3.1.3. Photovoltaic Conversion Efficiency (IPCE). Photovoltaic conversion efficiency (IPCE) is a measure of the efficiency of incident light energy to solar cells after the final conversion into electricity, which is usually used as the EQE. The EQE is usually used as the index of IPCE. The defining equation is shown in the following equation:

$$\mathrm{IPCE}(\%) = \frac{n_e}{n_p} = \frac{1240 \times J_{SC}}{\lambda \times P_{in}} \times 100\%, \quad (2)$$

where λ denotes the wavelength of incident monochromatic light and P_{in} denotes the incident light power.

The photovoltaic conversion efficiency of solar cells generally depends on the following three factors.

(1) The absorption efficiency of the material for photons;
(2) The separation efficiency of the carriers;
(3) Carrier transport efficiency.

In addition, its value is also related to the wavelength or energy of light.

3.1.4. Maximum Output Power P_{max}. The maximum output power P_{max}, that is, in a certain load resistance R, the output of the product of operating current and operating voltage can reach the maximum value, also known as rated power (rated power density), in the voltammetric characteristic curve shown in Figure 5 is called the best working point, respectively, expressed in V_{mp}, J_{mp}.

3.1.5. Filling Factor FF. The defining equation is shown in the following equation:

$$\mathrm{FF} = \frac{P_{max}}{V_{oc} \times J_{sc}} = \frac{V_{mp} \times J_{mp}}{V_{oc} \times J_{sc}}. \quad (3)$$

In Figure 5, the area of the rectangle corresponding to the optimal operating point $P_{max} = V_{mp} \times J_{mp}$. The series and parallel resistance of the solar cell device has a large impact on FF. The smaller the parallel resistance of the device, the higher the shunt current.

3.1.6. Energy Conversion Efficiency PCE. The defining equation and its relationship are shown in the following equation:

$$\mathrm{PCE} = \frac{P_{max}}{P_{in}} = \frac{V_{mp}, J_{mp}}{P_{in}} = \frac{FF \times V_{oc} \times J_{sc}}{P_{in}}. \quad (4)$$

Table 2: Performance parameters statistics of some different types of solar cells.

Battery type	Bandgap Eg (eV)	Cell area (A/cm^2)	V_{OC}/V	$J_{SC}/(\mathrm{mA/m^2})$	FF (%)	PCE (%)
Monocrystalline Silicon	1.13	79.1	0.739	42.66	84.91	26.8
Cadmium Telluride (CdTe)	1.45	1.0624	0.8760	30.26	79.5	21.1
Gallium Arsenide (GaAs)	1.43	0.997	1.1271	29.77	86.6	29.0
Copper Indium Gallium Selenide (CIGS)	1.20	1.042	0.732	39.57	80.3	23.34
CZTS	—	1.112	0.7085	21.79	65.2	10.1
Dye Sensitization (DSSC)	—	1.004	0.745	22.49	68.8	13.47
Organic Cells	—	1.025	0.8423	23.27	68.5	13.47
Calcium Titanite (PSCs)	~1.5	1.0236	1.194	21.65	83.7	21.4

The energy conversion efficiency curve is shown in Figure 5. Since energy conversion efficiency is closely related to solar irradiance, a standard solar irradiance condition needs to be defined. The standard test condition (STC) prevailing in the industry is defined as

(1) Atmospheric mass (Air mass) AM1.5.

(2) Solar Irradiance (Solar Irradiance) $P = 1000\,\mathrm{W/m^2}$.

(3) Ambient temperature $T_a = 25 \pm 1^{\circ}C$.

Through statistical records of the energy shown in Table 2: in general, the solar cell is also relatively larger, resulting in a larger open-circuit voltage, while a large band gap makes it more difficult for electrons, and vice versa.

The FF is an artificially specified parameter $FF = (V_{\max} \times J_{\max}/V_{oc} \times J_{sc})$, which is the maximum output power divided by the maximum current and voltage that the device can provide.

And for obtaining the value of R_s, R_{sh} in the analog circuit, we can obtain it by fitting the $J-V$ curve of the device. From this we can obtain the following relationship:

$$J_{sh} = \frac{V_{sh}}{R_{sh}}. \tag{5}$$

$$J = J_{sc} - J_{\mathrm{dark}} - J_{sh.} \tag{6}$$

$$V_{sh} = V + JR_{s.} \tag{7}$$

Through the Shockley equation,

$$J_{\mathrm{dark}}(V) = J_0\left(\exp\left(\frac{qV}{k_B T}\right) - 1\right). \tag{8}$$

The dark state current density J_{dark}, where J_0 is the reverse saturation current density that can be obtained by performing a dark state $J-V$ curve test on the device.

Substituting equations (5), (7), and (8) into (6), we get

$$\mathrm{J}(V) = J_{sc} - J_0\left(\exp\left(\frac{q(V + J(V)R_s)}{k_B T}\right) - 1\right) - \frac{V + J(V)R_s}{R_{sh}}. \tag{9}$$

The value of R_s, R_{sh} for the device is obtained by fitting the $J-V$ curve of the device with equation (9).

4. Experiments

The reagents and materials used for the preparation of CdSeTe QDs included oleylamine (OAm, 80%–90%) and anhydrous methanol (CH_3OH), anhydrous ethanol (CH_3CH_2OH), acetone (CH_3COCH_3), dichloromethane(CH_2CI_2)), and trichloromethane ($CHCI_3$). The transparent electrodes for QDSCs were conductive glass (FTO, 14 Ω/square) purchased from Pilkington.

Scanning electron microscope (SEM) testing is a test method that uses the interaction between an electron beam and a material to analyze the morphology of the material surface. The SEM test mainly detects the secondary electron signal generated by the excitation of the material after the surface is bombarded by the electron beam. The SEM test equipment used in this work is a Shimadzu JSM-6700F scanning electron microscope.

4.1. Characterization Analysis Based on Cu_2SnS_3 Quantum Dot Material. We prepared Cu_2SnS_3 quantum dots by the thermal injection method, dissolved them in tetrachloroethylene solution, and then spin-coated them on the chalcogenide absorbing layer under nitrogen atmosphere after ultrasonic stirring and homogenization. It was reported that the reactivity of the precursor and the binding strength of the encapsulant had a great influence on the crystal structure of Cu_2SnS_3. By changing the reactivity of the precursor and/or the binding strength of the encapsulant, certain high-temperature and substable phases of the material can be obtained by wet chemistry at low temperatures, such that sphalerite structures, fibrillated zinc structures, and mixtures of sphalerite and fibrillated zinc structures can be obtained under different conditions. In this experiment, Cu_2SnS_3 quantum dots with sphalerite and fibrillar zincite structures were synthesized by wet chemistry at low temperature, and their structures are shown schematically in Figure 6.

In order to further determine the structure of the prepared Cu_2SnS_3 quantum dots, X-ray diffraction (XRD) analysis was performed to characterize them. Figure 7 shows the X-ray diffraction pattern of Cu_2SnS_3 quantum dots. The results show that we can prepare Cu_2SnS_3 quantum dots with sphalerite and sillimanite structures, respectively, and our diffraction patterns are consistent with the simulated and experimental patterns reported in the relevant literature.

As shown in Figure 8, in order to further determine the ratio of each element in the prepared Cu_2SnS_3 quantum dots and to avoid the formation of impurity phases such as Cu_3SnS_4, Cu_4SnS_4, and $Cu_2Sn_2S_7$, we performed energy dispersive spectroscopy (EDS) analysis on the Cu_2SnS_3 quantum dot films. The ratios of Cu, Sn, and S are basically

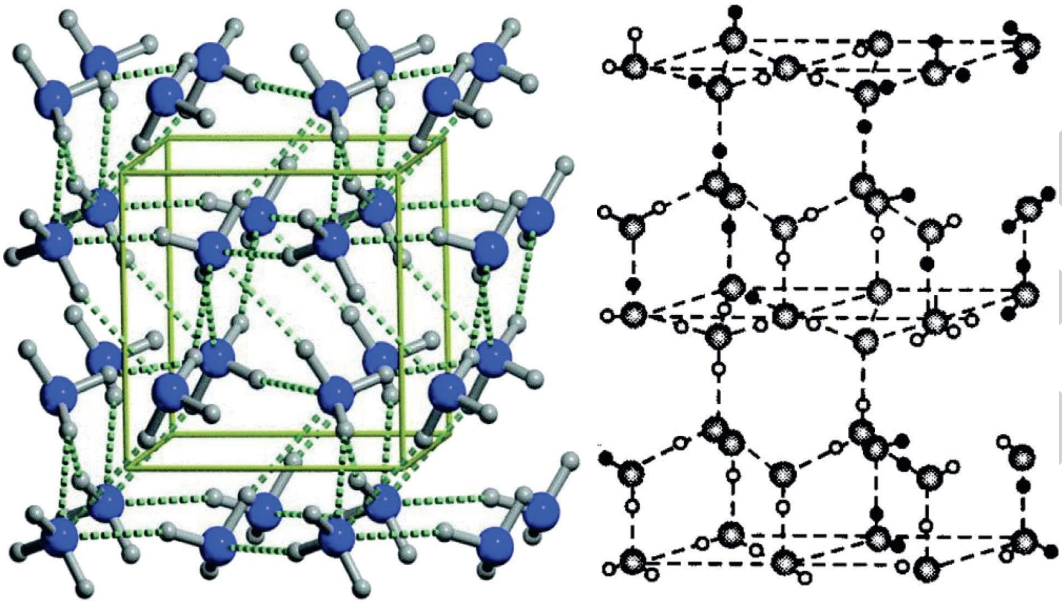

Figure 6: Schematic structure of sphalerite and sillimanite of Cu_2SnS_3 quantum dots.

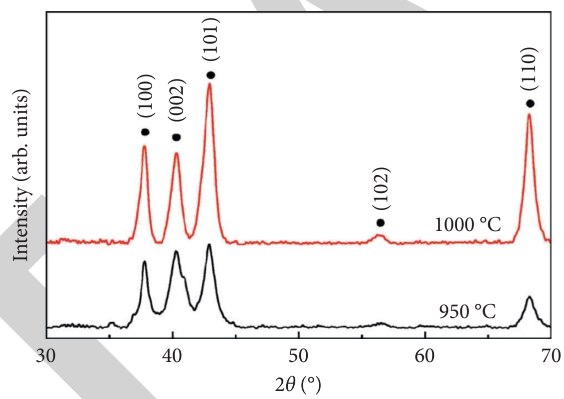

Figure 7: XRD patterns of sphalerite and fibrillar zincite structures of Cu_2SnS_3.

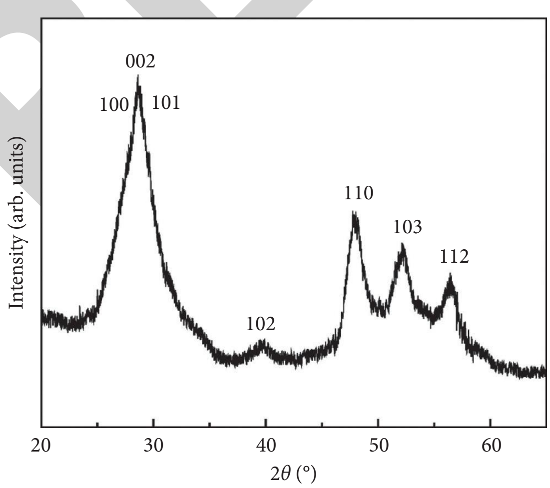

(a)

Element	Wt%	At%
SK	27.62	49.17
SnL	34.02	16.36
CuK	38.37	34.47
Matrix	Correction	ZAF

(b)

Figure 8: (a) EDS spectra of Cu_2SnS_3 quantum dots and (b) proportion of each element of Cu_2SnS_3 quantum dots measured by EDS.

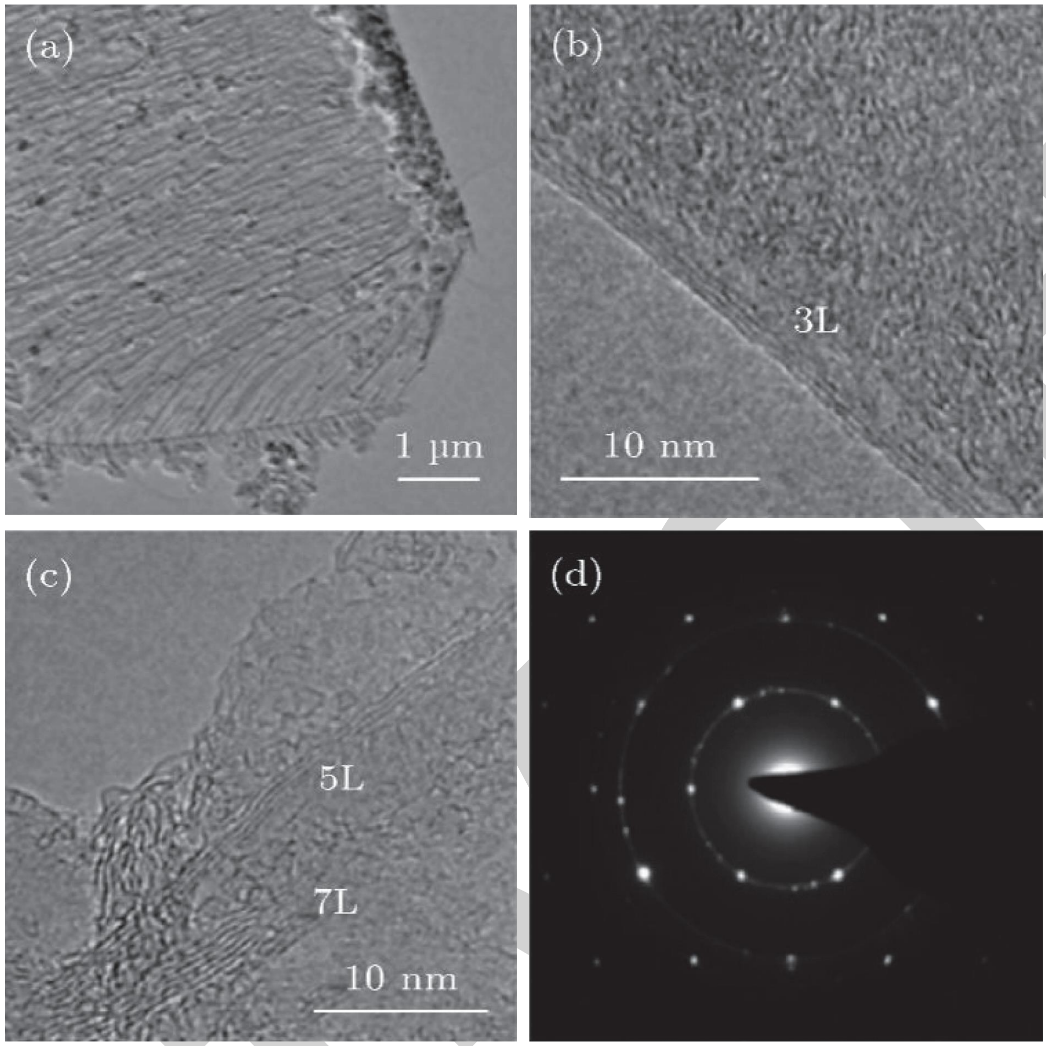

Figure 9: TEM images of Cu_2SnS_3 quantum dots at different magnifications: (a) 50,000x; (b) 80,000x; (c) 100,000x; (d) 150,000x.

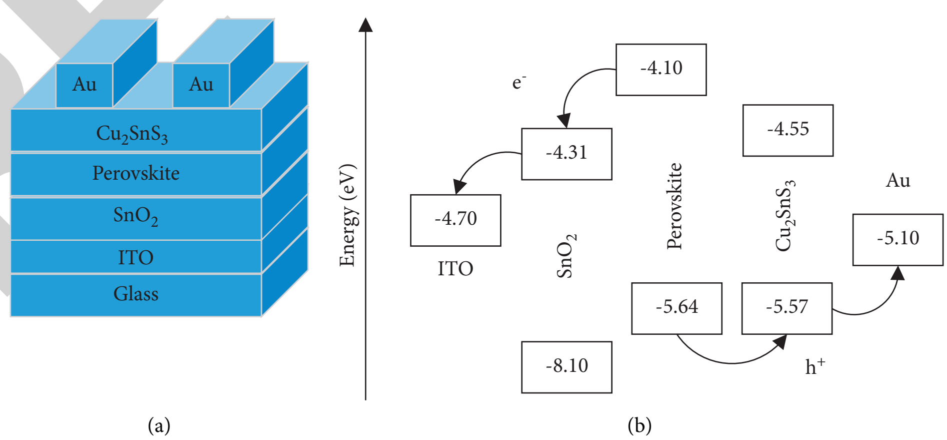

Figure 10: (a) Schematic diagram of the device structure of the prepared PSCs. (b) Energy band arrangement of each material in the prepared PSCs.

Table 3: $J-V$ test parameters of InN ultra-thin layer batteries grown at different temperatures.

Samples	$J_{SC}/(mA/m^2)$	V_{OC}/V	$FF/\%$	$n/\%$
Reference	13.27	0.55	62.36	4.67
InN-170°C	13.34	0.59	67.99	5.24
InN-200°C	14.44	0.59	69.99	5.48
InN-230°C	13.58	0.56	66.54	4.67

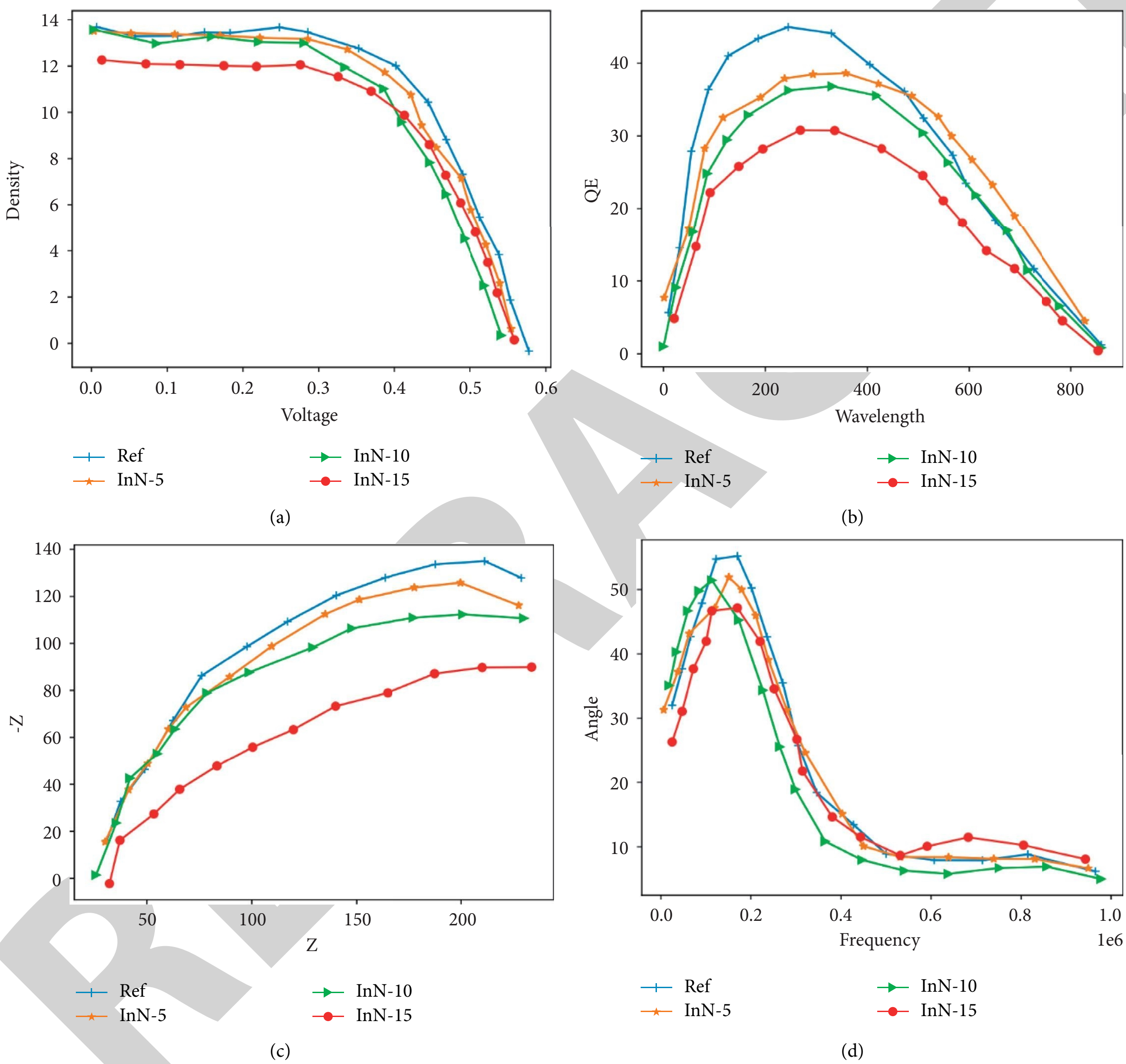

Figure 11: (a) $J-V$ curves of QDSCs based on different InN thickness; (b) quantum efficiency of QDSCs based on different thickness of InN; (c) Nyquist curves of QDSCs based on different thicknesses of InN; (d) bode curves of QDSCs based on different thicknesses of InN.

close to $Cu:Sn:S=2:1:3$, which is consistent with the stoichiometric ratios of the quantum dots we prepared.

In order to better observe the morphology and size of the prepared quantum dots, transmission electron microscopy (TEM) characterization of Cu_2SnS_3 quantum dots was carried out. The TEM images of Cu_2SnS_3 quantum dots at different magnifications are shown in Figure 9. Based on the TEM images, it was found that the Cu_2SnS_3 quantum dots prepared by us have good dispersion ability, the size distribution is in the range of about 2–10 nm, and the morphology is mainly irregular polygons. The morphology and size of Cu_2SnS_3 quantum dots are mainly influenced by the reaction temperature and reaction time of the solution. The specific characteristics of Cu_2SnS_3 quantum dots are described in detail in the following section on the structural characterization of PSCs. The specific characteristics of

Cu_2SnS_3 quantum dot films are described in the next section on structural characterization of PSCs.

4.2. Device Film Characterization Based on Cu_2SnS_3 Hole Transport Material. Based on the preliminary research and characterization of the prepared Cu_2SnS_3 quantum dots, we believe that Cu_2SnS_3 quantum dots can be applied as HTM in PSCs. So we prepared the structure shown in Figure 10(a), in which SnO_2 is used as the ETM, Cu_2SnS_3 is used as the HTM, and the material used for the chalcogenide absorber layer is $(FAPbI_3)_{1-X}(MAPbBr_3)_X$. As shown in Figure 10 that the energy level diagram of each material shown in Figure 10(b) further demonstrates the degree of bandgap matching for each transmission layer of the prepared chalcogenide devices. After reviewing the literature, the conduction band position of ITO is −4.7 eV, the conduction band (Ec) and valence band (Ev) positions of SnO_2. As shown in Figure 10(b), the correlation between the band gaps of the layers is more intuitively demonstrated. The valence band value of Cu_2SnS_3 layer indicates that Cu_2SnS_3 quantum dots can replace Spiro-OMeTAD, effectively extract the holes generated by the chalcogenide layer.

The calculated *FF* is 69.98%. The *FF* is calculated as

$$\mathrm{FF} = \frac{P_m}{J_{sc} V_{oc}}. \tag{10}$$

Comparing the reference cell with the cell deposited with InN film at 200°C, it can be seen from the parameters in Table 3 that J_{sc} increases from 13.28 mA/cm^2 to 14.43 mA/cm^2 with little change, V_{oc} increases from 0.56 V to 0.58 V with little change; while *FF* increases from 62.37% to 69.98% with a large change.

To further investigate how the introduction of InN ultra-thin layers affects the internal performance of the cell system of QDSCs, as shown in Figure 11 that the transport characteristics of electrons in the photoanodes of QDSCs are investigated in detail.

5. Conclusion

The photovoltaic performance of CdSeTe-based QDSCs can be enhanced to a certain extent by depositing InN ultra-thin layers using PEALD, and different deposition temperatures and thicknesses of InN show different influence patterns. The conversion efficiency of CdSeTe-based QDSCs was significantly improved by the introduction of InN ultra-thin layers in a certain thickness and deposition temperature range. Among them, the InN films at 200°C and 10 cycles are more ideal, and the conversion efficiency of the CdSeTe cells obtained can reach 5.47% and *FF* up to 69.98%. The introduction of InN can promote carrier transport, significantly increase *FF*, accelerate electron extraction, and reduce the transmission impedance $R_{ct-Tio2}$ at the photoanode.

Data Availability

The experimental data used to support the findings of this study are available from the corresponding author upon request.

Conflicts of Interest

The authors declared that they have no conflicts of interest regarding this work.

References

[1] N. Malek, N. Alias, S. Saad, N. A. Abdullah, and Y. Zhan, "Ultra-thin mos2 nanosheet for electron transport layer of perovskite solar cells," *Optical Materials*, vol. 104, Article ID 109933, 2020.

[2] S. Benabbas, Z. Rouabah, H. Heriche, and N. E. Chelali, "A numerical study of high efficiency ultra-thin cds/cigs solar cells," *African Journal of Science Technology Innovation & Development*, vol. 8, pp. 1–3, 2016.

[3] A. Sylla, N. Guessan Armel Ignace, T. Siaka, and J. P. Vilcot, "Theoretical analysis of the effect of the interfacial mose2 layer in cigs-based solar cells," *Open Journal of Modelling and Simulation*, vol. 9, no. 4, p. 12, 2021.

[4] K. Wang, C. Liu, C. Yi et al., "Efficient perovskite hybrid solar cells via ionomer interfacial engineering," *Advanced Functional Materials*, vol. 25, no. 44, pp. 6875–6884, 2016.

[5] Z. P. Li, S. Li, Y. Zheng et al., "The study of origin of interfacial perpendicular magnetic anisotropy in ultra-thin cofeb layer on the top of mgo based magnetic tunnel junction," *Applied Physics Letters*, vol. 109, no. 18, Article ID 12352, 2016.

[6] Q. Qin, Q. Shi, S. Wen, J. Wan, and Z. Hu, "Fabrication and interfacial electron transfer of ultrathin g-c3n4 nanosheet/tnt@cnts ternary nanostructure heterojunction for high-efficiency visible-light-driven photocatalysis," *Journal of Materials Science: Materials in Electronics*, vol. 29, no. 10, pp. 1–15, 2018.

[7] Q. Liu, C. Liu, and Y. Wang, "etc. Integrating external dictionary knowledge in conference scenarios the field of personalized machine translation method," *Journal of Chinese Informatics*, vol. 33, no. 10, pp. 31–37, 2019.

[8] P. An, Z. Wang, and C. Zhang, "Ensemble unsupervised autoencoders and Gaussian mixture model for cyberattack detection," *Information Processing & Management*, vol. 59, no. 2, Article ID 102844, 2022.

[9] R. Ali, M. Hameed Siddiqi, and S. Lee, "Rough set-based approaches for discretization: a compact review," *Artificial Intelligence Review*, vol. 44, no. 2, pp. 235–263, 2015.

[10] Y. Jia, H. Wang, Y. Wang, N. Shibayama, and H. Segawa, "High-performance electron-transport-layer-free quantum junction solar cells with improved efficiency exceeding 10%," *ACS Energy Letters*, vol. 6, no. 2, pp. 493–500, 2021.

[11] F. S. Shoyebmohamad, K. Hyeok-Chan, Y. Wooseok, and M. Jooho, "Performance enhancement of mesoporous tio 2-based perovskite solar cells by zns ultrathin-interfacial modification layer," *Journal of Alloys and Compounds: An Interdisciplinary Journal of Materials Science and Solid-state Chemistry and Physics*, vol. 738, pp. 405–414, 2018.

[12] E. Itoh, Y. Goto, Y. Saka, and K. Fukuda, "Interfacial energy alignment at the ito/ultra-thin electron selective dielectric layer interface and its effect on the efficiency of bulk-heterojunction organic solar cells," *Journal of Nanoscience and Nanotechnology*, vol. 16, no. 4, pp. 3248–3253, 2016.

[13] E. Etoh and M. Iwamoto, "Interfacial electrostatic phenomena and capacitance–voltage characteristics of ultrathin polyimide Langmuir–blodgett films," *Electrical Engineering in Japan*, vol. 134, no. 3, pp. 9–15, 2015.

[14] X. Zhang, Y. Li, R. Liu, Y. Rao, H. Rong, and G. Qin, "High-magnetization feco nanochains with ultrathin interfacial gaps

Hindawi
Advances in Materials Science and Engineering
Volume 2022, Article ID 4438419, 8 pages
https://doi.org/10.1155/2022/4438419

Research Article

Parametric Optimization of Wire Electrical Discharge Machining in AA7075 Metal Matrix Composite

K. Raju[1] **M. Balakrishnan**[1] **C. B. Priya**[2] **M. Sivachitra**[3] **and Dasari Narasimha Rao**[4]

[1]*Department of Mechanical Engineering, M. Kumarasamy College of Engineering, Karur 639113, Tamilnadu, India*
[2]*Department of Mechanical Engineering, Dhanalakshmi Srinivasan Institute of Technology, Samayapuram, Trichy, India*
[3]*Department of Department of Electrical and Electronics Engineering, Kongu Engineering College, Perundurai 638060, Tamilnadu, India*
[4]*Department of Electrical Power Engineering, Defence University College of Engineering, Bishoftu, Ethiopia*

Correspondence should be addressed to Dasari Narasimha Rao; dasari.narasimha@dec.edu.et

Received 11 March 2022; Revised 25 April 2022; Accepted 24 May 2022; Published 24 June 2022

Academic Editor: Francesco Colangelo

Aluminium 7075 metal matrix composite reinforced with silicon nitride was fabricated using the stir casting technique. Composite fabricated was machined and subjected to wire electrical discharge machining to study the significant process parameter. Taguchi design of experiment using L9 orthogonal array was selected with three factors, current, pulse ON time, and wire feed at three levels. Influencing process parameters were identified using analysis of variance. Pulse ON time of 130 μs, current of 20 A, and wire feed of 1 mm/min were identified as optimized parameters for higher material removal rate. For a good surface finish, the optimized parameter was identified as 130 μs pulse ON time, 20 A current, and wire feed rate of 2 mm/min. Pulse ON time was identified as an influencing parameter followed by the current in achieving better material removal rate with good surface finish, whereas wire feed has no influence on the output parameters. Results of experimentation showed improved machining characteristics for higher pulse ON time and current for machining the synthesized composite through the Taguchi design of the experiment.

1. Introduction

Wire electrical discharge machining (WEDM) is advanced machining method to machine harder materials with accuracy at faster rate. Materials such as aluminium 7075 composites used in aerospace, defence, and military are in need of good surface finish and accuracy. Conventional machining methods find it difficult to machine harder materials and complex shapes with accuracy and good surface finish to meet the requirements. Adding ceramic materials in aluminium metal matrix composite makes the surface hard leading to more wear rate of the tool and poor surface finish [1]. Due to high fatigue and tensile strength, good corrosion resistance, aluminium alloy (AA) 7075 is predominantly used as matrix material [2]. Increasing the content of silicon nitride (Si_3N_4) as reinforcement increases the hardness of the composite. Decreasing in hardness is found with increased load and dwell time [3]. Hybrid metal matrix composite (MMC) reinforced with aluminium oxide (Al_2O_3) and silicon carbide (SiC) showed decreased material removal rate (MRR) and lower surface finish for increased reinforcement percentage [4]. Increased cutting speed for machining ceramic-reinforced MMC increases tool wear with reduced MRR [5]. In analyzing the input parameters such as voltage, current, and pulse on and off time using the response surface methodology (RSM) technique on MRR and surface roughness (R_a), the current was identified as the most influencing parameter [6]. In turning operations, to control R_a, depth of cut along with feed and speed is to be considered [7]. In machining aluminium metal matrix composite (AMMC) containing 10 percentage fly ash and SiC, speed of cutting was identified as significant parameter [8]. The weight percentage of reinforcement influences R_a along with gap voltage for MRR [9]. Stir-casted AA7075 with 10 percentage of SiC particles showed lower R_a when turned using carbide and polycrystalline diamond (PCD) inserts

[10]. AMMC with SiC reinforcement showed surface defects when optimized using Box–Behnken design [11]. Modelling of a process parameter, dielectric medium, and electrode material is the main objective of WEDM [12]. SiC-reinforced AA6063 MMC showed decreased MRR for an increased percentage of reinforcement using the Taguchi L9 orthogonal array [13]. MMC-containing ceramic reinforcements showed lower MRR and surface finish for increased volume of SiC and Al_2O_3 reinforcements [14]. Increased current and pulse on time increases MRR and R_a in machining Al–SiC MMC [15]. Increasing gap voltage increases current leading to increased MRR. MRR is found to be directly proportional to current [16]. The thickness of the workpiece is to be considered for a good surface finish when maintaining a pulse on time at constant with a lower power supply [17]. Current, pulse time, and flow of dielectric liquid are to be considered to get better MRR and lower R_a [18]. Die steels and hard metals and MMC use WEDM for machining with good accuracy [19]. Kerf width and R_a are influenced majorly by pulse on time [20]. MRR is decreased when increasing gap voltage and pulse off time. Increased pulse ON time and current increase MRR [21]. MRR has direct proportional to pulse on time and inverse proportional to pulse off time [22]. In machining DC53 die steel, the significant variable was concluded as current and pulse on time [23]. In optimization, pulse off time, pulse on time, servo voltage, current, wire tension, and gap voltage are to be considered as input parameters [24]. Regression equation in Taguchi design of experiment (DOE) is used to correlate MRR to get optimized process parameters [25]. Pulse on and off time are the major parameters in attaining hardness and better surface finish [26]. Pulse on time is seen to have direct proportional to wire wear and MRR whereas surface finish is seen to be inversely proportional to pulse on time [27]. Their different studies focus on the optimization of process parameters in machining with coated cutting tools, steels, and composite materials [28–30]. Lots of investigations were seen on optimization of process parameters using WEDM using SiC and Al_2O_3, with AA7075. In this study, AA7075 reinforced with Si_3N_4 MMC was machined using WEDM to identify the optimal process parameter. Si_3N_4 reinforcement was selected for this study due to its high hardness, wear resistance, and thermal conductivity.

2. Materials and Methods

2.1. Composite Fabrication. Composite was fabricated using stir casting process with 90% of aluminium alloy 7075 reinforced with 10% of silicon nitride ceramic reinforcement of particle size ranging from 20 to 40 μm. The stir-casting process was selected for composite fabrication due to its easy fabrication at low cost. Matrix material AA7075 was melted to 750°C and maintained at the same temperature. Preheated silicon nitride at 600°C for an hour was then added to the melt and stirred well and cast in the mould to get a defect-free casting for the analysis. Electronica Wire electrical discharge machine was selected for machining the prepared composite. A brass wire of 0.25 mm with water as the dielectric liquid was taken for machining the composite.

Figure 1: Photograph of composite specimen for WEDM.

Table 1: Parameters and its levels.

S.No	Parameters	Symbol	Units	Level		
1	Pulse ON time	T_{ON}	Microseconds (μs)	110	120	130
2	Current A	I	Ampere (A)	10	15	20
3	Wire feed	W_f	(mm/min)	1	2	3

Table 2: Experimental data for experimentation.

S.No	Pulse ON time (T_{ON}) (μs)	Current (I) (A)	Wire feed (W_f) (mm/min)
1	110	10	1
2	110	15	2
3	110	20	3
4	120	10	2
5	120	15	3
6	120	20	1
7	130	10	3
8	130	15	1
9	130	20	2

Standard test samples of 30 mm diameter with 10 mm thickness were prepared for WEDM as shown in Figure 1.

2.2. Design of Experiments

2.2.1. Analysis of Variance. Analysis of variance (ANOVA) is a logical approach to identify the factors that considerably affect the experimental outcome. ANOVA includes (i) all experimental values allocated for summing squares, (ii) impartial difference, (iii) decaying total sum of squares considering all elements taken for analysis, (iv) calculating impartial variances of all elements above the DOF, (v) determining the variance ratio, and (vi) analyzing the error variance to identify the significant factors affecting the experimental values. ANOVA-based regression equation generated was considered to calculate the predicted values for MRR and R_a. The obtained values are then compared with the experimental values to identify the error percentage and accuracy of the analysis.

2.2.2. Taguchi Analysis. Taguchi DOE is the process in which design parameters are investigated to identify the optimal values to get improved efficiency that is not influenced by noise factors. Taguchi DOE gives the entire study of parameters with a low number of experiments. Designed experimental data were identified using an L9 orthogonal

Table 3: Experimental results of Taguchi-based DOE.

S.No	Pulse on time (μs)	Current (A)	Wire feed (mm/min)	MRR (g/min)	R_a (μm)	Predicted MRR (g/min)	Predicted R_a (μm)	MRR error (%)	R_a error (%)
1	110	10	1	0.158	2.252	0.157	2.254	0.63	0.09
2	110	15	2	0.162	2.311	0.163	2.304	0.62	0.30
3	110	20	3	0.165	2.326	0.165	2.332	0	0.26
4	120	10	2	0.181	2.920	0.181	2.926	0	0.21
5	120	15	3	0.188	2.931	0.187	2.933	0.53	0.07
6	120	20	1	0.192	2.990	0.193	2.983	0.52	0.23
7	130	10	3	0.211	3.112	0.212	3.105	0.47	0.22
8	130	15	1	0.220	3.128	0.22	3.134	0	0.19
9	130	20	2	0.224	3.202	0.223	3.204	0.45	0.06

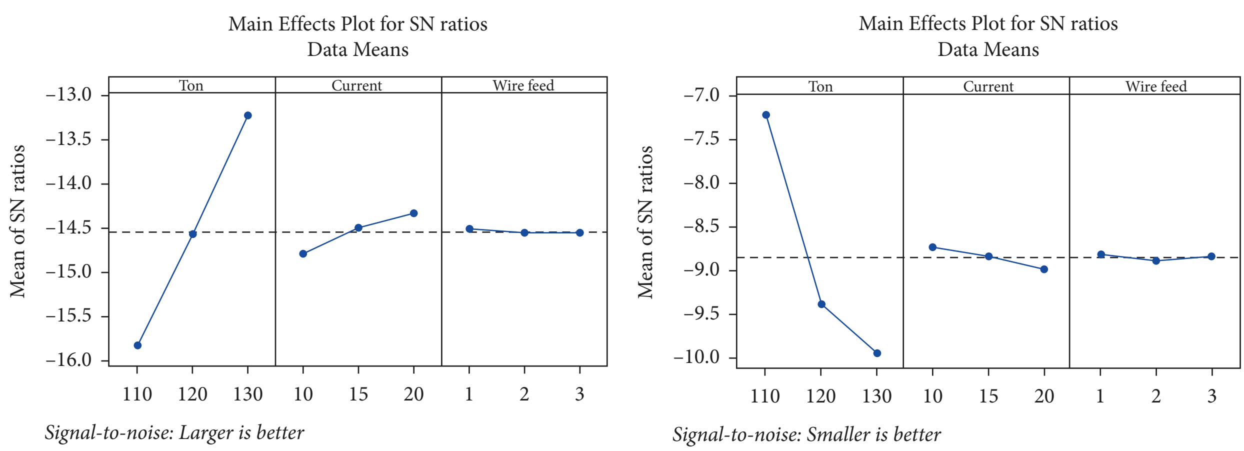

(a)

(b)

Figure 2: Mean effect plots for MRR and R_a. (a) MRR. (b) R_a.

array to find the parameters influencing MRR and R_a. The superiority characteristics considered for MRR are larger the better, and similarly, the superiority characteristics considered for R_a are smaller the better which takes continuous and nonnegative values ranging between 0 and 1. Parameters and its levels are listed in Table 1. Table 2 shows the identified experimental data for conducting the experiment using MINITAB 19 software. Experimental levels of parameters were selected based on the studies of Bisaria and Shandilya 2020 [31].

3. Result and Discussion

3.1. Experimental Results. Experimental results for the L9 orthogonal arrayed input parameters are listed in Table 3. MRR was tabulated by calculating the difference in weight of the specimen before machining and after machining using the weighing balance of 0.001-gram accuracy. R_a was found using a surface roughness tester of make: Mitutoyo Surf test and model: SJ-201P.

3.2. Taguchi Analysis. Figures 2(a) and 2(b) show the mean effect plots for MRR and R_a. The larger the better signal to noise ratio (S/N ratio) is selected for MRR, and the smaller the better S/N ratio is selected for R_a. From Figure 2(a), increased values of pulse ON time and current showed increased MRR whereas the increase in wire feed has no influence on MRR. Figure 2(b) shows decreased R_a for increased current and pulse ON time.

Table 4: ANOVA table for MRR.

Source	DF	Adj SS	PCR (%)	Adj MS	F value	*P* value
Ton	2	0.004835	96.5	0.002417	1036.00	0.001
Current	2	0.000165	3.29	0.000082	35.29	0.028
Wire feed	2	0.000006	0.12	0.000003	1.29	0.437
Error	2	0.000005	0.11	0.000002		
Total	8	0.005010				

3.2.1. Analysis of Variance. Table 4 indicates the ANOVA for MRR. *P* value closer to zero and F value greater than one indicate the significant parameter to be concentrated during machining. From Table 4, it is clearly identified that MRR is highly influenced by pulse ON time (T_{ON}) followed by current (I) and wire feed (W_f).

Table 5 indicates the ANOVA for R_a. Similar to MRR, it is clearly identified that R_a is highly influenced by pulse ON time (T_{ON}) followed by current (I) and wire feed (W_f) from Table 5.

From Tables 4 and 5, the percentage contribution ratio confirms pulse ON time as the most influencing parameter towards MRR and Ra [32].

Table 5: ANOVA table for R_a.

Source	DF	Adj SS	PCR (%)	Adj MS	F value	P value
Ton	2	1.18770	99.1	0.593851	4406.15	0.000
Current	2	0.00934	0.78	0.004670	34.65	0.028
Wire feed	2	0.00090	0.07	0.000448	3.32	0.231
Error	2	0.00027	0.05	0.000135		
Total	8	1.19821				

Table 6: Regression equation for MRR and R_a.

MRR = 0.189000–0.027333 Ton_110–0.002000 Ton_120 + 0.029333 Ton_130–0.005667 Current_10 + 0.001000 Current_15 + 0.004667 Current_20 + 0.001000 wire feed_1 + 0.000000 wire feed_2–0.001000 wire feed_3
R_a = 2.79689–0.50056 Ton_110 + 0.15011 Ton_120 + 0.35044 Ton_130–0.03556 Current_10–0.00689 Current_15 + 0.04244 Current_20–0.00689 wire feed_1 + 0.01411 wire feed_2–0.00722 wire feed_3

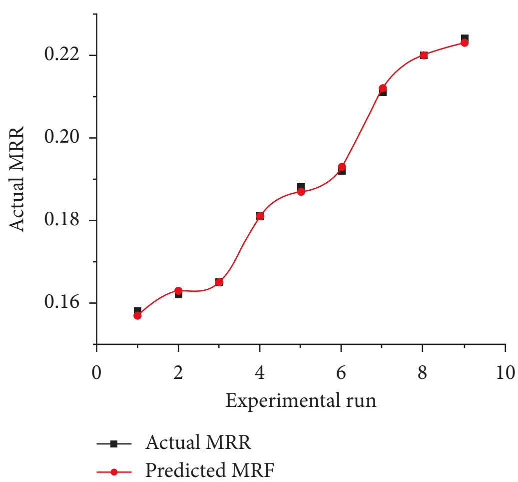

(a)

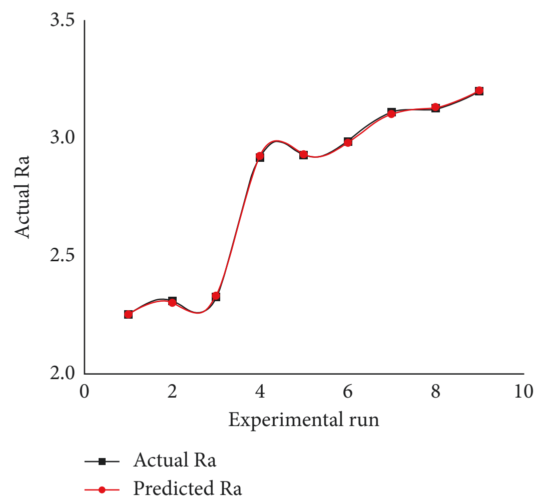

(b)

Figure 3: Comparison graph for experimental values with predicted values: (a) MRR, (b) R_a.

3.2.2. Regression Equation. Table 6 shows the regression equation generated for the experimental results of MRR and R_a. The equation is used to identify the predicted results used to analyze the error % by comparing it with the actual obtained experimental values. Error % less than 5 indicates the accuracy of the analysis.

Figures 3(a) and 3(b) indicate the comparison of experimental values with predicted values for MRR and R_a. From the graph, it is understood that the error percentage is less than 1 which is too minimum to prove the accuracy of the experiment.

3.2.3. Model Summary. Table 7 shows the model summary for MRR and R_a. R^2 and actual R^2 values were noted from the general linear model of Taguchi design from MINITAB 19 software. R^2, actual R^2, and predicted R^2 values for both MRR and R_a are much closer indicating the accuracy of the analysis for the designed input parameters. The values obtained are 99.5% indicating that there is no external factor influencing the analysis.

Table 7: Model summary for MRR and R_a.

Model summary	S	R-sq (%)	R-sq(adj) (%)	R-sq(pred) (%)
MRR	0.0015275	99.91	99.63	98.11
R_a	0.0116094	99.98	99.91	99.54

3.2.4. Interaction Plot. Figures 4(a) and 4(b) indicate the interaction plot of each input parameter for MRR and R_a. Figure 4(a) shows the interaction plot for MRR from which it is noted that an increase in T_{ON} increases the MRR. For the increase in wire feed, there is a decreased MRR and similarly increased current increases MRR. Thus, it is noted that T_{ON} and current are the influencing parameters for MRR as confirmed in Figure 4(a). Figure 4(b) shows the interaction plot for R_a showing the similar trend as noted in the

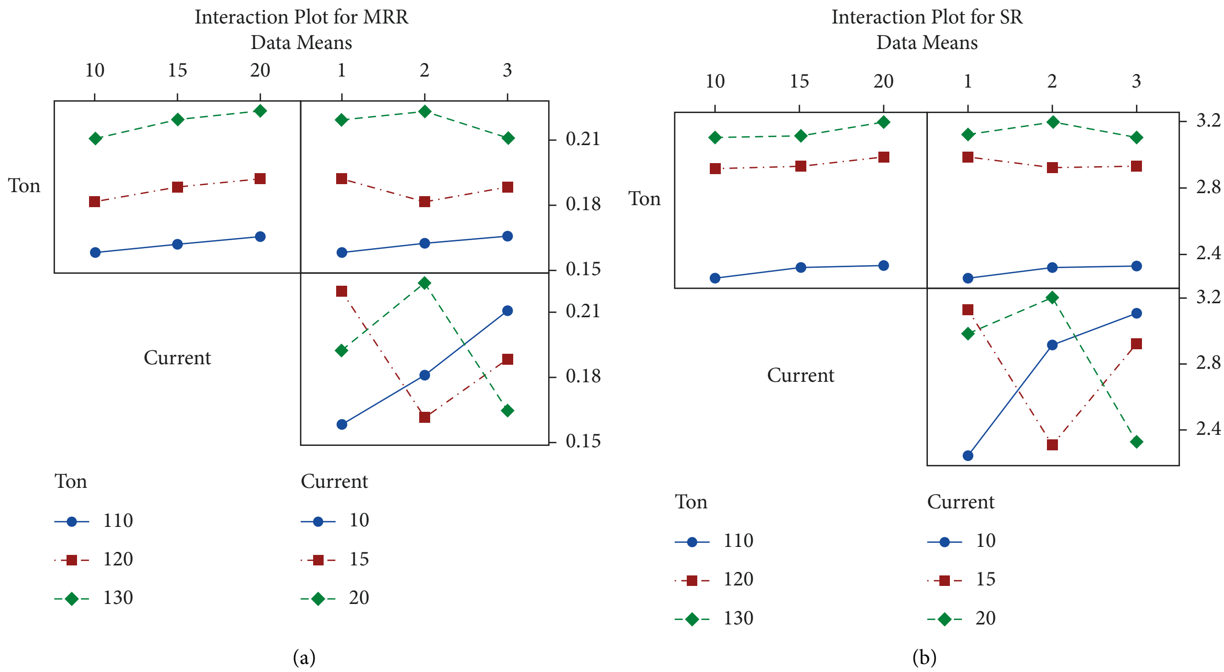

FIGURE 4: Interaction plots for (a) MRR and (b) R_a.

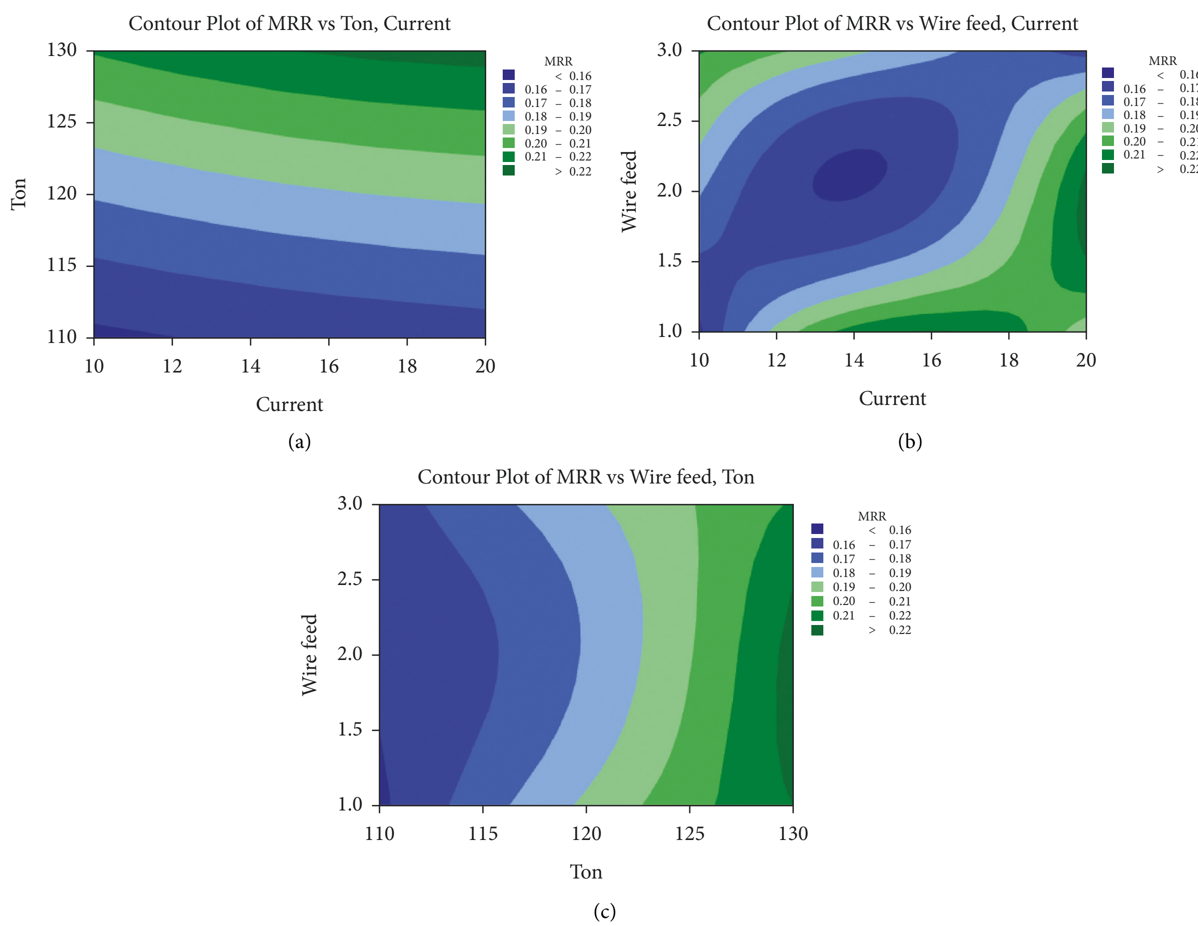

FIGURE 5: Contour plot for MRR: (a) T_{ON} and current, (b) wire feed and current, and (c) T_{ON} and wire feed.

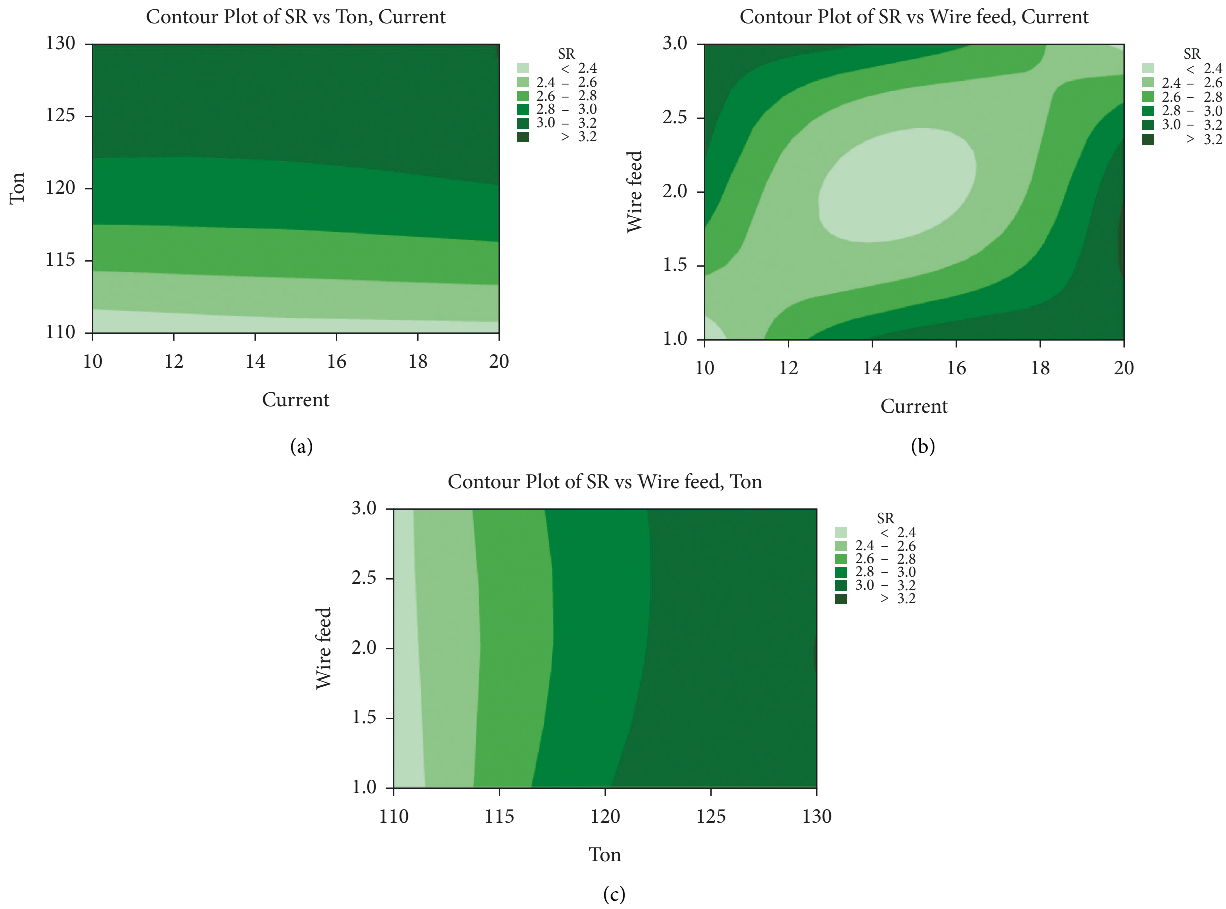

Figure 6: Contour plot for R_a: (a) T_{ON} and current, (b) wire feed and current, and (c) T_{ON} and wire feed.

interaction plot of MRR. Figure 4(b) also confirms T_{ON} and current are the influencing parameters for R_a.

3.2.5. Contour Plot. Figures 5(a)–5(c) indicate the contour plot for MRR. It is noted that higher MRR is attained for higher T_{ON} and current from Figure 5(a). Figure 5(b) shows better MRR for increased current and lower wire feed. Higher T_{ON} with lower wire feed showed improved MRR as seen in Figure 5(c).

Figures 6(a)–6(c) indicate the contour plot for R_a. It is noted that higher R_a is attained for higher T_{ON} and current noted from Figure 6(a). Figure 6(b) shows better R_a for increased current at lower wire feed and lower current with higher wire feed. Higher T_{ON} with higher wire feed showed improved R_a as seen in Figure 6(c). Thus, R_a increases with the increase in pulse on time and discharge energy [33, 34].

Thus, from the interaction plots of Figure 4, it is obviously understood that T_{ON} and current are the parameters mainly influencing both MRR and R_a. Contour plots of MRR and R_a also confirm the same which can be noted in Figures 5 and 6. A confirmatory test was conducted for the optimal parameter results with an error percentage of less than one confirming the accuracy of the study [35].

4. Conclusion

The conclusions derived from the WEDM analysis on AA7075 metal matrix composite reinforced with silicon nitride are as follows:

(1) Taguchi-based ANOVA analysis confirms Pulse ON time as the influencing parameter in achieving higher MRR and R_a

(2) Pulse ON time of 130 μs, current of 20 A, and wire feed of 1 mm/min were identified as optimized parameters for higher material removal rate

(3) For a good surface finish, the optimized parameter was identified as 130 μs pulse ON time, 20 A current, and wire feed rate of 2 mm/min

(4) Regression equation obtained shows minimal error indicating the accuracy of the analysis

(5) Pulse ON time and current have a direct influence on MRR and R_a

(6) Interaction plot and contour plot also confirm the ANOVA analysis proving pulse ON time as the influencing parameter followed by current

Data Availability

The data used to support the findings of this study are included within the article.

Conflicts of Interest

The authors declare that there are no conflicts of interest.

References

[1] A. K. Sahoo and S. Pradhan, "Modeling and optimization of Al/SiCp MMC machining using Taguchi approach," *Measurement*, vol. 46, no. 9, pp. 3064–3072, 2013.

[2] B. S. Sowrabh, B. M. Gurumurthy, Y. M. Shivaprakash, and S. S. Sharma, "Reinforcements, production techniques and property analysis of AA7075 matrix composites – a critical review," *Manufacturing Review*, vol. 8, no. 31, p. 31, 2021.

[3] M. Irfan Ul Haq and A. Anand, "Microhardness studies on stir cast AA7075-Si3N4 based composites," *Materials Today: Proceedings*, vol. 5, no. 9, pp. 19916–19922, 2018.

[4] H. P. Raturi, L. Prasad, M. Pokhriyal, and V. Tirth, "Estimating the effect of process parameters on metal removal rate and surface roughness in wedm of composite AL6063/SIC/AL2O3 by TAGUCHI method," *Journal of Mechanical Engineering*, vol. 67, no. 2, pp. 25–36, 2017.

[5] B. RajeshKumar, S. Kumar, and S. Das, "Machining performance of 7075 Al alloy SiC metal matrix composite with HSS and carbide tool," *Journal of Manufacturing Technology Research*, vol. 5, no. 1, pp. 17–41, 2014.

[6] A. Sharma, P. M. Mishra, and P. M. Mishra, "Machining characteristics, tribological and corrosion behaviour of AA7075 Hybrid Composites," *International Journal of Engineering and Advanced Technology*, vol. 9, no. 5, pp. 556–571, 2020.

[7] M. K. Sathish Kumar, B. Sravan Kumar, and S. K. Channankaiah, "Manufacturing and machining of aluminium metal matrix composites- an Overview," *International Journal of Applied Engineering Research*, vol. 10, no. 9, pp. 9312–9315, 2015.

[8] V. Venkata Reddy and K. Srinivasulu Reddy, "Multi objective optimization of machining parameters of AA7075 hybrid MMC by desirability function analysis," *International Journal of Advanced Research in Science, Engineering and Technology*, vol. 6, pp. 543–549, 2019.

[9] S. Suresh and D. Sudhakara, "Investigations on wire electric discharge machining and mechanical behavior of Al 7075/nano-SiC composites," *Journal of The Institution of Engineers (India): Series D*, vol. 100, no. 2, pp. 217–227, 2019.

[10] R. K. Bhushan, S. Kumar, and S. Das, "Effect of machining parameters on surface roughness and tool wear for 7075 Al alloy SiC composite," *The International Journal of Advanced Manufacturing Technology*, vol. 50, no. 5-8, pp. 459–469, 2010.

[11] H. Kumar, A. Manna, and R. Kumar, "Modeling of process parameters for surface roughness and analysis of machined surface in WEDM of Al/SiC-MMC," *Transactions of the Indian Institute of Metals*, vol. 71, no. 1, pp. 231–244, 2018.

[12] A. S. Gore and N. G. Patil, "Wire electro discharge machining of metal matrix composites: a review," *Procedia Manufacturing*, vol. 20, pp. 41–52, 2018.

[13] S. Prashantha, R. B. Veeresha, S. M. Shashidhara, U. S. Mallikarjun, and A. G. Shivasiddaramaiah, "A study on machining characteristics of Al6061-sic metal matrix composite through wire - cut electro discharge machining," *Materials Today: Proceedings*, vol. 4, no. 10, pp. 10779–10785, 2017.

[14] N. G. Patil and P. K. Brahmankar, "Semi-empirical modeling of surface roughness in wire electro-discharge machining of ceramic particulate reinforced Al matrix composites," *Procedia CIRP*, vol. 42, pp. 280–285, 2016.

[15] M. Kumar, A. Manna, S. K. Mangal, and A. Malik, "An experimental investigation during wire electrical discharge machining of Al/SiC-MMC," in *Proceedings of the International Conference on Research and Innovations in Mechanical Engineering ICRIME*, pp. 261–271, Ludhiana, Punjab, India, January 2014.

[16] M. S. Rao, "Venkaiah, review on wire-cut EDM process," *International Journal of Advanced Trends in Computer Science and Engineering*, vol. 2, no. 6, pp. 12–17, 2013.

[17] I. Maher, A. A. D. Sarhan, and H. Marashi, "1.9 effect of electrical discharge energy on white layer thickness of WEDM process," *Comprehensive Materials Finishing*, vol. 1, pp. 231–266, 2017.

[18] S. S. Mahapatra and A. Patnaik, "Optimization of wire electrical discharge machining (WEDM) process parameters using Taguchi method," *The International Journal of Advanced Manufacturing Technology*, vol. 34, no. 9-10, pp. 911–925, 2007.

[19] S. Vijayabhaskar, T. Rajmohan, T. V. P. Sisir, J. V. S. P. Abishek, D. Sharukh khan, and R. M. Reddy, "Review of WEDM studies on metal matrix composites," in *Proceedings of the The 3rd International Conference on Materials and Manufacturing Engineering 2018*, p. 390, Series, Materials Science and Engineering, Tamilnadu, India, 2018.

[20] M. Durairaj, D. Sudharsun, and N. Swamynathan, "Analysis of process parameters in wire edm with stainless steel using single objective taguchi method and multi objective grey relational grade," *Procedia Engineering*, vol. 64, pp. 868–877, 2013.

[21] G. Amitesh and K. Jatinder, "An investigation into the machining characteristics of Nimonic 80A using cnc wireEDM," *International Journal of Advances in Engineering & Technology*, vol. 3, pp. 170–174, 2012.

[22] H. Singh and R. Garg, "Effects of process parameters on material removal rate in WEDM," *Journal of Achievements in Materials and Manufacturing Engineering*, vol. 32, pp. 70–74, 2009.

[23] K. Kanlayasiri and S. Boonmung, "An investigation on effects of wire-EDM machining parameters on surface roughness of newly developed DC53 die steel," *Journal of Materials Processing Technology*, vol. 187-188, pp. 26–29, 2007.

[24] J. Yuan, K. Wang, T. Yu, and M. Fang, "Reliable multi-objective optimization of high-speed WEDM process based on Gaussian process regression," *International Journal of Machine Tools and Manufacture*, vol. 48, no. 1, pp. 47–60, 2008.

[25] L. T. Rao and N. Selvaraj, "Optimization of WEDM process parameters on titanium alloy using taguchi method," *International Journal of Modern Engineering Research*, vol. 3, no. 4, pp. 2281–2286, 2013.

[26] K. Zakaria, Z. Ismail, N. Redzuan, and K. W. Dalgarno, "Effect of wire EDM cutting parameters for evaluating of additive

manufacturing hybrid metal material," *Procedia Manufacturing*, vol. 2, pp. 532–537, 2015.

[27] S. Sharma and A. Sharma, "Review on process parameters of WEDM," *Journal Of Composition Theory*, vol. 12, no. 7, pp. 686–692, 2019.

[28] E. Nas, O. Özbek, F. Bayraktar, and F. Kara, "Experimental and statistical investigation of machinability of AISI D2 steel using electroerosion machining method in different machining parameters," *Advances in Materials Science and Engineering*, vol. 2021, Article ID 1241797, 17 pages, 2021.

[29] M. Akgün and F. Kara, "Analysis and optimization of cutting tool coating effects on surface roughness and cutting forces on turning of AA 6061 alloy," *Advances in Materials Science and Engineering*, vol. 2021, Article ID 6498261, 12 pages, 2021.

[30] N. A. Özbek, O. Özbek, and F. Kara, "Statistical analysis of the effect of the cutting tool coating type on sustainable machining parameters," *Journal of Materials Engineering and Performance*, vol. 30, no. 10, pp. 7783–7795, 2021.

[31] H. Bisaria and P. Shandilya, "Wire electric discharge machining induced surface integrity for Ni55.95Ti44.05 shape memory alloy," *Proceedings of the Institution of Mechanical Engineers, Part E: Journal of Process Mechanical Engineering*, vol. 235, no. 2, pp. 178–185, 2021.

[32] E. A. Ayyıldız, M. Ayyıldız, and F. Kara, "Optimization of surface roughness in drilling medium-density fiberboard with a parallel robot," *Advances in Materials Science and Engineering*, vol. 2021, Article ID 6658968, 8 pages, 2021.

[33] H. Bisaria and P. Shandilya, "Study on crater depth during material removal in WEDC of Ni-rich nickel-titanium shape memory alloy," *Journal of the Brazilian Society of Mechanical Sciences and Engineering*, vol. 41, no. 3, p. 157, 2019.

[34] H. Bisaria and P. Shandilya, "The machining characteristics and surface integrity of Ni-rich NiTi shape memory alloy using wire electric discharge machining," *Proceedings of the Institution of Mechanical Engineers, Part C: Journal of Mechanical Engineering Science*, vol. 233, no. 3, pp. 1068–1078, 2019.

[35] H. Bisaria and P. Shandilya, "Surface integrity of Ni-Rich NiTi shape memory alloy at optimized level of wire electric discharge machining parameters," *Journal of Materials Engineering and Performance*, vol. 28, no. 12, pp. 7663–7675, 2019.

Hindawi
Advances in Materials Science and Engineering
Volume 2022, Article ID 4344083, 8 pages
https://doi.org/10.1155/2022/4344083

Research Article

Comparative Study of Different Controllers for Levitating Ferromagnetic Material

T. Deepa,[1] **D. Subbulekshmi**,[1] **P. Lakshmi**,[2] **Marabathina Maheedhar**,[1] **E. Kishore**,[3] **M. Vinodharanai**,[4] **and T. Chockalingam**[5]

[1]*School of Electrical Engineering, Vellore Institute of Technology Chennai Campus, Vandalur-Kelambakkam Road, Chennai 600127, India*
[2]*Department of Electrical Engineering, Anna University, Chennai 600025, Tamilnadu, India*
[3]*Power Electronics, University of Colorado Boulder, Boulder, USA*
[4]*Robotics and Control, University of Colorado Boulder, Boulder, USA*
[5]*Department of Electrical and Computer Engineering, University of Gondar, Gondar, Ethiopia*

Correspondence should be addressed to T. Deepa; deepa.t@vit.ac.in, D. Subbulekshmi; subbulekshmi.d@vit.ac.in, and T. Chockalingam; chockalingam.t@uog.edu.et

Received 12 March 2022; Revised 15 April 2022; Accepted 22 April 2022; Published 20 May 2022

Academic Editor: Albert Alexander Stonier

The purpose of the analysis is to levitate and stabilize a spherical ball of magnetic levitation system at the desired position using various controllers and determine the one which gives better performance. The ball which is used to levitate is a ferromagnetic material such as stainless steel. This study talks about the proportional derivative controller, proportional integral derivative (PID) controller, and linear quadratic regulator (LQR) controller in place of a physical system. The transient response of the magnetic levitation system can be modified for desirable results due to the implementation of the controller. Simulation and experimental methods are used to verify the results. Both the techniques have been made to stabilize the ball position in the desired position. PID and LQR are designed to achieve the ball position to the desired level, and it is observed that the LQR controller gives the best result.

1. Introduction

The state-feedback control with the inertial delay observer (IDO) was proposed by Singru et al. [1] for precise control of a one-inch diameter steel ball in a magnetic levitation device. The levitation control differs from torque control, as demonstrated by Xue et al.'s levitation efficiency study of a type of the bearing-less switched reluctance motor (BLSRM).

Ginoya et al. compared the output of a cascaded sliding mode control designed for magnetic levitation systems with electrical and electromechanical loops to that of a standard linear quadratic regulator combined with a PI controller [2]. In their paper, Azukizawa et al. [3] succeeded in enhancing the system's levitation properties by increasing the magnetic field of the HTS magnet. A magnetic levitation control system is developed by linearizing the nonlinear system model around the operating point by Ghodsi et al. [4]. According to the results of Kim et al. [5], under cogging powers, magnetic levitation can achieve stable lavation and produce enough power for continuous operation. A prototype levitation platform with the steady-state power consumption per each HEM was created by designing a zero-power controller.

The object which is used to levitate the object is stainless steel which is a ferromagnetic material. The utilization of these materials is due to their ferromagnetism, as well as their outstanding corrosion, radiation, and heat resistant qualities [6]. From an application standpoint, the magnetic properties of ferromagnetic stainless steels SUS 403, TAF, and SUS 405 can be summarised as follows. They are harder than standard soft magnetic materials but weaker than semihard materials in terms of magnetic properties, and heat treatment changes the magnetic properties. The coercive force and rectangularity are increased by quenching and tempering. Full annealing reduces saturation induction and permeability marginally.

Core separation can be changed. According to Lim et al. [7], the levitation force ripples and cogging force are reduced, and the electromagnetic properties of the levitation magnet are investigated using the finite element analysis. Takao et al. [8, 9] used three models and proposed a few modifications that featured different arrangements to increase the levitation force in the system and identified that the common rail model's levitation force was seven times greater than the maximum levitation force of the common model. According to Liu et al. [10], AC superconducting windings that are used to increase levitation forces are well suited for hydraulic turbo-generator de-load applications. The inductive eddy magnetic field interacts with the primary field, producing levitation force and rotation torque between the primary and secondary fields, as well as ac loss power analysis and estimation.

Instead of incorporating both a levitation coil and a ready-made base, Bai and Lee [11] constructed an electromagnetic levitation coil with a pulse-width-modulation signal to change the magnetic levitation height. Amal et al. [12] devoted to a lumped circuit method based on a magnetic equivalent circuit for modelling and sizing of a tubular linear permanent-magnet synchronous motor (T-LPMSM). By implementing the output oversampling scheme to collect the input-output data, the subspace characteristics are used to complement the excitation of the observed data; Sun et al. [13] express the formula that can easily explore the unstable dynamics of the magnetic levitation model.

Andreev's. [14] mathematical model calculates the polarization of the sphere, and the factors affecting effective magnetic charges are determined by an axially magnetized torus. Yuming Gong analyses and concludes that, for better levitation performance of the field distribution, levitation force, and guiding force, the iron shim with 4 mm thickness is the best among 4, 6, and 8 mm iron shims due to decrease in suspension gap, which is experimented in [15]. To investigate the effect of magnetic field gradient on LFD of MP-added superconductors to the device, Abdioglu et al. [16] used the effect of magnetic flux distribution and magnetic power addition on magnetic levitation force with superconductors.

Pandey et al. [17] discuss the design of a fractional sliding mode controller for a nonlinear magnetic levitation device dynamic to regulate the current through an electromagnetic coil to levitate a ferromagnetic ball. Hernandez et al. [18] build a controller as a combination of a fact and an LQR gain matrix to replace the proportional operation of fractional PID to LQR gain matrix. By using the context of LQR optimal control, Miller [19] has demonstrated that the optimally decentralized system has strong controllability and observability performance, which is the same as the optimally centralized system which has been considered. This performance of the LQR control decentralized system is enhanced by the linear periodic controller with its graphs strongly associated with the system. By minimizing the objective function of the plant system such as electronic devices and vibration reduction of structures, Teppa Garran et al. [20] have smoothened the transient response of the measured output which contains linear quadratic regulator (LQR) in the quadratic form. Norman [21] mentioned his development of a state-space approach with LQR for the modern control theory which is used to analyse the system. The developed state-space method is relatively easier for multioutput systems.

Eswaran et al. [22] have derived the transfer function for the DC servo motor and controlled the motor's speed by the PID controller. Later, they have discussed the vulnerabilities and threats that can be caused by IoT-connected devices and proposed a cybersecurity solution for safeguarding privacy. Nagarajan et al. [23] has designed a PI controller for the AC servo motor after deriving its transfer function.

Furthermore, they have analysed the step response of the system obtained to the time-domain specifications. The inverted pendulum is a difficult control issue that constantly moves into an unregulated state, and the result from A.N.K. Nasir and 1M.A. Ahmad shows that LQR provided a better response than PID control strategies and is presented in the time domain [24]. Munder and Yaseen have experimented on the SIMLAB platform based on three parameters such as peak overshoot, settling time, and rise time for LQR, PID, and lead compensation controllers for magnetic levitation system. This study backs up our claim that LQR performs best in terms of peak overshoot, settling time, and rise time, with 14.6 percent, 0.199, and 0.064 for peak overshoot, settling time, and rise time, respectively [25].

Novelty of the work is improving the magnetic levitation system performance by using the LQR controller than the PID controller, and comparative analysis was carried our by comparing the settling time, rise time, and peak overshoot of the magnetic levitation system when operated with PID and LQR controllers.

2. Physical Model

2.1. Magnetic Levitation System. Magnetic object and magnetic field interaction is used to suspend or levitate a magnetic object. This technique is used in the magnetic levitation system to suspend a ball in its electromagnetic field. With electronic feedback control, a magnetic object can be stabilized and levitated by dynamically adjusting one or more electromagnets in the magnetic system to stabilize the magnetically levitated object at the desired position. To stabilize the levitated magnetic platform, servo control is maintained to control the field of magnetic force that levitates it.

Figure 1 shows the magnetic levitation system with parts labelled. The basic principle of magnetic levitation system operation is to keep ferromagnetic objects levitated using the applied voltage on the electromagnet. The object's position is determined through a sensor.

2.2. Modelling of Magnetic Levitation System. The mathematical representation of the system can be categorized into 3 parts: electrical, mechanical, and sensor models. The electrical model can be viewed from the electrical equation derived using Kirchhoff's law, where Figure 2 shows the

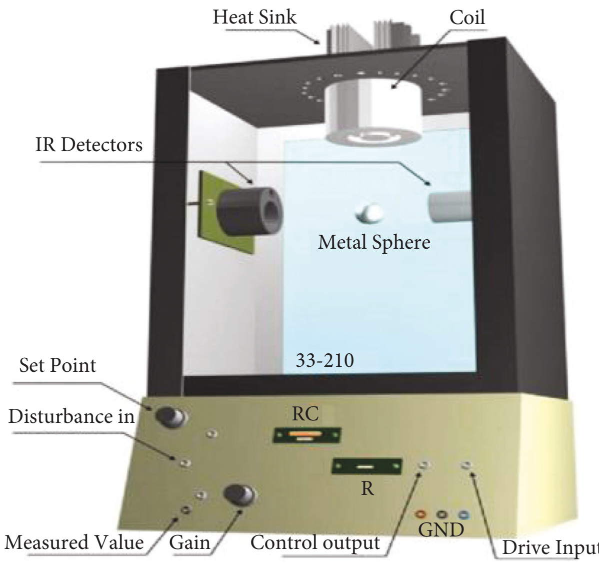

Figure 1: Magnetic levitation system.

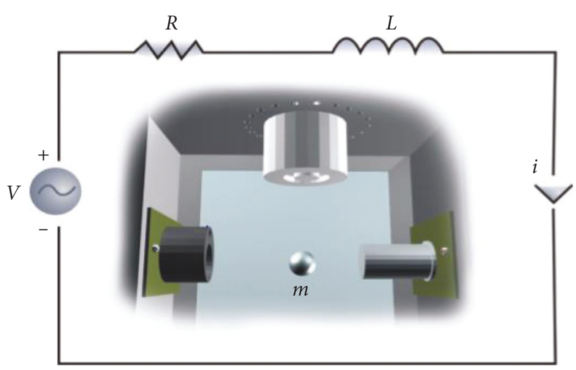

Figure 2: Electrical circuit of the Maglev system: electrical model of the system.

equivalent electrical circuit of the magnetic levitation system, and the system parameters are shown in Table 1.

$$v = iR + L\frac{di}{dt}. \tag{1}$$

Considering the inductance resistance as R_L,

$$v = i(R_L + R_S) + L\frac{\mathrm{di}}{\mathrm{dt}}. \tag{2}$$

Taking Laplace transform from equation (2),

$$V(s) = I(s)(R_L + R_S) + Ls * I(s), \tag{3}$$

$$V(s) = I(s)[Ls + (R_L + R_S)], \tag{4}$$

$$\frac{I(s)}{V(s)} = \frac{1}{Ls + (R_L + R_S)}. \tag{5}$$

The mechanical model of the system is

$$F = mg - k_f\left[\frac{i}{x}\right]^2. \tag{6}$$

Table 1: The parameter value of the Maglev system.

Variables	Values
Mass of ball (m)	0.0571 kg
Inductance (L)	0.017521 H
Resistance (R)	0 .0243 ohm
A	0.005831
x_0	0.0225
Spring constant (K)	0.0001477 $\mathrm{Nm^2/A^2}$
Gravity (g)	9.81 $\mathrm{m/s^2}$

By Newton's second law,

$$F = m\frac{d^2x}{dt^2}, \tag{7}$$

$$m\frac{d^2x}{dt^2} = mg - k_f\left[\frac{i}{x}\right]^2. \tag{8}$$

For obtaining steady-state ball position X_{ss} which gives steady-state current i_{ss},

$$\begin{aligned} \frac{d^2x}{dt^2} &= 0, \\ mg &= k_f\left[\frac{i_{ss}}{X_{ss}}\right]^2, \\ \sqrt{\frac{mg}{k_f}}X_{ss} &= i_{ss}. \end{aligned} \tag{9}$$

According to vector standard of shifted variables defined,

$$\hat{x}(t) \triangleq x(t) - X_{ss}, \tag{10}$$

$$\hat{i}(t) \triangleq i(t) - i_{ss}. \tag{11}$$

Rearranging (10) and (11),

$$\begin{aligned} \hat{x} + X_{ss} &\triangleq x(t), \\ \hat{i} + i_{ss} &\triangleq i(t). \end{aligned} \tag{12}$$

Applying the shifted variables to mechanical (8),

$$m\frac{d^2x}{dt^2} = mg - k_f\left[\frac{\hat{i} + i_{ss}}{\hat{x} + X_{ss}}\right]^2. \tag{13}$$

Linearizing (13) $(\hat{x} = 0, \hat{i} = 0)$,

$$\begin{aligned} \frac{d^2x}{dt^2} = \frac{1}{m}\Bigg[&\left|\frac{\partial}{\partial x}\left(mg - k_f\left[\frac{\hat{i} + i_{ss}}{\hat{x} + X_{ss}}\right]^2\right)\right|_{(\hat{x}=0,\hat{i}=0)}\hat{x} \\ &+ \left|\frac{\partial}{\partial x}\left(mg - k_f\left[\frac{\hat{i} + i_{ss}}{\hat{x} + X_{ss}}\right]^2\right)\right|_{(\hat{x}=0,\hat{i}=0)}\hat{i}\Bigg], \end{aligned} \tag{14}$$

$$\frac{d^2x}{dt^2} = \frac{2k_f i_{ss}^2}{mx_{ss}^3}\hat{x} - \frac{2k_f i_{ss}}{mx_{ss}^2}\hat{i}. \tag{15}$$

Laplace transform of (15) is

$$\frac{X(s)}{I(s)} = \frac{2k_f i_{ss}/mx_{ss}^2}{s^2 - 2k_f i_{ss}^2/mx_{ss}^3}. \quad (16)$$

Equating electrical (5) and mechanical equation (16),

$$\frac{X(s)}{V(s)} = \frac{2k_f i_{ss}/mx_{ss}^2}{s^2 - 2k_f i_{ss}^2/mx_{ss}^3} * \frac{1}{Ls + (R_L + R_S)}. \quad (17)$$

Table 1 gives the detailed system parameters, and by substituting the above values in equation (17), the transfer function of the system is as follows:

$$\frac{x(s)}{v(s)} = \frac{77.44}{s^3 + 70.16s^2 - 849.2s - 0.5947}. \quad (18)$$

3. Controller Design for the Magnetic Levitation System

3.1. PID Controller. PID (proportional integral derivative) controllers are the most accurate and stable controllers, which controls process variables using the control loop feedback mechanism. To keep the actual output from a process as close to the set point or target output as possible the PID controller uses a closed-loop control feedback mechanism. PID controller's main purpose is to force feedback to match a set point. The proportional, integral, and derivative are individually adjusted or turned in a PID controller.

General PID algorithm form is given as

$$u(t) = K_p * e(t) + K_i \int e(t)dt + K_d \frac{de(t)}{dt}. \quad (19)$$

The PID controller is designed, and the proportional, integral, and derivative values were derived using the Ziglar Nicholas method.

The mechanism of PID controller gain is proportional term generates a result that is proportionate to the current error value. By multiplying the error by a constant Kp, also known as the proportional gain constant, the proportional response can be changed. The integral term's impact is proportional to the magnitude of the error as well as the duration of the error. In a PID controller, the integral is the total of the instantaneous error over time, which represents the accumulated offset that should have been corrected earlier. The integral gain (Ki) is then multiplied by the accumulated error and added to the controller output. Determine the slope of the error over time and multiply this rate of change by the derivative gain Kd to get the derivative of the process error. The derivative gain, Kd, is the magnitude of the derivative term's contribution to the total control action.

For the magnetic levitation system,

(i) Kp = 0.000547

(ii) Ki = 5.94e-09

(iii) Kd = 12.6

This value is fed to the PID controller of the closed-loop system.

3.2. LQR Controller. The linear quadratic regulator (LQR) enables the high-performance design and the closed-loop stable state of the system using a method that provides optimally controlled feedback gains. It uses the state-space method to analyse a system which is a method in modern control theory. A multioutput system is relatively simple when working with the state-space method. Full-state feedback can be used to stabilize the system.

Algebraic Riccati equation is

$$A^T P + PA - PBR^{-1}B^T + Q = 0, \quad (20)$$

$$K = R^{-1}B^T P. \quad (21)$$

Table 4 shows the LQR method decreases the amount of work that the control systems' engineer has to undertake in order to optimise the controller. However, the engineer must still define the cost function parameters and compare the results to the design objectives. This usually means that controller development will be an iterative process in which the engineer evaluates the "best" controllers generated by simulation and then tweaks the parameters to produce a controller that is more in line with the design goals. The linear-quadratic regulator (LQR), a feedback controller whose equations are given below, provides one of the theory's fundamental results.

To find LQR gain values, Ricatti equation (20)is

$$-A^T P + PA - PBR^{-1}B^T + Q = 0, \quad (22)$$

where the LQR gain values were found using the Ricatti equation (20):

$$A^T P + PA - PBR^{-1}B^T + Q = 0, \quad (23)$$

where

$$\begin{aligned} A &= A - BR^{-1}B^T, \\ Q &= Q - BR^{-1}B^T, \\ K &= R^{-1}B^T P. \end{aligned} \quad (24)$$

Substituting the values of A, B, Q, and R in equation (20), the gain values obtained are 0.0211, 1.6985, and 0.0018 as derived.

4. Results and Discussion

4.1. PID Controller Output. Experimental output of the control signal and ball position of a magnetic levitation system using the PID controller for various input signals are shown in Figure 3. The values are

(i) Kp: 32

(ii) Ki: 0.05

(iii) Kd: 0.17

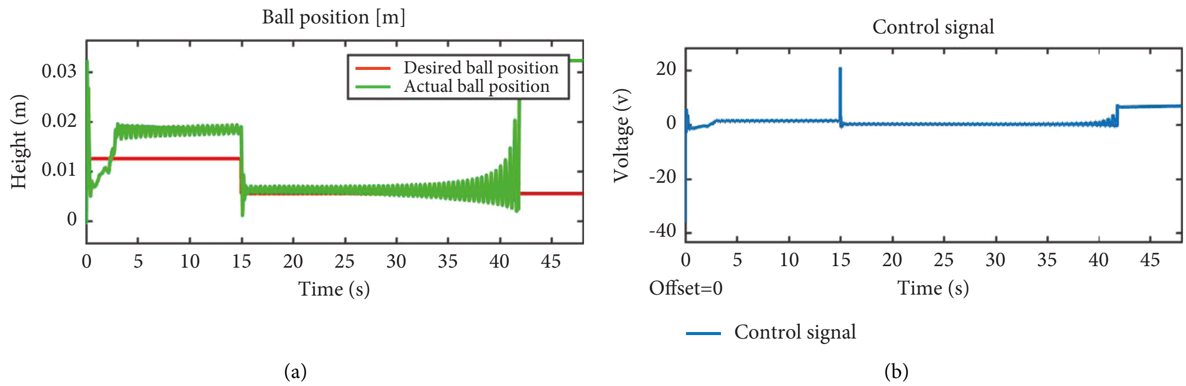

Figure 3: STEP output and control signal for the PID controller.

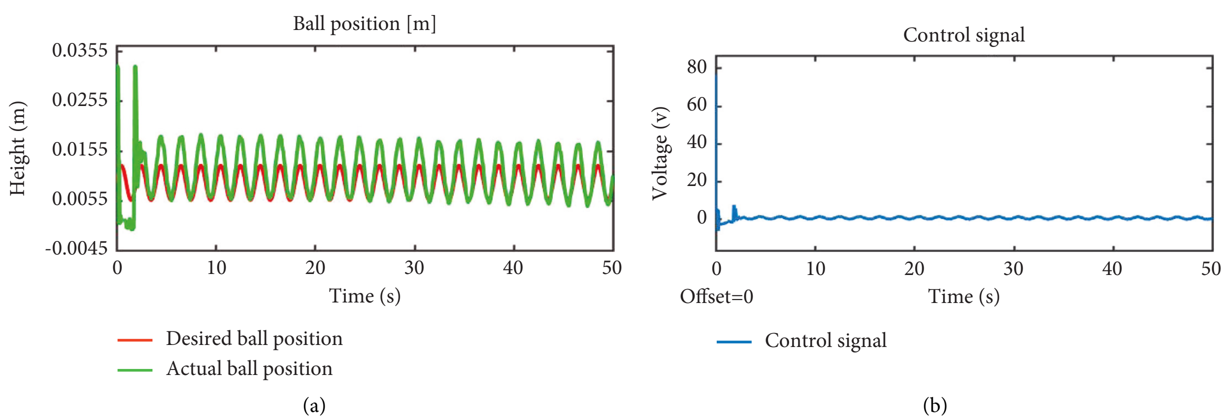

Figure 4: SINE output and control signal for the PID controller.

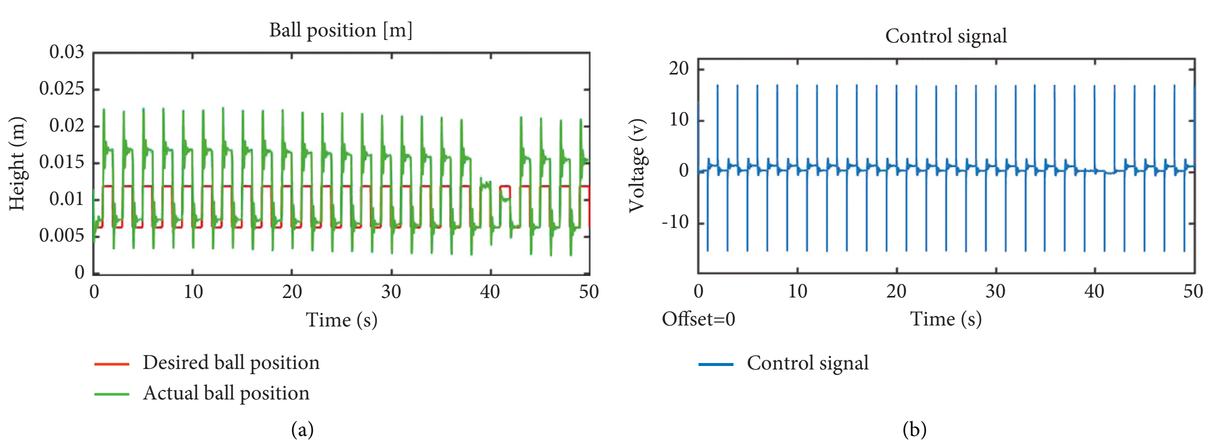

Figure 5: SQUARE output and control signal for the PID controller.

Table 2: PID output inference.

PID controller	Step	Square	Sine
Peak overshoot	3.081×10^{-2}	3.13×10^{-2}	1.943×10^{-2}
Settling time	0.5079×10^{-2}	0.7765×10^{-2}	1.102×10^{-2}
Rise time	1.43×10^{-2}	1.0067×10^{-2}	1.26×10^{-2}

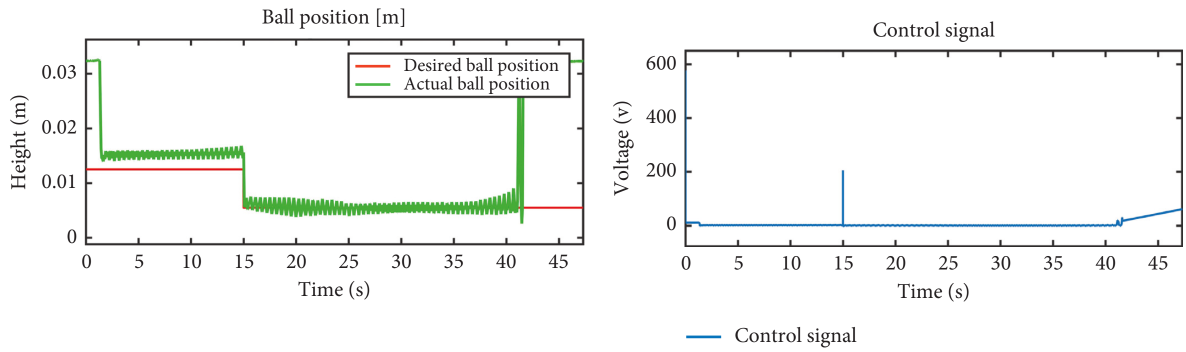

(a) (b)

Figure 6: STEP output and control signal for the LQR controller.

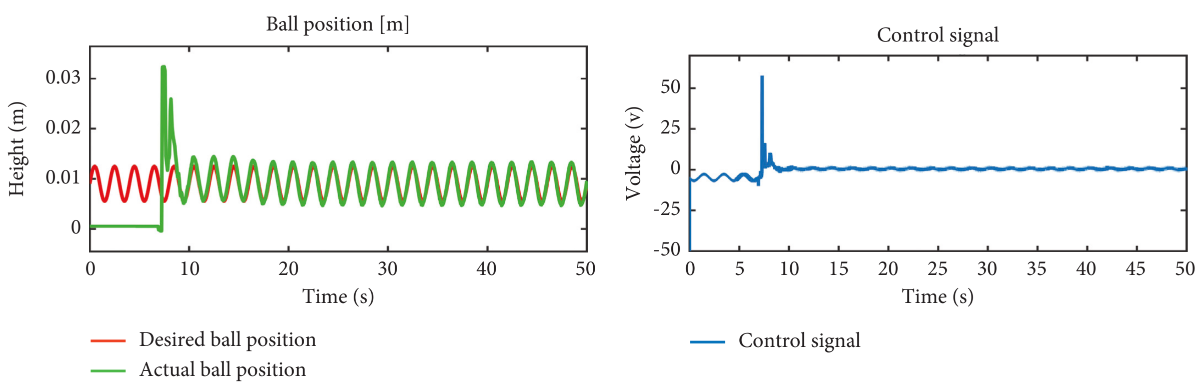

(a) (b)

Figure 7: SINE output and control signal for the LQR controller.

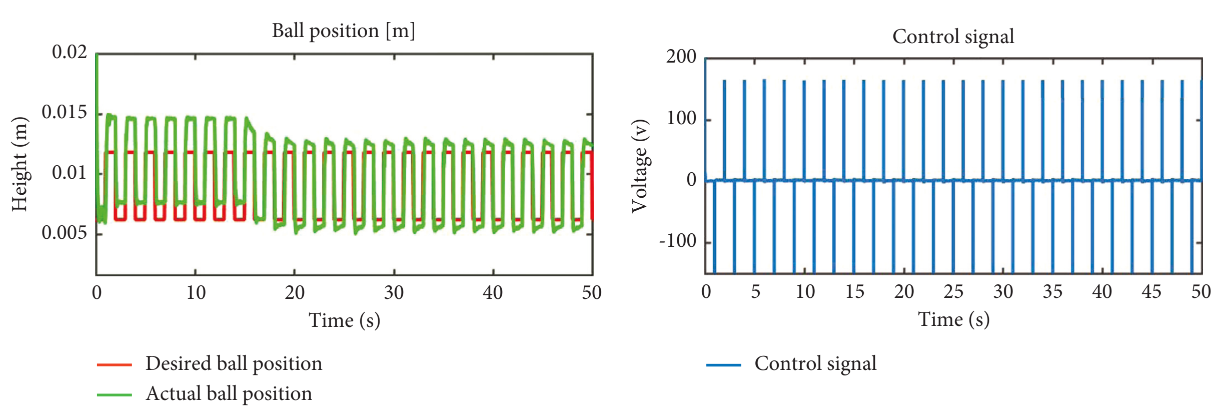

(a) (b)

Figure 8: SQUARE output and control signal for the LQR controller.

Table 3: LQR output inference.

LQR	Step	Square	Sine
Peak overshoot	1.56×10^{-2}	1.441×10^{-2}	3.1×10^{-2}
Settling time	0.588×10^{-2}	1.075×10^{-2}	0.8802×10^{-2}
Rise time	1.154×10^{-2}	0.8357×10^{-2}	0.546×10^{-2}

Table 4: Response of the magnetic levitation system with PID and LQR controllers.

Controllers	Response	Step	Square	Sine
PID	Peak overshoot	3.081×10^{-2}	3.13×10^{-2}	1.943×10^{-2}
	Settling time	0.5079×10^{-2}	0.7765×10^{-2}	1.102×10^{-2}
	Rise time	1.43×10^{-2}	1.0067×10^{-2}	1.26×10^{-2}
LQR	Peak overshoot	1.56×10^{-2}	1.441×10^{-2}	3.1×10^{-2}
	Settling time	0.588×10^{-2}	1.075×10^{-2}	0.8802×10^{-2}
	Rise time	1.154×10^{-2}	0.8357×10^{-2}	0.546×10^{-2}

Step, sinusoidal, and square response of the magnetic levitation system is shown in Figures 3–5, respectively, by using the PID controller. When we observe the response of actual ball position, it is unable to reach desired ball position. Table 2 shows the PID output inference.

4.2. Inference from the PID Graph

4.3. LQR Controller Output. The experimental output of the ball position and control signal of a magnetic levitation system using an LQR controller are shown in Figure 4.

Figures 6–8 show the step response, sinusoidal, and square response of the magnetic levitation system by using the LQR controller. By using the PID controller, when we observe the response of actual ball position, compared to the PID controller, it is able to reach desired ball position. Table 3 shows the LQR output inference.

4.4. Inference from the LQR Graph. Table 4 shows the response of the magnetic levitation system for various response using PID and LQR controllers. For the PID controller, peak overshoot for step, square, and sine is 3.081×10^{-2}, 3.13×10^{-2}, and 1.943×10^{-2}, respectively. Settling time is 0.5079×10^{-2}, 0.7765×10^{-2}, and 1.102×10^{-2} for step, square, and sine response, respectively. Rise time for step, square, and sine is 1.43×10^{-2}, 1.0067×10^{-2}, and 1.26×10^{-2}. For the LQR controller, peak overshoot for step, square, and sine is 1.56×10^{-2}, 1.441×10^{-2}, and 3.1×10^{-2}, respectively. Settling time is 0.588×10^{-2}, 1.075×10^{-2}, and 0.8802×10^{-2} for step, square, and sine response, respectively. Rise time for step, square, and sine is 1.154×10^{-2}, 0.8357×10^{-2}, and 0.546×10^{-2}.

5. Conclusion

From the implementation of the PID and LQR controller, we have analysed the transient response of the physical magnetic levitation system. For step response, peak overshoot is 1.56×10^{-2} by using the LQR controller. Similarly, by using the LQR controller, peak overshoot of the square response is 1.441×10^{-2}, and for sine response, peak overshoot is 3.1×10^{-2}. For step response, peak overshoot is 3.081×10^{-2} by using the PID controller. Similarly, by using the PID controller, peak overshoot of the square response is 3.13×10^{-2}, and for sine response, peak overshoot is 1.943×10^{-2}. It is observed from the obtained results that the LQR controller gives us more satisfactory results among the PID controllers tested. This is verified using the difference between the graphs and the obtained peak overshoot, settling point, and oscillation of the output signal response.

Data Availability

The data used to support the findings of this study are included within the article. Further data or information can be obtained from the corresponding author upon request.

Disclosure

This study was performed as a part of the Employment of University of Gondar, Ethiopia.

Conflicts of Interest

The authors declare that there are no conflicts of interest regarding the publication of this paper.

Acknowledgments

The authors appreciate the supports from University of Gondar, Ethiopia. The authors thank Anna University, Chennai, and Vellore Institute of Technology, Chennai, for the technical assistance to support this study.

References

[1] N. Singru, D. Ginoya, P. D. Shendge, and S. B. Phadke, "A state-feedback control approach via inertial delay observer for Magnetic Levitation system," in *Proceedings of the 2015 International Conference on Industrial Instrumentation and Control (ICIC)*, pp. 1670–1674, Pune, India, May 2015.

[2] D. Ginoya, C. M. Gutte, P. Shendge, and S. Phadke, "State-and-disturbance-observer-based sliding mode control of magnetic levitation systems," *Transactions of the Institute of Measurement and Control*, vol. 38, no. 6, pp. 751–763, 2016.

[3] T. Azukizawa, S. Yamamoto, and N. Matuso, "Feasibility study of a passive magnetic bearing using the ring shaped permanent magnets," *IEEE Transactions on Magnetics*, vol. 44, no. 11, pp. 4277–4280, 2008.

[4] M. Ghodsi, T. Ueno, and T. Higuchi, "Improvement of magnetic circuit in levitation system using HTS and soft magnetic material," vol. 41, no. 10, pp. 1–3, 2005.

[5] C. H. Kim, H. W. Cho, J. M Lee, H. S. Han, B. S. Kim, and D. S. Kim, "Levitation Control of a Hybrid-Excited Magnetic Levitation Vehicle," in *Proceedings of the 11th International Conference On Control Automation and Systems (ICCAS)*, pp. 1020–1024, Gyeonggi-do, Korea (South), October 2011.

[6] K. Ara, "Magnetic characteristics of ferromagnetic stainless steels," *IEEE Transactions on Magnetics*, vol. 25, no. 3, pp. 2617–2623, 1989.

[7] J. Lim, C. H. Kim, J. M Lee, H. S. Han, and D. Y. Park, "Design of magnetic levitation electromagnet for high-speed maglev train," in *Proceedings of the International Conference on Electric Machines And Systems (ICEMS)*, Busan, Korea (South), October 2013.

[8] T. Takao, S. Yasukawa, N. Negishi, T. Usami, and H. Kamijo, "Increase in levitation force due to multifaceted arrangement of a magnetic levitation system using HTS bulk," *IEEE Transactions on Applied Superconductivity*, vol. 26, no. 4, pp. 1–5, 2016.

[9] T. Takao, T. Horie, T. Usami, M. Takahashi, and H. Kamijo, "Levitation property of parallel magnetic levitation system with magnetic shielding effect of HTS bulks," *IEEE Transactions on Applied Superconductivity*, vol. 24, no. 3, pp. 1–4, 2014.

[10] J. Liu, H. Ma, P. Ju, and L. Huang, "Design and analysis of a superconducting induction magnetic levitation device for vertical hydraulic generator," *IEEE Transactions on Magnetics*, vol. 53, no. 6, pp. 1–4, 2017.

[11] Y.-W. Bai and C.-F. Lee, "Magnetic Levitation Wireless Charging Platform with Adjustable Magnetic Levitation Height and Resonant Frequency for a Better Charging Efficiency," in *Proceedings of the International IEEE 7th Global Conference on consumer Electronics (GCCE)*, Nara, Japan, October 2018.

[12] S. Amal, W. Z. Mohamed, I. Abdennadher, and M. Ahmed, "MEC-based modelling and sizing of a tubular linear PM synchronous machine," *IEEE Transactions on Industry Applications*, vol. 51, no. 3, pp. 2181–2194, 2015.

[13] L. Sun, A. Sano, and X. Liu, "Direct closed-loop identification approach to magnetic levitation system," *IFAC-PapersOnLine*, vol. 51, no. 15, pp. 610–615, 2018.

[14] K. Andreev, "Levitation of a soft magnetic sphere in a field of superconducting coils simulating an axially magnetic torus," *Moscow Aviation Institute*, vol. 47, 2017.

[15] Y. Gong, G. Liang, L. Zhao, Y. Zhang, Y. Zhao, and X. Chen, "Magnetic levitation performance of high-temperature superconductor over three magnetic hills of permanent magnet guideway with iron shims of different thicknesses," *Journal of modern transportation*, vol. 22, no. 3, pp. 187–193, 2014.

[16] M. Abdioglu, K. Ozturk, S. Kutuk, S. Bolat, and E. Yanmaz, "Effect of magnetic flux distribution and magnetic powder addition on the magnetic levitation force of Sm123 superconductors," *Journal of Superconductivity and Novel Magnetism*, vol. 25, no. 4, pp. 923–929, 2012.

[17] S. Pandey, V. Dourla, P. Dwivedi, and A. Junghare, "Introduction and realization of four fractional-order sliding mode controllers for nonlinear open-loop unstable system: a magnetic levitation study case," *Nonlinear Dynamics*, vol. 98, no. 1, pp. 601–621, 2019.

[18] O. Hernandez, P. Ortiz, and J. Herrera, "Fractional PID controller with LQR proportional action applied to fractional model of cement rotary kiln," *IEEE Latin America Transactions*, vol. 13, no. 1, pp. 37–42, 2015.

[19] D. E. Miller, "A comparison of LQR optimal performance in the decentralized and centralized settings," *IEEE Transactions on Automatic Control*, vol. 61, no. 8, pp. 2308–2311, 2016.

[20] P. Teppa Garran, V. Nardone, and J. Rodriguez Diez, "LQR control employing output derivative measures," *IEEE Latin America Transactions*, vol. 13, no. 8, pp. 2538–2544, 2015.

[21] N. Norman, *Control System Engineering*, John Wiley & Son, Hoboken, New Jersey, 2000.

[22] K. Eswaran, M. S. S. Kumar, D. Thangavelusamy, and V. Murugadoss, "Smart Servomotor for Robotics and its Cyber Security," in *Proceedings of the 2020 Advanced Computing And Communication Technologies For High Performance Applications (ACCTHPA)*, pp. 231–236, Cochin, India, July 2020.

[23] S. Nagarajan, S. Senthilkumar, K. Eswaran, and D. Thangavelusamy, "Study of AC servo motor and extraction of step response characteristics," in *Proceedings of the IEEE International Conference on Power, Control, Signals and Instrumentation Engineering (ICPCSI)*, pp. 1732–1735, Chennai, India, September 2017.

[24] A. N. K Nasir, M. A Ahmad, and M. F Rahmat, "Performance comparison between LQR and PID controllers for an inverted pendulum system," in *Proceedings of the AIP Conference Proceedings*, vol. 1052, no. 1, pp. 124–128, American Institute of Physics, Chiangmai, Thailand, July 2008.

[25] M. H. A. Yaseen and H. J. Abd, "Modeling and control for a magnetic levitation system based on SIMLAB platform in real time," *Results in Physics*, vol. 8, pp. 153–159, 2018.